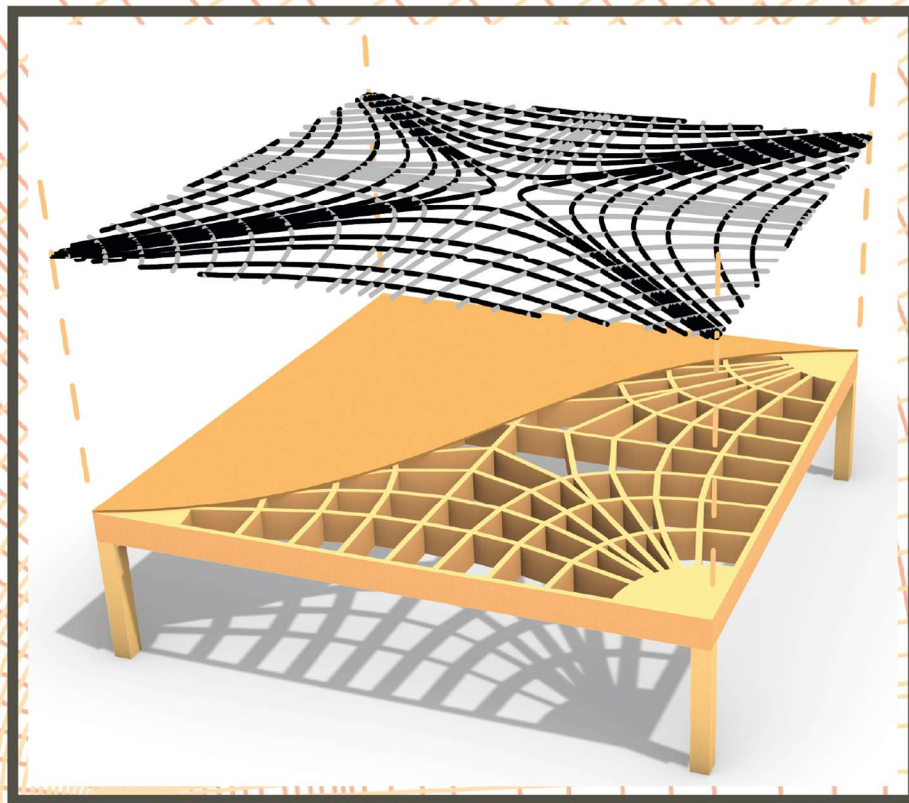# INVESTIGATION OF ISOSTATIC SLABS IN TIMBER

Matthew Church

TUDelft

INVESTIGATION OF
ISOSTATIC SLABS IN TIMBER

BY

MATTHEW CHURCH

In partial fulfilment of the degree Master of Science
in Civil Engineering – Building Engineering
at the Delft University of Technology,
to be publicly defended on Friday, February 12th, 2021

TUDelft

PREFACE

This thesis marks the end of my time as a student at the Delft University of Technology, and is the last necessary part to obtain a Master of Science Degree in Civil Engineering.

The initial idea for this thesis began from a discussion I had with John Harding and Stephen Melville back in November 2019, where John proposed the idea of investigating a slab which was similar to the ribbed slabs produced by Pier Luigi Nervi but made from CLT. From this moment, my interest in principal stress lines and isostatic slabs was hooked.

I would like to thank my committee members for their continued support throughout my thesis, their critical and constructive questions about my work, all of the feedback that they gave me, and their guiding hands from start to end. I would like to particularly thank Roy Crielaard for regularly meeting with me and helping me to keep going even when my progress was slow.

A special thanks goes to my friends at Format Engineers for helping me with the coding parts of my thesis and answering all of my questions; especially Will Pearson for providing a working implementation of the Farthest Point Seeding Method.

I can't be happier with all the support I received from my family and friends, who I wouldn't have been able to complete this journey without. I'm especially grateful for all of the incites Vincent Huigen gave me about the finite element method and how I could use it. I'm immensely thankful for having Laura Āboltiņa as my flatmate for the last year and for always being happy to chat with me while we were locked down in that small flat in Delft. Lastly, but by no means least, I would like to thank my friend Felicia Baily and her family for inviting me into their home and giving me somewhere to complete this journey.

Matt Church
Dartmoor, February 2021

ABSTRACT

The isostatic slab was developed by Pier Nervi and his colleague Aldo Arcangeli to create an elegant and easy to produce floor system, with efficient use of material. These slabs are designed with ribs aligned to the principal bending stress lines that support a flat deck. Concrete isostatic slabs are no longer constructed due to their expensive formwork. However, this system could be advantageous when made from timber as the grain direction will be aligned to the optimal flow of forces. Additionally, isostatic slabs can be designed for any support conditions, so an isostatic timber slab may be more desirable than the typical one-way spanning timber systems.

The isostatic timber slab is a new concept and has not been previously used. Therefore, before the system can be applied, there needs to be a greater understanding of the design process. This research achieves this goal by splitting the process into two parts. Firstly, the rib geometry is created by generating the principal bending stress lines. Secondly, the system is designed and analysed for a case study. The aim is achieved by creating a functional design and identifying the critical areas in the design process.

An approach for measuring the accuracy of stress lines is developed and used to test different methods for improving the stress line generation process. The improved process uses a more advanced integration method and a holistic seeding method. Additionally, a novel method for interpolating the principal stress trajectories from finite element analysis (FEA) results is established by utilising the shape functions from the theory of FEA.

An iterative approach used to select stress lines to create optimised truss geometries in in-plane-loaded plates is tested for its applicability to out-of-plane loaded plates (i.e. slabs). The rib geometry produced was measured by the approximation error and the deck elements' span lengths. This iterative approach does not apply to slabs as it creates clustered areas and excludes symmetries.

Analysis of principal stresses under different load cases shows that the most considerable difference from the primary load case is when half of the slab is loaded with a maximum load and half with a minimum load. (The primary load case is the condition used to create the stress lines for the rib geometry). Using FEA to calculate the stresses under each load case shows that uneven loading of the slab does not produce higher stresses than the primary load case.

A functional isostatic timber slab design is made for the case study using laminated veneer lumber (LVL) for the ribs and plywood for the deck. Linear elastic FE modelling of the structure shows that increasing the deck thickness and decreasing the rib depth, causes the deck to carry more load and the ribs to carry less and vice versa. Increasing the rib thickness has a small effect on the force distribution due to the available LVL thicknesses. The FE modelling also showed that the torsional load transfer mechanisms are reduced by increasing the rib slenderness.

The design is made based on the ultimate limit state (ULS) stress requirements for the elements and three critical connections, and the deflection under the serviceability limit state (SLS). The rib-to-deck joint requirements determine the deck thickness, and the deck has a low utilisation for the stress conditions, meaning that the deck span lengths are not critical.

The ribs' depth is heavily dependent on the rib-to-rib moment connection as a large lever is needed. The cross-sectional properties of the ribs are also dependant on the standard LVL sizes.

This system is compared to several conventional one-way spanning alternatives based on the total material volume, the structural weight, and the structural depth. The isostatic timber slab has a reduced volume and weight compared to a flat cross-laminated timber (CLT) slab, a Kerto-Ripa slab, and a concrete hollow-core slab; however, the isostatic timber slab has a larger structural depth. A 'T'-beam equivalent to the two-way spanning isostatic slab has less volume and weight while maintaining the same structural depth, but has a larger average deflection.

Timber isostatic slabs are complex to design with a highly connected network of parameters. The system should be designed by minimising the peak moment forces at connections, curating the support conditions to reduce stress line clustering, and selecting stress lines for the rib geometry which ensure sufficient stiffness at the peak deflection location. It is advised to produce a parametric model of the slab that can quickly assess the design performances and efficiently complete design cycles.

TABLE OF CONTENTS

1 BACKGROUND

1.1 Introduction

This chapter will give all the relevant background information required to understand the base level of knowledge on which this thesis is built. This will provide the reader will all the background they require provided that they already have knowledge about civil and structural engineering.

1.2 Isostatic Slabs

Pier Nervi is known for his large span shell structures, but he also spent a part of his early career developing a system for concrete slabs which could be easily produced and look elegantly designed. These were referred to as isostatic slabs. The technique is accredited to an employee of Nervi: Aldo Arcangeli (Halpern, et al., 2013). Arcangeli determined that if a thin slab is loaded under a certain condition and then if the slab is replaced by a series of ribs which follow the principal bending moments (or isostatic lines as they were referred to then; these will be discussed further in section 1.3), then the two structures will behave in the same way (Halpern, et al., 2013). It is not explicitly known how Nervi's team developed their isostatic line geometry as a range of different methods were available at the time. However, Halpern et al. (2013) suggest that they were produced using Photoelasticity, a technique using a transparent material and shining polarised light through it. When the material is stressed, the stress lines could be seen from the polarised light. Halpern et al. showed that using a newly developed tool they could confirm that almost all of Nervi and Arcangeli's slab designs do in fact follow the lines of principal bending stress given by modern Finite Element Analysis (FEA) programs as can be seen in Figure 1-2.

This shows that although Nervi and Arcangeli only had access to primitive tools, they were still able to produce geometries that represent the results produced today. Halpern et al. (2013) showed that these geometries can now be redeveloped using these modern tools if their existing problems are solved.

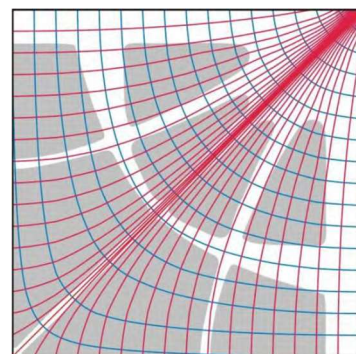*Figure 1-1: Gatti Wool Factory Floor System (Halpern, et al., 2013)*

Figure 1-2: Demonstration of Halpern et al.'s Isostatic Line Tool. Source: (Halpern, et al., 2013)

The isostatic slab system was produced using a set of formwork placed on movable beds which could be easily and periodically moved onto evenly spaced columns.

Other than Arcangeli and Nervi's work, there are few other examples of this technique's use. There are potentially two reasons for this: the first is that Nervi had a patent on the technique, restricting its use. The second is the rise in labour cost, which would have made the production of the formwork for the concrete more expensive and so, therefore, the technique was less beneficial.

The only other building, found by the author, to have used this technique was the Old Zoology Lecture Hall in Freiburg. The building's roof structure can be seen in Figure 1-3 and Figure 1-4 to have dramatically more complexity than the works of Nervi and Arcangeli. Hans-Dieter Hecker designed the building at the University of Freiburg in the 1960s; the ceiling is circular in plan with a 23.86m diameter and is supported by 2 curved walls and one hollow circular column, and the area of the slab around the column has an increased thickness (Antony, et al., 2014). Unlike the works of Nervi, this cannot be produced with a repeating formwork and must therefore have had a bespoke construction. This shows a small demand for concrete slabs that are more intricate than a regular flat slab or slab and beam system.
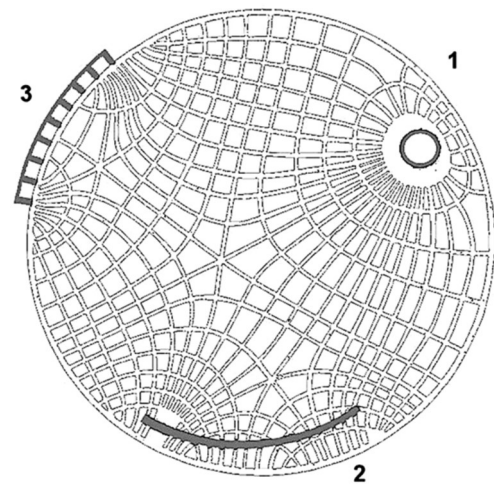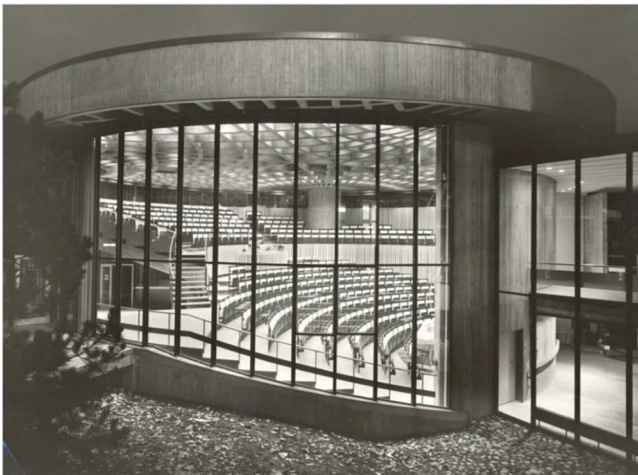
Figure 1-3: The Old Zoology Lecture at Freiburg University © Bruno Krupp, Freiburg.

Figure 1-4: Plan of the roof structure of the building. Source the archive of the building authority of the University Freiburg, Germany; found by (Antony, et al., 2014)

Antony et al. (2014) evaluated the Old Zoology Lecture Hall's ribbed slab to alternatives of a bubble deck system and a prestressed slab. They found that the two alternatives were comparable, but the ribbed slab had significantly higher material usage and labour cost. Due to the slab's complex topology, the formwork volume was 3.7 to 3.8 times larger than the alternatives. The ribbed slab's material cost was found to be roughly equal to the other options, but the labour cost was ~3 times higher. This highlights the reasoning why principally ribbed slabs have become less common over the last decades as due to increasing labour costs it is no longer economically viable, to produce them in concrete using traditional methods.

This shows that where there was once a market for these structures in concrete, there longer is. However, as these structures' increased cost was mainly due to the formwork, it may now be possible to produce similar structures using modern techniques and materials.

1.3 Principal Stresses and Principal Stress lines

1.3.1 Introduction to Principal Stress lines

An important concept within structural mechanics is the idea of principal stresses. Principal stresses can be expanded to create principal stress lines which will be introduced here. To explain this, take an example of a beam, as shown in Figure 1-5. The beam carries the forces applied to it to the supports through bending and shear transfer. These two mechanisms produce two types of stresses onto the particles (a small segment of the beam): normal stresses and shear stresses. Equilibrium can be used to find rules which dictate these stresses: Normal stresses must be equal and opposite, shear stresses must all be equal and in the opposite rotational direction to the adjacent sides.

Eq. 1.1 and Eq. 1.2 give the distribution of shear (τ) and normal (σ) stresses in a typical slender beam with a rectangular cross-section, plotted graphically in Figure 6. V is the applied shear force, M is the applied moment, h is the height of the section, I is the second moment of area, and y is the distance from the neutral axis to the point of interest.

$$\tau = \frac{V\left(\frac{h^2}{4} - y^2\right)}{2I} \qquad Eq.\,1.1$$

$$\sigma = \frac{My}{I} \qquad Eq.\,1.2$$

Using this, three points in the beam can be examined, which are shown in Figure 1-7. Point A has only normal stresses applied, point B has both normal and shear stresses, and point C has only shear stresses. However, when these particles are rotated, the stresses changed. Mohr created the Mohr's circle diagram to be able to analyse different rotation angles of each particle. Take point B as an example; in Figure 1-8, the Mohr's circle for this stress state is produced. The first point of note is the axes. The vertical axis measures the shear stress from positive to negative (where positive shear is in the anticlockwise direction). The horizontal axis measures the normal stress from positive to negative (where positive normal stress is a tensile force). Two points are plotted, which represent the stresses on each pair of faces. A circle is created through the two points, with the centre at the middle distance between them. The second point of note is the "pole". The pole is found by drawing a line from each point in the direction parallel to that of the face which the point represents.

Now that the pole has been found, the stress states in rotated particles can be calculated. This is shown graphically in Figure 1-9. The two lines representing the particle's faces are rotated about the pole to find the rotated particles and their stress states. The intersections between the new lines and the circle give the new values for the normal and shear stresses. The inclination of the lines gives the directions parallel to the new faces.

There are two essential points on every Mohr's circle: the points of principal stress. The principal stress points are located where the circle crosses the normal stress axis. There is zero shear stress at these locations, and the normal stresses are maximum and minimum. For every particle in the beam, it is possible to rotate it by an angle so that each of the faces is represented by these points; as shown in Figure 1-10.

Figure 1-6: Cut Beam Showing Normal and Shear Stress Distributions

Figure 1-5: Beam Example with Moment and Shear Diagrams
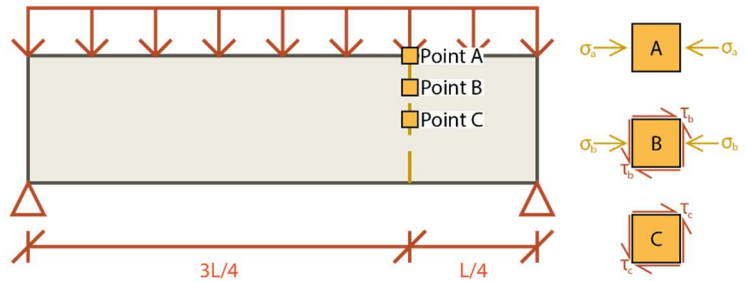
Figure 1-7: Location of Points within the Beam
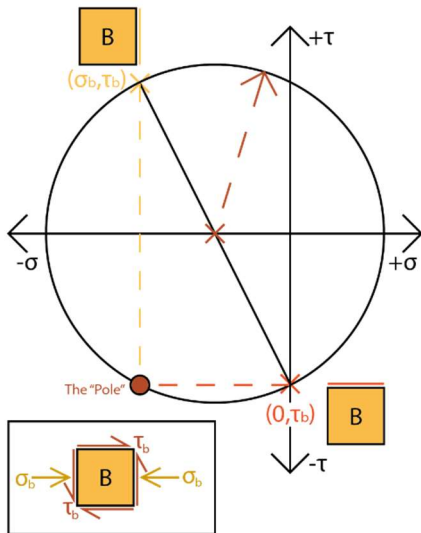
Figure 1-8: Construction of the Mohr's Circle for Point B
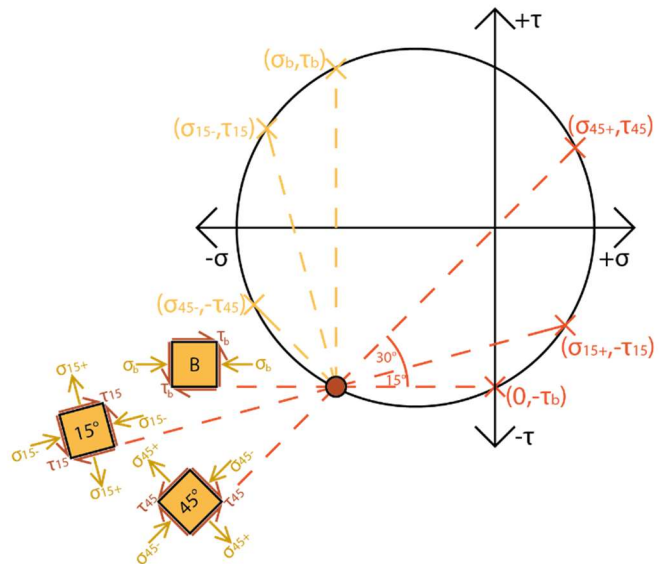
Figure 1-9: Using a Mohr's Circle to Find Rotated Particles

The values of the principal stresses and the angle of rotation are found by the following formulae which can be derived from the Mohr's circle:

$$\sigma_1 = \frac{\sigma_x + \sigma_y}{2} + \sqrt{\frac{(\sigma_x - \sigma_y)^2}{4} + \tau_{xy}^2} \quad Eq.\,1.3 \qquad \sigma_2 = \frac{\sigma_x + \sigma_y}{2} + \sqrt{\frac{(\sigma_x - \sigma_y)^2}{4} + \tau_{xy}^2} \quad Eq.\,1.4$$

$$\tan(2\theta) = \frac{2\tau_{xy}}{\sigma_x - \sigma_y} \quad Eq.\,1.5$$

Where σ_x and σ_y represent the normal stresses on each face, and τ_{xy} represents the shear stress. The reason for these exact notations will be discussed later.

Using the above equations, the principal stress values and their directions can be calculated for every point in the beam, as shown in Figure 1-11. Using the principal stress directions as vectors (often referred to as the stress trajectories), the principal stress lines can be drawn, which are always parallel to the principal stresses for any point in the beam, shown in Figure 1-12. Although this may sound like an easy task to perform, these lines are challenging to produce accurately and consistently (this will be discussed in Chapter 4 and Chapter 5).
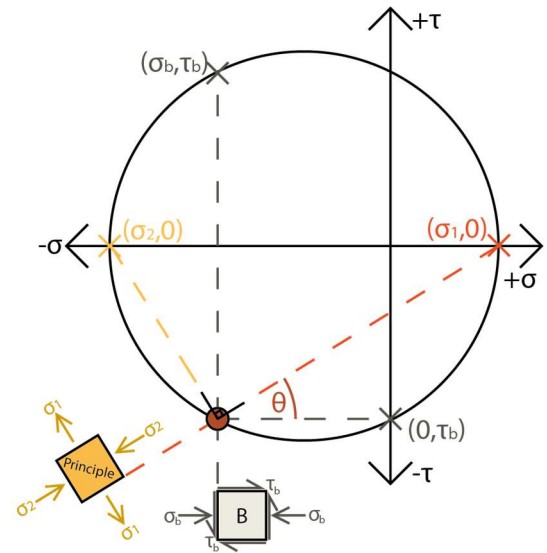
Figure 1-10: Finding the Principal Stress Particle Using a Mohr's Circle
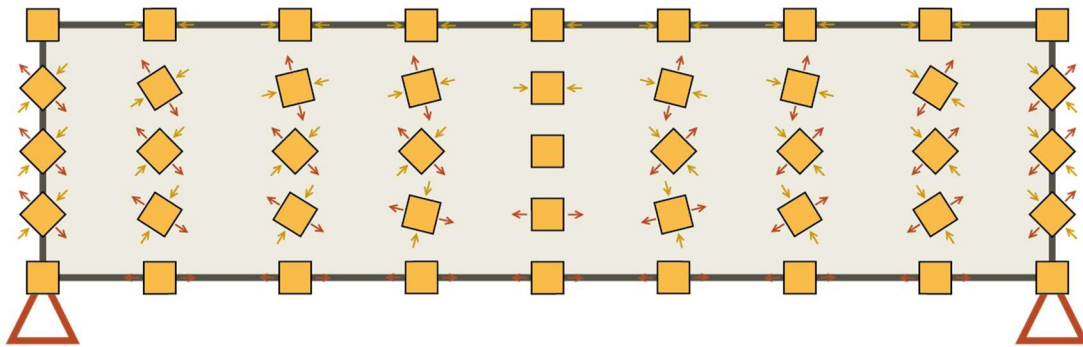
Figure 1-11: Principal Stress Directions at Multiple Points in the Beam
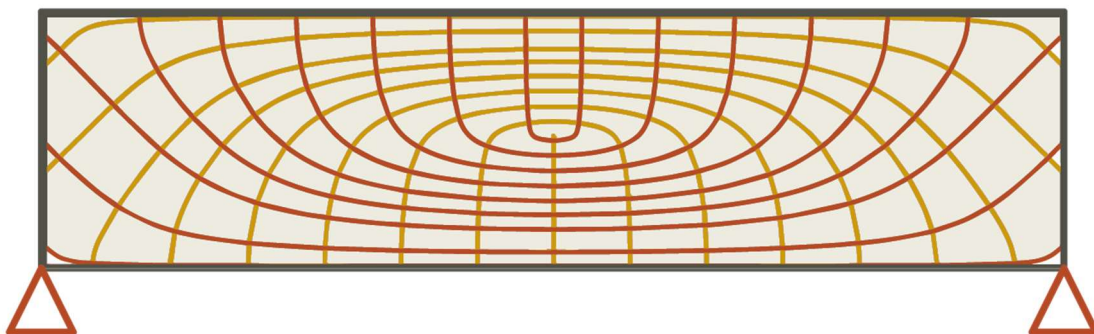
Figure 1-12: Principal Stress lines Through the Beam. The yellow lines show the minimum principal stresses (σ_2) and the red lines show the maximum principal stresses (σ_1).

In every particle, there are two orthogonal principal stress trajectories. These mean that there are two separate groups of stress lines which are always orthogonal to each other. The groups are referred to as the two stress line families. In Figure 1-12, one family is shown in yellow and the other is shown in red.

Currently, only stresses in two-dimensional plates loaded in-plane have been discussed; however, a similar process can be performed for slabs loaded out-of-plane. Slabs are similar

to beams in that they transfer shear and bending, but unlike beams, slabs transfer these forces in two directions.

Slabs behave like many plates stacked on top of each other, as shown in Figure 1-13 (left), in this way the normal stresses σ_x and σ_y become bending stresses m_x and m_y as they now act over a depth (Figure 1-13 (right)). Similarly, the shear stresses in the plate particle (τ_{xy}) become torsional stresses m_{xy}. As the shear stresses had to be equal and opposite on adjacent faces, so do the torsional stresses. Stresses acting out out-of-plane are not accounted for in the stacked plates. These are the shear stresses in the slab: τ_{xz} and τ_{yz}. An entire slab can be imagined to be made up of these individual elements, representing a tiny part of the slab.

Figure 1-14: A Rectangular Slab with a Uniformly Distributed Surface Load and Corner Point Supports.
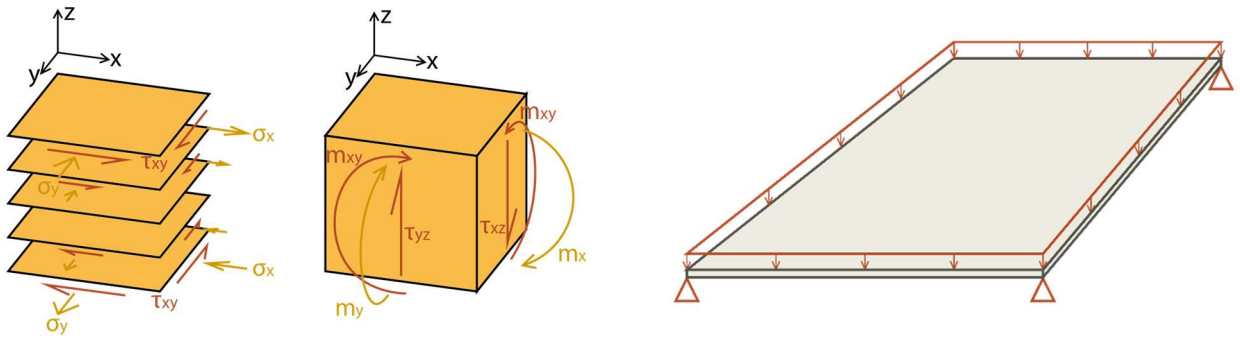
Figure 1-13: Transition from Plates to Slabs. The left image shows a stack of plates which integrate into the slab particle on the right.

Mohr's Circles can also be drawn for the bending and torsional stresses in a slab, shown in Figure 1-15. In the Mohr's circle, sagging bending stress is taken as a positive value. Positive torsional stress occurs when the direction of the stress is in the anticlockwise direction when
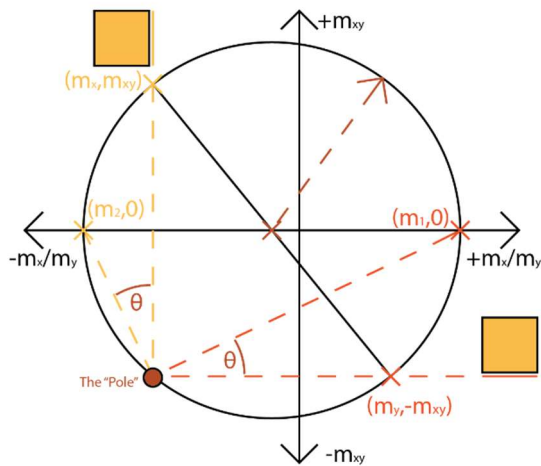
$$m_1 = \frac{m_x + m_y}{2} + \sqrt{\frac{(m_x - m_y)^2}{4} + m_{xy}^2} \qquad Eq. 1.6$$

$$m_2 = \frac{m_x + m_y}{2} + \sqrt{\frac{(m_x - m_y)^2}{4} + m_{xy}^2} \qquad Eq. 1.7$$

$$\tan(2\theta) = \frac{2m_{xy}}{m_x - m_y} \qquad Eq. 1.8$$

looking face-on. Principal stresses in this Mohr's circle represent the stress state when only bending stresses and no torsional stresses occur, referred to as the principal bending stresses. The equations used to find the principal bending stresses and the rotated particle's angle are shown below in Eq. 1.6, Eq. 1.7, and Eq. 1.8.
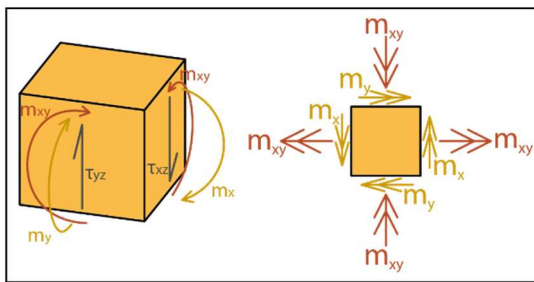
Figure 1-15: Creating a Mohr's Circle for a Slab. The 2D representation of the particle shows the normal vector of the moment stresses using the right-hand rule.

The principal bending stresses and directions can be found for every point in the slab. The principal bending stress lines are drawn so that they are

always parallel to the principal bending stresses. The result of this is shown in Figure 1-13. It is important to note that the two sets of principal stress lines are always orthogonal to each other as the principal stresses are always separated by 90°.
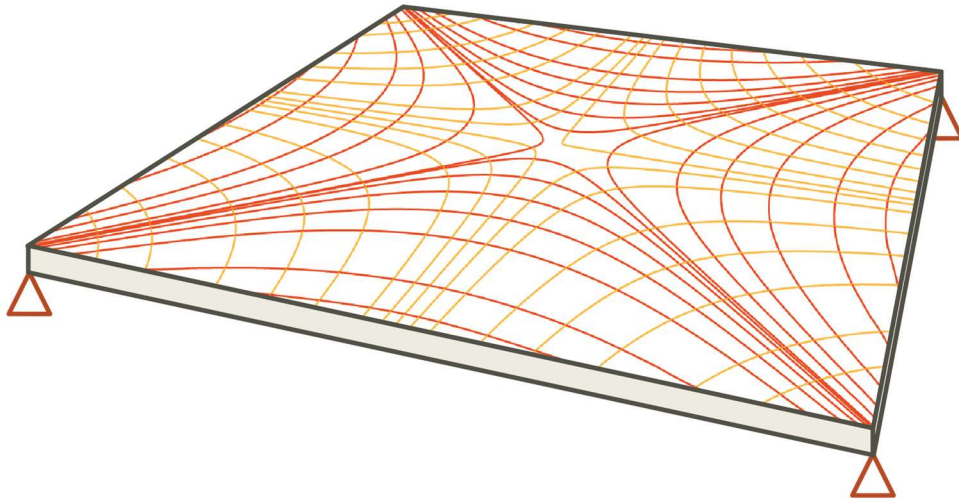
Figure 1-16: Principal Bending Stress lines for a Square Slab on Corner Point Supports

1.3.2   The Use of Principal Stress lines

One of the most notable contributions in producing structures from principal stress lines is Tam and Mueller's work from MIT. Tam and Mueller (2017) showed that by using their newly developed SLAM 3D printing technique, they could produce deep beams that had an equivalent strength but an enhanced stiffness of 1.9 times, when compared to a regular orthogonal grid with the same total material volume. The SLAM technique is a method of 3D printing where the material is extruded so that it creates a uniform material without deposition layers, through the lines of principal stress. This shows that using principal stress lines to produce optimal structures could be beneficial where the serviceability limit state is critical. Figure 1-17 shows examples of the 3D printed test samples after failure, and Figure 1-18 shows the normalised load-displacement graphs for a total of 6 samples. Figure 1-18 shows how there is an increase in yield strength and stiffness in the SLAM samples, but the ultimate capacity is comparably equal. It is also worth noting here that the SLAM samples were more brittle.

This same technique was used to produce various shell geometries created using a robotic arm (Tam & Mueller, 2017). Load tests were also performed on these samples, showing good results for the new SLAM technique with enhanced stiffness and strength after normalising for the volume. However, as the authors themselves mention, there was an insufficient number of tests produced for a statistical conclusion. Figure 1-19 shows some examples of the shell geometries produced.
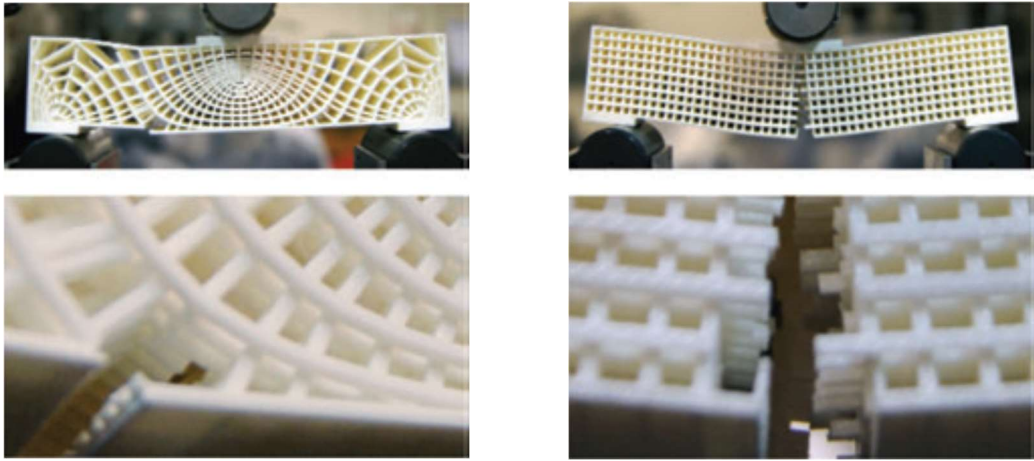
Figure 1-17: 3D Printed Test Samples after Failure; Left: Principal Stress line Grid (SLAM-XY); Right: Regular Orthogonal Grid (GRID-XY) (Tam & Mueller, 2017)
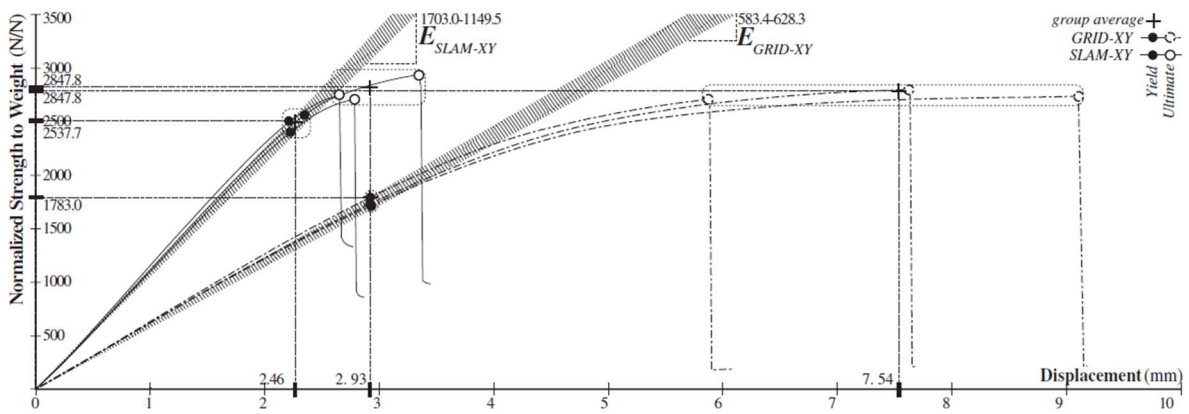
Figure 1-18: Normalised Load-Displacement Graph of 3 Principal Stress line Grid Samples (SLAM-XY) and 3 Regular Orthogonal Grid Samples (GRID-XY) (Tam & Mueller, 2017)
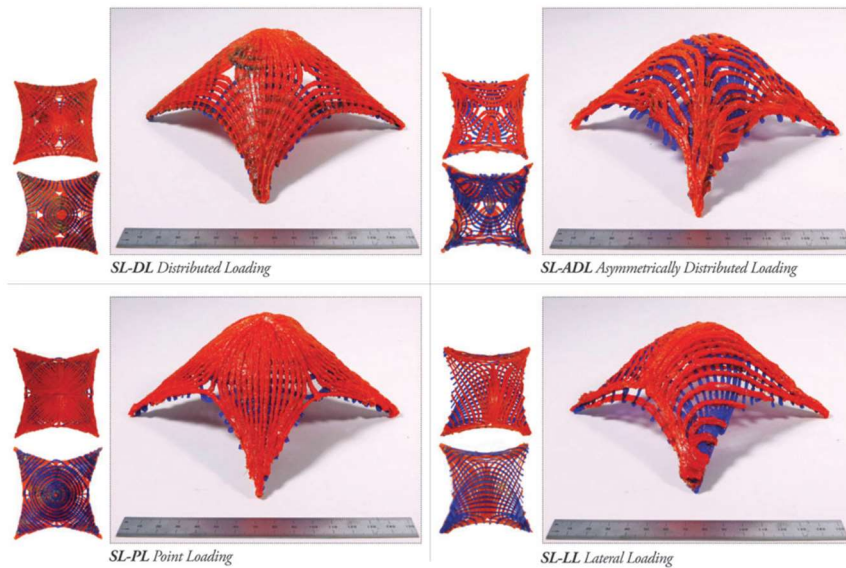
Figure 1-19: 3D Printed SLAM Shell Models (Tam & Mueller, 2017)

1.4 Optimised Floor Systems

In recent years there has been significant interest in creating optimised floor systems constructed from concrete. Of particular note is the development of a "thin-vaulted" floor panel created by the Block Research Centre, as seen in Figure 1-20. The floor system is designed using shallow arching action to achieve a structure that carries load through compressive forces instead of flexural bending; this creates a very stiff (a peak deflection of span/2500) and a light-weight floor panel (Liew, et al., 2017).

The thin-vaulted floor system was further developed into a segmented, 3D-printed, floor system made from sand, see Figure 1-21. This prototype floor panel showed significant weight savings of 70% compared to standard concrete slabs and could be constructed with no internal reinforcement (Rippmann, et al., 2018).

An optimised "Smart Slab" was made from reinforced concrete as part of the DFAB house project (NCCR Digital Fabrication, n.d.), see Figure 1-22. The Smart Slab used 3D printed formwork to create a structurally optimised floor system with a weight saving of 70% compared to a standard concrete flat slab. Unlike the vaulted floor systems, the Smart Slab utilises flexural bending and internal reinforcement.

There has been little development in creating optimised floor systems made from timber. It is easy to create optimised structures from mouldable materials like concrete as they can flow into the desired shape and then harden; the same process also occurs in additive manufacture. However, timber is significantly harder to work with, as it is produced through a natural process, taking decades to grow. Also, its dominant strength can only be achieved along a single axis, the grain direction. This property makes it challenging to create any floor systems which span more than a single direction.
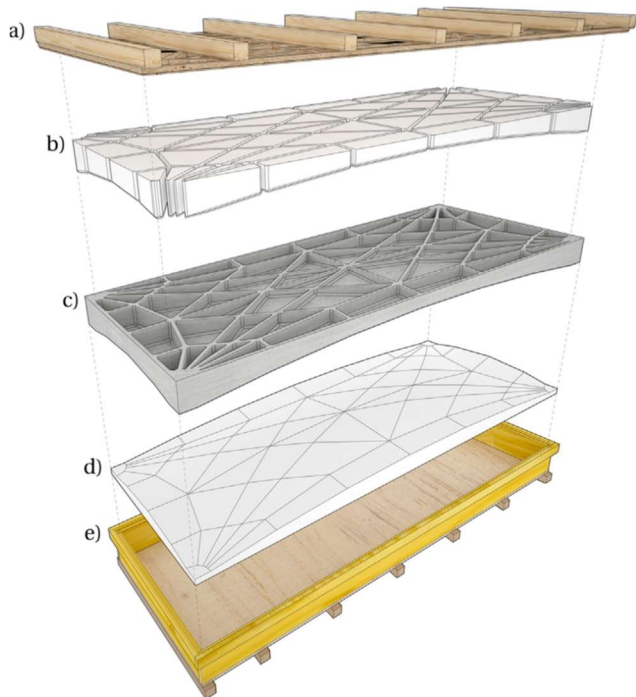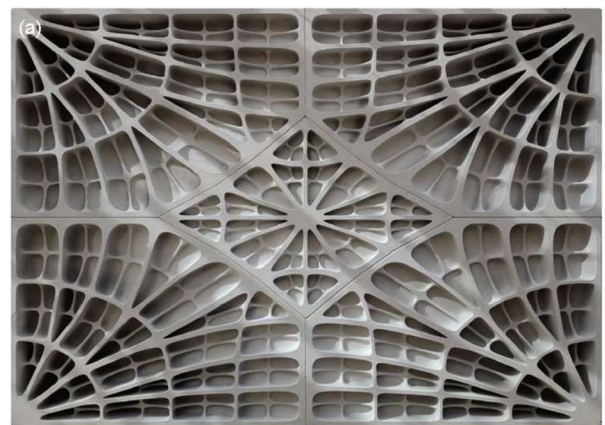
Figure 1-20: Prototype Thin-Vaulted Floor System (Liew, et al., 2017)

Figure 1-21: Prototype 3D Sand-Printed Floor System (Rippmann, et al., 2018)

Some commercially available products can be used to span in two directions: plywood, Cross Laminated Timber (CLT), and Laminated Veneer Lumber (LVL). These work by alternating the grain direction in layers. CLT is frequently used in the building industry to produce slabs and walls in timber buildings. Although CLT is advertised as two-way spanning, this can only be achieved in a limited number of scenarios (e.g., Brock Commons in Vancouver) as these

panels have a limited width (≤3m). This means that even though CLT has two orthogonal grain directions, it is still mostly used as one way spanning elements.

Stress line structures could provide an efficient method for creating optimised two-way spanning timber slabs. By aligning material along the stress lines, the material is loaded only along its grain axis. It will thereby potentially produce a structure with a more efficient use of timber.

Efficiency is not the sole benefit of optimised structures. A core reason to develop these systems is that they are more interesting aesthetically than common systems, due to their complexity. An efficient use of material naturally leads to a weight reduction which could be particularly beneficial for a wood-based system as timber is a lightweight material. Therefore, an optimised timber slab would add to an architectural portfolio and could be used to minimise the load onto the foundation.

Figure 1-22: The DFAB House Smart Slab During Construction, Source: NCCR Digital Fabrication

2.1 Isostatic Timber Slab

For this thesis, a new structural system will be developed, the Isostatic Timber Slab. The isostatic timber slab is a re-imagining of the concrete isostatic slabs but produced in timber materials. The slab consists of two main components the deck and the ribs. The deck is made of plywood panels. The deck is strengthened by the ribs made from LVL beams which are attached to its underside. The ribs follow the principal bending stress lines. See Figure 2-1.
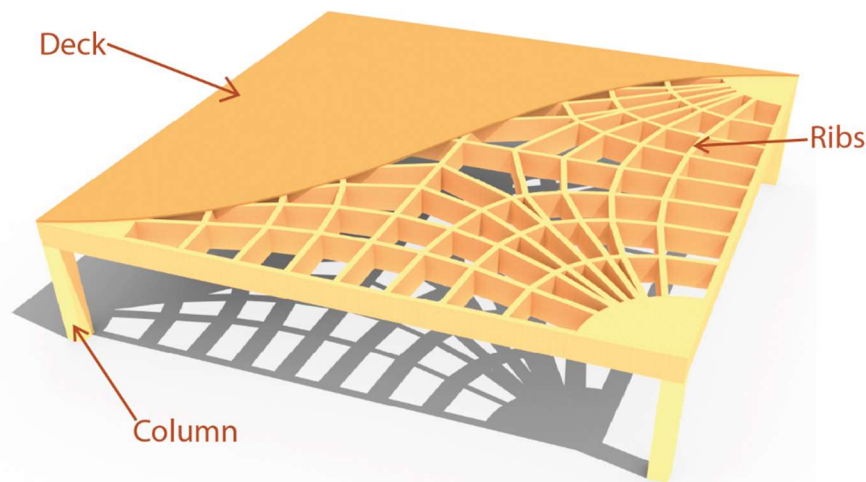
Figure 2-1: An Isostatic Timber Slab with Corner Supports Showing the Rib and Deck Assembly

As this is a new system, there are many open questions about how a slab of this kind should be designed and manufactured, and whether the system is worth using. Therefore, there needs to be a greater technical understanding and background of knowledge for the system to be used in practice.

2.2 Motivation

This thesis is motivated by the need for interesting architectural forms, and the lack of optimised timber slabs. In industry, architects and clients are often looking to produce buildings that are attention-grabbing and stand out. This often leads to freeform architecture, which can be inefficient in terms of the structural design. Isostatic slabs provide a structural system that is architecturally interesting and potentially structurally efficient. Therefore, they can be a useful addition to designers' portfolios.

For many decades no one has built isostatic slabs, likely because they are not cost-effective to build. However, using engineered timber and new automated manufacturing techniques to produce timber elements, it could now be possible to reinvent the isostatic slab in a cost-effective timber alternative.

Through this slab's development, academic value can be obtained by developing a clearer understanding of how principal stress lines can be generated and used in the design process. On top of this, it is also envisaged that some industrial value will be created in showcasing the benefits and applications of engineered timber.

Producing a new architecturally interesting, optimised timber floor system could further increase timber use in buildings that (when designed with a sufficient cradle-to-grave life cycle assessment) can reduce the CO_2 levels in the atmosphere through carbon sequestration.

2.3 Scope

The design limit states are found for the ultimate limit state and the deflection-based serviceability limit state. The vibration-based serviceability limit state is considered outside this thesis's scope due to the complex dynamic modelling needed to achieve accurate results. The fire limit state is also not considered. Although a reduced section model can be produced to evaluate the fire criterion, this does not meet the requirement of a fire compartment's self-extinguishment. The determination of whether this slab could self-extinguish is far beyond the scope of the preliminary research into this system. These two limitations will limit the slab system's applicability, but it is hoped that further research will be undertaken to investigate these.

The case study only covers a limited situation in which the system could be applied. These serve only as an indication of how the slab could be utilised, and many more variations could be imagined.

The ribs could be designed with curved or straight elements, and the choice between these will result in different structural systems. In this thesis, the ribs will be made of short straight elements which connect to form a discretisation of the curved stress line.

2.4   Research Questions

This section will explain the main research question of the thesis and the subsequent sub-questions. Through these, the objectives of this thesis are outlined.

2.4.1   Main Question: How should an Isostatic Timber Slab be designed?

The focus of this thesis is to determine how an isostatic slab made of timber should be designed. This main research question is broken down into further sub-questions which cumulatively answer this thesis. The sub-questions are broken down into parts to distinguish the two areas of this thesis: a) An investigation into stress line geometry for use in isostatic slabs. b) The translation of this geometry into a design of an Isostatic Timber Slab. Figure 2-2 shows the structure of the thesis. Each chapter in Part A and Part B is based on one of the research questions, showing how these questions feed into later questions.
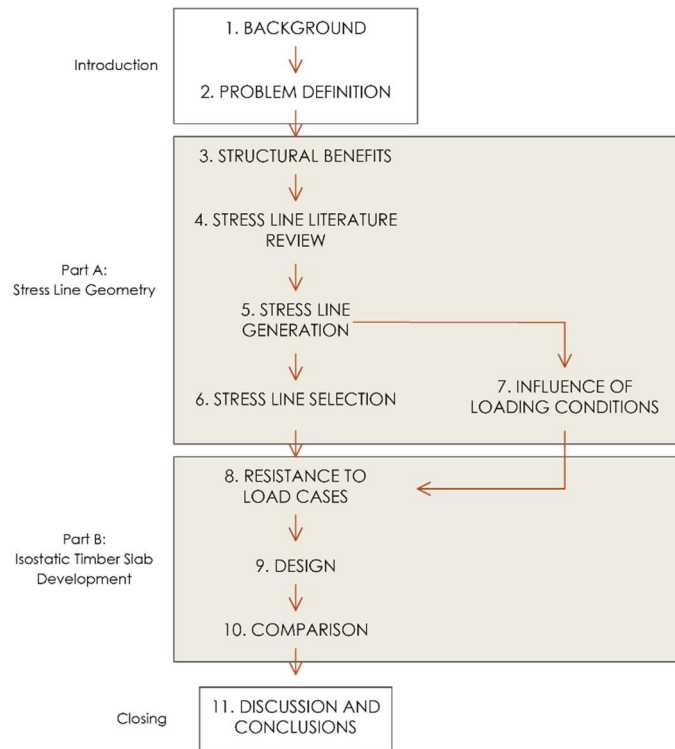
Figure 2-2: Thesis Structure Showing the Chapters and Sections and How Each Engages with One Another

2.4.2 Part A: Investigation into Stress line Geometries for Use in Isostatic Slabs

This part is made of a mixture of literature studies into the reasoning behind, and creation of, principal stress lines and testing of different methods and parameters to inform the design of isostatic slabs. This part looks at isostatic slabs in general, not those made specifically out of timber. In this way, the outcomes will be more useful to future research into principal stress in slabs.

Research Question A1: What is the structural benefit of isostatic slabs?

A literature study is undertaken to determine the key structural benefits of isostatic slabs compared to conventional slab systems and thus inform how they should be designed to better take advantage of these. Chapter 3 covers this question.

Research Question A2: How can principal stress lines be generated?

A literature study is used to find all the available techniques which could be used to produce stress lines from finite element results. This study investigates the methods used in the similar problem of viewing streamlines in fluid flows, and whether these methods could apply to stress line visualisation. Chapter 4 covers this question.

Research Question A3: What is the most reliable method for generating principal stress lines?

The methods found in question A2 are tested to analyse which method can produce the most reliable principal stress lines for any general boundary and loading conditions. The methods

are compared based on their compliance with principal stress line axioms, created from structural mechanics requirements. Chapter 5 covers this question.

Research Question A4: How can a subset of stress lines be selected for use in an Isostatic Slab?

The best method from question A3 can be used to find the principal stress lines in a slab. In this question, an algorithm from literature to select an appropriate combination of stress lines that can be used to find the ribs' geometry in an isostatic slab with discretised ribs, is investigated through testing. The results are compared to geometry that is produced by selecting the stress lines manually. Chapter 6 covers this question.

Research Question A5: What influence do the loading conditions have on the stress lines?

In producing the stress lines, a single load case (the primary load case) defines the stress lines. This question investigates the effect the choice of primary load case has on the stress lines and the impact secondary load cases have on the stress lines. This will also investigate the effect of assuming a uniform self-weight compared to including the ribs' localised load. Chapter 7 covers this question.

2.4.3 Part B: Development of the Isostatic Timber Slab Design

In this part, the system's practical design and construction aspects will be determined and resolved using finite element analysis software, design standards, and information from manufacturers. Through this, the theoretical system is transferred into a preliminary design. A case study is developed of a single application, and a design is made for this case.

Research Question B1: What effect do the design parameters have on the primary and secondary load cases?

In this question, the case study is outlined. A centreline geometry for the slab's ribs is be produced using the methods from Part A. Different values for deck thickness, rib depth, and rib thickness will be investigated using finite element models to find what effect they have on the structural response to the primary and secondary load cases. Additionally, the difference in stresses between the primary and secondary load cases will be investigated within this question. Chapter 8 covers this question.

Research Question B2: How can an Isostatic Timber Slab be designed?

To prove that it is possible to design and construct this system, the slab's critical components must be designed. This includes the deck and ribs based on the Ultimate Limit State (ULS) stresses, the rib-to-rib connections, the rib-to-deck connections, and the overall slab in the Serviceability Limit State (SLS). A final centreline geometry for the slab's ribs is created to answer this question, taking account of the manufacturing and connection constraints. Chapter 9 covers this question.

Research Question B3: How does an Isostatic Timber Slab compare to other systems?

The Isostatic Timber Slab system will be compared to other alternative systems. For this, the preliminary design tables from manufacturers of standardised systems will be used to compare the designs based on material usage, cost, structural depth, and embodied CO2e. Chapter 10 covers this question.

3.1 Introduction

In this chapter, the question of "What is the structural benefit of the Isostatic Slab?" is investigated by reviewing the literature on isostatic slabs and stress lines. The key benefit of the isostatic slab system is determined and the fundamental reasons behind this. This knowledge can thus determine the design principles this system should follow to result in the best outcome for a project.

3.2 Flow of Forces

Within papers relating to principal stress lines, the principle of the flow of forces through a structure (also referred to as the load path) is frequently mentioned (Tam, 2015) (Magan, 2016) (Tam & Mueller, 2017). J. Fonseca (1997) gives a basic introduction into what the load path is and how it can be used to understand how a structure performs. They compare the load path to the application of the flow of particles in fluids. Where in fluids, a vector field of the flow direction at points in the domain is used to define the flow; the author shows that by creating a vector field which represents the forces internally within a structure then the flow of this vector field can be used to illustrate the flow of forces. Namely, J. Fonseca uses stress vectors for in-planed loaded plates, thus creating the flow of forces shown by the principal stress lines.

The idea of the load path of a structure and principal stress lines is of particular importance in struct-and-tie models used to design reinforced concrete structures. Schlaich et al. (1987) produced a method for developing strut-and-tie models by utilising the flow of forces shown by the principal stress lines. The compression stress lines represent the location of concrete structs, and tension stress lines represent ties and reinforcement requirements at these locations. Through some examples, they showed how this principle could be applied to a range of in-plane loaded plates. Their method shows how principal stress lines can determine the natural locations of internal axial members and how this can be used to create efficient reinforcement layouts.

Memduh Ali Tayar (1986) explains why this method produces optimised structures. As he states, "When a homogenous and continuous solid is loaded, a specific organization within the body is achieved to transfer the forces according to one very important rule in nature which is that the total work done (in this case the total strain energy stored) is always minimum." He also supplements this with a quote from the lecture notes of Waclaw Zalewski "it means that it (the stored strain energy) is less than the energy or work which might be associated with any hypothetical -statically possible- force distribution in the same structure under the same load" (Tayar, 1986). This means that when a structure is designed using stress line principles, it will have minimal work-done for the load case the stress lines are produced from compared to the same volume of material orientated in any other arrangement. This is of significance as the work-done is equal to the load multiplied by the

displacement. If the load remains constant between alternatives, the displacement must be minimised. This can thus be used to produce structures which fulfil the serviceability limit state with a minimal amount of material.

3.3 Michell Structures

Principal stress lines are also frequently compared to Michell Structures (Tayar, 1986) (Tam, 2015) (Magan, 2016). Michell (1904) developed a mathematical solution to truss structures. They showed that the theoretical structure connecting an applied force to a set of supports has a minimum volume of material when the strain is equal in every element. Michell used this theory to create several truss solutions. Figure 3-1 shows their solution to a system where a point load is applied at the centre of the domain and supported to the right and the left.

The comparison between these two structural ideas is clear; both Michell and stress line structures have only axially loaded members and are produced with orthogonal connections. Also, to produce the optimal solution found through these methods, there must be an infinite number of elements in the structure. The difference between these two systems is that the Michell structures have the minimal amount of material to carry the forces from the load to the support irrespective of the domain or with only a minor constraint on it (i.e., that the design space is split in half and only one part is used). In contrast, stress line structures are created within the solid body domain for which there are produced. Nevertheless, the visual comparison between these two systems is difficult to ignore.

Another significant difference between the two is that while Michell structures are analytically derived and can only be produced for a few specific cases, stress line structures can be numerically derived and can be used wherever a Finite Element (FE) model for the structure can be produced.

Li and Chen (2010) showed how stress lines could be used to approximate Michell structures. They compared their method to the ground structure method, which is another common method to approximate Michell structures. They found that adding additional elements to a structure that follows the principal stress lines could create more optimal results. Figure 3-3 shows their approximation of the Michell structure shown in Figure 3-1.
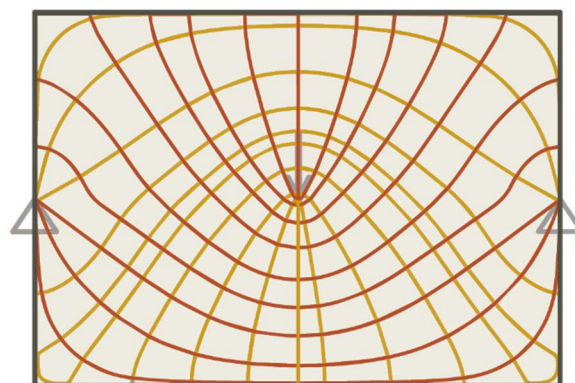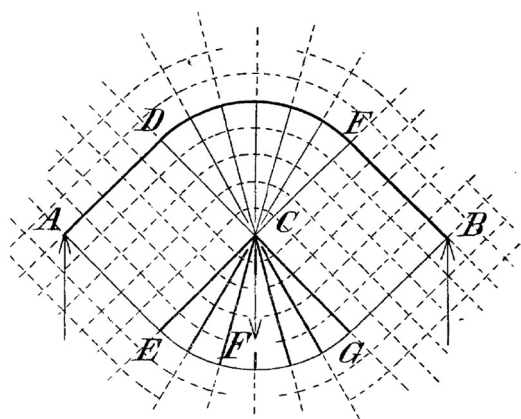
Figure 3-1: Michell's Solution for a Centrally Loaded Truss (Mitchell, 1904)

Figure 3-2: Stress Lines for a 14.14mx10m Plate Loaded in-Plane at it's Centre
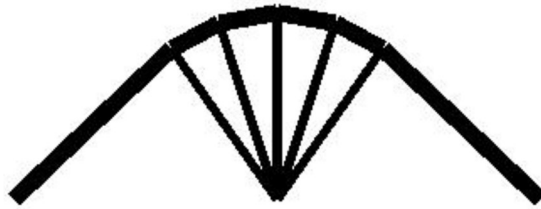
Figure 3-3: Li and Chen's Approximation of a Mitchell Truss with a Point Load at the Mid-Span (Li & Chen, 2010)

3.4 Out-of-Plane Loaded Plates

The ideas of the flow of forces and Michell structures apply very well to in-plane loaded plates; however, when the step is made to out-of-plate loaded plates, it gets more complicated due to the added dimension.

Firstly, Michell only produced one three-dimensional solution in the form of the torsion sphere which carried the applied torque on one side of the domain, to the other side. Obviously, Michell structures cannot produce anything of use concerning slabs. The theory of Michell structures only applies to tension and compression members and therefore, does not consider the required bending needed in a slab. However, when considering the top or bottom particles of a slab, these can be only in tension and compression. Therefore, there may be a relation.

The complication of out-of-plane loaded plates arises from the existence of both bending forces and shear forces that act across the slab. This leads to an apparent ambiguity in the idea of the flow of forces. On the one hand, the flow of forces could be interpreted as the lines of principal bending stress, which directly applies the theory of in-plane loaded plates to out-of-plane loaded plates. However, another interpretation is the rain shower analogy or principal shear force lines. This is the interpretation that J. Fonseca (1997) uses to apply load paths to out-of-plane loaded plates.

The first step of determining the principal shear force is to combine the bending stresses in each axis into a single formula for 'm' as shown in Eq. 3.1 (Blaauwendraad, 2006). This equation can be visualised as a 'hill'. The shear force is the derivative of the moment, so the principal shear force is the derivative of m in maximum slope direction. This is visualised by plotting m as a hill diagram where the vertical coordinate is the value of m. At any point on the hill, the directions of the maximum and minimum slope can be found. The direction of the minimum slope is along constant m and creates 'contour lines'. The direction of the maximum slope is always 90° to the minimum slope. If a drop of water were placed onto the hill, it would flow to the supports along the maximum slope path. The paths of raindrops and direction of maximum can be considered as the principal shear stress lines.

$$m = \frac{m_{xx} + m_{yy}}{1 + \nu} \qquad Eq.\,3.1$$

(Blaauwendraad, 2006)
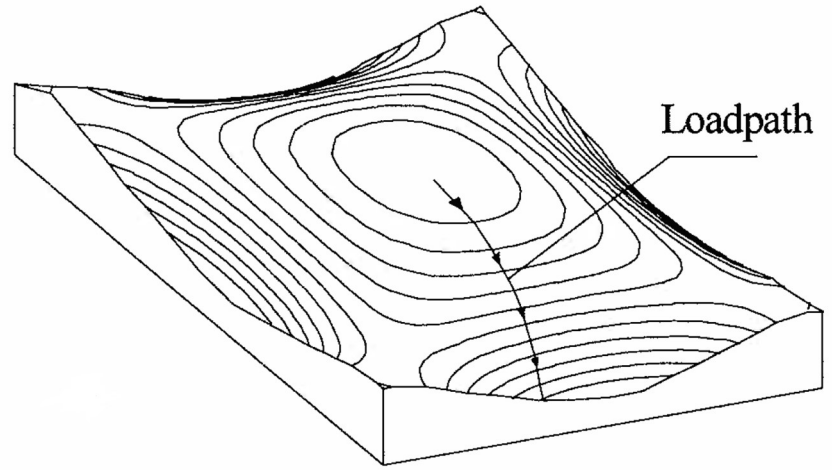
Figure 3-4: Rain-Shower Analogy for a Slab with Clamped Edges and UDL (Fonseca, 1997)

The isostatic slabs of Nervi assume that the lines of principal bending stress represented the flow of forces. The system which was developed by Aldo Arcangeli on the principle that when a slab is replaced by two families of beams, which follow the lines of principal bending stress, then the resulting system will respond similarly to the slab the stress lines were developed from if the loading and boundary conditions are the same (Halpern, et al., 2013). This same reasoning can be used for principal stress lines in in-plane loaded plates (Tayar, 1986).

These are two conflicting ideas for the flow of forces within slabs as the principal shear stress lines, and principal bending stress lines are not the same. However, an intuitive distinction could be drawn to determine which of these two load paths is correct for a slab. When referring to beams, a difference can be drawn between pure flexural beams (i.e., Euler beam theory) and beams which have both a bending and shear method of force transfer (i.e., Timoshenko beam theory). The same is true for slabs, where a thin slab has neglectable shear deformation and thus only deforms through bending; a thick slab has both flexural and shear deformations. Therefore, if a slab can be considered thin, as determined by the theory of out-of-plane loaded plates, then the primary load transfer mechanism is through bending, and the load-path will follow the lines of principal bending stress. For this thesis, it is assumed that the slabs can be considered thin, and therefore, the shear stress lines can be neglected.

4.1 Introduction

To design a structure that incorporates principal stress lines, the stress lines need to be calculated. The generation of useable stress lines is still an open question with many different tools being developed and used. In this chapter, the current tools that have been used in the field of structural analysis and design will be discussed, and the different algorithms that have been developed in the field of computer imaging for creating streamlines (which is a similar problem) will also be investigated.

The generation of stress lines works by taking a vector field, which contains the principal stress directions, and producing a set of curves that are always parallel to the vector field. This can be visualised as placing an object into the vector field and tracing its path as if the principal stress vectors pushed it. It is important to note that for each point in the field there are two principal stress directions at 90° to each other (one in the major direction and one in the minor direction) and that a principal stress vector is not completely equal to a regular vector as it can points forwards and backwards at the same time.

It is useful for the reader to understand some key terminologies for this chapter:

- **Vector field –** a domain where a vector can be calculated for any point within it.
- **Streamline –** a streamline is a curved line representing the movement of a particle through a vector field.
- **Stress line –** equivalent to a streamline where the vector field represents the principal stress directions.
- **Seeds / Seeding point –** the starting point of a streamline or stress line.
- **Interpolation method –** This is used to define a continuous vector field from discrete values (i.e., transforming a **finite** number of results into **infinite** results). See Section 5.1.1 for a more detailed description.
- **Integration method –** A way of constructing a curve from the vector field by finding the movement direction and 'taking a small step' along it (the curve produced through this is a polyline, where each segment is a step). See Section 5.1.2 for a more detailed description.
- **Seeding method –** A method for determining where seeds should be placed to create the best distribution of streamlines/stress lines. See Section 5.1.3 for a more detailed description.

4.2 Stress line Generation in the Field of Structural Analysis

In structural analysis, there have been two opposing objectives in developing stress line tools: the visualisation of stresses for interpreting the forces and for production into structures. Many programs have tools which apply to the former case, but there has been little development for the latter case as this is not of concern to most engineers (Halpern, et al., 2013). However, as the focus of this thesis is to develop a system using principal stress lines, a tool of the latter case needs to be developed.

Halpern et al. (2013) created an "Isostatic Line Tool" used to compare the isostatic slabs produced by Nervi with stress lines produced using FEA software. See Figure 4-1 for an example of the tool in comparison to one of Nervi's slabs. The tool works by using the Euler integration method to produce the stress lines. The Euler integration method is the simplest integrator, where the vector at a point is found, and then a step is taken directly along that vector. This is a computationally quick method, but it is the least accurate. The integrator is finished when the stress line meets the boundary. The biggest downfall in this method is the seeding strategy that is user-specified and could require a large about of user input to generate the results. Although it is worth mentioning that Halpern et al. (2013) have used a regular division of the boundary edge as the input for the seeds, which is applicable in the cases they have shown. However, in situations where stress lines do not meet a boundary, this no longer works. This occurs when there are hoop or looping stresses. Halpern et al. do not specify their interpolation method for obtaining the step directions.
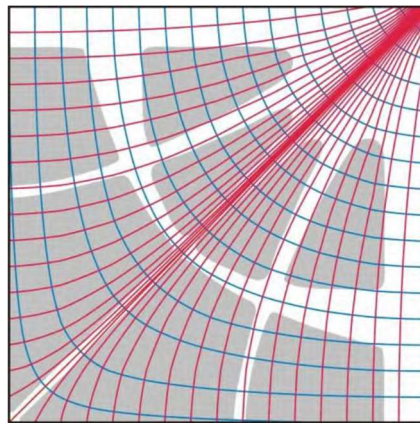
Figure 4-1: Demonstration of Halpern et al.'s Isostatic Line Tool. Source: (Halpern, et al., 2013)

There are commercially available tools which can be used to generate stress lines. Karamba 3D is a plug-in for Grasshopper that performs FEA and can also output the principal stress lines for various situations (Karamba3D, 2020). Millipede is another plug-in for Grasshopper that can create the principal stress lines for some applications (Michalatos, 2014). However, these tools have limited controls over the stress line production and/or produce incorrect results, such as discontinuous stress lines and collisions between stress lines that should not occur (Tam, 2015).

Tam (2015) created a stress line generation tool which attempts to solve many of the issues with commercially available tools. This tool was used to generate stress line fields for the 3D printed structures shown in Section 1.3.2. Tam created an "N+1 order" interpolation method, see Figure 4-3. The method works by finding the closest principal stress vector result from the FE results and all the vectors within a set radius of the point. A weighted average of the vectors is calculated based on the distance from the investigated point. Tam found that this produced more accurate principal stress lines than other methods that used a single principal stress trajectory for each element.

The stress lines were produced using the Euler integration method. Tam (2015) implemented a series of "rule-based corrections" during the generation process to reduce the stress lines' errors. These include "detection of circumferential stress", "enforce offset", and "bypass seeding" (see Figure 4-2). 'Detection of circumferential stress' was used to detect looping stresses so that the stress lines can be joined to themselves, forming a closed curve. 'Enforce offset' prevented stress lines from intersecting when they should be parallel by altering the

step direction when a new stress line is about to meet an existing one. The 'enforce offset' rule will include some inherent bias as the early stress lines are given priority over the stress lines produced later. Bypass seeding removed any seeds before integrating them when they were too close to existing stress lines. Tam implemented multiple seeding strategies and compared them; however, they all required a user-determined seeding plan which is why the bypass seeding rule was required as new seeds could overlap with previously drawn lines.
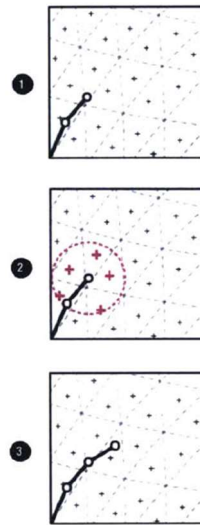
Figure 4-3: Tam's N+1 order interpolation method: 1) Start of the step, 2) Find the weight average of all the stress trajectories within the circle, 3) Find the new step point using Euler integration (Tam, 2015)
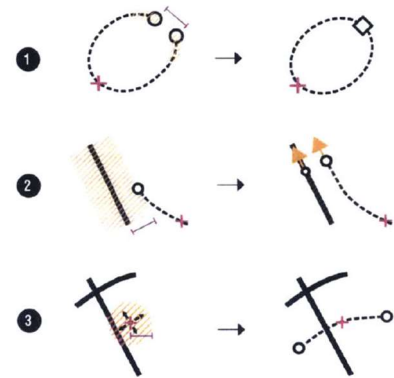
Figure 4-2: Tam's Rule Based Corrections: 1) Detection of circumferential stress, 2) Enforce offset, 3) Bypass Seeding (Tam, 2015)

4.3 Stress line Generation in the Field of Computer Imaging

Within the field of structural analysis, there has not been a deep investigation into the best way to produce principal stress line fields. Therefore, it is useful to look at solutions produced in computer imaging to solve the problem of streamline generation in steady flows.
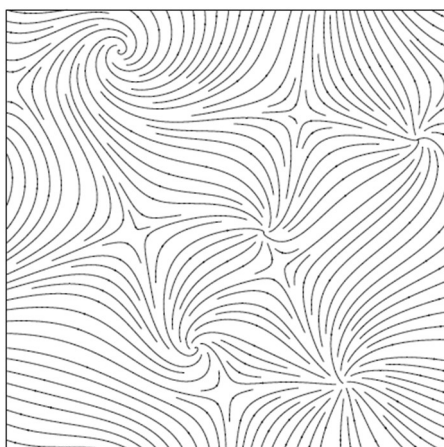
Figure 4-4: An Example of a Streamline Pattern. The small black dots show the seeding points. (Mebarki, et al., 2005)
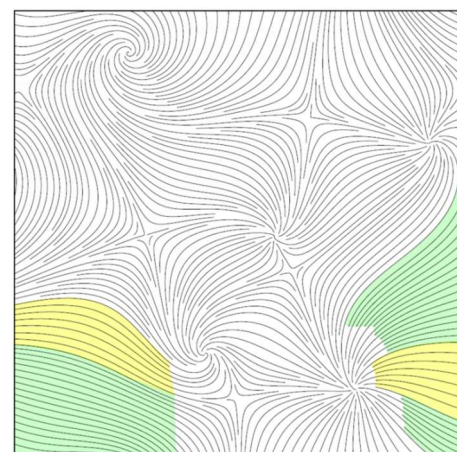
Figure 4-5: Example of Mebarki et al's Farthest Point Seeding Algorithm with Indication of Disparity of Density in Adjacent Areas. Source: (Mebarki, et al., 2005)

McLoughlin et al. (2010) give a clear overview of the available techniques for visualising flows, mainly focused on streamline analysis. They highlight the key issue of flow

visualisation: to visualise the data in a meaningful way where the features of the flow can be identified and analysed. This issue is not directly comparable to the stress line generation, but many solutions to this problem are applicable. The biggest challenge with these algorithms is the seeding method as this directly affects the result and computational time. The streamline analysis methods that apply to stress lines are classified as integration-based methods. In these a single seeding point is used to track the flow of a massless particle through the velocity field. The solution to this must be approximated using numerical integration methods. This highlights the second challenge in these algorithms, which is the choice of the integration method.

McLoughlin et al. (2010) explain that the first decade of research in this area was focused on the numerical integration methods, and the second was focused on the seeding strategy. McLoughlin et al. (2010) explain that before the Turk and Banks (1996) paper, seeding algorithms were based only on "regular girds, random sampling and interactive seeding". They state that this will give unsatisfactory results due to critical features being missed. As many of the methods from this time were focused on producing images that looked like hand-drawn visualisations, the goal was to produce a uniformly dense streamline coverage. Therefore, the techniques used in structural engineering are outdated.

Turk and Banks were the first to create a holistic seeding strategy. Their method was to take an initially random seeding and iteratively manipulate the resulting streamline pattern. The manipulations included: moving seeds, inserting seeds, lengthening streamlines, shortening streamlines, and combining streamlines (McLoughlin, et al., 2010). This algorithm resulted in good quality images but was computational expensive (Mebarki, et al., 2005).

Jobard and Lefer (1997) produced an improved algorithm which had the goal of "produce long and evenly spaced streamlines in a single pass". They proposed that for each seed point the streamline in computed in both directions until it meets the surface's edge, a critical point, or it becomes too close to another streamline. The user uses two parameters to define the streamline network: d_{sep} is the distance between the existing streamlines and the new seed point. d_{test} terminates streamlines when distances between the new streamline and the existing ones are smaller than this value. Their algorithm uses a "neighbour seeding strategy". Each new seed point is selected at a distance d_{sep} from the latest streamline created. Therefore, the new streamline 'neighbours' the previous one. Jobard and Lefer do not define where along the existing streamline the new seed point is created. Therefore, this creates much ambiguity in the seed location, and this choice will affect the final image of the streamlines. They used a "Midpoint integrator" to produce their streamlines but recommend that an adaptive step size integrator should be used to reduce computational time. Their method results in comparative image quality compared to Turk and Banks's algorithm but with reduced computational time. See Figure 4-6 left for an example of their algorithm.

Mebarki et al. (2005) created a new seeding strategy based on Jobard and Lefer's algorithm's limitations, which arise from the stopping of streamlines close to critical points causing empty spaces and short streamlines (See Figure 4-6 right). A Delaunay mesh is generated between all the "test points" (points along the boundary, and each streamline). For each triangle in the mesh, the "circumcircle" (the circle that inscribes the triangle) is used to estimate the distance between points—providing a quick method for distance calculation. To start a new streamline the circumcircle with the largest diameter is taken from the list and its centre is the new seeding point. It is thereby placing the new seed in the largest void in the space. The algorithm stops when no circumcircle exists with a diameter larger than d_{sep}. Each

streamline terminates when it is closer than d_{test} to an existing streamline. The streamlines are generated using Euler and second-order Runge-Kutta integration. They found that this method equally distributes the spaces across the domain and creates longer streamlines than Jobard and Lefer's method.

The Mebarki et al. (2005) algorithm has improved results compared to Jobard and Lefer's algorithm, particularly concerning consistently connected streamlines. The Mebarki et al. algorithm is 200 times faster than the Turk-Banks algorithm with comparable results, and it is two times faster than the Jobard and Lefer algorithm (Mebarki, et al., 2005). However, due to their algorithm's nature, it results in higher density areas next to lower density areas. This occurs as the spacing between streamlines in one area is slightly above the saturation level, and the spacing in the adjacent area is slightly below the saturation ratio; see Figure 4-5.
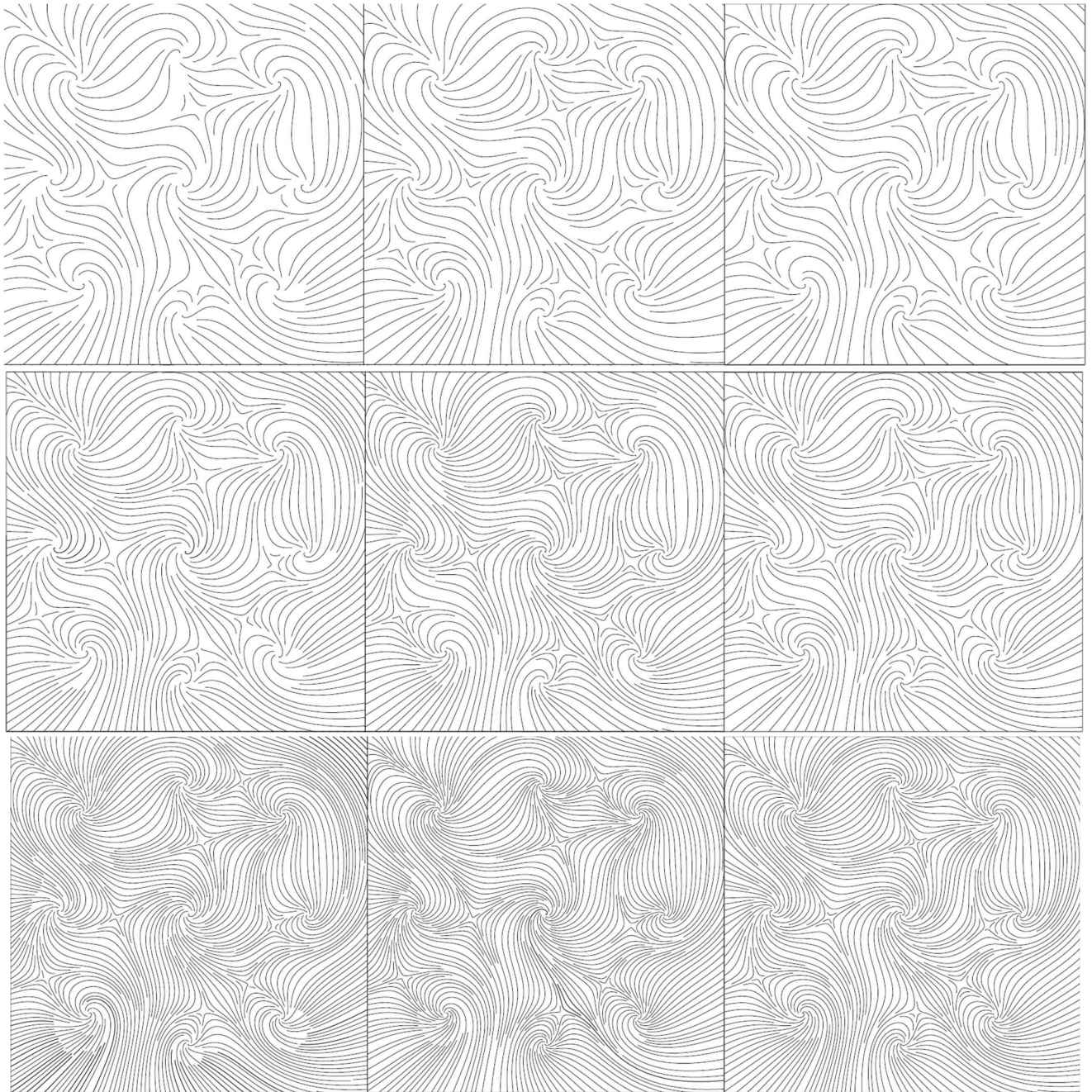

Figure 4-6: Comparison of Different Seeding Algorithms with Increasing Density for Top to Bottom; Left Column: Jobard and Lefer's; Middle Column: Liu et al.'s; Right Column: Mebarki et al.'s. Source: (Liu, et al., 2006)

Liu et al. (2006) created a more sophisticated system that utilised many ideas from previous advances and introduced new optimisations to the methods (See Figure 4-6 middle). Unlike previous work, a fourth-order Runge-Kutta integrator was used. This was combined with an adaptive step size to reduce the overall number of steps needed in streamline generation. Additionally, error checking was incorporated to give a greater density of steps where higher errors would occur. The streamline needed interpolating between the step points to produce a more even spacing of sampling points for distance checking due to the varying step size. Liu et al. (2006) used cubic Hermite polynomial interpolation to generate points at a designated spacing, which they set to d_{test}. They have used the same d_{test} and d_{sep} parameters as defined previously. In this adapted method, a new seeding strategy utilises two seeding queues: a primary queue and a secondary queue. The primary queue has an ordered list weighted by preference. The user inputs an initial set of seeds with a maximum weighting at the critical flow points. The algorithm adds to this list with seeds found by neighbour seeding and the length of the streamline weights these. The secondary queue contains a list of regular samples which are unordered. The algorithm thus ends when both queues are empty.

To deal with the spiralling loops caused by slight inconsistencies in the integration method, Liu et al. (2006) created a robust loop detection algorithm to detect and close loops. Their method works by calculating the two vectors' dot product at the location where a streamline meets itself. The loop can be closed if the angle between the vectors is small enough. This algorithm was visually similar to the previously developed algorithms and was four times faster than the Mebarki et al. algorithm (Liu, et al., 2006).

4.4 Conclusion

Section 4.2 covered the tools developed for creating principal stress lines. The commercially available tools are ineffective at producing high-quality stress lines that could be used to design a structure. Halpern et al. (2013) created a stress line tool to analyse Nervi's isostatic slabs using FEA results. The tool worked well for their applications, but they omitted critical information, and the tool would not work for all slabs. For example, creating a vector field from the FEA results was not explained, a robust seeding strategy was not created, and the looping stresses were not detected. Tam (2015) developed a new method for interpolating the FE results to produce continuous results for the principal stress trajectories. For this Tam assumed each element only produces a single principal stress trajectory – this is correct if the elements have three nodes. However, high-order elements (≥4 nodes) have continuous stress results; therefore, higher-order elements could be used as an alternative interpolation method. Tam also developed three corrections for their algorithm. The circumferential stress (i.e., loop stress) detection correction was a necessary addition to the tool. However, the enforce offset rule was required to correct the calculation errors, and the bypass seeding rule was required as the seeding strategy was not holistic. A better alternative would be to remove these issues from the stress line generation by reducing the calculation errors and using an advanced seeding strategy.

The methods used to generate streamlines have solutions to some of these problems. In Section 4.3, three different holistic seeding methods were described. The 'Neighbour Seeding' method places new seeds adjacent to the existing streamlines. The 'Farthest Point Seeding' method places new seeds at the centre of the largest void between existing streamlines. Liu et al. (2006) used a combination seeding method: the first seeds were at the critical flow

locations, and then subsequent seeds were created using the neighbour seeding method. The neighbour seeding and farthest point seeding methods can be applied to stress lines. However, the combination seeding method cannot be applied to stress lines as this would require knowledge of where the umbilic points occur (the stress line equivalent to critical flow points), which cannot be determined before the stress lines are drawn.

All the stress line generation tools have used an Euler integration method. However, Liu et al. (2006) showed that using a fourth-order Runge-Kutta method can reduce the integration errors for streamlines. Liu et al. also used an adaptive step size in their integration method to reduce the error accumulation. Therefore, this method can also be applied to stress lines to reduce calculation errors.

<div style="border:2px solid #d4491f; text-align:center; padding:12px;">

5 STRESS LINE GENERATION

</div>

5.1 Introduction

Chapter 4 reviewed the current methods that can generate stress lines and described where some advances could be made using techniques for generating streamlines. In this chapter, these methods will be tested and compared to find the best stress line generation method. The methods are broken down into three parts: interpolation methods, integration methods, and seeding methods.

The methods are evaluated on their applicability to *in-plane loaded plates* with regular element shapes. This is equal to their applicability to *out-of-plane loaded slabs* because the same challenges arise in both. The methods which produce the best results will then be developed for out-of-plane loaded slabs with irregular element shapes and sizes.

5.1.1　　Interpolation Methods

The finite element method calculates the displacement vectors for each node in the model. From this, postprocessing steps can be taken to calculate other results like the stresses and reaction forces. FEA software provides the results at specific points. However, a stress result is needed at every point on the model to create a stress line. Therefore, the results must be presented in the form of continuous data. The interpolation method takes discrete data and interpolates it into continuous data using a mathematical function. An example of this is shown in Figure 5-1.
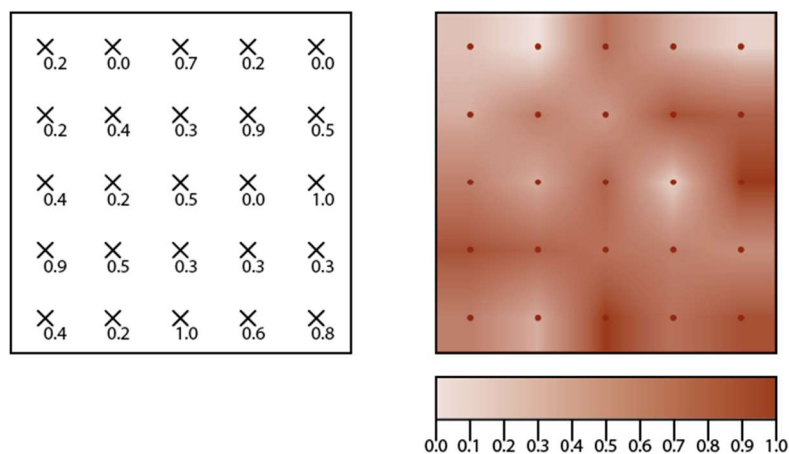
Figure 5-1: Interpolation Method; Left) Discrete Data for a Grid of 5x5 Points, Right) a Bilinear Interpolation of the Discrete Data into Continuous Data Shown Using a Colour Gradient

In this chapter, two interpolation methods will be tested. The first is the N+1 order method created by Tam (2015). The discrete data inputs for this method are the principal stress trajectories ($\hat{s}_i$) at the centre of every element (c_i). The principal stress trajectory '$\hat{x}$' can be found at a point 'x' using Eq. 5.1, Eq. 5.2, and Eq. 5.3. Where r is the user-specific inclusion radius.

$$\hat{x} = \frac{\vec{x}}{|\vec{x}|} \qquad Eq.\,5.1$$

$$\vec{x} = \sum_i^n \vec{s_i} \cdot \left(1 - \frac{d_i}{r}\right) \qquad Eq.\,5.2$$

$$d_i = \min \left\{ \begin{matrix} |x - c_i| \\ r \end{matrix} \right. \qquad Eq.\,5.3$$

The author has developed the second interpolation method from the FEA theory, and is referred to as the 'Shape Function Method'. The discrete data inputs are the displacement values '$\vec{u_n}$' at each node for every element. Eq. 5.4 shows the vector input when the displacements are two dimensional, and there are n nodes per element. In FEA, a displacement field for the elements '$u(x, y)$' is created by interpolating between the nodes (i) using so-called shape functions '$N_i(x, y)$'. Eq. 5.5 shows the calculations of the displacement field, and Eq. 5.6. defines the shape function matrix 'N'.

$$\vec{u_n} = \begin{bmatrix} u_{1x} \\ u_{1y} \\ u_{2x} \\ u_{2y} \\ \vdots \\ u_{ny} \end{bmatrix} \qquad Eq.\,5.4$$

$$u(x, y) = N \cdot \vec{u_n} \qquad Eq.\,5.5$$

$$N = \begin{bmatrix} N_1 & 0 & N_2 & 0 & \cdots & N_n & 0 \\ 0 & N_1 & 0 & N_2 & \cdots & 0 & N_n \end{bmatrix} \qquad Eq.\,5.6$$

Two element types are tested for the shape function method: four-node quadrilateral elements and eight-node quadrilateral elements. Eq. 5.7 and Eq. 5.8 give the shape function forms for the four-node and eight-node elements, respectively. Where (x, y) is the coordinate for any point within the element. The constants in N_i are found by solving Eq. 5.7 or Eq. 5.8 for when there is a unit result at node i and a result of zero at the other nodes.

$$N_i = c_1 xy + c_2 x + c_3 y + c_4 \qquad Eq.\,5.7$$

$$N_i = c_1 x^2 y + c_2 xy^2 + c_3 x^2 + c_4 y^2 + c_5 xy + c_6 x + c_7 y + c_8 \qquad Eq.\,5.8$$

The strains at a point (x, y) can be calculated using Eq. 5.9 and Eq. 5.10. Then the stresses can be found using Eq. 5.11 and Eq. 5.12. A field for principal stresses is created by combining this with Eq. 1.3, Eq. 1.4, and Eq. 1.5. The process is mathematically identical for slabs, excepted that the displacement are rotations, and the stresses become distributed moments when $\frac{E}{1-v^2}$ is replaced with $\frac{Et^3}{12(1-v^2)}$.

$$\vec{\varepsilon}(x, y) = \begin{bmatrix} \varepsilon_x \\ \varepsilon_y \\ \gamma_{xy} \end{bmatrix} = B \cdot \vec{u_n} \qquad Eq.\,5.9$$

$$B = \begin{bmatrix} \dfrac{\partial N_1}{\partial x} & 0 & \dfrac{\partial N_2}{\partial x} & 0 & \cdots & \dfrac{\partial N_n}{\partial x} & 0 \\[2mm] 0 & \dfrac{\partial N_1}{\partial y} & 0 & \dfrac{\partial N_2}{\partial y} & \cdots & 0 & \dfrac{\partial N_n}{\partial y} \\[2mm] \dfrac{\partial N_1}{\partial y} & \dfrac{\partial N_1}{\partial x} & \dfrac{\partial N_2}{\partial y} & \dfrac{\partial N_2}{\partial x} & \cdots & \dfrac{\partial N_n}{\partial y} & \dfrac{\partial N_n}{\partial x} \end{bmatrix} \qquad Eq.\,5.10$$

$$\vec{\sigma}(x,y) = \begin{bmatrix} \sigma_x \\ \sigma_y \\ \tau_{xy} \end{bmatrix} = \frac{E}{1-v^2} \cdot D \cdot \vec{\varepsilon} \qquad Eq.\,5.11$$

$$D = \begin{bmatrix} 1 & v & 0 \\ v & 1 & 0 \\ 0 & 0 & (1-v)/2 \end{bmatrix} \qquad Eq.\,5.12$$

The statement given in Eq. 5.13 can be used to prevent 90° rotations. These occur due to the limitations of Eq. 1.5. Eq. 5.13 is derived from the Mohr's circle. The principal stress trajectory fields are given by Eq. 5.14 and Eq. 5.15.

$$\boldsymbol{for\ \sigma_y > (\sigma_x + \sigma_y)}: \quad \begin{matrix} \theta - \dfrac{\pi}{2} \ \ (for\ \theta > 0) \\[2mm] \theta + \dfrac{\pi}{2} \ \ (for\ \theta < 0) \end{matrix} \qquad Eq.\,5.13$$

$$\widehat{x_1}(x,y) = \begin{bmatrix} cos\theta \\ sin\theta \end{bmatrix} \qquad Eq.\,5.14$$

$$\widehat{x_2}(x,y) = \begin{bmatrix} -sin\theta \\ cos\theta \end{bmatrix} \qquad Eq.\,5.15$$

The pseudo-code that has been used for these methods is shown in Annex A.2.

5.1.2   Integration Methods

The interpolation methods provide a way of sampling the principal stress trajectory at any point within the model - providing a field of vectors. For any point in the field '$x(t)$', a stress trajectory vector '$\vec{x}\big(x(t)\big)$' can be found, where 't' is a pseudo time dimension. Integrating the field shows a particle path through it (i.e., a stress line) – this is a particular solution.
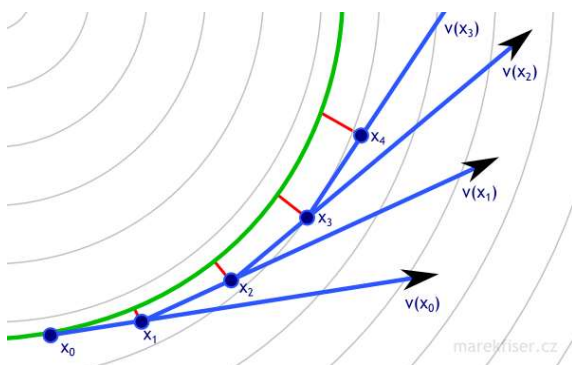
Figure 5-2: Euler Integration Method – The blue arrows show the step directions at each step point (x_0, x_1, x_2...). The green curve shows the exact solution, and the red lines show the approximation error. Source: MarekFiser.com
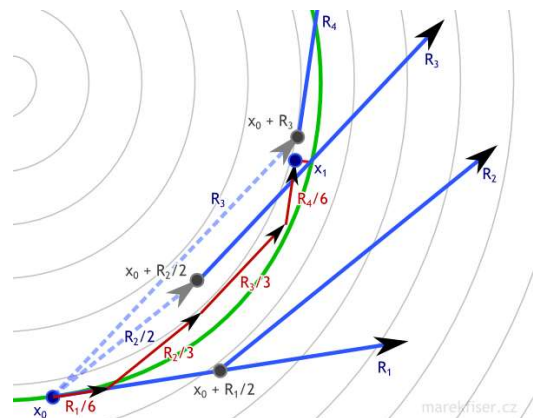
Figure 5-3: Runge-Kutta 4th Order Method – The blue arrows show each sample point's directions. The red arrows show each sample vector's contribution to the next step point (x_1). The green curve shows the exact solution, and the red lines show the approximation error. Source: MarekFiser.com

This chapter evaluates two step-by-step integrators: the Euler integrator and the fourth-order Runge-Kutta (RK4) integrator (see Figure 5-2 and Figure 5-3). The Euler integrator samples the vector field at a single location. $Eq.\,5.15$ and $Eq.\,5.16$ show the integrator for increasing and decreasing values of t. 's' is the step size and '$\hat{x}_T$' is the vector sample. The integrator starts from the seed '$x(0)$'.

$$x(t+s) = x(t) + \vec{x}_T(t) \qquad Eq.\,5.15$$

$$x(t-s) = x(t) - \vec{x}_T(t) \qquad Eq.\,5.16$$

$$\vec{x}_T = s \cdot \hat{x}(x(t)) \qquad Eq.\,5.17$$

The RK4 integrator samples the vector field at four locations. Eq. 5.18 gives the integrator for increasing values of t. The vector samples are given by Eq. 5.18 to Eq. 5.22. For decreasing values of t, the vector samples are be made negative.

$$x(t+s) = x(t) + \vec{x}_T(t) \qquad Eq.\,5.18$$

$$\vec{x}_T = \frac{\vec{x}_1 + 2 \cdot \vec{x}_2 + 2 \cdot \vec{x}_3 + \vec{x}_4}{6} \qquad Eq.\,5.19$$

$$\vec{x}_1 = s \cdot \hat{x}(x(t)) \qquad Eq.\,5.20$$

$$\vec{x}_2 = s \cdot \hat{x}\left(x(t) + \frac{\vec{x}_1}{2}\right) \qquad Eq.\,5.21$$

$$\vec{x}_3 = s \cdot \hat{x}\left(x(t) + \frac{\vec{x}_2}{2}\right) \qquad Eq.\,5.22$$

$$\vec{x}_4 = s \cdot \hat{x}(x(t) + \vec{x}_3) \qquad Eq.\,5.23$$

An error correction is added to these integrators to reduce the step size where the estimated error 'ε' is greater than the user-specified maximum error 'ε_{max}'. The step size is halved when $\varepsilon > \varepsilon_{max}$, and doubled when $\varepsilon < \frac{\varepsilon_{max}}{2}$. Although the step size is never increased beyond the initial user-specified value. Eq. 5.23 and Eq. 5.24 are used to estimate the Euler and RK4 integrators' error, respectively.

$$\varepsilon_{Euler} = |\hat{x}_1 - s \cdot \hat{x}(x(t+s))| \qquad Eq.\,5.24$$

$$\varepsilon_{RK4} = \frac{|\hat{x}_4 - s \cdot \hat{x}(x(t+s))|}{6} \qquad Eq.\,5.25$$

The angle between successive steps also modifies the step size. The integrators produce polyline curves, so to maintain a smooth curvature, the step size is reduced when the angle between steps 'α' is larger than $\frac{\pi}{10}$. See Eq. 5.26 for α. The step size is halved when $\alpha > \frac{\pi}{10}$ and doubled when $\alpha < \frac{\pi}{20}$.

$$\cos \alpha = \frac{\vec{x}_T(t) \cdot \vec{x}_T(t+s)}{|\vec{x}_T(t)| \cdot |\vec{x}_T(t+s)|} \qquad Eq.\,5.26$$

Loop detection is added to the integrators by checking the distance between the seed point and the new point in the stress line. If the distance is less than the step size and if β is less than $\frac{\pi}{10}$, then the integrator is stopped and a closed polyline is created.

$$\cos\beta = \frac{\vec{x}_T(0) \cdot \vec{x}_T(t + s \cdot n)}{|\vec{x}_T(0)| \cdot |\vec{x}_T(t + s \cdot n)|} \qquad Eq.\,5.27$$

The pseudo-code that has been used for these methods is shown in Annex A.3.

5.1.3   Seeding Methods

The integrator can produce stress lines starting from a seed. The seeding method provides the seeds to the integrator. Two holistic seeding methods are tested in this chapter: the neighbour seeding method, and the farthest point seeding method. The user gives the seed of the first stress line as an input into both methods. Once the first stress line is generated, the subsequent seeds are produced by the seeding methods. The pseudo-code that has been used for these methods is shown in Annex A.4.
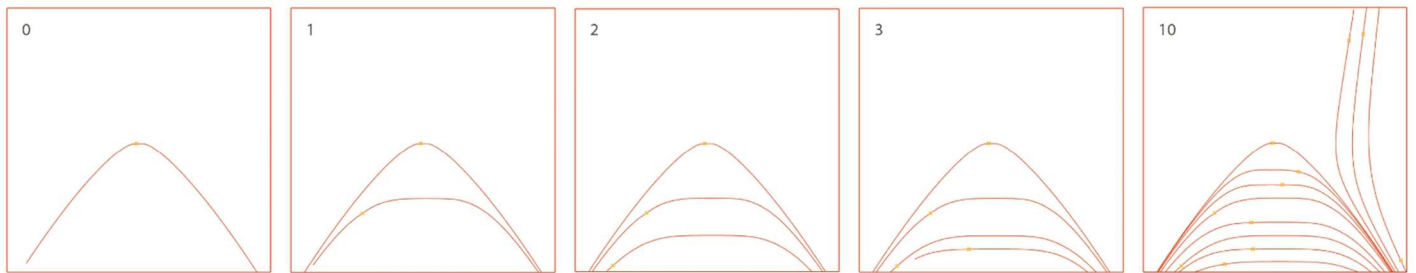
Figure 5-4: Illustration of the Neighbour Seeding Method
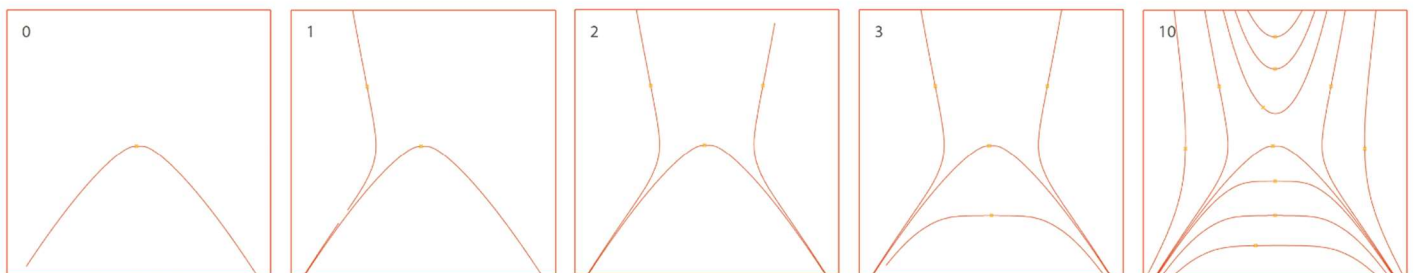
Figure 5-5: Illustration of the Farthest Point Seeding Method

The neighbour seeding method creates new seeds at every 10th point from the stress line. Two new seeds are created perpendicularly to the stress line and are added into the seed list. When a new seed is needed the first seed in the list is taken and evaluated to check that it is not closer than d_{sep} to an existing stress line, if it is the seed is deleted and the next seed is taken. d_{sep} is the user-defined 'separating distance' that controls the density of the stress lines. The process is repeated every time a new stress line is finished, and the process ends when the seed list is empty. See Figure 5-4.

The farthest point seeding method creates a Delaunay mesh using the first stress line's points and points located along the model's edge. The points on the model's edge are spaced d_{sep} apart. A circle that circumscribes every triangle in the mesh is drawn – these are called the 'circumcircles'. The new seed is positioned at the centre of the circumcircle with the largest diameter. The new stress line's points are then added into the Delaunay mesh, and the process is repeated. The seeding method ends when the diameter of the largest circumcircle is less than d_{sep}. See Figure 5-5.

5.1.4　　The Stress Line Axioms

The stress line fields generated by each method will be tested and compared on their accuracy. There are no generalised solutions for stress line fields, so the stress line axioms will measure the accuracy. The stress line axioms are derived from the theory of principal stresses and Mohr's circle. The three axioms are:

- Stress lines within the same family should not cross.
- Stress lines of different families should cross perpendicular to each other.
- Stress lines should meet free edges at a perpendicular angle.

Stress lines within the same family should not cross because each family's principal stresses are always parallel over small distances. Stress lines of opposite families should always cross perpendicularly because the two principal stress directions are always perpendicular to each other. For the same reason, stress lines should always meet the free edge perpendicularly because the normal stress perpendicular to the edge is zero, and no shear acts all the edge. The bending moment perpendicular to the edge is zero for slabs, and the torsion along the edge is zero.

5.2 Methodology

The methods need to be tested to find the best way of generating stress line fields. An interpolation, an integration, and a seeding method need to be combined to create a stress line field. There are two options for each method type. Each method type will be tested independently by first testing the two integration methods, then the seeding methods, and finally, the interpolation methods.

The seeding methods are not strictly required to create accurate stress lines as combining the two other methods creates the individual stress lines. The purpose of the seeding methods in these tests is to create a stress line field with a consistent density so that the other methods are compared fairly. Both seeding methods aim at creating an even distribution between the stress lines, so this will mean that the stress lines are evenly spaced apart. The spacing between the stress lines is controlled by the parameter d_{sep}. The seeding methods are tested to ascertain whether one method produces better results in the axiom measures and to determine which method is better for creating a visual representation of the stress line field.

Three plate geometries are used to evaluate the performance: a cantilevering plate with two corner supports, a simply supported beam, and a deep fixed beam (see Figure 5-6, and note that, in the simply supported beam additional line support is attached to the left and right edges to restrain vertical displacement only). These are chosen as they show ranging scenarios and complexity. These are modelled in FEA using DIANA FEA. For each of the geometries, two models are made: one using 4-node elements and the second using 8-node elements. The N+1 Order method's vector results are calculated from the stress values at the centres of the 4-node elements. Each model has a Poisson's ratio of 0.3 and the element size in the 8-node element models are twice that in the 4-node element models; to account for the increase in nodes. In the cantilever model, the stress lines within the four elements surrounding the point supports are discounted as these are influenced by the singularities.
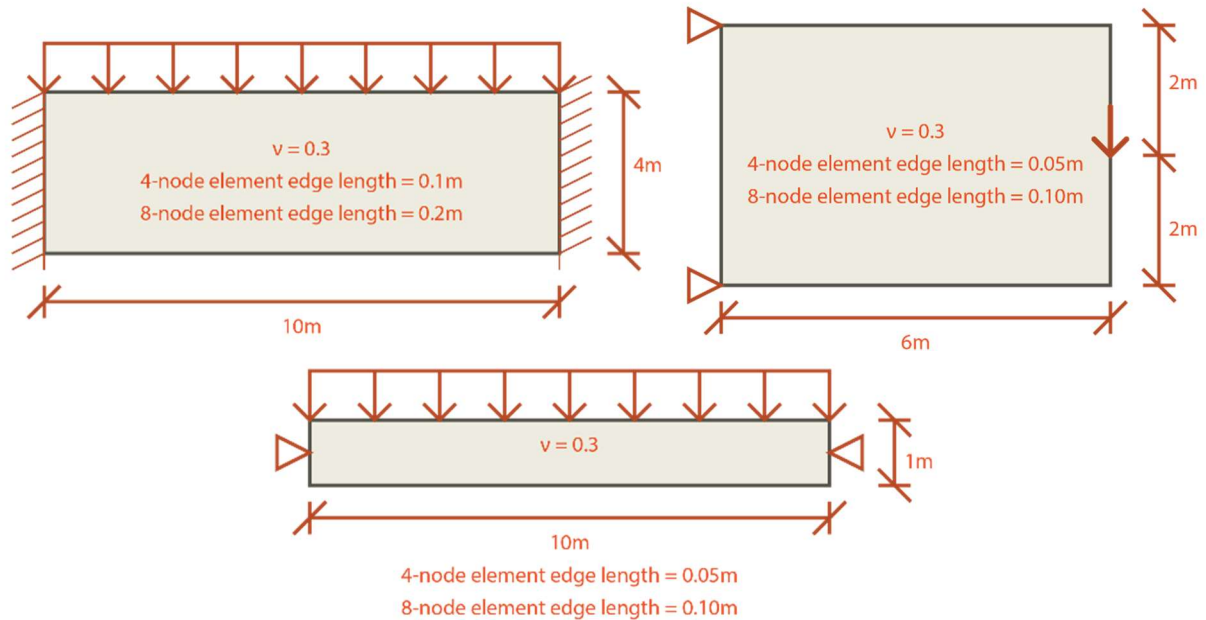
Figure 5-6: Models Used to Test Stress line Generation. Top Left: Deep Beam, Top Right: Cantilever, Bottom: Simple Beam
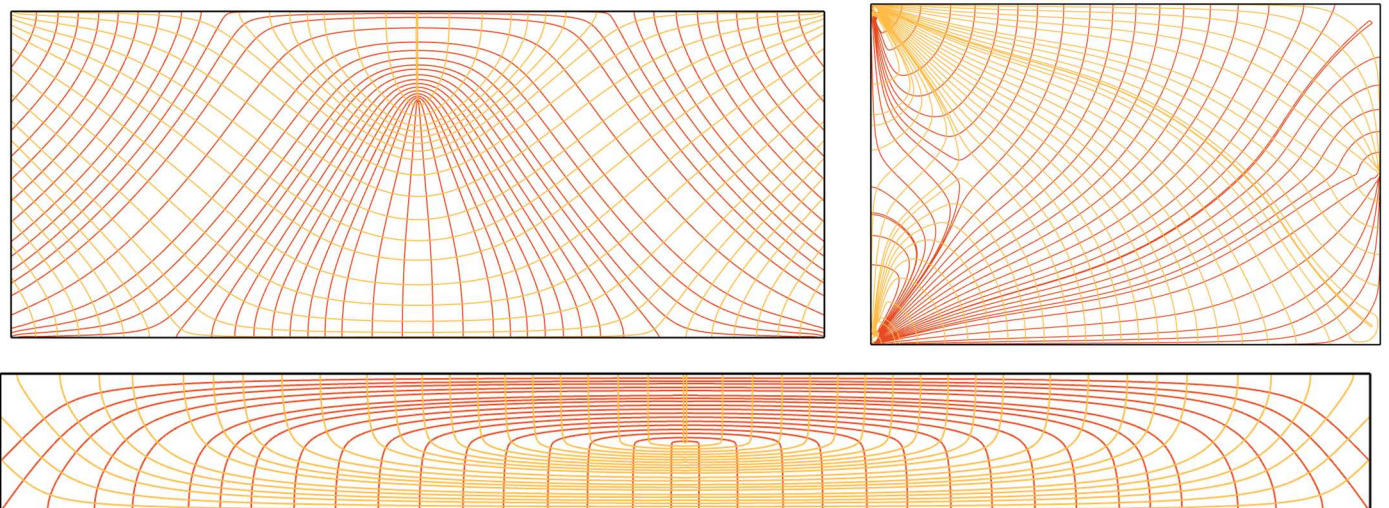
Figure 5-7: Illustrations of the Principal Stress Lines. Top Left: Deep Beam, Top Right: Cantilever, Bottom: Simple Beam

The axioms are evaluated by values measured from the resulting stress line field. The first axiom, stress lines within the same family should not cross, is measured by calculating the number of times that the same family's stress lines do cross. The second axiom, stress lines of different families should cross perpendicular to each other, is evaluated by the angle of deviation from 90° at every intersection between different families. The third axiom, stress lines should meet free edges at a perpendicular angle, is measured by the deviation angle from 90° where each stress line meets a free edge. For each of these measures, they should ideally be zero for every evaluation point

For each plate, ten different initial step sizes are used from 0.01m to 0.1m as this is considered a critical variable which has a considerable influence on the results. Also, six samples are taken for each plate using randomly selected seeds for the first stress line. For all tests, d_{sep} is set to 0.1m, and ε_{max} is 0.001m. The maximum error is given this value as preliminary tests showed a good balance between accuracy and computational time.

For the purposes of illustration and clarity, Figure 5-7 shows what the stress lines look like for each of the plates.
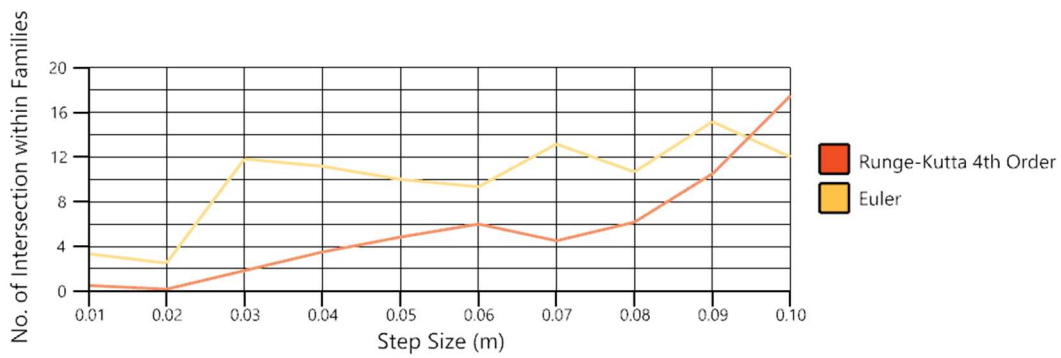
A: Amount of Collisions of within Families
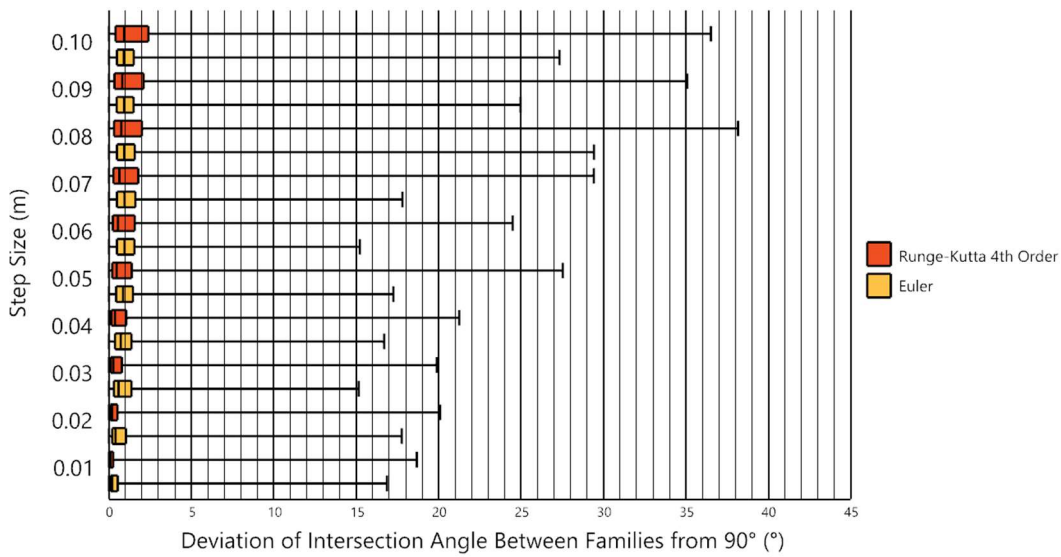
B: Box Plots of Intersection Angles between Families
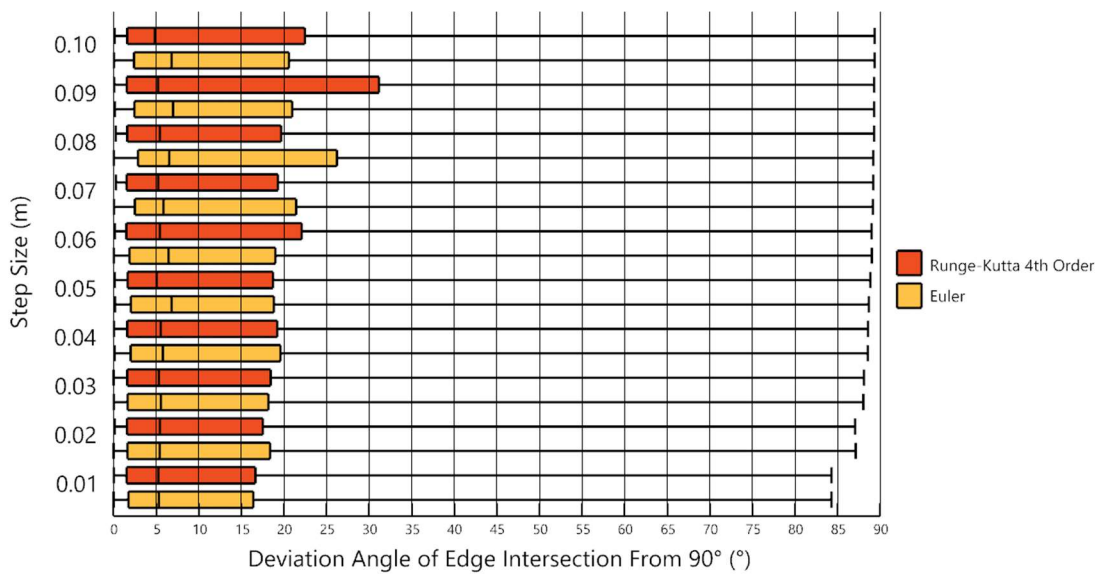
C: Box Plots of Edge Intersection Angles

Figure 5-8: Charted Data from the Results of the N+1 Order Interpolation, with Neighbour Seeding, in the Cantilever Model

5.3 Integration Methods

Two integration methods are tested: the Euler method, and the 4th order Runge-Kutta (RK4) method. The literature has shown that the RK4 method has significantly better results when creating streamlines; therefore, it needs to be tested if it holds for stress lines. Stress line fields are created for the three plates using the neighbour seeding method and the N+1 order interpolation method as fixed variables.

Figure 5-8 shows the results for streamlines calculated using the Euler and RK4 integration methods for the cantilever FE model. From Figure 5-8-A, it can be seen in the Euler method that a positive linear relationship occurs between the step size and the number of intersections within each family. Thus, the smaller the step size, the more axiom one is met. The same effect can be seen for the RK4 integration, but this method has fewer intersections at any given step size.

Performance to the second axiom is shown in Figure 5-8-B. There is an improvement in both integration methods with decreasing step size. Overall, the RK4 method provides better results; although the improvement is minimal at the smallest step size of 0.01m.

Figure 5-8-C shows that a smaller step size for the Euler method has a small improvement on the edge intersection angle. Generally, the RK4 integrator performs better until a step size of 0.01m where they are about equal. However, even with the smallest step size, the results are not impressive with median values around 5° and the upper quartile still lying between 15° and 25°. The upper bound is located close to 90°, as there are some stress lines which should run parallel with the edge, but instead, meet it acutely.

From the other plates (the simple and deep beams), the same conclusions can be drawn for each of the three axioms. The only difference is that the number of intersections for RK4 in the deep beam and the simple beam is close to zero for all step sizes., as shown in Figure 5-9.
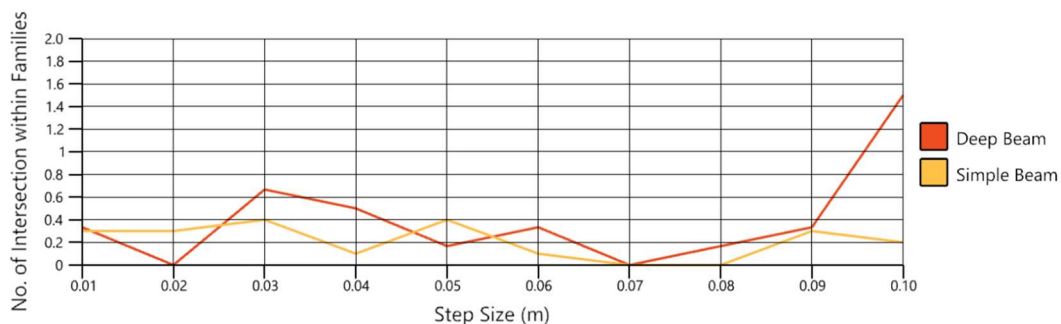
Figure 5-9: Amount of Collisions within Families from the Results of the N+1 Order Interpolation, with Neighbour Seeding and RK4 Integration

5.4 Seeding Method

Two seeding strategies are tested: the neighbour seeding strategy, and the farthest point seeding strategy. Figure 5-10 shows the cantilever plate's data when using the neighbour and farthest point seeding methods, where an RK4 integration method and a N+1 order interpolation method are used in both case. However, the charts show no significant improvement to any of the three axioms by using one seeding strategy or the other. This is expected as the seeding strategies were developed for increased computational time and
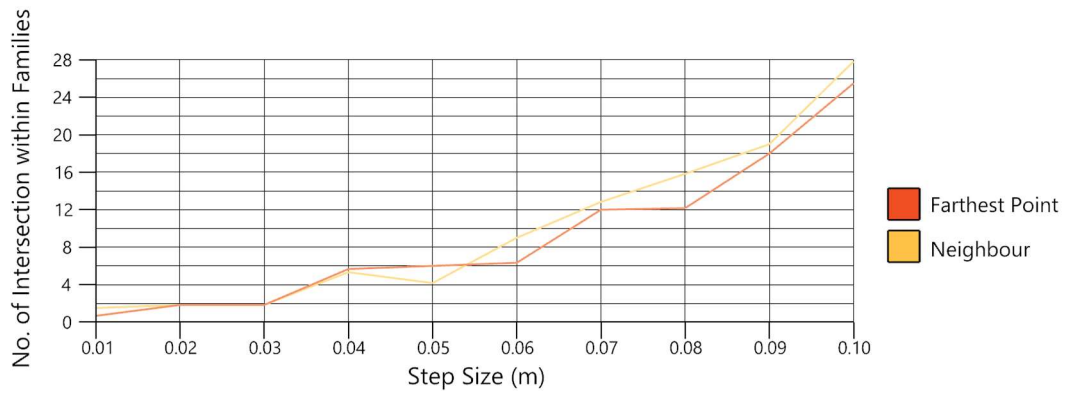
A: Amount of Collisions within Families
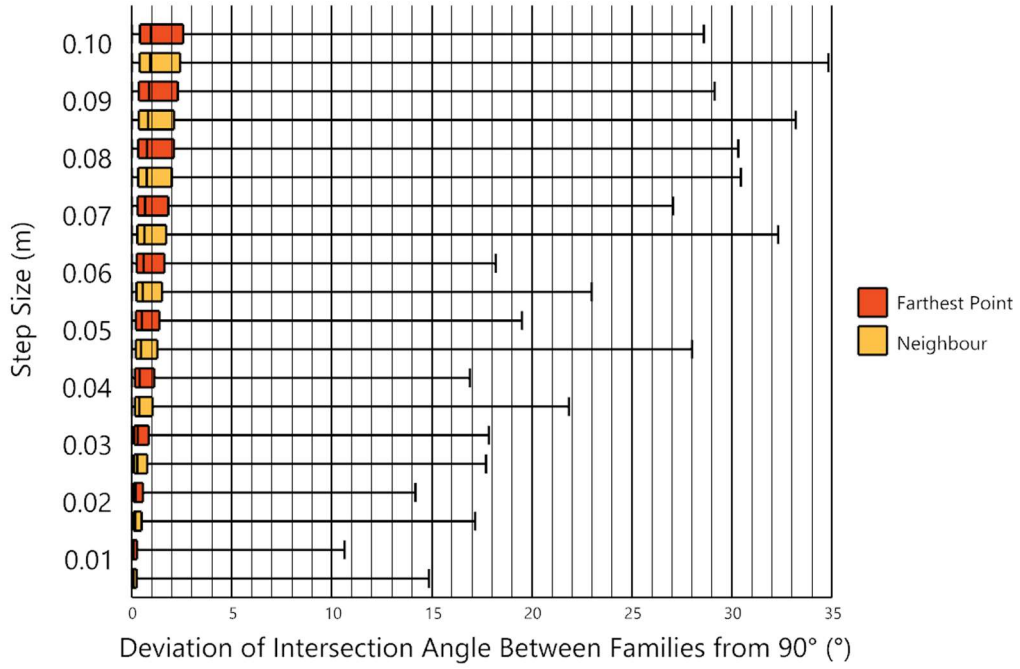
B: Box Plots of Intersection Angles between Families
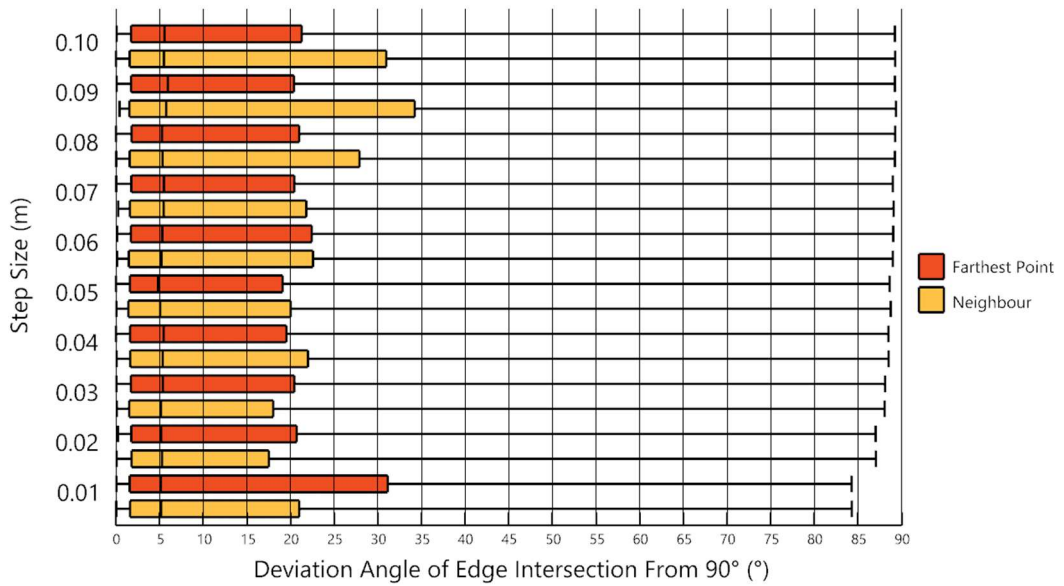
C: Box Plots of Edge Intersection Angles

Figure 5-10: Charted Data from the Results of the N+1 Order Interpolation with RK4 Integration, in the Cantilever Model
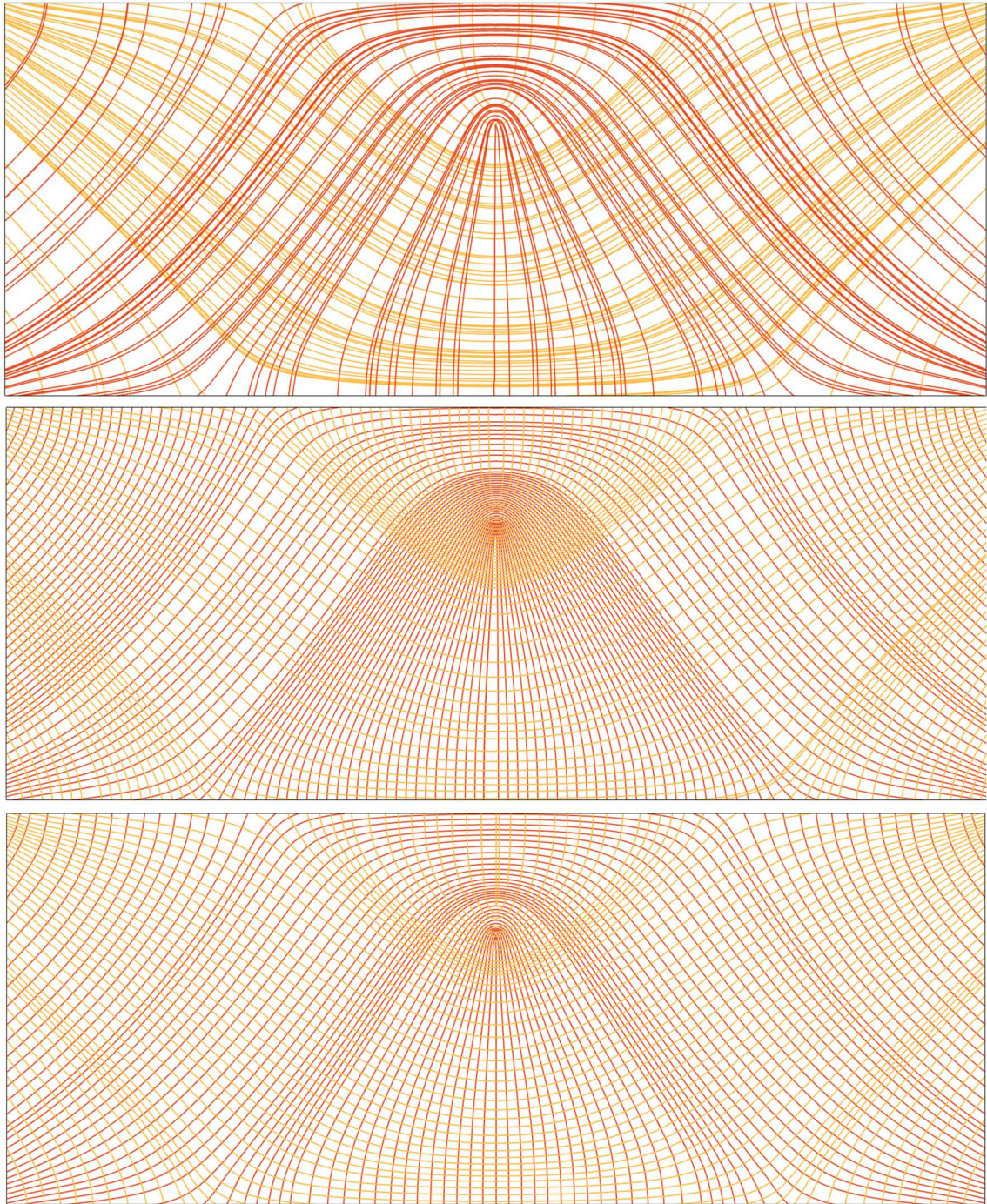
Figure 5-11: Visual Comparison of Different Seeding Methods for the Deep Beam Plate; Top: Random, Middle: Neighbour, Bottom: Farthest Point

better visual performance. They also ended streamlines as they approached existing streamlines to create an even visual density across the image. The premature ending of stress lines is not considered in this thesis, as complete stress lines are required. However, ending the stress lines is useful when trying to create visual imagery of the flow of forces. Figure 5-11 shows the two seeding methods in visual comparison to each other and a seeding "method" where the seeds are positioned randomly.

Each of the images has approximately the same number of stress lines. It is apparent how much better the two seeding strategies are than placing seeds randomly. It can also be seen that the farthest point method has a better distribution of the stress lines across the plate which gives an even distribution of voids.

The same conclusions are also drawn from the other two plate models.

5.5 Interpolation Method

Two types of interpolation are tested: The N+1 order method and the shape function method. For the shape function method, two alternatives are tested. The first where 4-node elements are used and the second using 8-node elements. It is hoped that by using higher-order elements that the results will be more accurate. For this final set of tests, the same three plates are used with RK4 integration and neighbour seeding to produce the streamlines.

Figure 5-12 shows the cantilever model's graphed data using the N+1 order method and the shape function method using 4-node and 8-node elements. Comparing, the 4-node element and the 8-node element method, the 8-node element provides better results in all three axioms, especially concerning collisions within families. However, note that from observing Figure 5-12-C, the 8-node element has a larger variance in data than the 4-node element at larger step sizes. The same conclusions are made about the data from the other two models.

In terms of the first axiom, Figure 5-12-A shows that the N+1 order method outperforms the shape function methods with the 8-node element method resulting in approximately two times more collisions than the N+1 order method. For the deep beam and simple, both the methods have two collisions or less for every step size. Although the shape function method is at a disadvantage for large step sizes, below a step size of 0.02m, the difference is small

Looking at Figure 5-12-B, it can be seen that the 4-node shape function method has an extensive range of intersection angle. The range of the 8-node shape function method is comparable to the N+1 order method. The median and upper quartile values for the shape functions methods are lower than the n+1 order method, with the 8-node method being the better of the two. The most perpendicular intersections occur when using the 8-node shape function method with a step size of 0.01m resulting in 75% of the results having an intersection angle >89.82°.

Using the shape function method has a significant improvement on the edge intersections, see Figure 5-12-C. However, there are still some intersections occurring at acute angles, so it is not easy to see all the results on the box plots. Figure 5-13, Figure 5-14, and Figure 5-15 are histograms of the three plates' edge intersection angles when the step size is 0.01m. Even with this small step size, there are still stress lines with meet the edge at non-perpendicular angles. This is particularly evident in the cantilever plate. The best stress lines are produced using the 8-node shape function method for the simply supported beam as 97.1% of the intersections have an angle of >80° with the edge.
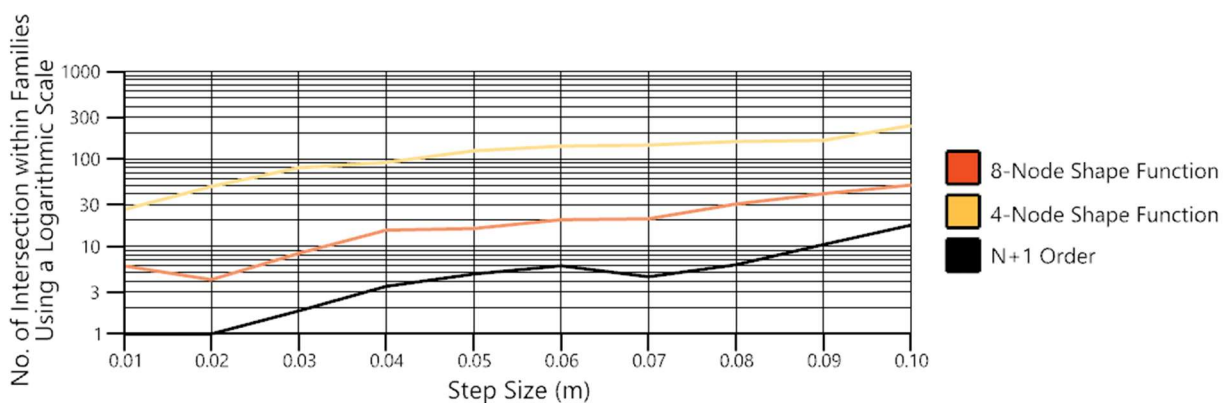
A: Amount of Collisions within Families
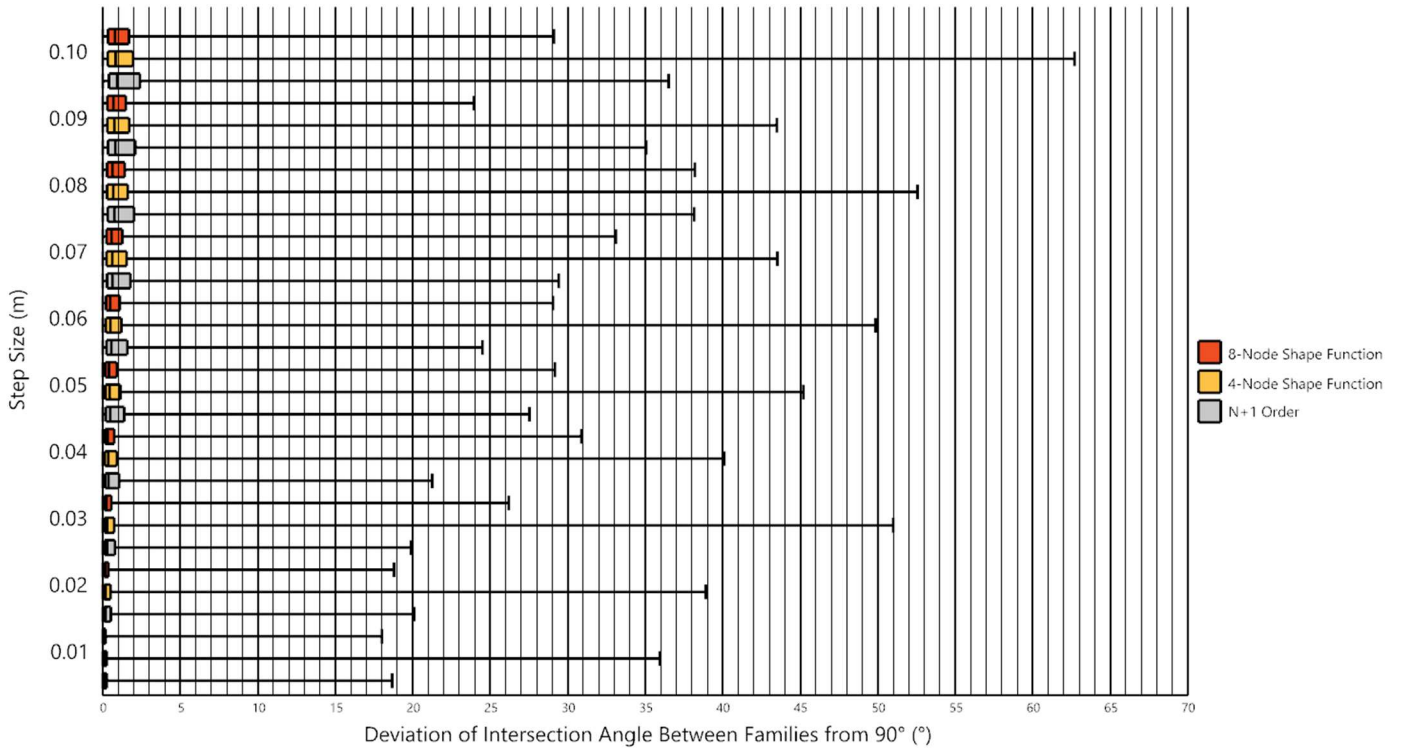
B: Box Plots of Intersection Angles between Families
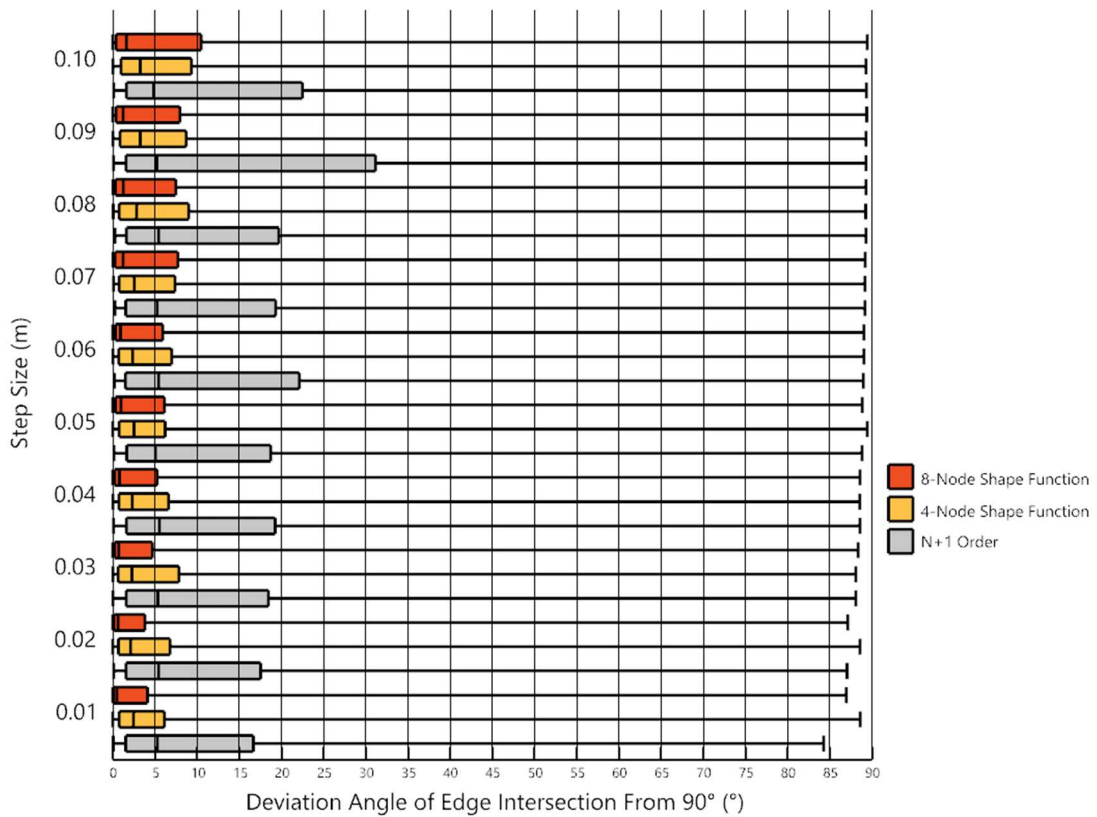
C: Box Plots of Edge Intersection Angles

Figure 5-12: Charted Data from the Results of the Shape Function and N+1 Order Interpolation, Neighbour Seeding and RK4 Integration, in the Cantilever Model
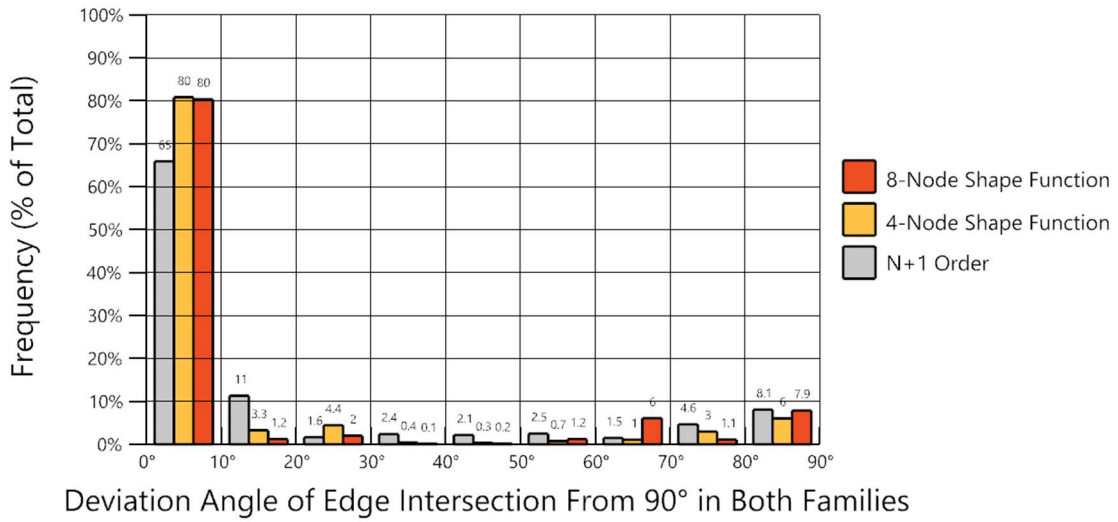
Figure 5-13: Histogram of Edge Intersection Angles from the Results of the Three Integration Methods with Neighbour Seeding and RK4 Integration and a Step Size of 0.01m, in the Cantilever Model
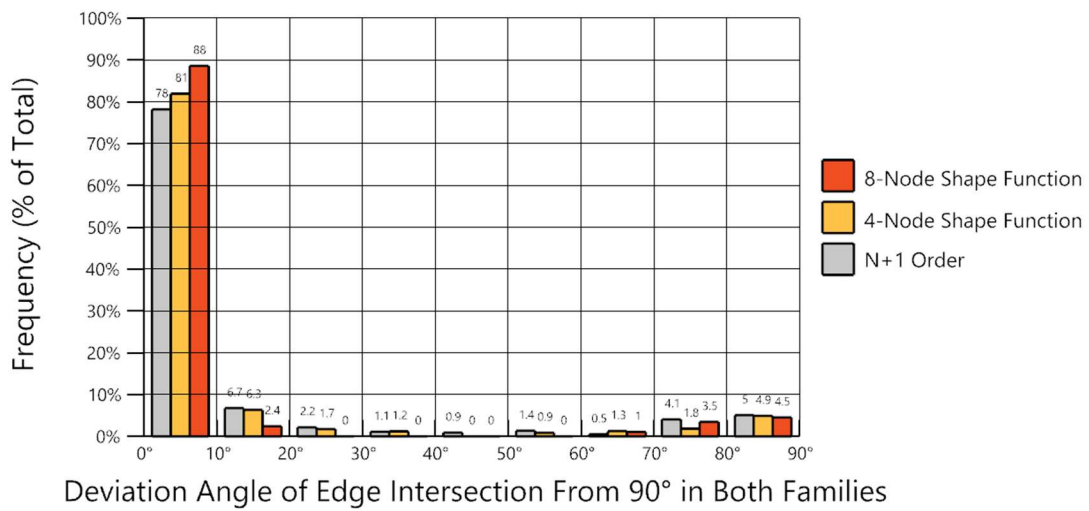
Figure 5-14: Histogram of Edge Intersection Angles from the Results of the Three Integration Methods with Neighbour Seeding and RK4 Integration and a Step Size of 0.01m, in the Deep Beam Model
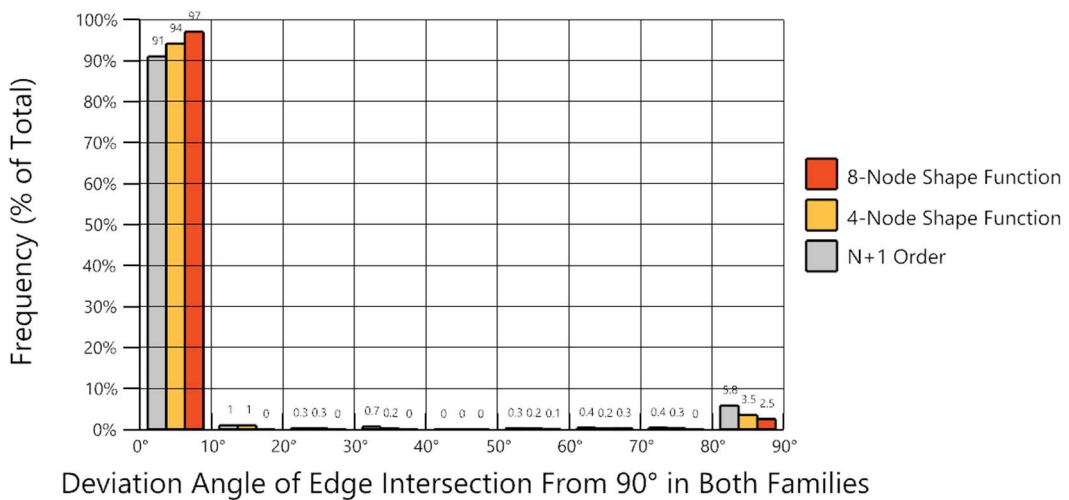
Figure 5-15: Histogram of Edge Intersection Angles from the Results of the Three Integration Methods with Neighbour Seeding and RK4 Integration and a Step Size of 0.01m, in the Simply Supported Beam Model

5.6 Conclusion

The stress line generation tools that are commercially available and are described in the literature have many limitations. In this chapter, the theory of stress generation has been developed by distinguishing three need components: the interpolation method, the integration method, and the seeding method.

A new interpolation method has been developed using the shape functions from the theory of FEA. When 4-node elements are used, the stress lines are inaccurate compared when compared against the N+1 order interpolation method developed by Tam (2015). However, using elements with eight nodes showed that the shape function method could produce more accurate intersections with the edge and opposing stress lines. Although the N+1 order method does create stress line fields with fewer collisions between the same family's stress lines.

The previous stress line tools all used the Euler integration method; however, this chapter showed that the stress line accuracy could be improved by replacing this with a fourth-order Runge-Kutta method.

The tools developed for generating streamline in fluid flows provide two holistic seeding strategies which were tested to see how well they could create an entire stress line field. Neither the neighbour seeding method nor the farthest point method reduced the errors in the stress lines. This was expected, as they were developed for creating visually clear images. Both methods provided clean images with an even spread of density; however, the farthest point method did provide the images with the best distribution of stress lines. This provides a remarkable improvement to the stress line generation theory as all the previous seeding methods placed the seeds arbitrary.

Therefore, it is recommended that the RK4 integrator is used with the farthest point seeding method and the 8-node shape function interpolation method to produce the most accurate field of principal stress lines. The initial step size should also be made as small as possible, but consider the computational time required to achieve this. For all subsequent chapters, this arrangement of methods will be used.

Unfortunately, it was not possible to remove the errors altogether and create a perfect stress line field. The author's recommendation to improve this further are:

- Develop an additional interpolation method that can be used to create smooth curves from the step points. This would mean that the stress lines would no longer be made of straight segments.
- Investigate whether increasing the mesh density around the critical areas (e.g. the edges and the umbilic points) reduces the stress lines' errors.

6.1 Introduction

In Chapter 4, the literature relating to the generation of stress lines was reviewed. These methods were tested in Chapter 5, where the most accurate method for generating principal stress lines was revealed. In this chapter, the step between the stress line field and the geometry required to create a design will be taken. An arrangement of stress lines needs to be selected to create an isostatic slab or any other stress line based system. This stress line selection process replaces the seeding step from Chapter 5.

Li and Chen (2010) developed a method for selecting stress lines for fabrication by using an iterative process, which incrementally increases the discretised form's accuracy. This process is beneficial because it produces a discretised structure which can accurately approximate the non-discretised stress lines. Figure 6-1 illustrates the iterative process.

Li and Chen (2010) only tested this method for in-plane loaded plates. However, this algorithm (hereafter referred to as the 'Li and Chen growth method') could be beneficial for selecting stress lines to be used in isostatic slabs. Therefore, in this chapter, Li and Chen's algorithm will be tested on out-of-plane loaded slabs to determine whether it can be a useful tool for isostatic slabs.

Li and Chen (2010) outline how their growth method works. First, an initial set of stress lines are inputted that connect the supports to the load which are referred to as the 'skeleton

Figure 6-1: Li and Chen's Growth Method Used to Create a Cantilevering Truss (Li & Chen, 2010)

principal stress lines'. It is worth noting that Li and Chen only applied this method to point loaded and point-supported plates. From the skeleton principal stress lines, the following process is followed:

"(1) Identify new principal stress lines that can reduce the approximation errors between the beam structure and the principal stress lines the most;

(2) Use the identified principal stress lines to compute a set of intersection points as the positions of inserted nodes (shape optimization);

(3) Construct a beam structure by connecting the computed nodes following the connection of the principal stress lines (topology optimization).

(4) Optimize the cross section size of each beam for the constructed beam structure (size optimization). The strain energy of the whole beam structure can be computed, which can measure the stiffness of the beam structure." (Li & Chen, 2010)

The original use of this method was to approximate Michell structures for in-plane loaded domains. There are significant differences between this and using it for isostatic slabs. Firstly, the ribs in an isostatic slab need to 'fill' the domain, meaning that there cannot be large voids where the deck would be unsupported. Secondly, the slabs are not loaded at a single point, and therefore, the ribs must support a load from the deck along their length. Finally, the elements will have a consistent cross-section so step (4) of the original method will not be considered.

Methodology

The Li and Chen growth method's applicability is evaluated by first implementing it into C# code, and then testing it on the following cases:

1. 10x10m corner-supported slab with a central point load.
2. 10x10m corner-supported slab with a UDL.
3. 10x10m multi slab with a UDL.

In each case, an initial set of skeleton principal stress lines are chosen depending on the stress line field generated through the method from Chapter 5. The results are evaluated at iterations which produce symmetrical structures.

As outlined in section 6.1, the Li and Chen growth method must fulfil conditions that were not required in the original application. These conditions relate to the rib's support of the deck; the load distribution diagrams are produced inside each of the voids in the stress line structure (Figure 6-2) to evaluate this. This is used to find the maximum load span for each element, and the range of load spans across the slab are evaluated. The objective is to have the lowest standard deviation and range possible, meaning that the deck is uniformly supported. This is essential because the worst-case locations will determine the deck's thickness. The load distribution diagram simplifies the actual distribution behaviour, but this metric serves as a good indication.

6.2 Code Implementation

Figure 6-3 shows how the Li and Chen growth method has been implemented into C# code for this thesis. A detail description of the pseudo-code can be found in Annex A-5. The code is validated by testing it against two of the cases Li and Chen used in their work.

Figure 6-4 and Figure 6-5 show how the code produced for this thesis can replicate the same results as Li and Chen. For both models the following properties are used: Young's modulus = 200 GPa, Poisson's ratio = 0.33, plate thickness = 15mm, and density = 7850 kg/m³. The plate in example 1 has a height of 1m and a width of 1.5m, a point load of 1 kN is applied at the middle of the right edge, and two point supports are attached on the top and bottom of the left edge. The plate in example 2 has a height of 1m and a width of 2m, a point load of 1 kN is applied to the middle of the bottom edge, and two point supports are attached at the bottom-left and bottom-right corners.

The skeleton principal stress lines' exact locations could not be obtained from Li and Chen (2010); however, visually similar stress lines were selected. For example 1, the seeding points are at (1.1,0.1) and (1.1,0.9). For example 2, the seeding point is at (1.0,0.7).

In both examples the following stress line integration parameters were used: max. step size = 0.01m, integration method = RK4, and max. error = 0.0001m.
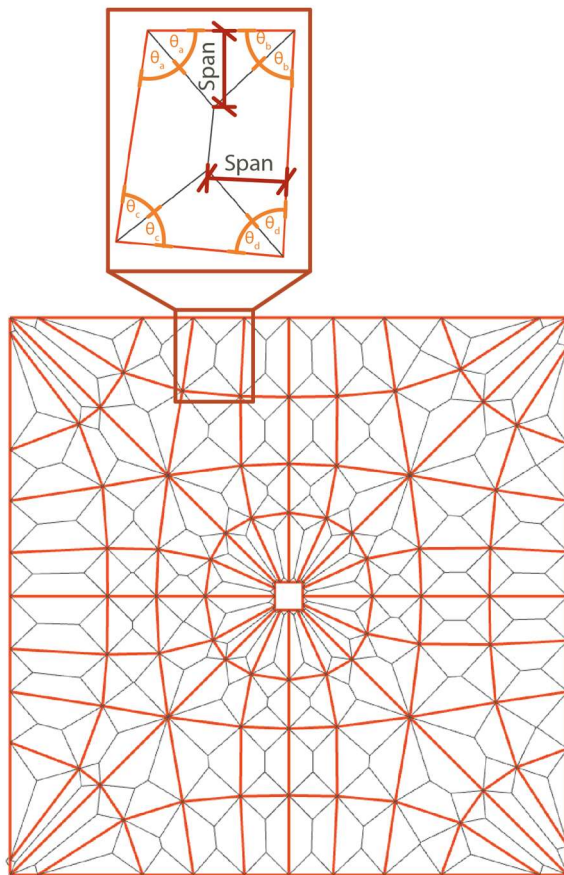
Figure 6-2: Load Distribution Analysis of a Discretised Rib Structure
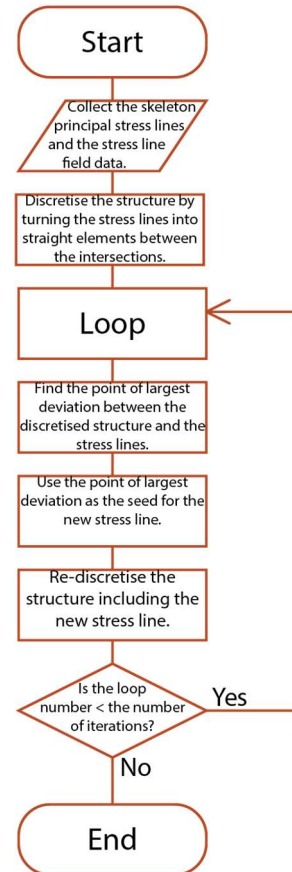
Figure 6-3: Li and Chen Growth Method Pseudocode Flow Chart
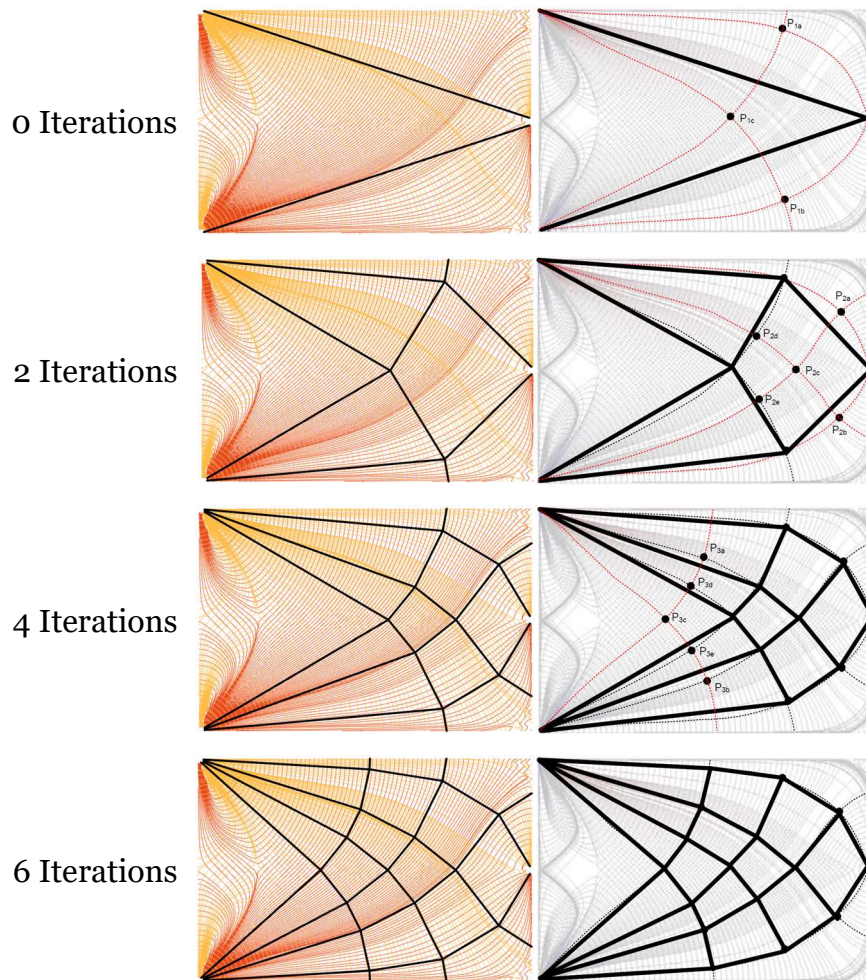
Figure 6-4: Validation Example 1 of Stress Line Structures: Left - Produced from C# Code, Right - Taken from Li and Chen (2010)
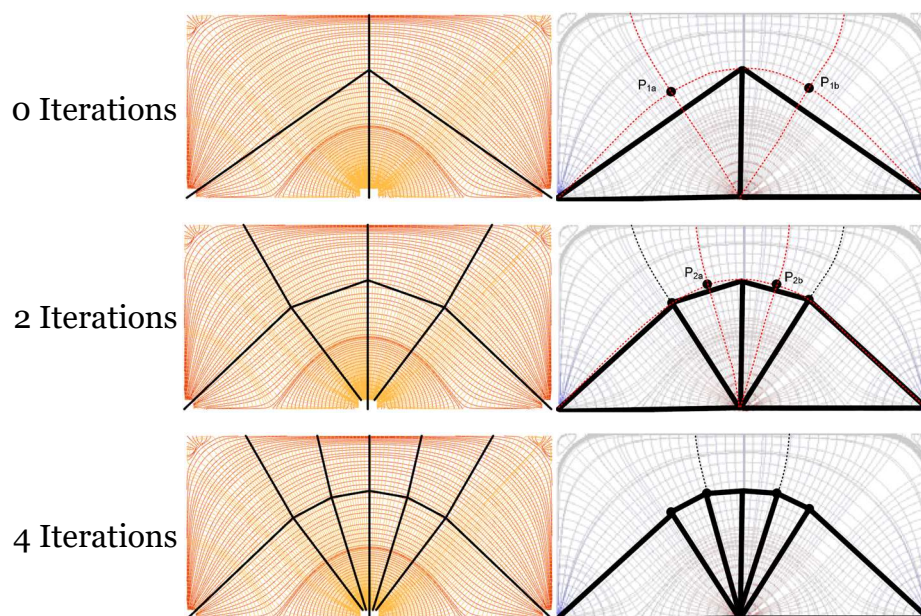
Figure 6-5: Validation Example 2 of Stress Line Structures: Left - Produced from C# Code, Right - Taken from Li and Chen (2010)

6.3 Testing and Results

To test the growth method on out-of-plane slabs, three cases are used: a corner-supported slab with a UDL, a corner-supported slab with a central point load, and a multi-span flat slab with a UDL. In each case, the same mesh is used, as shown in Figure 6-6.
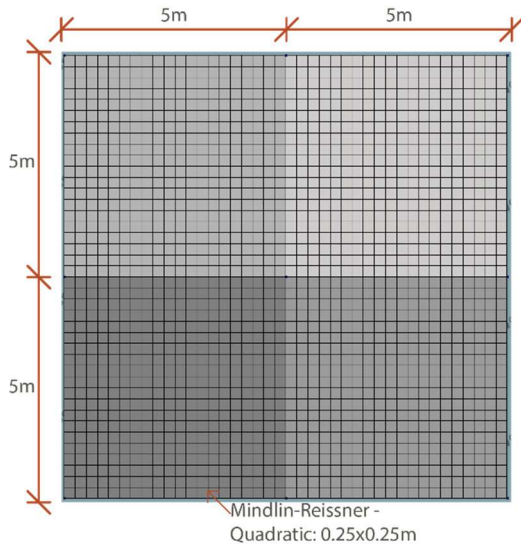
Figure 6-6: Mesh used for Testing the Li and Chen Growth Method
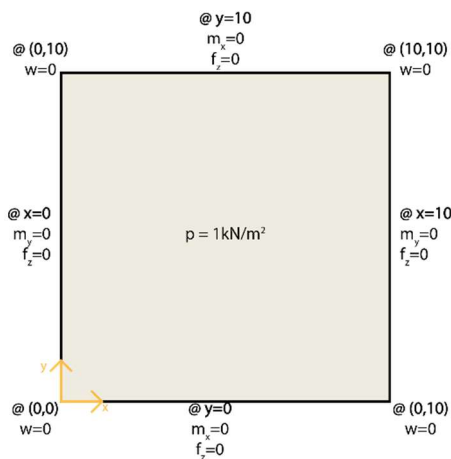
Figure 6-7: Boundary and Loading Conditions – Corner-Supported Slab with a UDL

Figure 6-7, Figure 6-8, and Figure 6-9 show the boundary and loading conditions applied to each case's mesh. Note that φ_x and m_x represent a rotation and moment about the x-axis and likewise with the y-axis terms. Also, be aware that the multi-span slab is not modelled with multiple spans but instead by fixing the rotations to zero at the edges.

A static linear analysis was performed using Diana FEA, and the geometric and material properties of the elements are:

- Thickness = 0.1m,
- Shape factor = 1.5,
- Youngs Modulus = 20 GPa,
- Poisson's ratio = 0.15.

Although Mindlin-Reissner elements have been used, an insufficiently large element size is used in the mesh which cannot encompass the concentrated shear effect at the edges. This is purposely done, as otherwise at the edges the torsional stresses rapidly change to zero, causing the stress lines to bend directly towards the supports. This effect can be seen in Figure 6-10 and is in-line with the actual load transfer mechanism along the edge to the support. However, this causes significant problems for the automated discretisation of the structure, so the effect is discounted, but this load transfer mechanism should not be forgotten. The cases' stress line fields are displayed in Figure 6-11, Figure 6-12, and Figure 6-13.
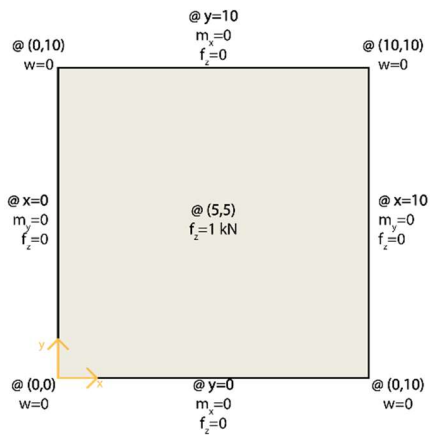
Figure 6-8: Boundary and Loading Conditions – Corner-Supported Slab with a Point Load
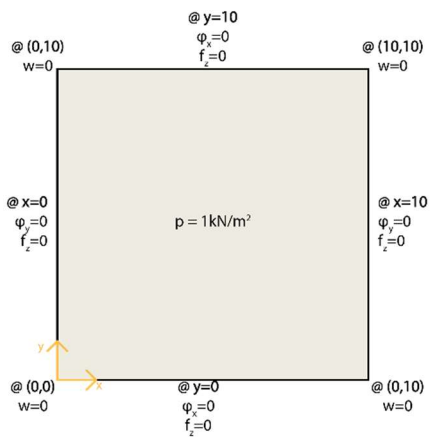
Figure 6-9: Boundary and Loading Conditions – Multi-Span Slab with a UDL
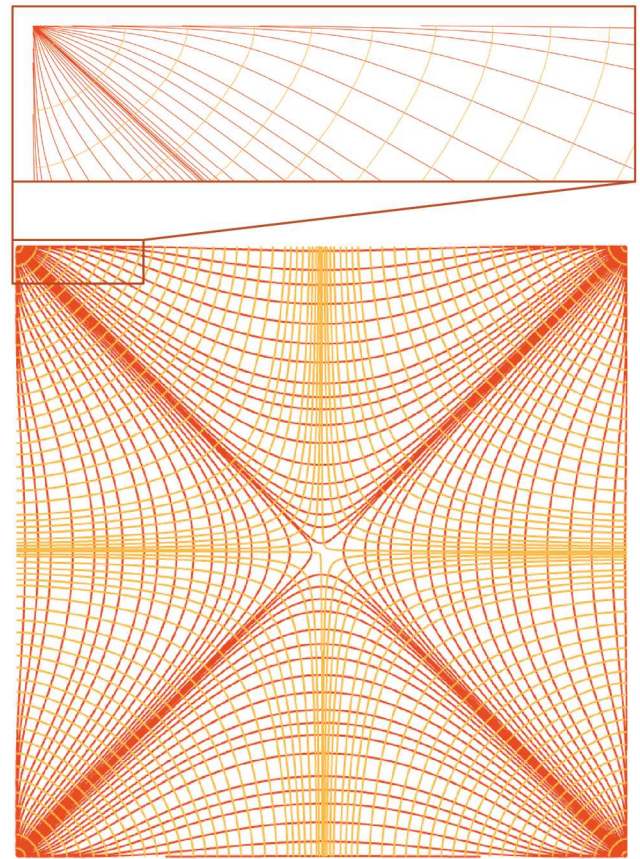
Figure 6-10: The Effect of the Concentrated Shear Force on the Principal Bending Stress Lines

Figure 6-14, Figure 6-15, and Figure 6-16 show the resulting structures produced for the three cases. The structures shown are where the number of iterations (I) produce symmetrical or near-symmetrical results. For the point loaded slab, the mesh elements surrounding the centre point were removed as the singularity causes inaccuracies in the results. The yellow lines show the rib geometry and the voids between them are filled by a greyscale where pure white shows to the deck parts with the lowest load span and pure black shows the parts with the largest load span. Therefore, if the slab were entirely filled with black, it would indicate that the rib geometry evenly supports the deck. Alongside the images, data about the maximum load spans is given by the mean (μ), the standard deviation of these (σ), and the absolute largest load span in the slab (Max.). The mean and standard deviation represent the spans' overall distribution; the maximum value shows the worst part of the slab for which the deck is designed.

The stress lines used as initial input for generating the geometry are made up of the straight stress lines and the 'ridge lines' (these are the curves that connect the umbilic points). These are used as they break the slab into distinct zones. In addition to the ridge lines, four more stress lines are used for the cases with a UDL as the ridge lines have zero curvature; the seeds used for these are: (0.25, 0.5), (0.5, 0.25), (0.5, 0.75), and (0.75, 0.5).
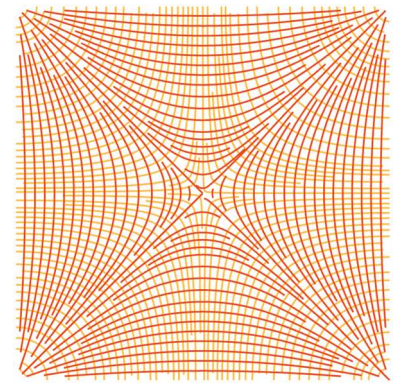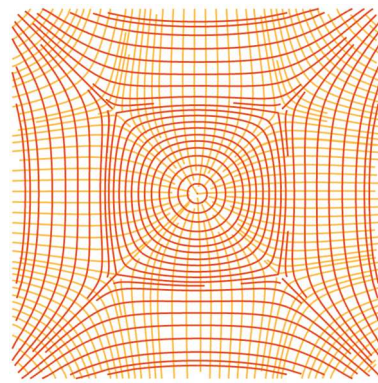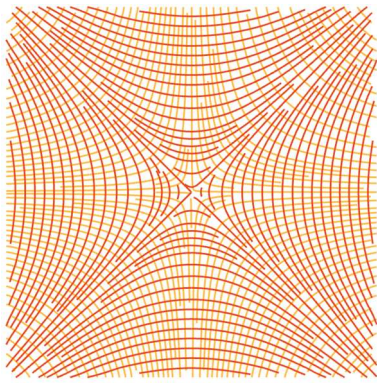
Figure 6-11: Stress Lines of the Corner-Supported Slab with a UDL

Figure 6-12: Stress Lines of the Corner-Supported Slab with a Point Load

Figure 6-13: Stress Lines of the Multi-Span Slab

Looking to the result of the corner-supported slab with a UDL, few steps create a significant improvement in antecedent iterations. I=20 improves on the previous steps, as although the standard deviation has increased the difference between the maximum value and the mean has significantly decreased. This is not the same for I=24, as although the maximum span is decreased by 0.04 m, the mean value is reduced by 0.10 m. There is also a cascading effect due to the tight curvature in the stress lines close to the centre; this is seen from I=24 to I=44 where each iteration creates a new stress line with tighter curvature which creates another stress line with even tighter curvature.

There is a similar story for the point loaded case. Only I=17 produces a significant improvement by reducing the maximum span by 0.34m and the standard deviation by 0.11m while maintaining a similar mean value. The method's asymmetry becomes apparent in this slab; particularly in result I=38 where two stress lines are added into the corners on the left-hand side, their mirrored counterparts are not added until the steps between I=45 and I=47. This happens as these slabs have both mirror and rotational symmetry; when a new stress line is added into the system, it is not directly added into the symmetrical locations. This is exacerbated when a new stress line is added which has a larger deviation than the stress line it was created to improve, meaning that the next stress line is not added at the symmetrical location.

The results for the multi-span slab are like the corner-supported slab with a UDL. I=20 also gives good results in this case. The same cascading effect can be seen here, although I=56 shows that the deck parts with the largest load span are eventually split apart, but the slab has large concentrations of elements by this iteration, making it challenging to fabricate.

It appears that small changes could be made in many of these results to support the deck better. The figures on pages 52 and 53 show some manually developed structures compared to the structures produced through the Li and Chen growth method. The detailed data here shows how well the deck is supported and how accurate the discretised ribs are compared to the stress lines.
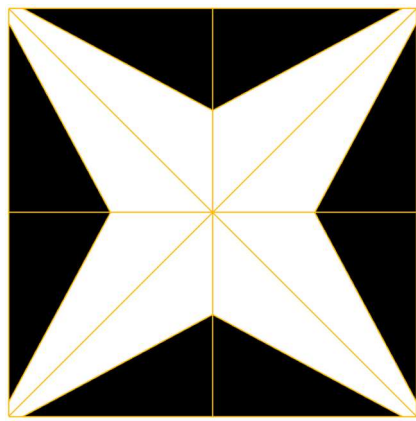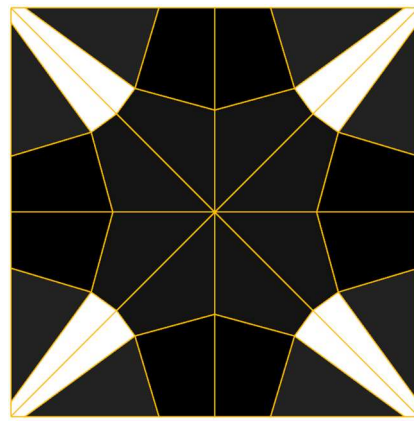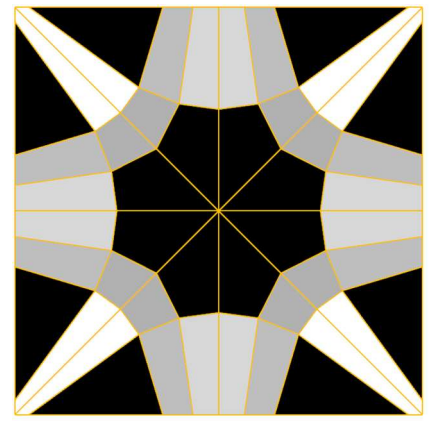
*I =0, μ=0.883m, σ=0.054m, **Max.**=0.935m*   *I =4, μ=0.689m, σ=0.201m, **Max.**=0.870m*   *I =8, μ=0.538m, σ=0.137m, **Max.**=0.745m*
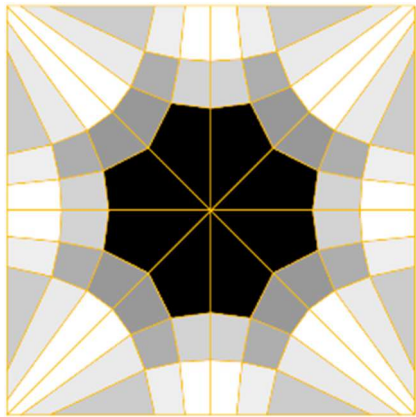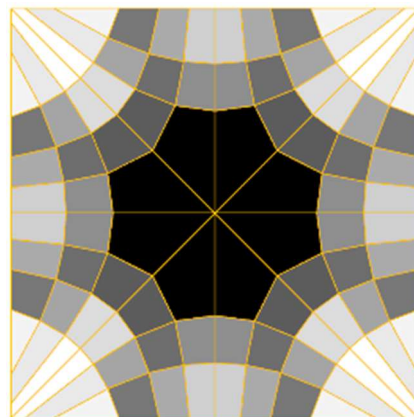
*I =12, μ=0.475m, σ=0.095m, **Max.**=0.689m*   *I =16, μ=0.414m, σ=0.114m, **Max.**=0. 689m*   *I =20, μ=0.33m, σ=0.127m, **Max.**=0.522m*
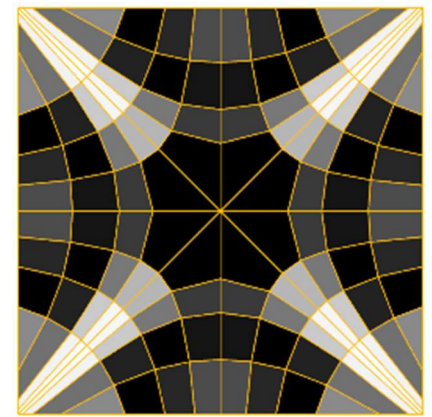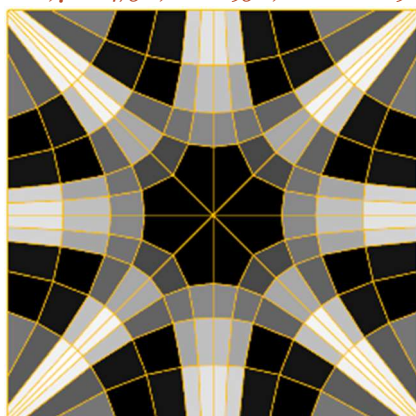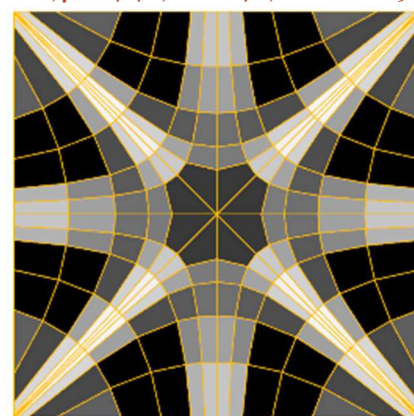
*I =24, μ=0.228m, σ=0.111m, **Max.**=0.482m*   *I =28, μ=0.239m, σ=0.124m, **Max.**=0. 482m*   *I =32, μ=0.209m, σ=0.122m, **Max.**=0.482m*
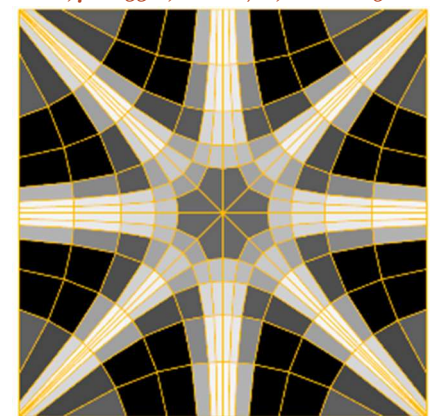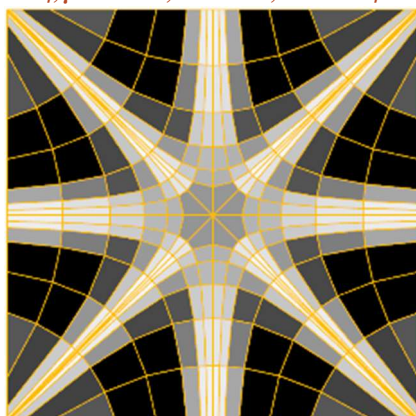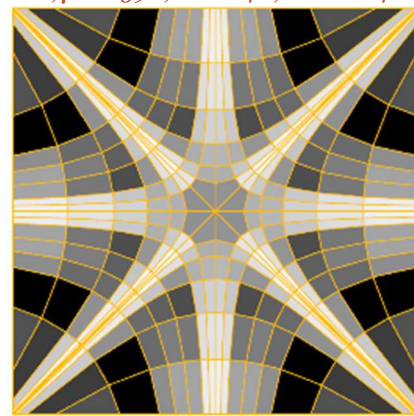
*I =36, μ=0.179m, σ=0.126m, **Max.**=0. 482m*   *I =40, μ=0.164m, σ=0.106m, **Max.**=0.470m*   *I =44, μ=0.147m, σ=0.105m, **Max.**=0. 470m*
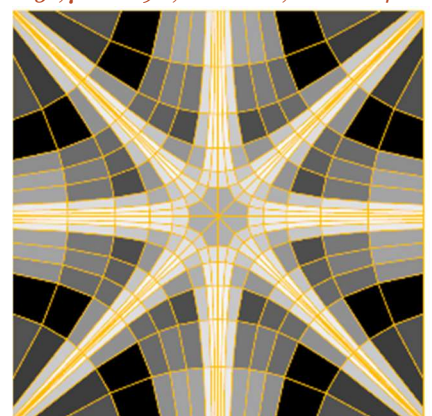
Figure 6-14: The Li and Chen Growth Method Applied to the Corner-Supported Slab with a UDL
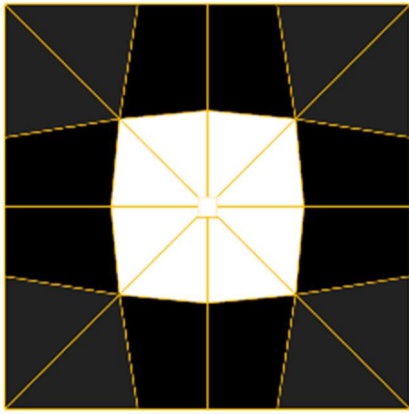
*I =0, μ=0.861m, σ=0.136m, **Max.**=0.990m*
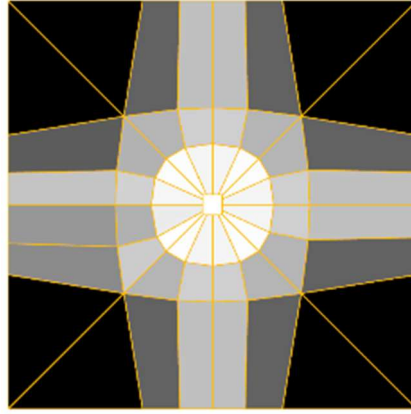
*I =9, μ=0.468m, σ=0.218m, **Max.**=0.916m*
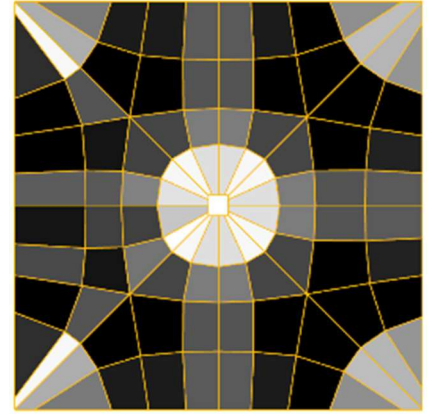
*I =17, μ=0.419m, σ=0.109m, **Max.**=0.591m*
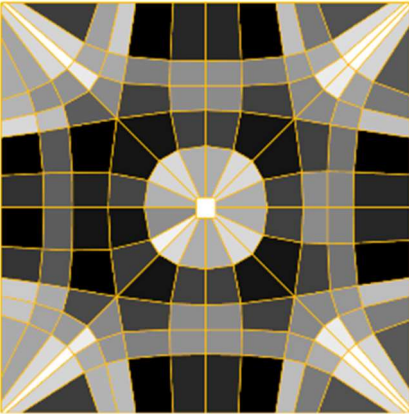
*I =25, μ=0.0.319m, σ=0.091m, **Max.**=0.525m*
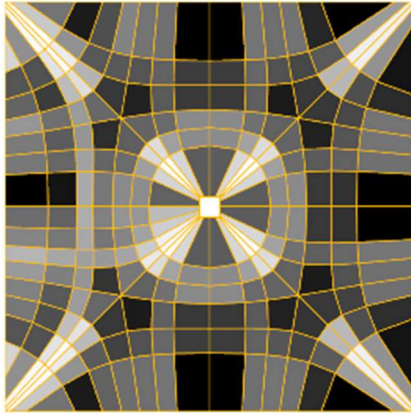
*I =38, μ=0.241m, σ=0.073m, **Max.**=0.423m*
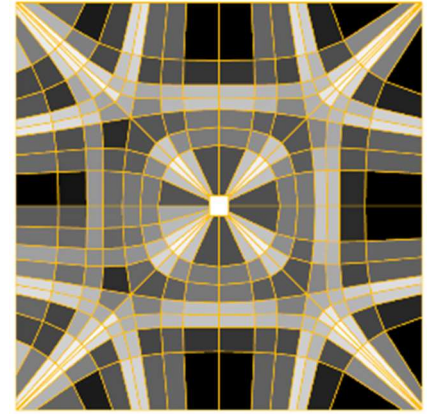
*I =45, μ=0.199m, σ=0.080m, **Max.**=0.423m*
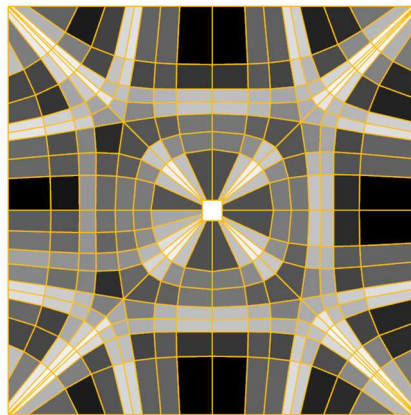
*I =47, μ=0.188m, σ=0.082m, **Max.**=0. 423m*

Figure 6-15: The Li and Chen Growth Method Applied to the Corner- Supported Slab with a Point Load

*I =0, μ=0.890m, σ=0.067m, **Max.**=0.955m*

*I =4, μ=0.697m, σ=0.245m, **Max.**=0.962m*

*I =8, μ=0.540m, σ=0.149m, **Max.**=0.740m*

*I =12, μ=0.470m, σ=0.102m, **Max.**=0.710m*

*I =16, μ=0.411m, σ=0.142m, **Max.**=0.710m*

*I =20, μ=0.326m, σ=0.151m, **Max.**=0.528m*

*I =24, μ=0.286m, σ=0.124m, **Max.**=0.506m*

*I =28, μ=0.238m, σ=0.134m, **Max.**=0.506m*

*I =32, μ=0.213m, σ=0.125m, **Max.**=0.506m*

*I =56, μ=0.138m, σ=0.082m, **Max.**=0.307m*
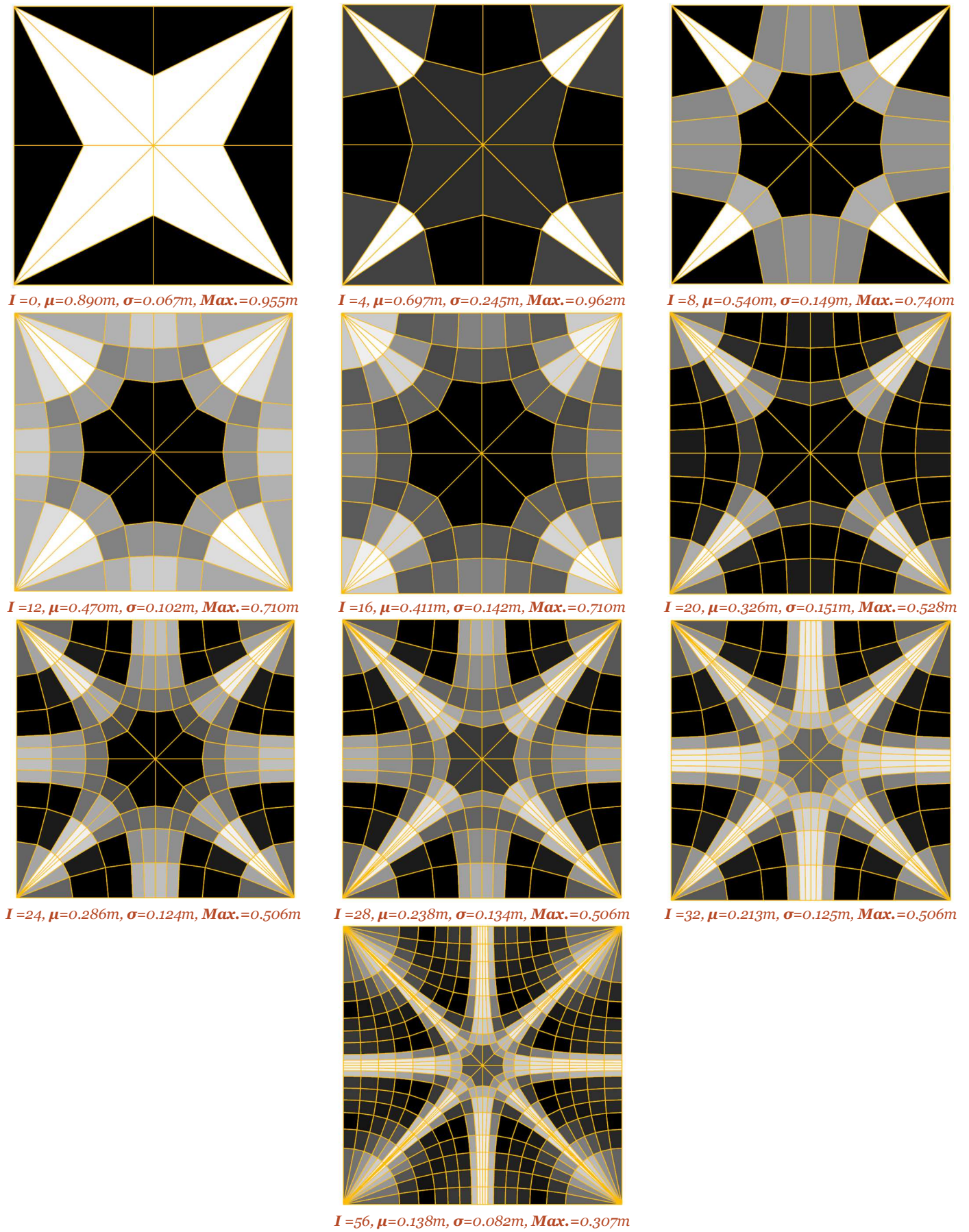
Figure 6-16: The Li and Chen Growth Method Applied to the Multi-Span Slab with a UDL
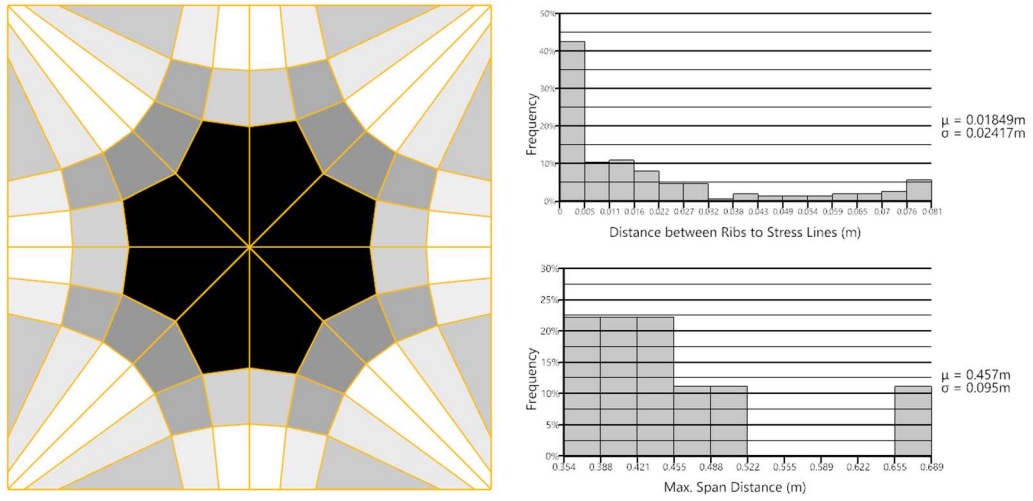
Figure 6-17: The Corner-Supported Slab Structure Produced using the Growth Method, I=12
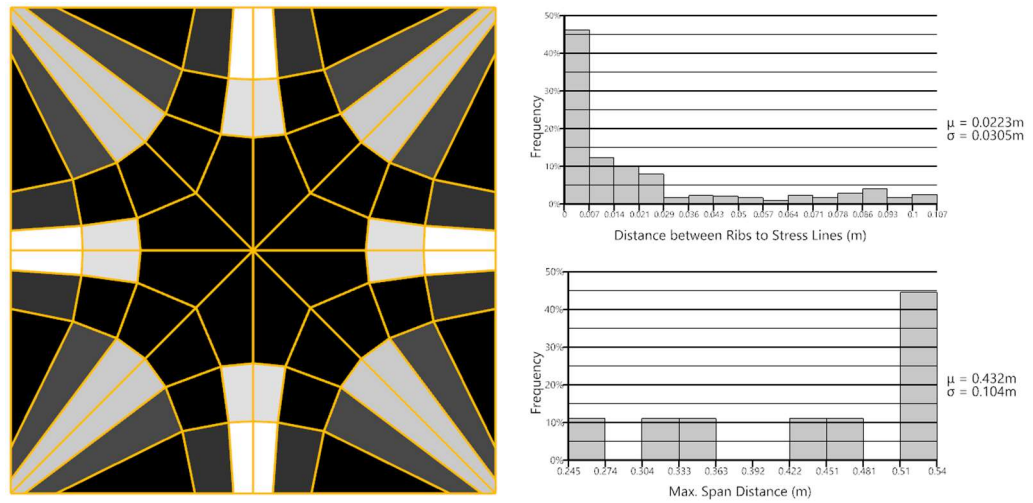
Figure 6-18: The Corner-Supported Slab Structure Produced Manually, I=12 Equivalent
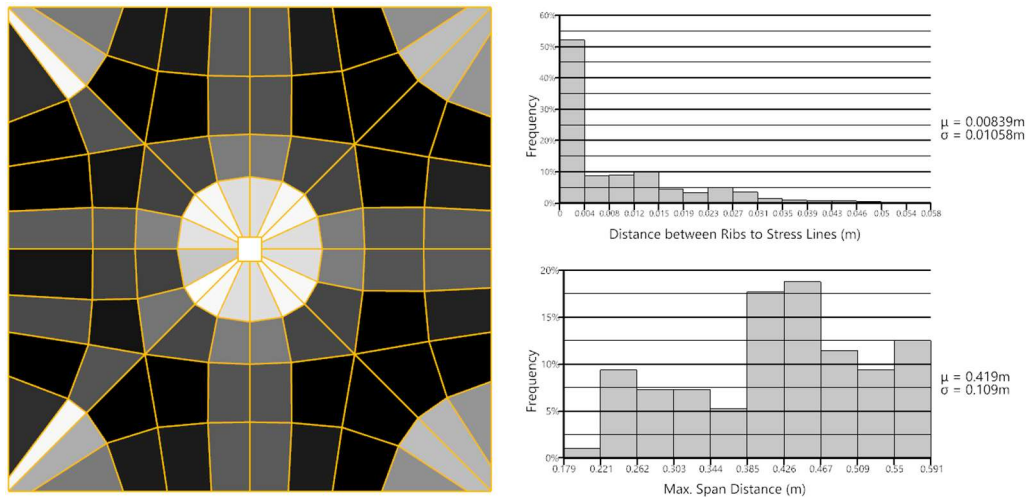
Figure 6-19: Point Loaded Slab Structure Produced using the Growth Method, I=17
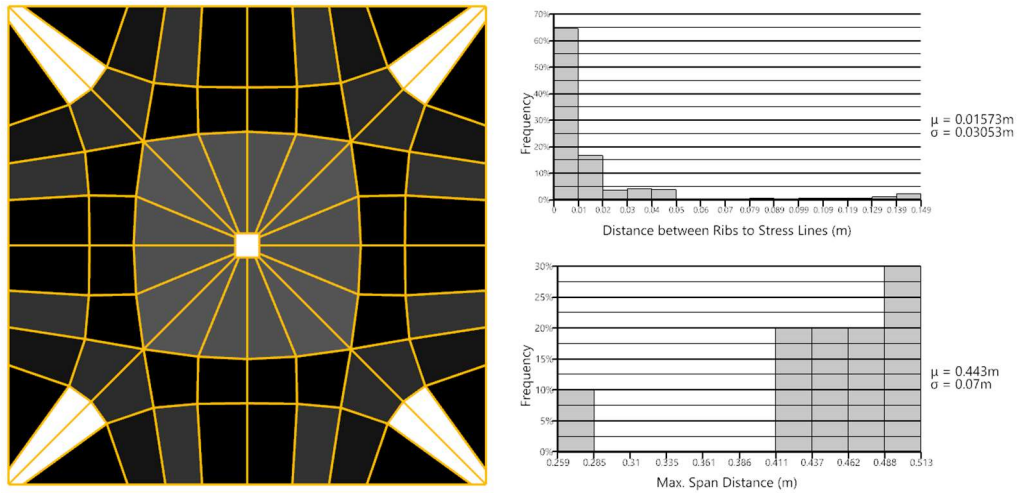
Figure 6-20: Point Loaded Slab Structure Produced Manually, I=16 Equivalent
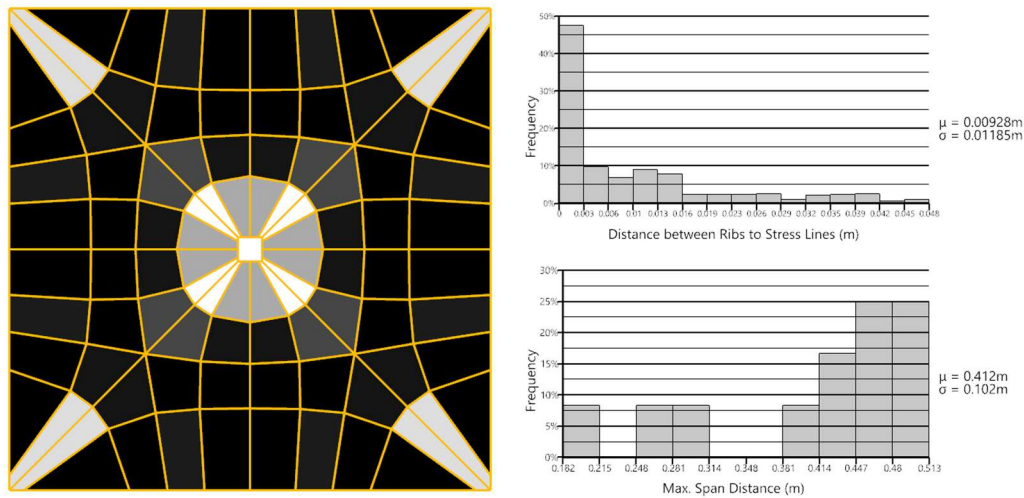
Figure 6-21: Point Loaded Slab Structure Produced Manually, I=17 Equivalent

In the images above, the top histogram's data is generated using Grasshopper by sampling the distance from each stress line to its discretised counterpart at 1000 evenly distributed points along each line.

Comparing Figure 6-17 to Figure 6-18 shows that a reduction in the maximum load span of 0.14m can be achieved by tweaking the stress lines while the mean value is only reduced by 0.02m. However, the discretised structure's accuracy is reduced, whereby the mean distance between the ribs and stress line is increased by 20.5%, and the standard deviation is increased by 26.0%.

The same result is seen when comparing Figure 6-19 and Figure 6-20. Here the maximum load span is reduced by 0.08m while the mean is increased by 0.02m. There is a significant change in the discretised structure accuracy where the mean distance is increased by 87.5% and the standard deviation by 188.6%. Looking at Figure 6-21, this is mainly caused by removing the stress line that loops around the centre.

6.4 Discussion and Conclusion

In this chapter, an automatic method was tested for selecting stress lines in slabs, where the stress lines have been generated using the method developed in Chapter 5. This automated method was based on the work of Li and Chen (2010). It was shown that the Li and Chen growth method could be applied to out-of-plane loaded slabs to produce accurate discretised geometries; where accuracy was defined by how closely the discretised structure approximated the curved stress lines. The method was tested with three slab cases, and the load distribution of the deck elements was measure and compared. It was shown that there were only a handful of scenarios where the automated method produced acceptable support mechanisms for the deck structure because the voids between the ribs were not evenly distributed.

The problems with applying this method to out-of-plane loaded slabs are that firstly, the method does not consider any form of symmetry within the stress line selection process; this creates unsymmetric structures that are undesirable. This was seen particularly in the case of the corner-supported slab with a point load. Secondly, in cases where the stress line field contains high curvature areas, a cascading effect can occur, creating large concentrations of elements. The cascading effect occurs because a better accuracy in the discretised structures is created, but this results in an uneven distribution of voids.

It was investigated whether better results could be produced by manually selecting the stress lines as the automated method did not produce the expected results. Manually selecting the stress lines through a trial and modification process did result in better support conditions for the deck (i.e., a more even distribution of voids between the ribs). However, this did result in a decrease in the discretised structure's accuracy compared to the Li and Chen growth method. This is expected, though as the Li and Chen method creates a highly accurate discretised structure by design.

The best approach to use will depend on the design scenario. However, manual tweaking of the result from the Li and Chen growth method, or producing the stress lines completely manually will likely give the most acceptable geometry. When creating the stress lines manually, the deck's load distribution should be as even as possible, but the discretised structure should also maintain a high level of accuracy. These two factors need to be balanced.

Although the Li and Chen growth method produces poor results for the out-of-plane loaded slabs, it still has utility in showing a discretised geometry optimised for accuracy. This information can be combined with engineering knowledge to find a solution that has an appropriate balance between design considerations. This requires consideration of how the deck will react to the load, how the ribs will be manufactured and connected, and how decreasing the discretised structure's accuracy will result in a less optimal solution for the stress state in the ribs. This approach is used in subsequent chapters.

7.1 Introduction

In this chapter, the loading condition's influence on the principal stress line field will be investigated. A single loading case needs to be selected to create the stress line field; however, there are many possible alternatives. It is sensible to assume that the dominant load case is when the total load onto the slab is maximum; this is referred to as the primary load case. There are many possible secondary load cases that have a smaller total load, but they could create vast changes in the stress line patterns due to their loading shapes.

In addition to this, the primary load case must be simplified when creating the stress lines by assuming that the structural dead load is distributed over the entire slab. In actuality, there will be local variations in the structural dead load because of the ribs. The effect of this will also be investigated in this chapter.

7.2 Methodology

A series of principal stress line models are created to ascertain the difference between the primary and secondary load cases. The first model is based on the primary load case with a UDL across the entire slab. The subsequent models analyse secondary load cases which can occur on a real slab. The following load combinations are defined for the secondary load cases:

- Imposed loading on only half of the slab,
- A concentrated live load (point load) at the centre of the slab,
- A concentrated live load (point load) applied half-way between the edge and the centre of the slab.

A separate series of secondary load cases are defined to analyse the local load effects of the ribs. In these cases, the dead load is applied partly as a UDL and partly as concentrated loads at the ribs' locations. Three separate load cases are created as the exact ratio between the ribs' self-weight and the rest of the dead load is unknown. These load cases are defined as follows:
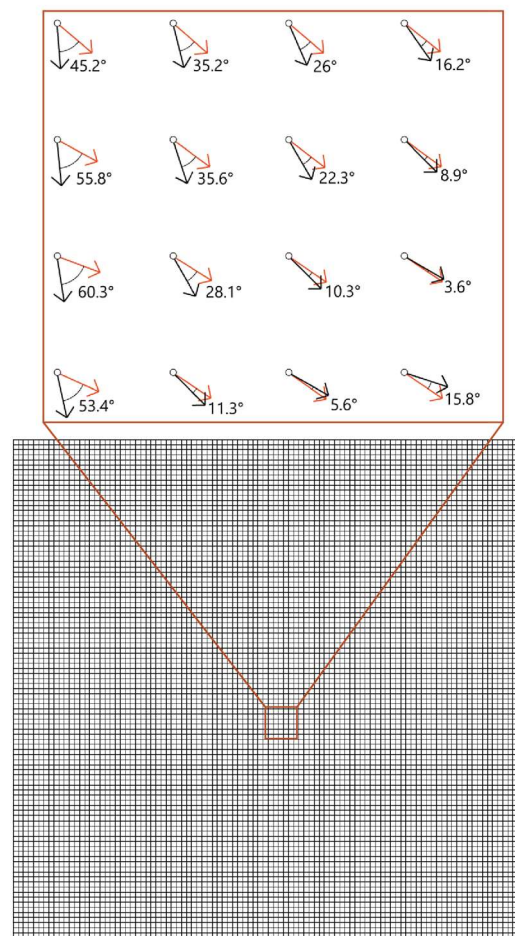
Figure 7-1: Measurement of the Principal Stress Trajectory: the Black Arrows Represent the Primary Load Case, and the Red Arrows Represent the Secondary Case

1. Concentrated loads at the rib locations: **30%** of the dead load; UDL: **70%** of the dead load.
2. Concentrated loads at the rib locations: **70%** of the dead load; UDL: **30%** of the dead load.
3. Concentrated loads at the rib locations: **100%** of the dead load; UDL: **0%** of the dead load.

The primary load case will be compared to the secondary cases by measuring the angles between the principal directions at each point in an evenly distributed grid of 100x100 points. These results will be displayed and compared. Figure 7-1 shows the sample grid for the 10x10m slab with an enlarged view of the principal stress trajectories' measurement.

7.3 Loading

The loading situation needs to be chosen to determine the forces onto the structure. Here is it is chosen that the slab will be loaded as if placed into a roof design. From this the imposed loads are taken as the recommended values from EN 1991-1-1-2002:

- Uniform Maintenance Load = 1.0 kN/m²,
- Concentrated Maintenance Load = 1.5 kN,
- Snow Load = 1.0 kN/m², *this is a conservative estimated value*

The wind load is not considered in the loading as it is heavily dependent on the overall building geometry and location.

The dead load also needs to be found, including the structural self-weight plus the finishes and services attached to the slab. An estimated value of 1.7kN/m² is used as the uniform dead load.

The loading combination is given by Eq 6.10 from EN 1990-2002:

$$Load\ case = \sum_{j=1}^{n} \gamma_{G,j} G_{k,j} + \gamma_{Q,1} Q_{k,1} + \sum_{j=2}^{n} \gamma_{G,j} \psi_{0,i} G_{k,j}$$

Where $G_{k,i}$ are the dead loads and $Q_{k,j}$ are the live loads. The partial factors are found in Table A1.2(B) of EN 1990-2002:

- $\gamma_{G,unfavourable}$ = 1.35
- $\gamma_{G,favourable}$ = 0.9
- $\gamma_{Q,unfavourable}$ = 1.5
- $\gamma_{Q,favourable}$ = 0.0

The value of $\gamma_{G,favourable}$ is chosen because the self-weight is calculated conservatively. The combination factors are found in Table A1.1 of EN 1990-2002:

- $\Psi_{0,roof}$ = 0
- $\Psi_{0,snow}$ = 0.5

7.3.1 Primary Load Case

The primary load case is taken as a maximum UDL across the entire slab. For this, every load is unfavourable, and the maintenance load is considered as the dominant live load:

$$Primary\ Load\ Case = 4.545\ kN/m^2$$

7.3.2 Secondary Load Case: Point Load

For the secondary load cases, the most unfavourable situation occurs when there is the most considerable difference with the primary load case. For the point loaded cases, the concentrated imposed load is unfavourable, and all other loads are favourable.

$$Point\ Load = 2.25\ kN$$

$$Uniformly\ Distributed\ Load = 1.53\ kN/m^2$$

This load case will occur when someone is working on the roof for maintenance purposes.

7.3.3 Secondary Load Case: Half Loaded Slab

In this case, half of the slab has a maximum uniformly distributed load, and the other half has a minimal value. The most considerable difference to the primary case occurs when the self-weight is minimal, and a maximum snow load and live load is applied to half of the slab.

$$Load\ on\ Part\ 1 = 3.78\ kN/m^2$$

$$Load\ on\ Part\ 2 = 1.53\ kN/m^2$$

This load case could occur when snow is partway through being cleared off the roof.

7.3.4 Secondary Load Case: Rib Self-Weight

This particular load case is determined by first analysing the stress lines produced from the primary load case and then using the manual method of stress line selection, discussed in Chapter 6, to create a geometry for the ribs. A portion of the self-weight is applied to the analysis model where the ribs are located (this will be discussed further in Section 7.4.1). The remaining percentage of the self-weight is applied as a UDL.

$$Self\ Weight = 1.7\ kN/m^2$$

7.4 Testing and Results

The secondary load cases' influence has been tested on two cases: a 10x10m corner-supported slab, and a 10x15m edge-supported slab. The mesh used for the former is shown in Figure 6-6; the mesh used for the latter is shown in Figure 7-13. For the primary load case and the secondary load cases, excluding the rib self-weight cases, a static linear analysis is performed using Diana FEA and the geometric and material properties of the elements are:

- Thickness = 0.1m,
- Shape factor = 1.5,
- Youngs Modulus = 20 GPa,
- Shear Modulus = 8.7 GPa
- Poisson's ratio = 0.15.

For the secondary load cases looking at the rib self-weight, a static linear analysis is performed in OASYS GSA using the same properties and meshes.

7.4.1 Corner-Supported 10x10m Slab

Figure 7-2: Corner-Supported 10x10m Slab Boundary Conditions

Figure 7-3: Diagram Showing the Calculation of Point Loads for the Rib Self-Weight: Thick Lines=Ribs; Crosses=Mesh Nodes; and Thin Lines=Areas per Node

Figure 7-4: Stress Lines of the Primary Load Case for the Corner- Supported Slab
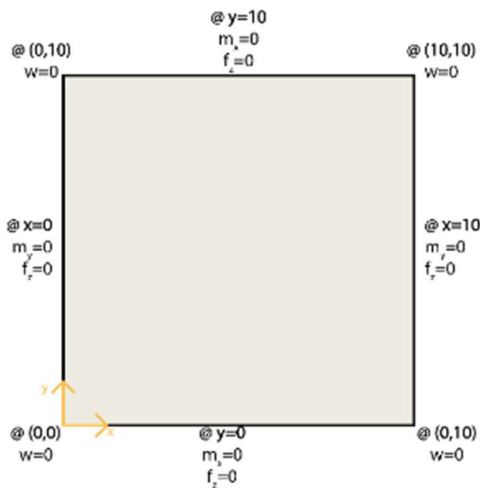
The boundary conditions of this case are shown in Figure 7-2. The loading condition for the primary case is $p(x,y) = 4.545kN/m^2$. The first three secondary loading conditions are:

- Centre point load:
  - $p(x,y) = 1.53kN/m^2$
  - $f_z(5.0m, 5.0m) = 2.25kN$
- Off-centre point load:
  - $p(x,y) = 1.53kN/m^2$
  - $f_z(5.0m, 7.5m) = 2.25kN$
- Half loaded slab:
  - $p(x, y < 5.0m) = 1.53kN/m^2$
  - $p(x, y > 5.0m) = 3.78kN/m^2$

The loading conditions are more complicated for the cases where 30%, 70%, and 100% of the self-weight of slab is attributed to the rib locations. The UDLs applied in these cases are:

- 30% of the self-weight attached to the ribs:
  - $p(x,y) = 1.071kN/m^2$
- 70% of the self-weight attached to the ribs:
  - $p(x,y) = 0.459kN/m^2$
- 100% of the self-weight attached to the ribs:
  - $p(x,y) = 0.0kN/m^2$.
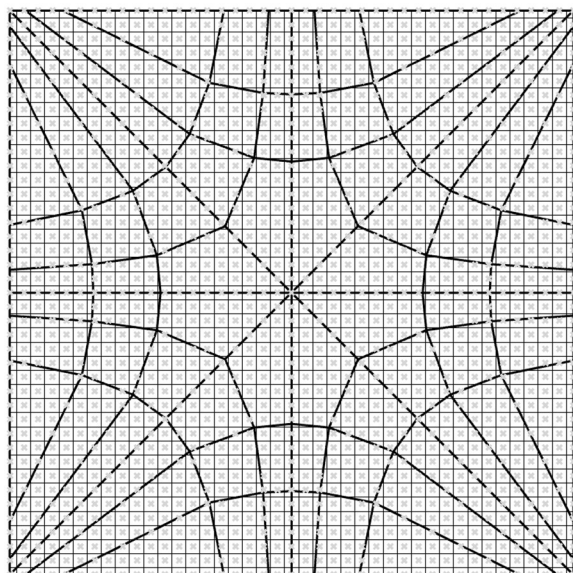
The self-weight of the ribs is applied to the model as point loads. The point loads are calculated by creating a Voronoi mesh of all the FE nodes and finding the rib lengths, which pass through each cell. Each point load is calculated using Eq. 7.1. Figure 7-3 shows the rib geometry, the node locations, and the Voronoi mesh.

$$Point\ Load = \frac{Rib\ Length\ in\ Voronoi\ Cell}{Total\ Rib\ Length} \cdot Rib\ Load \quad Eq.\,7.1$$
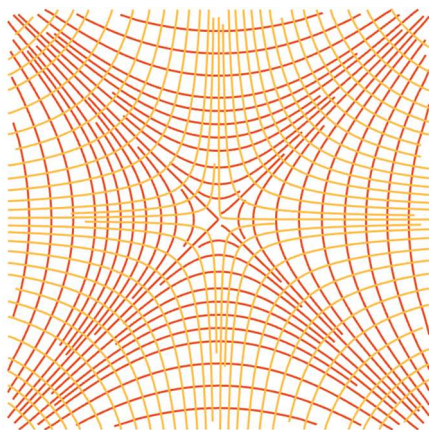
Figure 7-4 indicates what the stress lines look like for the primary load case. To evaluate the load cases' differences, the principal directions are calculated on a grid of 100x100 points inside the slab. The angles between the principal directions for each load case are measured and shown as a gradient image and a histogram. Figure 7-5, Figure 7-6, and Figure 7-7 show the first three secondary load cases.

Figure 7-5: Centre Point Load: Left - Stress Lines, Middle - Gradient Display of Principal Direction Differences, Right - Histogram of Principal Direction Differences.
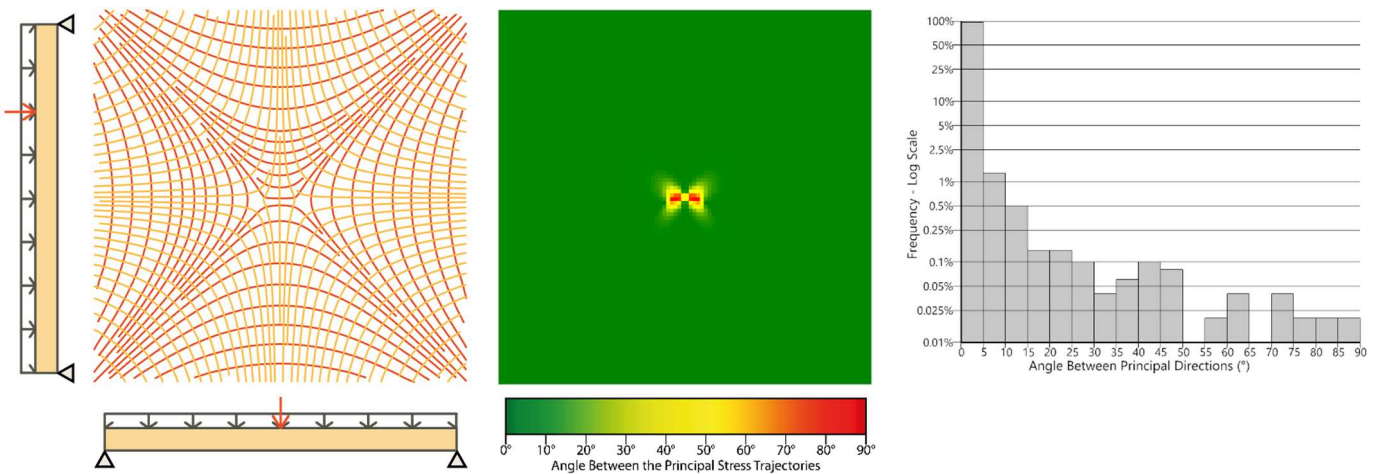
Figure 7-6: Off-Centre Point Load: Left - Stress Lines, Middle - Gradient Display of Principal Direction Differences, Right - Histogram of Principal Direction Differences.
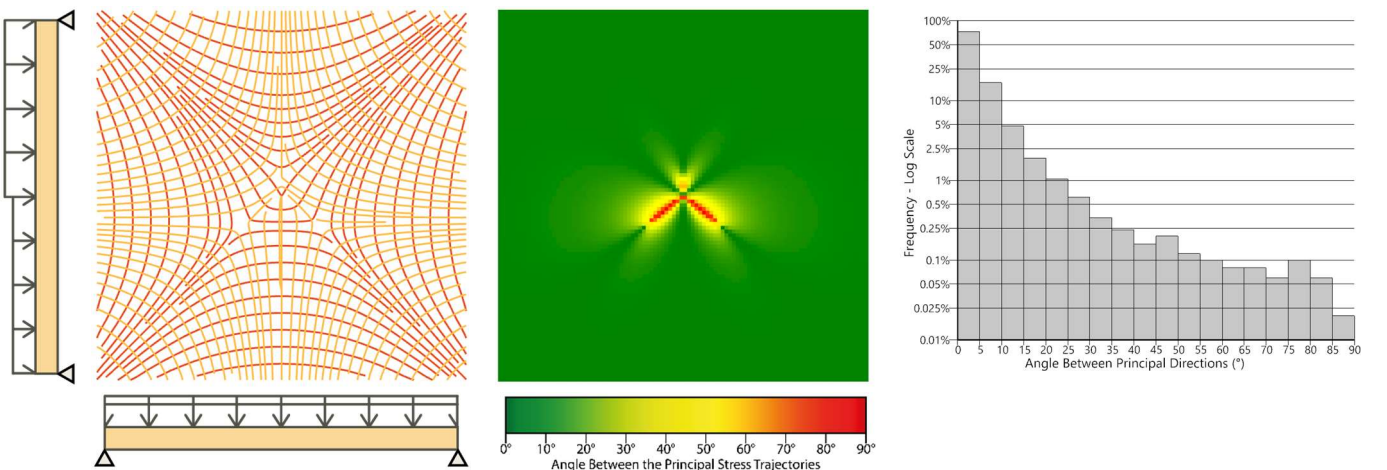
Figure 7-7: Half Loaded Slab: Left - Stress Lines, Middle - Gradient Display of Principal Direction Differences, Right - Histogram of Principal Direction Differences.

The change produced in the principal bending direction by adding a point load to the structure is relatively minimal. The effect is localised to the slab's centre even when the point load is not applied at the centre. When a point load is applied at the slab's centre, the change in principal directions results in hoop stresses forming around the centre, similar to what was seen in the previous chapter when a point load was applied exclusively. For the off-centre

point load, a different effect is seen in the stress lines; the single umbilic point for the primary load case has now been split into two adjacent umbilic points.

Applying a maximum UDL to one half of the slab is more significant, as seen in Figure 7-7. Again, the differences are localised to the centre of the slab, and the asymmetric loading gives an asymmetric result. In this load case, 26.8% of the evaluation points had a change larger than 5°. The stress lines also have a complicated structure at the centre of this load case where four umbilic points occur.

Figure 7-8, Figure 7-9, and Figure 7-10 show the results for the load cases where a proportion of the self-weight is applied to simulate the self-weight of the ribs. In all three cases, there are only tiny changes made to the principal bending directions and these are localised at the centre of the slab. The change between the load cases increases as more load is attributed to the ribs, but even when 100% of the load is applied, the effect is minimal.
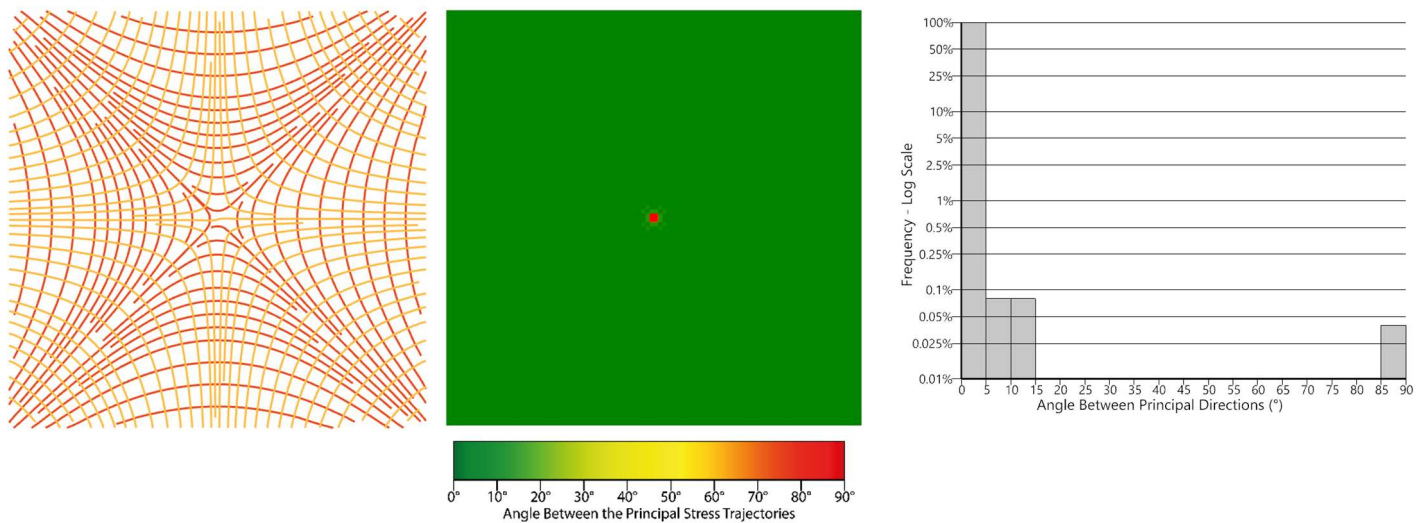
Figure 7-8: 30% of the Self-Weight Attached to the Ribs: Left - Stress Lines, Middle - Gradient Display of Principal Direction Differences, Right - Histogram of Principal Direction Differences.
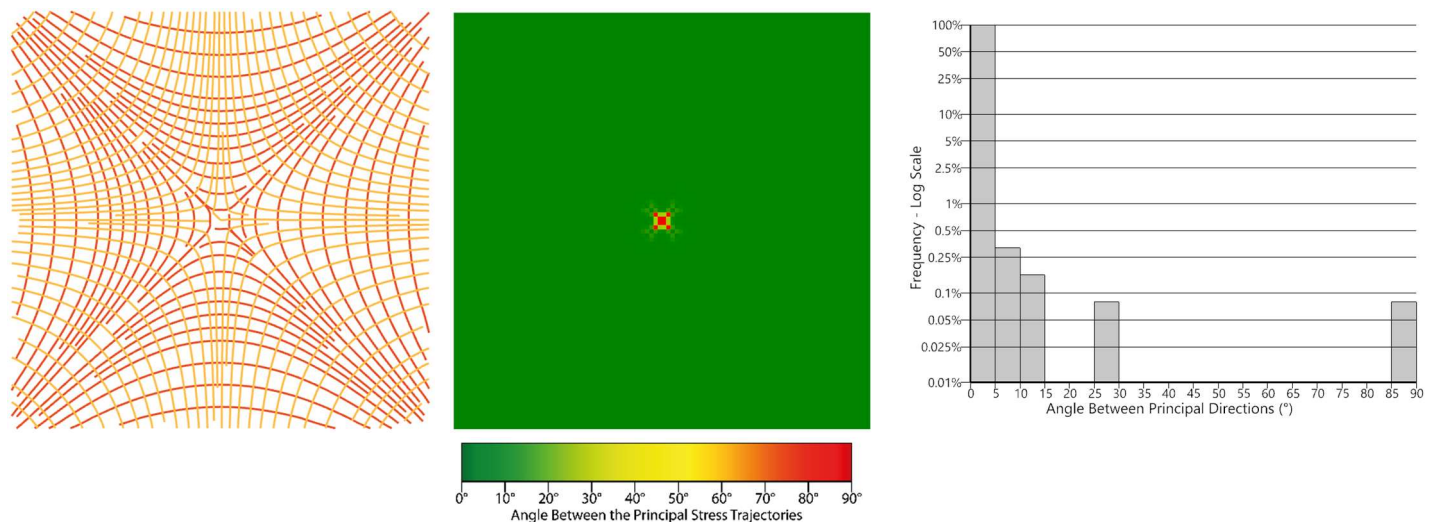
Figure 7-9: 70% of the Self-Weight Attached to the Ribs: Left - Stress Lines, Middle - Gradient Display of Principal Direction Differences, Right - Histogram of Principal Direction Differences.
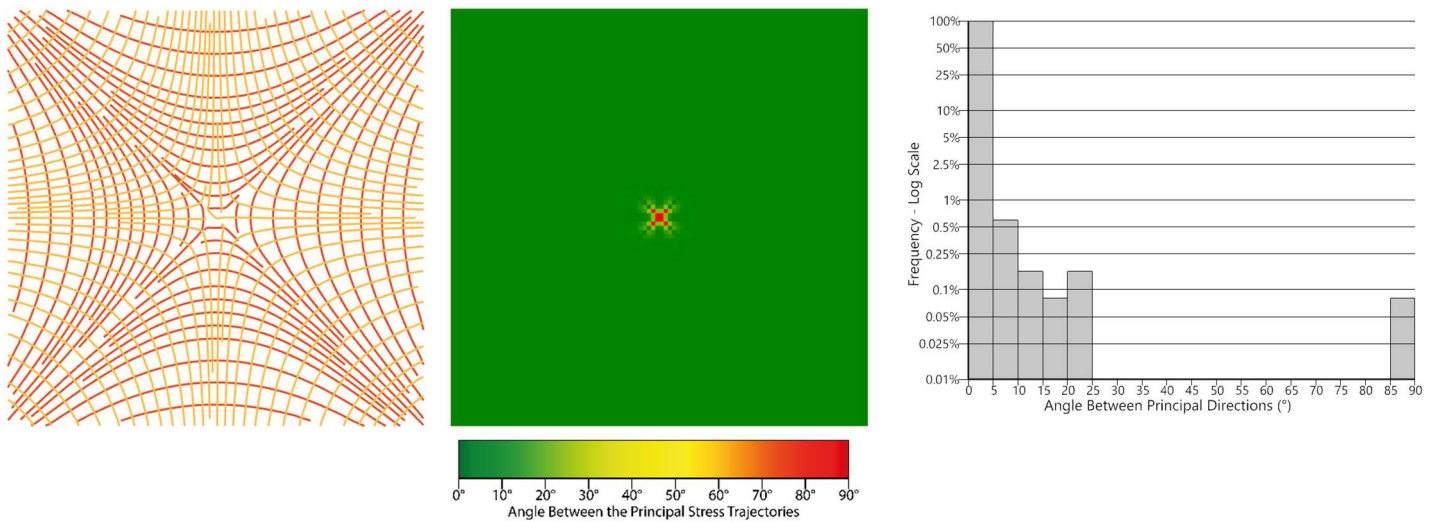
Figure 7-10: 100% of the Self-Weight Attached to the Ribs: Left - Stress Lines, Middle - Gradient Display of Principal Direction Differences, Right - Histogram of Principal Direction Differences.

7.4.2 Edge-Supported 10x15m Slab
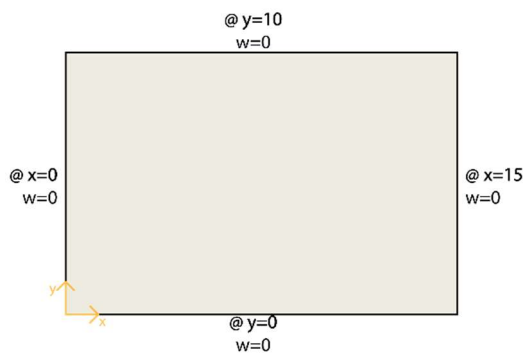
Figure 7-11: Edge-Supported 10x15m Slab Boundary Conditions
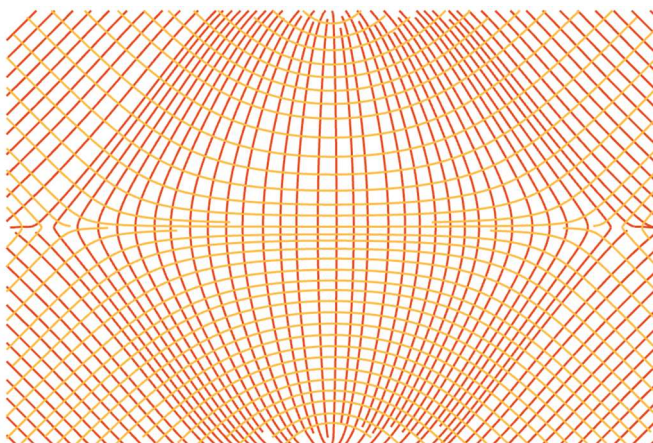
Figure 7-12: Stress Lines of the Primary Load Case for the Corner-Supported Slab

The boundary conditions of this case are shown in Figure 7-11. The loading condition for the primary case is $p(x,y) = 4.545 kN/m^2$. Due to the asymmetry of the slab, there are additional secondary load cases for the asymmetrically loaded cases. These are:

- Centre point load:
  - $p(x,y) = 1.53 kN/m^2$
  - $f_z(7.5m, 5.0m) = 2.25kN$
- Top point load:
  - $p(x,y) = 1.53 kN/m^2$
  - $f_z(7.5m, 7.5m) = 2.25kN$
- Left point load:
  - $p(x,y) = 1.53 kN/m^2$
  - $f_z(2.5m, 5.0m) = 2.25kN$
- Top-bottom half loaded slab:
  - $p(x, y < 5.0m) = 1.53 kN/m^2$
  - $p(x, y > 5.0m) = 3.78 kN/m^2$
- Left-right half loaded slab:
  - $p(x > 7.5m, y) = 1.53 kN/m^2$
  - $p(x < 7.5m, y) = 3.78 kN/m^2$

Figure 7-12 shows the stress lines for the primary loading condition, and Figure 7-14 to Figure 7-18 show the results for the first five secondary load cases.

Firstly, it is clear to see in these results that a point load onto the slab creates practically no change in the principal bending stress trajectories. Loading half the slab does have a significant effect. The loading condition with the most considerable change is when the slab's left side receives a maximum UDL, a change of >5° in 25.6% of the results. Although for the 'top-bottom half loaded slab' more results are clumped towards 90°. As in the previous case,
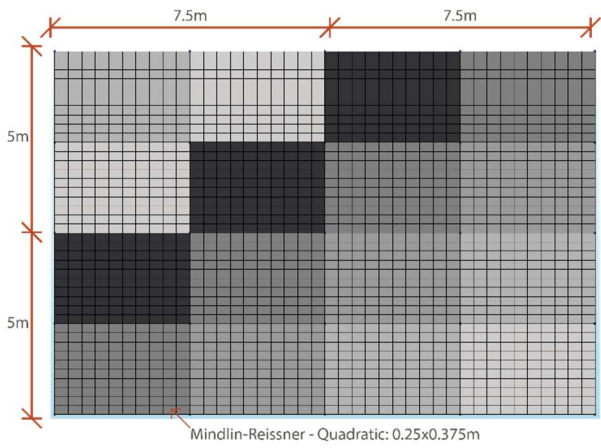
Figure 7-13: The Mesh Used for Testing the 10x15m Slab

the changes occur most intensely at the locations of the umbilic points. Comparing Figure 7-18 to Figure 7-12 shows that the internal umbilic points are shifted to the right, while the umbilic points on the top and bottom edges are shifted to the left. This shifting does cause changes in the stress lines across large areas of the slab.
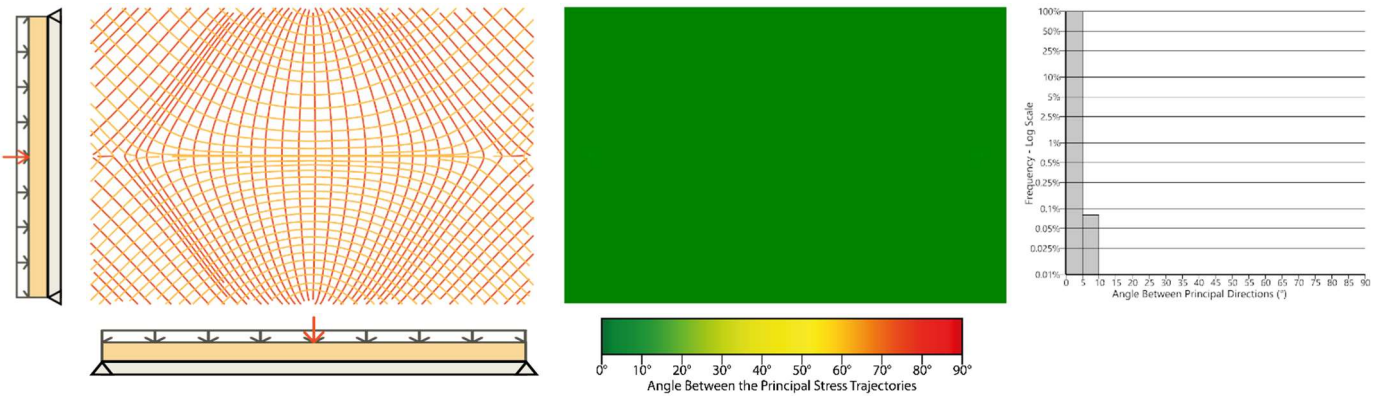
Figure 7-14: Centre Point Load: Left - Stress Lines, Middle - Gradient Display of Principal Direction Differences, Right - Histogram of Principal Direction Differences.
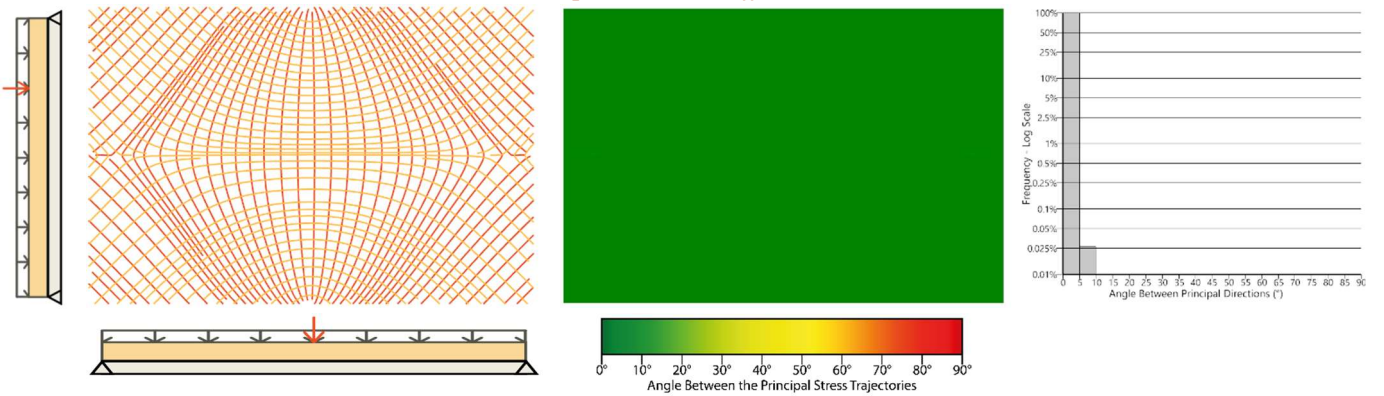
Figure 7-15: Top Point Load: Left - Stress Lines, Middle - Gradient Display of Principal Direction Differences, Right - Histogram of Principal Direction Differences.
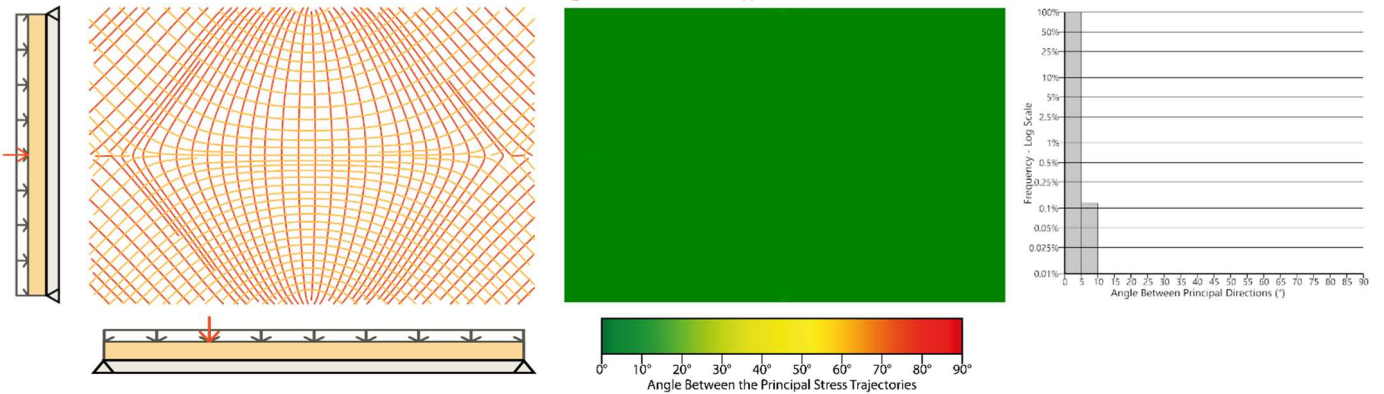
Figure 7-16: Left Point Load: Left - Stress Lines, Middle - Gradient Display of Principal Direction Differences, Right - Histogram of Principal Direction Differences.
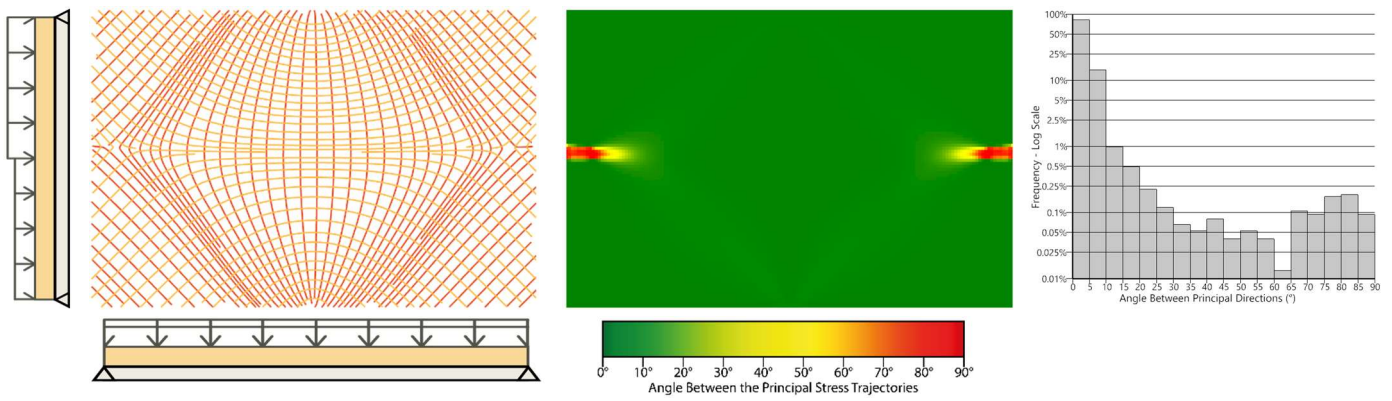
Figure 7-17: Half Loaded Slab Across the Short Span: Left - Stress Lines, Middle - Gradient Display of Principal Direction Differences, Right - Histogram of Principal Direction Differences.
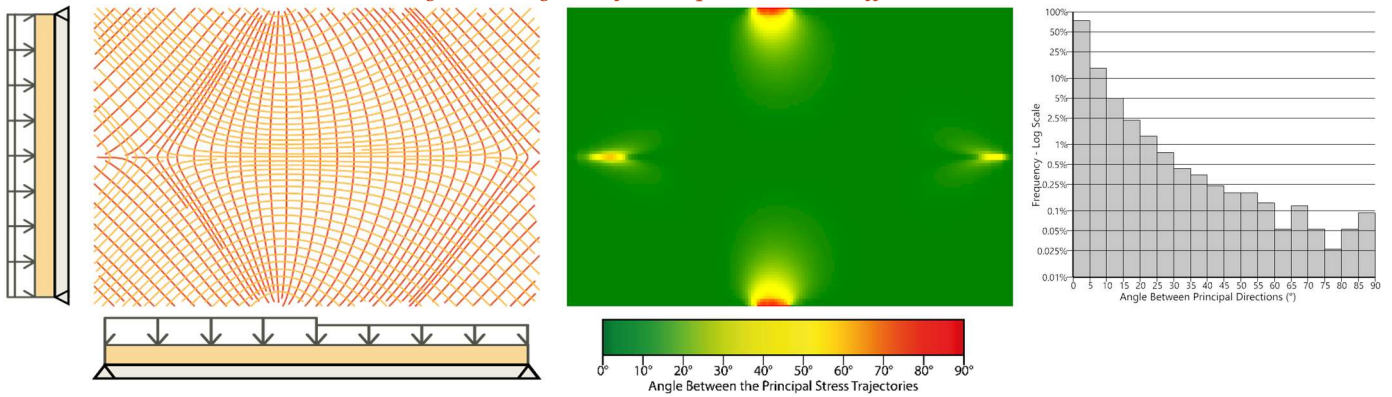
Figure 7-18: Half Loaded Slab Across the Long Span: Left - Stress Lines, Middle - Gradient Display of Principal Direction Differences, Right - Histogram of Principal Direction Differences.

7.5 Discussion and Conclusion

In this chapter, the secondary load cases have been analysed by investigating two case studies. In the first case study, the effect of assuming that the structural self-weight is evenly distributed was analysed. From the results, it is easy to conclude that this assumption has an insignificant effect, as the principal stress trajectories barely changed.

Applying concreated loads to the 10x10m corner-supported slab had a minor. However, particularly zero effect was seen by applying concreated loads to the 10x15m edge-supported slab. This difference is possibly explained by the increased indeterminacy of the edge-supported slab; this means that the slab has more mechanisms for transferring the load and can distribute the point load across the slab.

The most significant changes in the principal stress trajectories occurred when half the slab was loaded with a maximum UDL and the half with a minimum UDL. This was particularly significant for the corner-supported case and the 'left-right half loaded slab', where 26.8% and 25.6% of the principal stress field had a difference of >5°. It is unknown whether this will significantly impact the stresses in the final system. Therefore, this will be tested in Chapter 8.

A key finding in this chapter is that the changes in the principal stress trajectories are always located around the umbilic points. This occurs even when the load is applied off the umbilic points, like the off-centre point loaded case for the 10x10m slab. The reason behind this is unknown. Therefore, it would be of interest for further research to investigate the cause of this and how the principal stress fields change as the difference in loading between the load cases is increased.

8 RESISTANCE TO LOAD CASES

8.1 Introduction

The previous chapters have focused on developing the theory around principal stress trajectories, the generation of the principal stress lines, and the selection of principal stress lines for isostatic slabs. In this chapter and the subsequent chapters, the focus will be on how isostatic slabs can be designed using principal stress lines.

This chapter will investigate how an isostatic slab responds to difficult load cases and the effect three key design parameters have to the system: the deck's thickness, the rib's depth, and the rib's thickness.

Also, in Chapter 7, it was found that there were significant changes in the principal stress trajectories when half of a slab is loaded with a maximum UDL and the other half with a minimum UDL compared to when a constant UDL is applied. This secondary load case is investigated in this chapter to determine if it requires accommodation into the design.

8.2 Methodology

The design case study shown in Figure 8-1 is used to test the aspects outlined in the introduction. In this case study, a rectangular slab needs to be produced to support a 10x15m roof. The slab is supported vertically at the edges by columns; this means that it is assumed in the stress line generation stage the edges are pin-supported, like the edge-supported case shown in Chapter 7. There are many design parameters which can be considered; however, the following parameters are considered as the most crucial and are analysed:

- The deck thickness,
- The rib thickness,
- The rib depth.

The deck will always have a uniform thickness in the tests, and every rib part will have the same cross-section. To effectively compare these parameters, a "base situation" is chosen where:

- Deck thickness = 24mm
- Rib thickness = 69mm
- Rib depth = 400mm

In each test, one of the design parameters is varied (using the values given below), and the other design parameters take the values given in the base situation.

Deck thicknesses:

- 12mm
- 18mm
- 24mm
- 35mm
- 50mm

Rib thicknesses:

- 51mm
- 63mm
- 69mm
- 75mm
- 81mm

Rib depths:

- 300mm
- 400mm
- 500mm

These values are selected as they are the available sizes from the manufactures and give a reasonable range. The deck is modelled as plywood using the properties taken from the declaration of performance of the structural birch plywood produced by Metsä Wood (Metsä Wood, 2019). The ribs are modelled as LVL-S using the properties stated in the product certificate for Kerto-S produced by Metsä Wood (Eurofins, 2020).

Four load cases are applied to the slab system:

1. Full SLS
2. Full ULS
3. Horizontally Half-Loaded ULS
4. Vertically Half-Loaded ULS

So that comparable results are produced the self-weight is applied as line loads onto rib elements and area loads on the deck elements. The magnitude of these loads is calculated from the weight of the structure in the base situation. In this way, the loading is kept consistent when the parameters are changed.
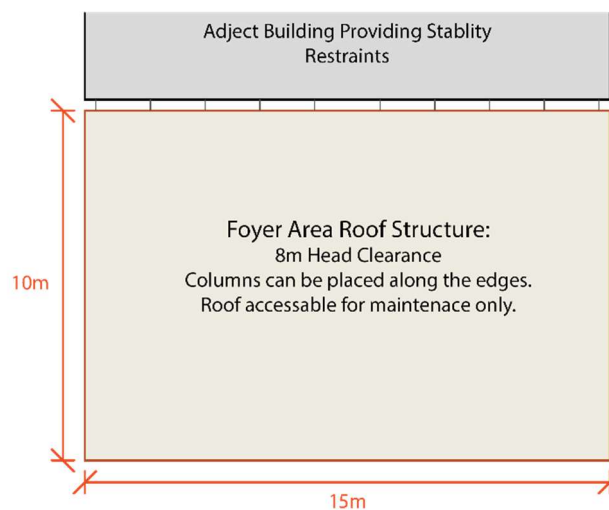
Figure 8-1: A Plan View of the Foyer Case Study

Three studies are conducted for evaluation and comparison purposes: Load Case Analysis, Primary Load Transfer Mechanisms, and Secondary Load Transfer Mechanisms.

In the Load Case Analysis study, the effect the different load cases have on the structure is investigated by comparing the maximum and minimum stress results from each load case with the parameters' base situation. In the other two cases, the design parameters' effect on the primary and secondary load transfer mechanisms is investigated. The primary load transfer mechanisms are defined as the intend paths of stress, i.e., composite bending in the deck and ribs, vertical shear forces in the ribs, and bending and shear in the deck between the ribs. The secondary load transfer mechanisms are defined as other unintended paths of stress, e.g. torsional bending.

8.3 Loading

For the case study, the loading needs to be specified. Like in Chapter 7, the loading conditions are those of a roof which is only accessible for maintenance. This means that the same values for the

applied variable loads can be used. However, the concreated live load is removed as it was found in Chapter 7 that this had a negligible effect on the principal stress directions.

- Uniform Maintenance Load (Q_{LL}) = 1.0 kN/m²,
- Snow Load = 1.0 kN/m² (Q_{Sn}), *this is a conservative estimated value*

In Chapter 7, a load of 1.7kN/m² was used for the dead load, including the structure's self-weight. However, in this chapter, the self-weight of the structure will be applied as a separate load. The main dead load case will account for the roofing material (i.e. waterproofing and insulation) and the internal elements (i.e. the ceiling and services). The roofing material load is assumed to be 0.5 kN/m2, and the load of the internal elements is 0.15kN/m² (Cobb, 2015) (ROCKWOOL, 2020).

- Dead Load (G_{Dead})= 0.65kN/m²

The structural self-weight is applied as line loads for the rib elements and uniform area loads for the deck elements. The mean density of the LVL ribs is 510kg/m³ (Eurofins, 2020), and the plywood deck is 680kg/m² (Metsä Wood, 2019). Assuming a deck thickness of 24mm, a rib thickness of 69mm, and a rib depth of 400mm for every model, results in the following loads:

- Deck Self-Weight Area Load (G_{SW})= 0.160kN/m²
- Rib Self-Weight Line Load (G_{SW})= 0.140kN/m

For the 'Full SLS' and 'Full ULS' cases, the imposed loading from snow and maintenance is applied across the entire slab. For the 'Horizontally Half-Loaded ULS' case the imposed loads are only applied to the left half of the slab, and for the 'Vertically Half-Loaded ULS' case the imposed loads are only applied to the upper half of the slab when viewed from above like in Figure 8-1.

The load case combinations are handled within the FE software. Using the same combination factors as in Chapter 7, the combinations are:

$$Full\ SLS =\ 1.0(G_{Dead} + G_{SW}) + 1.0(Q_{LL} + Q_{Sn})$$

$$Full\ ULS =\ 1.35(G_{Dead} + G_{SW}) + 1.5Q_{LL} + 0.75Q_{Sn}$$

$$Half-Loaded\ ULS =\ 0.9(G_{Dead} + G_{SW}) + 1.5Q_{LL} + 0.75Q_{Sn}$$

8.4 Model Creation and Validation

Before an FE model of the slab system can be tested and compared, it needs to be created and validated to ensure that the results are accurate. Unfortunately, there is no easy way of predicting the behaviour of the slab through hand calculations. Instead, the entire slab system model is built upon more basic models where the results can be compared in each step.

8.4.1   The Rib Geometry

The first step in creating the model is to determine the rib geometry. Stress lines are selected manually using engineering judgement and the guiding data of the load span lengths and deviation distances between the discretised and non-discretised stress lines, as was used in Chapter 6. The final geometry is found by iteratively changing the selected stress lines and finding an arrangement with a large clustering around the peak load span value. An aim of having a maximum load span of between 0.6m and 0.9m was used to achieve a specific density of ribs. This specific range was chosen as it would create a rib-to-rib distance of ~1.2m to ~1.8m which by reference to timber diagrid roofs is a reasonable intermediary range (TRADA, n.d.) (Tigg+Coll

Architects, n.d.) (Momentum structural engineers, n.d.). The final rib layout is shown in Figure 8-2, alongside the load span and deviation data in Figure 8-3.

The key assumptions in choosing this arrangement are: the span distance of the deck is a critical constraint in the design, using straight-discretised ribs is advantageous over curved ribs, and that the rib-to-column connections around the roof boundary transfer no moment forces.
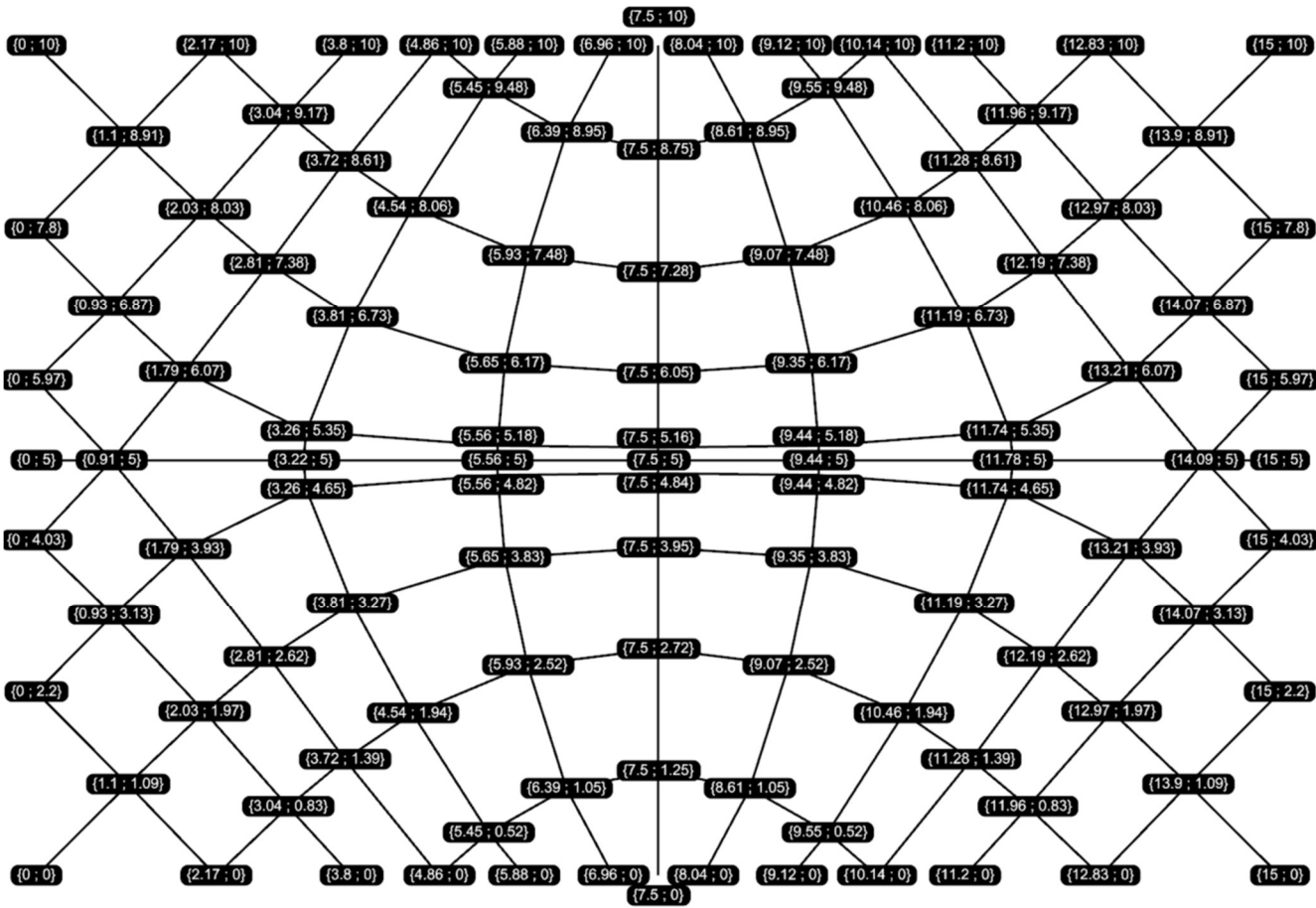
Figure 8-2: Foyer Case Study Rib Topology – Plan View
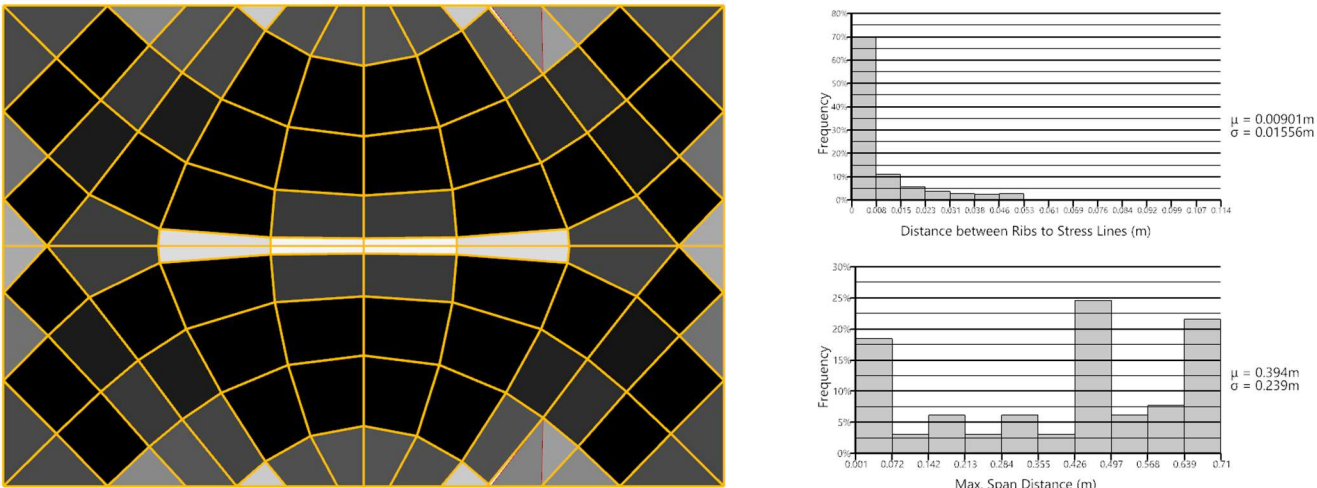
Figure 8-3: Longest Load Span Data and Rib and Stress Line Deviation Distance Data for the Foyer Case Study Rib Topology

8.4.2   The Beam Model

Firstly, a simple beam model is produced in Oasys GSA 10.1 (Oasys, 2020). This beam model only includes the rib elements modelled as 1D elements with flexural bending elements in both axes,

torsional effects, and axial extension/compression effects. Isotropic properties are applied to the beam with the following material values: E=13800 MPa, ν=0.0, and G=380MPa. With the beam elements having a cross-section of 400x69mm. All the beam elements are fully fixed to each other. The loads are applied as point loads at the connection points between elements; each point load represents the slab's attributing area – the area values per point have been calculated using a Voronoi mesh. These point loads exclude the self-weight of the beam, which is added as a line load. Pin supports are applied at the beam ends at the edges of the structure. Figure 8-4 shows the deflection of the Beam Model under the Full ULS condition. This model will be the basis for comparing the other models' results, so it has been double-checked by creating an identical model in Karamba3d (Karamba3D, 2020). The GSA and Karamba3d results are equal for deflections (mm), moment forces (kNm), and shear forces (kN) to 1 decimal place. Therefore the GSA model is accurate
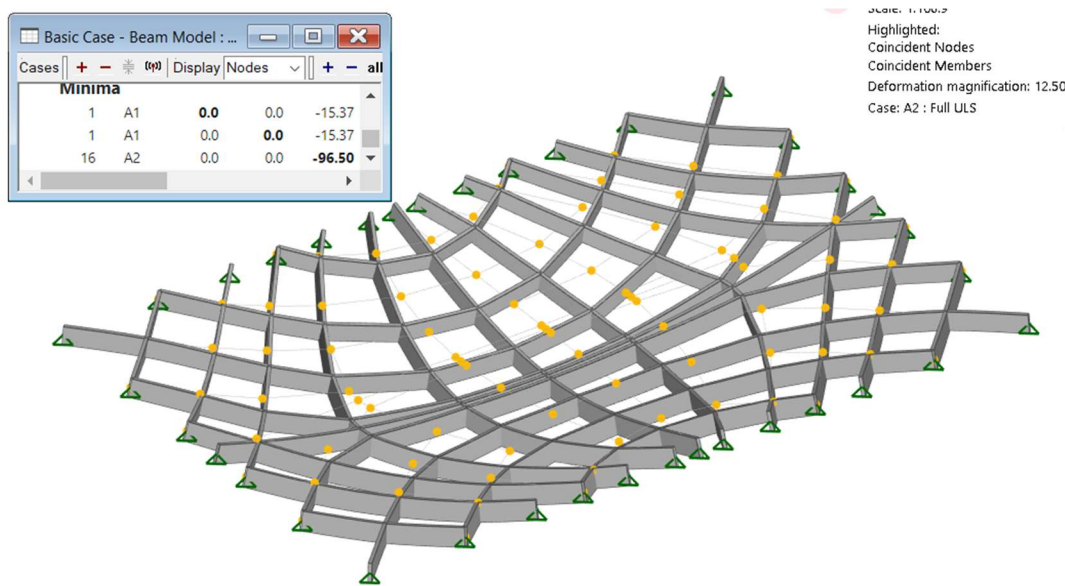
Figure 8-4: Deflection of the Beam Model under the Full ULS Combination

8.4.3 The Shell Rib Model

The next step is to model the rib elements with more complex behaviour. The ribs are modelled as shell elements in Diana FEA (DIANA FEA bv., 2020). This analyses the effect of the rib depth and includes shear deflection. The shell elements are created using the same centreline geometry extruded downward by 400mm to produce the depth required. The shell elements are given a thickness of 69mm and a shape factor 1.5. The material is modelled orthotopically, where the y-axis is aligned with the length of the rib, and the x-axis is aligned with the depth of the rib:

$$E_x = 430 \; MPa \qquad G_{xy} = 600 \; MPa \qquad v_{xy} = 0.001$$

$$E_y = 13800 \; MPa \qquad G_{yz} = 380 \; MPa \qquad v_{yz} = 0.001$$

$$E_z = 130 \; MPa \qquad G_{xz} = 1 \; MPa \qquad v_{xz} = 0.001$$

Note that the value of G_{xz} used as no value was provided by the manufacture, and the FE solver requires a non-zero value. The same is true for the Poisson's ratios.

Only vertical restraints support the shell elements at the edges that lie on the structure's boundaries, but pin-supports are added to the bottom corners of the shell elements along the line y=10m. The shell elements are fully fixed to each other at the internal connections. The shell

elements are not connected at the support locations as these elements will be connected to the deck and the columns only, and early tests showed that allowing a fixity here causes large torsional effects. The loads are applied in the same way as the Beam Model, where the line loads are applied to the top edges, and the point loads are applied to the top points where the elements meet. Figure 8-5 shows the deflection results for this model under the full ULS combination.
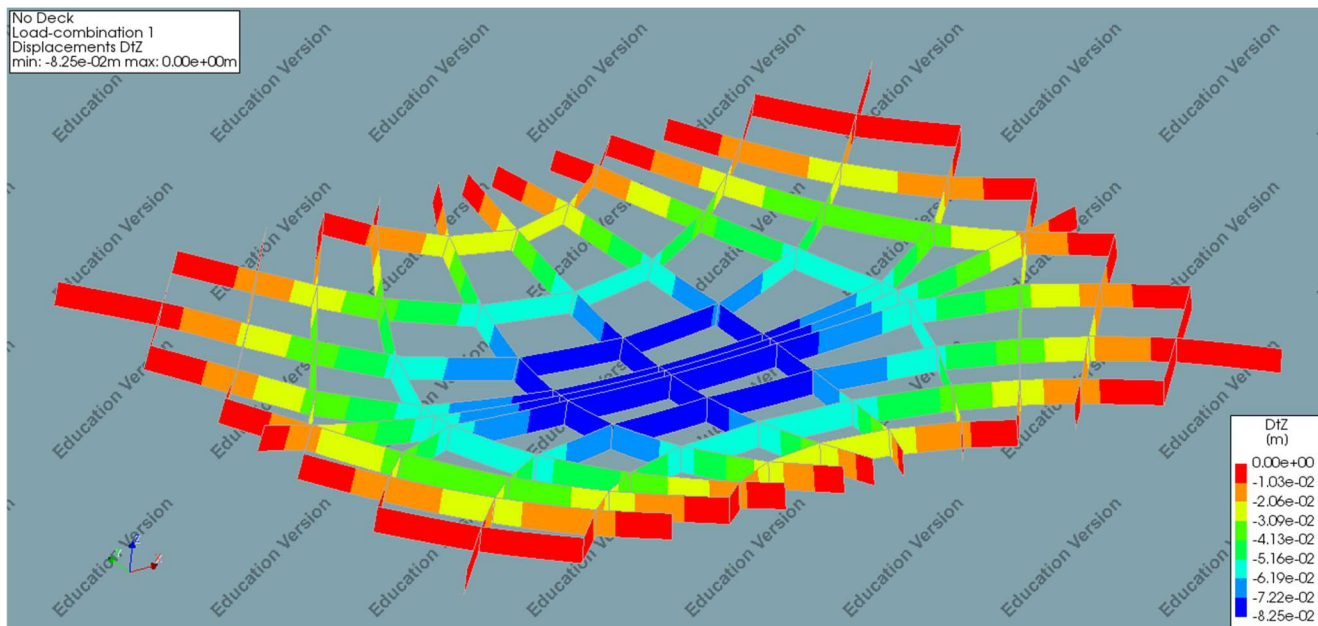
Figure 8-5: Deflection of the Shell Rib Model under the Full ULS Combination (scale factor: x 10)

8.4.4 The Shell Rib and Deck Model

The Diana model can now be adapted to add the deck elements into it as another set of shell elements. An individual element is added between rib shell elements, and the local axes of the elements are aligned with the global axes of model. The deck shell elements are assigned a thickness of 24mm and a shape factor of 1.5. The deck is also modelled with orthotropic properties:

$$E_x = 8500 \ MPa \qquad G_{xy} = 620 \ MPa \qquad v_{xy} = 0.001$$

$$E_y = 9100 \ MPa \qquad G_{yz} = 210 \ MPa \qquad v_{yz} = 0.001$$

$$E_z = 1 \ MPa \qquad G_{xz} = 190 \ MPa \qquad v_{xz} = 0.001$$

Note that in the declaration of performance for the plywood material there two values to use for E_x and E_y: the flexural stiffness in each direction and the axial stiffness (Metsä Wood, 2019). The difference between these values increases as the thickness of the plywood is decreased. It is assumed that the in-plane extension and compression are dominant over the flexural bending due to the composite actions between the ribs and the deck. For this model and all subsequent models, the axial stiffnesses are used.

No connection properties are set between the deck and rib elements, so every degree of freedom between elements, which can be fixed, is fixed. The rib-to-rib connections are the same as in the previous model. The supports are the same as in the previous Diana model. The self-weight of ribs is still applied as line loads. All of the other loads are applied as area loads onto the deck elements. Figure 8-6 shows the deflection for the completed model under the full ULS combination.
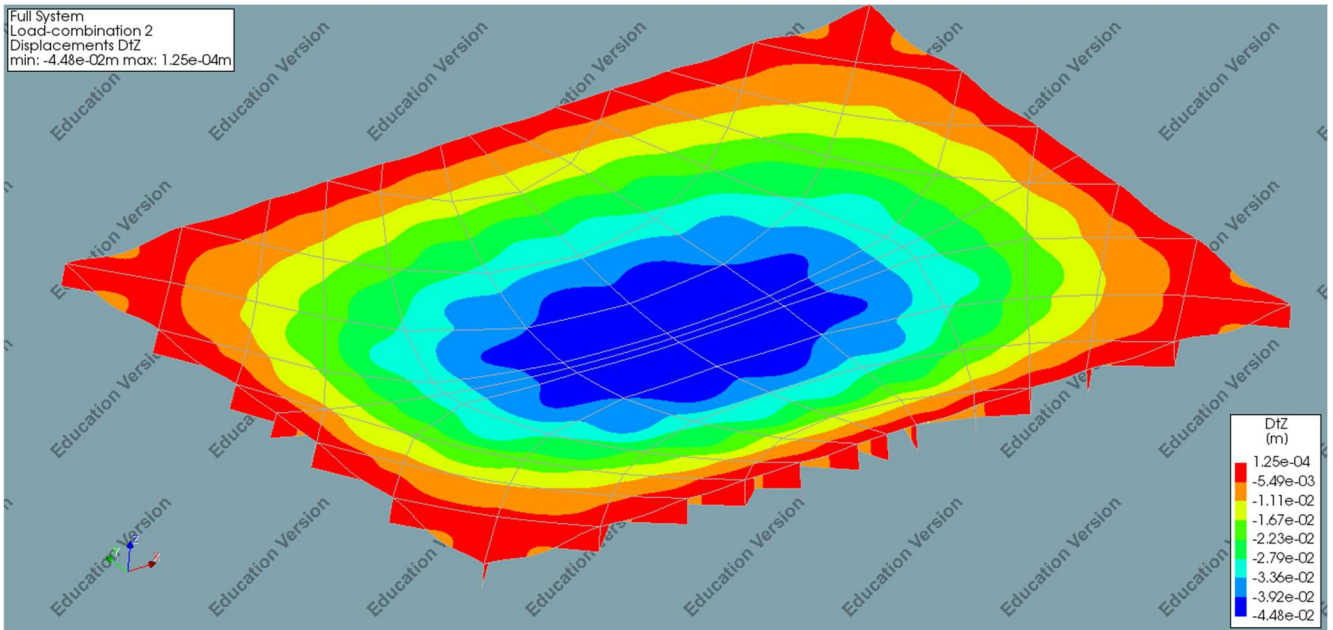
Figure 8-6: Deflection of the Shell Rib and Deck Model under the Full ULS Combination (scale factor: x 18)

8.4.5   Model Comparison and Validation

The three models' results are compared to determine what changes occur in each step and whether these are expected. All the models are compared using the Full ULS combination.

For the Beam Model, the forces and moments in each beam are outputted. The maximum and minimum values for these are displayed in Table 8-1. The total applied load for the full ULS combination is 546.8 kN, and the sum of all the reaction forces in the Beam Model is 546.8 kN in the z-axis.

From the results, it is clear that the forces are carried predominantly through bending and shear, with only minor torsional effects. The shear and bending results are as expected; increasing shear forces towards the supports, peak moments in the slab's centre, and some hogging in the corners.

Table 8-1: Member Forces of the Beam Model

	Fx (kN)	Fy (kN)	Fz (kN)	Mxx (kNm)	Myy (kNm)	Mzz (kNm)
Min.	0.0	0.0	-22.10	-0.058	-48.32	0.0
Max.	0.0	0.0	22.42	0.058	26.94	0.0
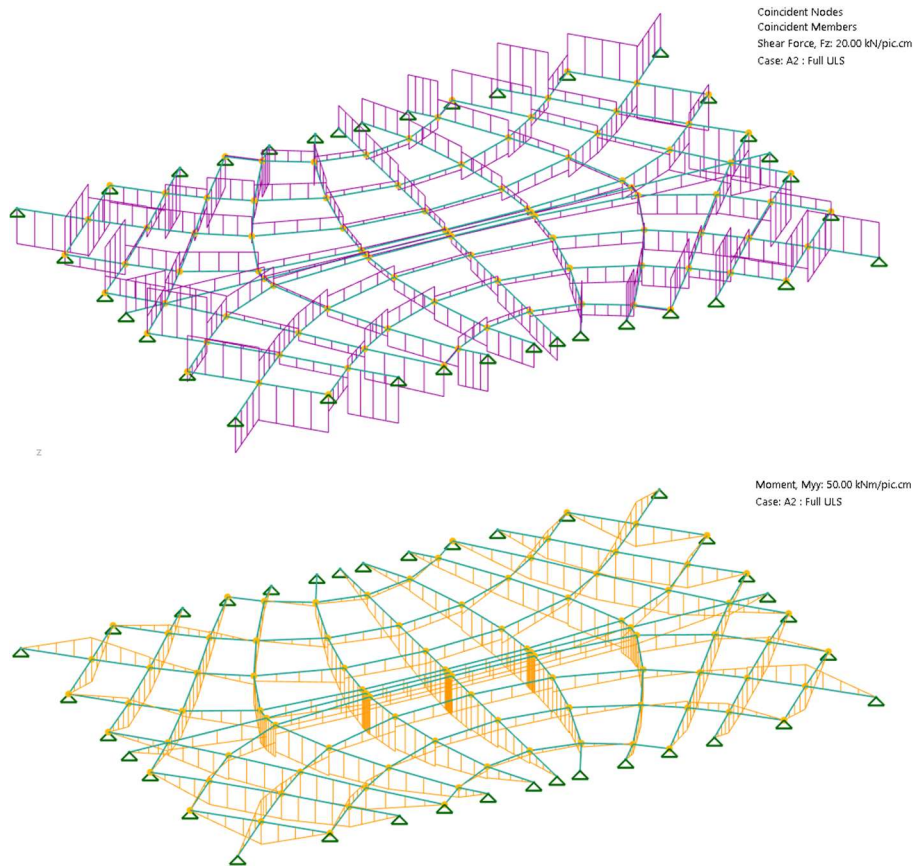
Figure 8-7: Beam Model - Force Diagrams; Top: Fz, Bottom: Myy

The structure should behave similarly for the Shell Rib Model; however, the output results will be displayed as distributed forces and moments. Table 8-2 shows the minimum and maximum disturbed forces and moments. The n_{ii} values are the in-plane normal and shear forces, the v_{ii} values are the out-of-plane shear forces, and the m_{ii} values are the in-plane normal and shear forces caused by out-of-plane bending. Note that the values for v_{xz} and m_{xx} occur due to singularities and are therefore unrealistic. Also, the minimum value of n_{xx} occurs due to the applied point loads, so it is also unrealistic.

The sum of the reaction forces for the model is 549.1kN in the vertical direction. The difference from the total applied load of 546.8kN is possibly due to applying the point loads with lower precision.

From Figure 8-8, it can be seen that the system behaves in a very similar way to the Beam Model: The bending moments, shown by n_{yy}, peak at the slab's centre and some hogging occurs in the corners, also the shear forces, shown by n_{xy}, increase towards the supports. Although some additional forces occur, namely the out-of-plane shear and the distributed bending forces, but these are insignificant compared to the in-plane-normal stresses.

Table 8-2: Distributed Forces of the Shell Rib Model

	n_{xx} (kN/m)	n_{yy} (kN/m)	n_{xy} (kN/m)	v_{xz} (N/m)	v_{yz} (N/m)	m_{xx} (N)	m_{yy} (N)	m_{xy} (N)
Min.	-33.9	-1790	-150	-2483	-52	-49	-139	-61
Max.	20.9	1780	150	2472	52	52	137	61
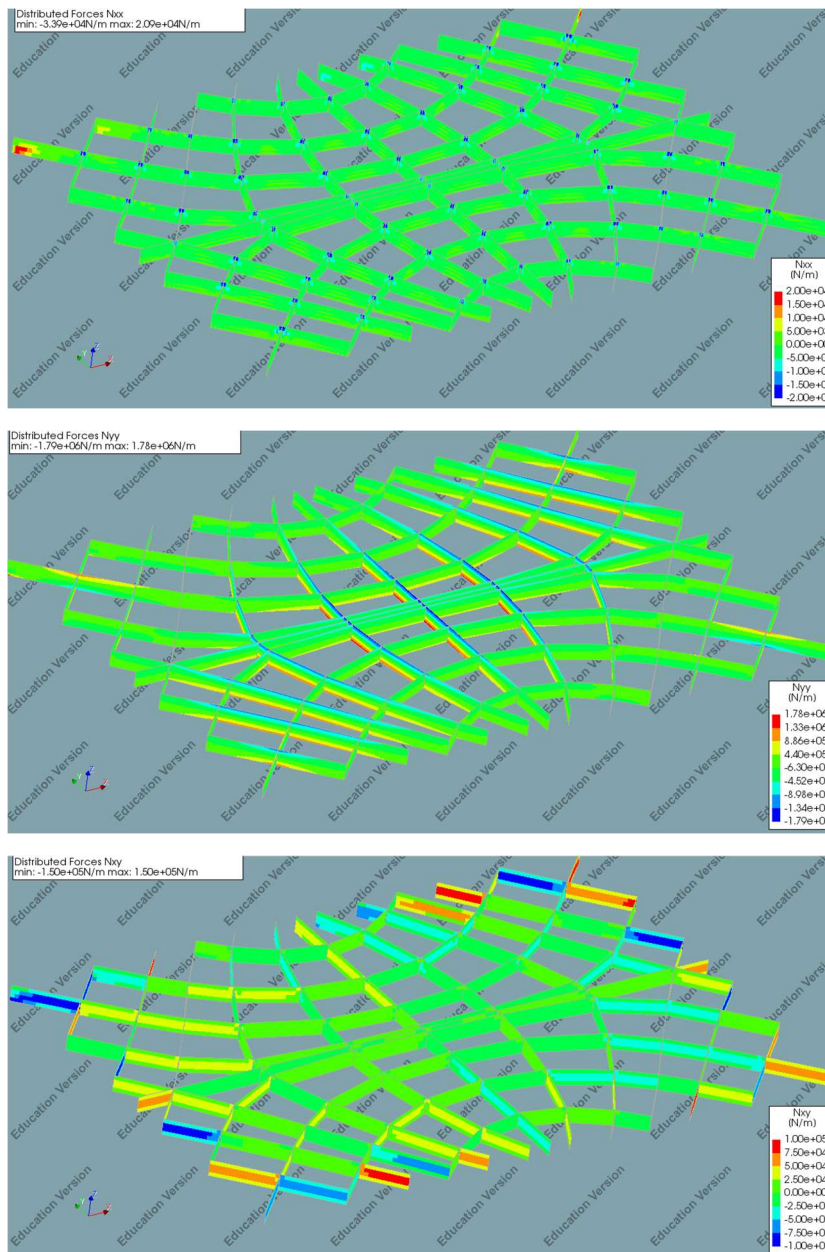
Figure 8-8: Shell Rib Model - Distributed Force Contour Plots; Top: n_{xx}, Middle: n_{yy}, Bottom: n_{xy}

Finally, looking to the Shell Rib and Deck Model, a significant difference should be observed due to the deck's inclusion. For this model, the total reaction force is 546.8kN in the z-direction.

Table 8-3 shows the distributed forces and moments for the ribs. Note that the values of v_{xz} and m_{xx} only arise because of singularities at the connections between elements. Table 8-4 shows the minimum and maximum values for the deck elements. As the deck is loaded out-of-plane, there are extensive bending, torsional, and out-of-plane shear forces.

Although the deck's inclusion causes an increase of out-of-plane shear, bending, and torsion forces in the ribs, these cause a comparatively small increase in stress compared to the in-plane normal and shear forces. Figure 8-9 shows the distributed normal and shear forces. Comparing these values to the Shell Rib Model's values shows that the deck's addition reduces the in-plane forces, especially the ribs' compression forces. The change from point loads to area loads onto the deck causes the compression in n_{xx} to be spread along the ribs' lengths.

	n_{xx} (kN/m)	n_{yy} (kN/m)	n_{xy} (kN/m)	v_{xz} (N/m)	v_{yz} (N/m)	m_{xx} (N)	m_{yy} (N)	m_{xy} (N)
Min.	-9.1	-678	-91.6	-5432	-174	-220	-398	-112
Max.	16.7	1474	91.6	4947	173	220	420	112

Table 8-4: Distributed Forces of the Shell Rib and Deck Model – Isolated for the Deck

	n_{xx} (kN/m)	n_{yy} (kN/m)	n_{xy} (kN/m)	v_{xz} (N/m)	v_{yz} (N/m)	m_{xx} (N)	m_{yy} (N)	m_{xy} (N)
Min.	-88.9	-129	-18.2	-2870	-2545	-281	-300	-47
Max.	70.0	54	18.2	2828	2300	323	344	47
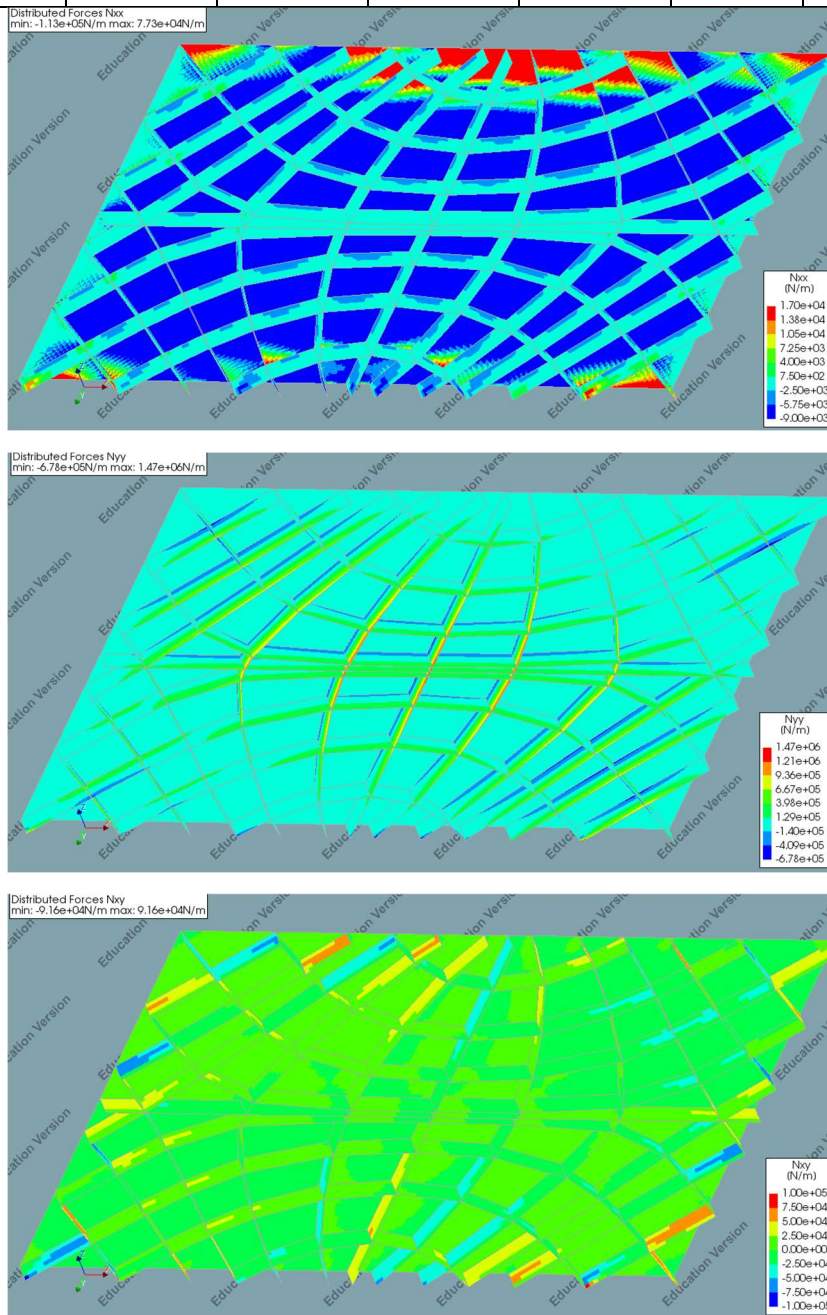
Figure 8-9: Shell Rib and Deck Model - Distributed Force Contour Plots for the Ribs; Top: n_{xx}, Middle: n_{yy}, Bottom: n_{xy}

The bending stresses at the centre of the slab can be compared to examine the models' differences. Figure 8-10 and Figure 8-11 show the ribs' stresses at the slab's centre. The results from the Beam Model and Shell Rib Model have identical values. The small differences occur due to shear beam effects. Once the deck is added, the stresses take an entirely different form as the deck contributes to the bending stiffness. As the deck is located at the top edge of the ribs, the total bending moment of deck-rib composite system can be found by taking moments about the top, thus excluding the deck's compression force from the equation. Using this the moment in the rib along x=7.5m for the Shell Rib and Deck Model is 53.5kNm, which is compared to a moment of 48.2kNm in the Beam Model and 46.8kNm in the Shell Rib Model. The same is done for rib along y=5.0m giving a moment of 11.7kNm in the Shell Rib and Deck Model, compared to 16.2kNm in the Beam Model and 15.3kN in the Shell Rib Model. There is quite a difference between the Shell Rib and Deck Model and the other models; however, the plywood is oriented such that its stiffer axis is aligned with the global y-axis. This means that the composite beams are stiffer when the rib is parallel to the y-axis. Therefore, the results are acceptable as the moment has increased in the rib along x=7.5m and decreased in the rib along y=5.0m. There will also be a proportional of the moment taken through bending of the deck, however as the peak flexural bending moment in the deck is only 0.334kNm/m this will not have a significant effect.
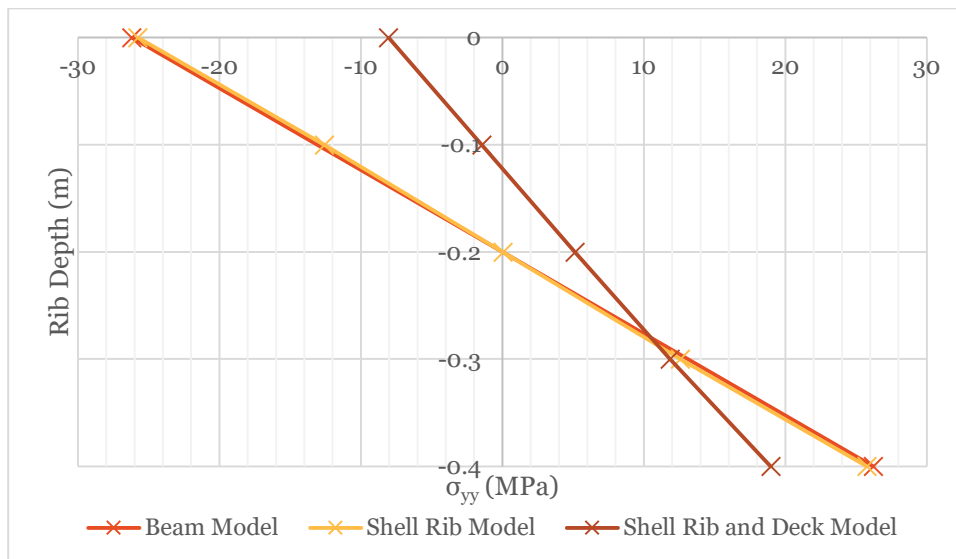
Figure 8-10: Axial Stresses at (7.5m;5m) in the rib along x=7.5m
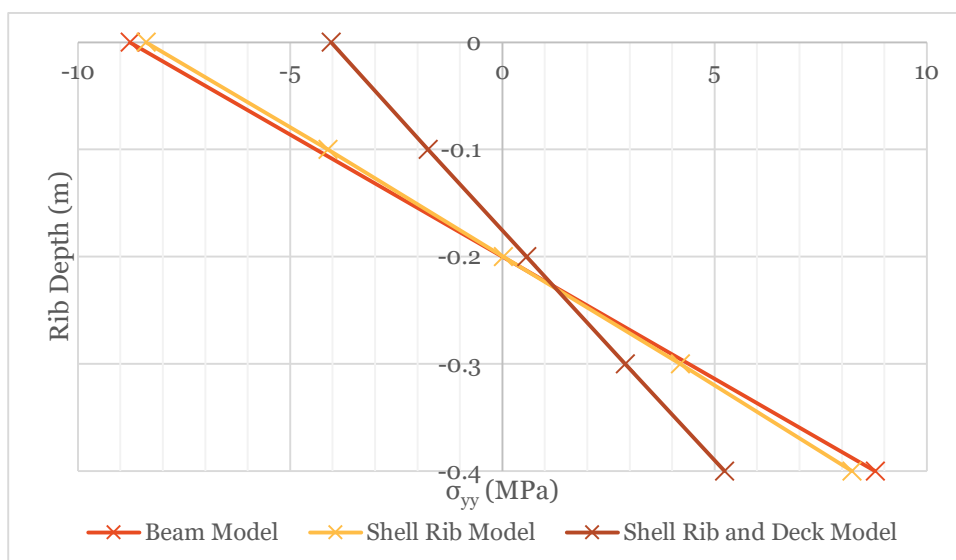
Figure 8-11: Axial Stresses at (7.5m;5m) in the rib along y=5.0m

8.5 Testing

8.5.1   Study 1: Load Case Analysis

In Chapter 7, the influence of the load cases on the stress lines was analysed. There were large deviations in the principal stress trajectories for the 10x15m edge-supported slab when a maximum UDL was only applied to half of it. However, it is difficult to determine from those results if this has a significant impact. Therefore, this impact is tested in this sub-section by comparing the distributed forces in the deck for the three load situations: Full ULS, Horizontally Half-Loaded ULS, and Vertically Half-Loaded ULS. To compare these, the base situation of design parameter is used.

Table 8-5 shows the maximum, minimum, mean, and median values for each of the distributed forces/moments in ribs, for the three load combinations. Table 8-6 shows the same data but for the deck. The values given for the maximum and minimum are not the true peaks but are instead the 10th highest and 10th lowest values; this is so that singularities are minimised. Also, excluding the n_{XX} and n_{YY} values, the means and medians are produced by first taking the results' absolute value and then producing the averages. This is done as the direction of these forces is not as crucial as their absolute value. Also, due to the slab's symmetry, there are often equal amounts of positive and negative values resulting in the true mean and median being almost zero.

From this data, it is clear that the highest average and peak forces are produced in the Full ULS load combination. So, although the distribution of stresses will differ in each case, the largest values will always occur with the most considerable total load.

*Table 8-5: The Distributed Forces and Moments in the **Ribs** for the Three ULS Load Combinations (Full=Full ULS, Hori.=Horizontally Half-Loaded ULS, and Vert.=Vertically Half-Loaded ULS)*

Load Combination	n_{xx} (kN/m)			n_{yy} (kN/m)			n_{xy} (kN/m)			v_x (N/m)		
	Full	Hori.	Vert.	Full	Hori.	Vert.	Full	Hori.	Vert.	Full	Hori.	Vert.
Maximum	16.5	11.5	9.2	1308.4	774.3	804.2	77.3	56.1	50.8	4886.2	2943.7	2956.1
Minimum	-8.5	-6.4	-4.7	-667.4	-454.9	-368.0	-68.6	-51.5	-47.4	-5144.0	-2732.5	-3746.4
Mean	-1.0	-0.5	-0.5	99.5	56.1	56.3	17.5	10.4	10.4	117.4	74.3	74.6
Median	-0.7	-0.3	-0.3	61.5	31.9	34.7	13.8	7.7	8.4	13.2	8.2	7.5

Load Combination	v_y (N/m)			m_{xx} (Nm/m)			m_{yy} (Nm/m)			m_{xy} (Nm/m)		
	Full	Hori.	Vert.	Full	Hori.	Vert.	Full	Hori.	Vert.	Full	Hori.	Vert.
Maximum	155.5	117.4	112.4	115.2	68.9	99.3	340.3	323.1	241.0	98.4	77.7	70.9
Minimum	-155.3	-113.3	-112.4	-115.5	-103.2	-99.6	-325.4	-279.7	-275.0	-95.0	-82.6	-71.2
Mean	15.8	10.5	10.3	7.9	5.0	4.9	23.3	14.8	14.7	11.7	7.6	7.3
Median	9.4	6.1	5.6	4.0	2.3	2.3	11.1	6.5	6.9	7.2	4.1	4.0

Load Combination	n_{xx} (kN/m)			n_{yy} (kN/m)			n_{xy} (kN/m)			v_x (N/m)		
	Full	Hori.	Vert.	Full	Hori.	Vert.	Full	Hori.	Vert.	Full	Hori.	Vert.
Maximum	63.7	10.1	36.1	44.1	30.9	26.8	17.5	12.4	11.3	2437.2	1862.4	2006.4
Minimum	-77.8	-13.8	-45.6	-127.7	-72.2	-80.9	-17.5	-12.6	-11.3	-2669.6	-2627.8	-2006.3
Mean	-25.7	-14.5	-14.3	-37.5	-21.2	-21.2	4.8	2.7	2.9	395.8	216.2	217.7
Median	-29.0	-13.0	-16.1	-33.8	-18.4	-18.8	3.9	2.1	2.4	243.8	95.5	92.1

Load Combination	v_y (N/m)			m_{xx} (Nm/m)			m_{yy} (Nm/m)			m_{xy} (Nm/m)		
	Full	Hori.	Vert.	Full	Hori.	Vert.	Full	Hori.	Vert.	Full	Hori.	Vert.
Maximum	2160.9	1895.7	1909.3	305.0	265.8	264.0	331.3	299.8	295.6	45.2	38.0	38.1
Minimum	-2166.7	-1906.9	-1842.7	-268.5	-237.5	-236.2	-287.6	-253.6	-252.6	-45.3	-38.8	-38.1
Mean	433.4	237.8	239.6	61.2	34.1	33.9	76.8	43.1	42.8	5.8	3.3	3.3
Median	291.7	104.9	117.4	48.8	19.2	19.9	63.0	27.2	26.8	3.2	1.4	1.4

8.5.2   Study 2: Primary Load Transfer Mechanisms

In this study, the load transfer mechanisms are analysed by comparing the primary load transfer paths for the Full ULS load case. This is assessed by observing the following forces: The axial distributed forces in the ribs at (x=7.5m, y=5m), and the in-plane distributed forces of n_{xx} and n_{yy} in the deck along the lines x=7.5m and y=5m, respectively. The results are outputted in the global coordinate systems as indicated by the capital "X" and "Y"

Firstly, the deck thickness design parameter is investigated. Figure 8-12 to Figure 8-15 show n_{xx} and n_{yy} for the deck and ribs with a varying thickness of the deck. Figure 8-12 and Figure 8-14 show that an increase in the deck thickness decreases the ribs' stresses in both directions, although the change in the tension stresses is less significant than the compression stresses.

Looking at the changes in the deck's distributed forces, there is a positive correlation between the deck thickness and the force per m in the deck. This is more significant for the n_{xx} forces as the peak n_{xx} distributed force increases by 134.9% and the peak n_{yy} distributed forces increase by 37.9% between the 12mm and 50mm deck. This occurs due to the deck's stiffness properties changing with its thickness. As the plywood is made thicker, it has more lamellas/plies, so the stiffness ratio between the orthogonal directions approaches 1. When a thin deck is used, the plywood is a lot stronger in the primary axis, which is in the global Y-axis. The composite actions are apparent in the deck by the local increases in force at the rib locations and the force built-up between the ribs. There are large tension forces in n_{xx} at the edge of y=0.0m, which occur on this edge only due to the lack of lateral supports, meaning that the deck provides the only laterally restraint. This does not occur in n_{yy} as the slab is symmetrical in this axis.
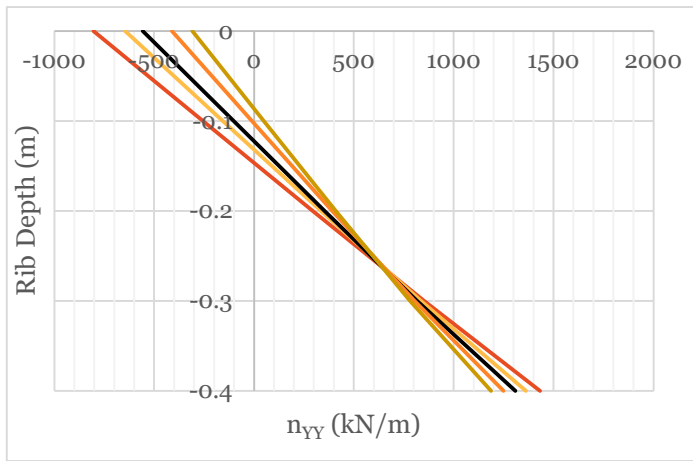
Figure 8-12: The Distributed Axial Forces n_{YY} at (7.5m;5m) in the Rib Along y=5.0m for Varying Deck Thicknesses
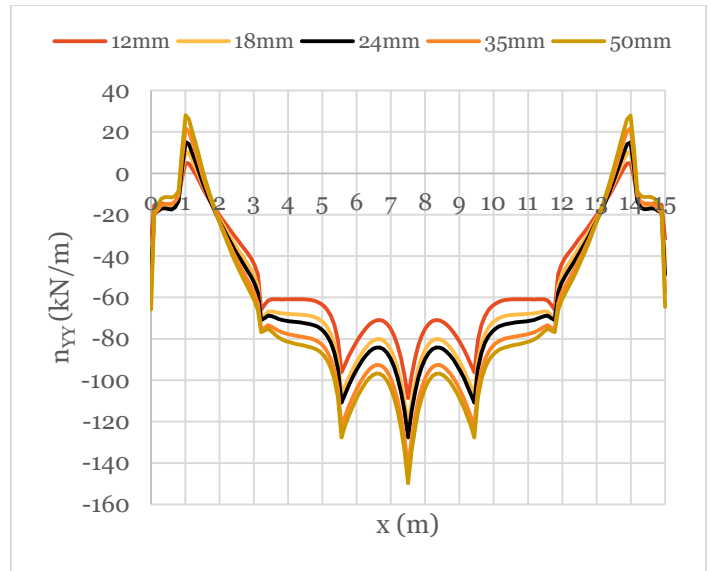
Figure 8-13: The Distributed Axial Forces n_{YY} in the Deck Along y=7.5m for Varying Deck Thicknesses
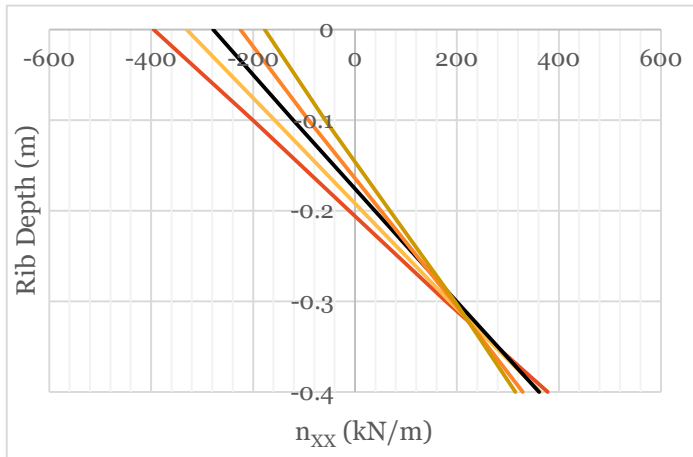
Figure 8-14: The Distributed Axial Forces n_{XX} at (7.5m;5m) in the Rib Along x=7.5m for Varying Deck Thicknesses
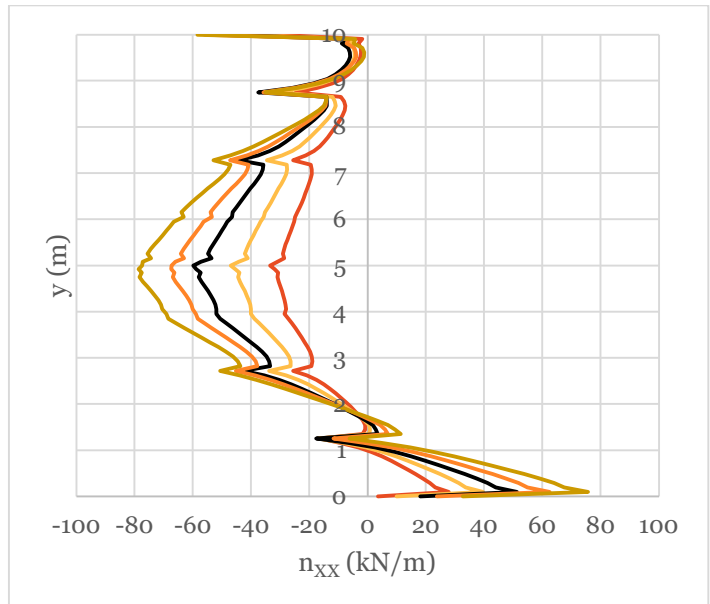
Figure 8-15: The Distributed Axial Forces n_{XX} in the Deck Along x=5.0m for Varying Deck Thicknesses

Variation of the rib depth has been analysed, and the same results are displayed for three rib depths in Figure 8-16 to Figure 8-19. For the n_{XX} and n_{YY} forces in the ribs, increasing the rib depth reduces the peak stresses, especially the tensile stresses, although the total moment is roughly constant. Also, by increasing the rib's depth, the deck's distributed forces are also reduced, which means that less composite action between the rib and deck is achieved as the rib gets stiffer. Unlike changing the deck's thickness, changing rib's depth has the same level of effect on the two directions; the peak n_{XX} and n_{YY} compression forces in the deck with a rib depth of 500mm are reduced to 50.4% and 52.0%, respectively, when a rib depth of 300mm is used.
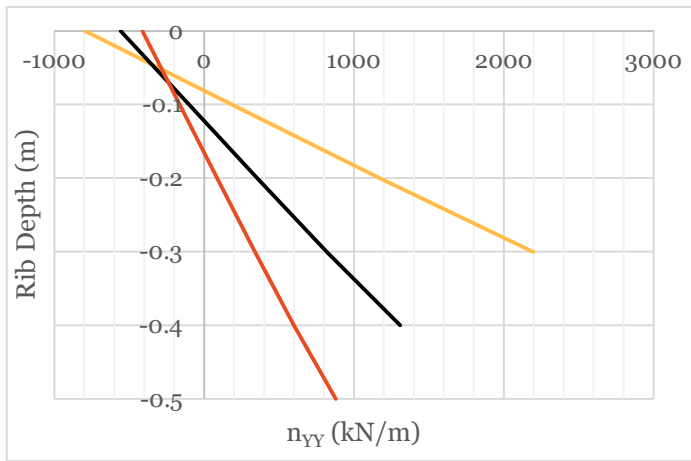
Figure 8-16: The Distributed Axial Forces n_{YY} at (7.5m;5m) in the Rib Along y=5.0m for Varying Rib Depths
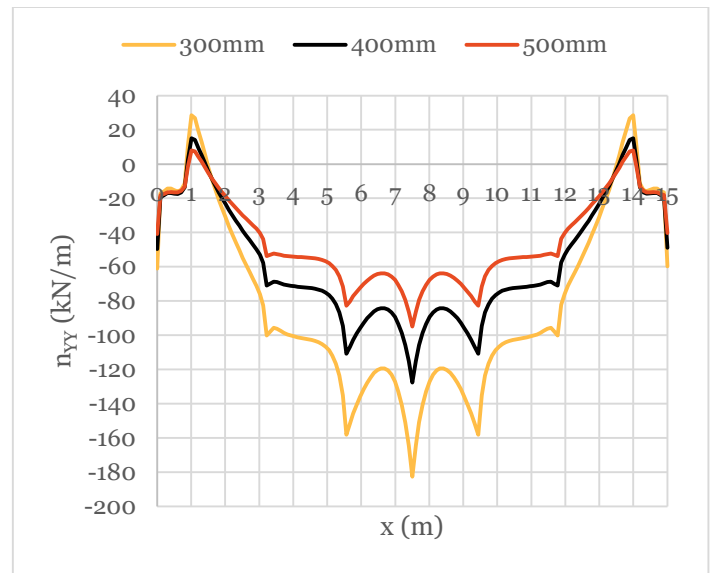
Figure 8-17: The Distributed Axial Forces n_{YY} in the Deck Along y=7.5m for Varying Rib Depths
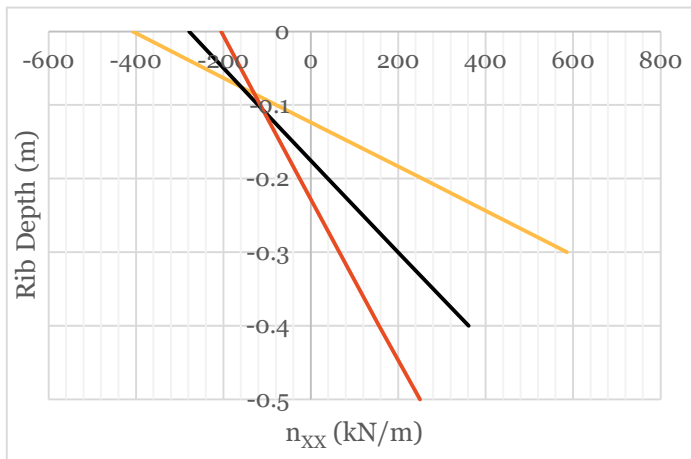
Figure 8-18: The Distributed Axial Forces n_{XX} at (7.5m;5m) in the Rib Along x=7.5m for Varying Rib Depths
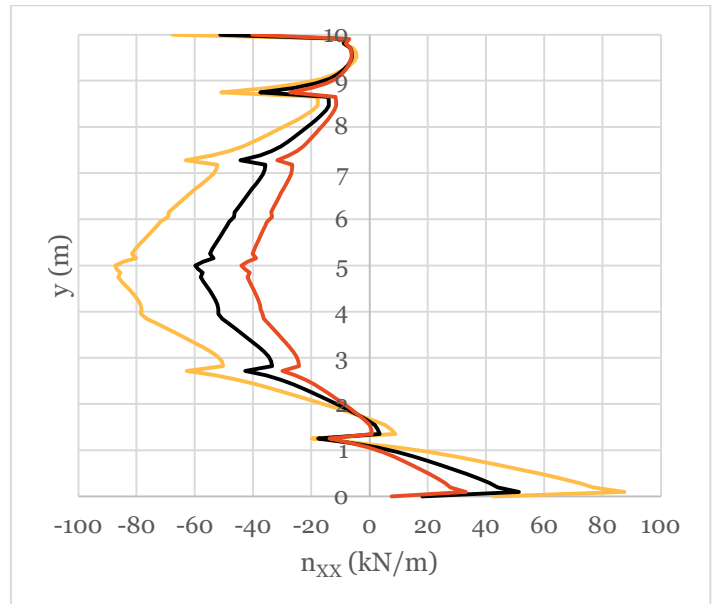
Figure 8-19: The Distributed Axial Forces n_{XX} in the Deck Along x=5.0m for Varying Rib Depths

Finally, the difference in rib thickness is analysed, as shown in Figure 8-20 to Figure 8-23. It is immediately apparent that changing the rib thickness is not as dramatic as changing the other parameters. However, the range of thicknesses used is small due to the range of standard thicknesses available from the supplier. A reduction in rib thickness causes a reduction in axial forces in the ribs (although, it should be noted that this will not lead to a reduction in stresses), and an increase in axial forces in the deck. There is a different percentage change to the distributed forces in each direction as between a 51mm and 81mm thick rib the peak n_{XX} and n_{YY} in the deck decreases by 19.8% and 12.6%, respectively, whereas in the rib the peak compression forces of n_{XX} and n_{YY} increase by 27.4% and 38.9%, respectively. This shows that increasing the rib's thickness causes a higher difference in the n_{XX} than n_{YY} for the deck, and the opposite is true for the ribs.
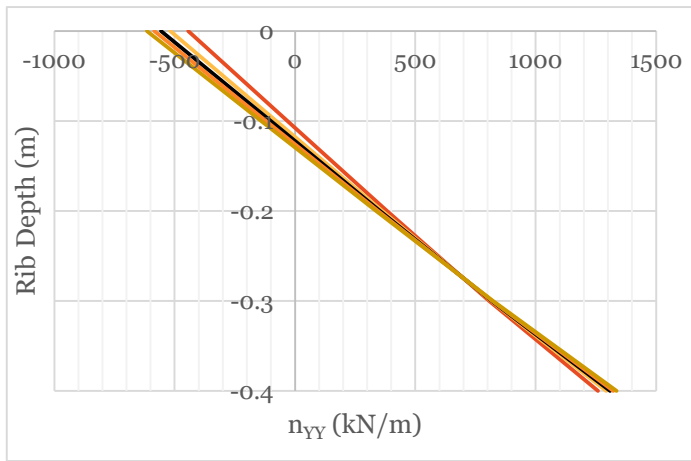
Figure 8-20: The Distributed Axial Forces n$_{YY}$ at (7.5m;5m) in the Rib Along y=5.0m for Varying Rib Thicknesses
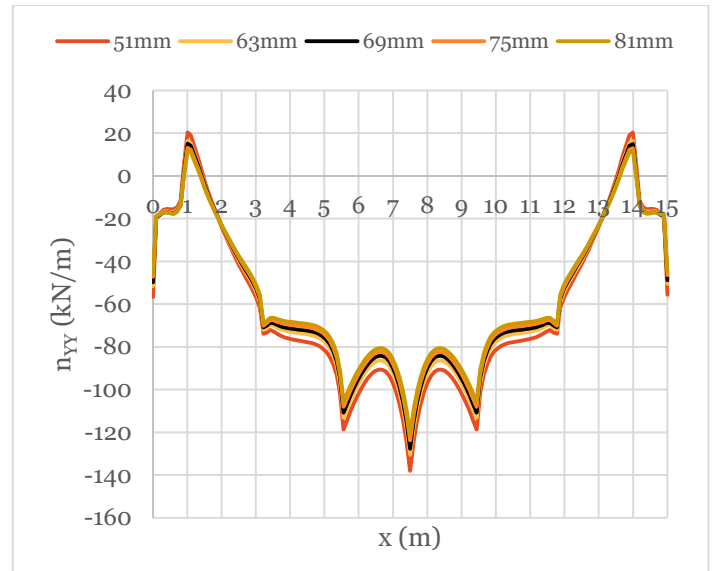
Figure 8-21: The Distributed Axial Forces n$_{YY}$ in the Deck Along y=7.5m for Varying Rib Thicknesses
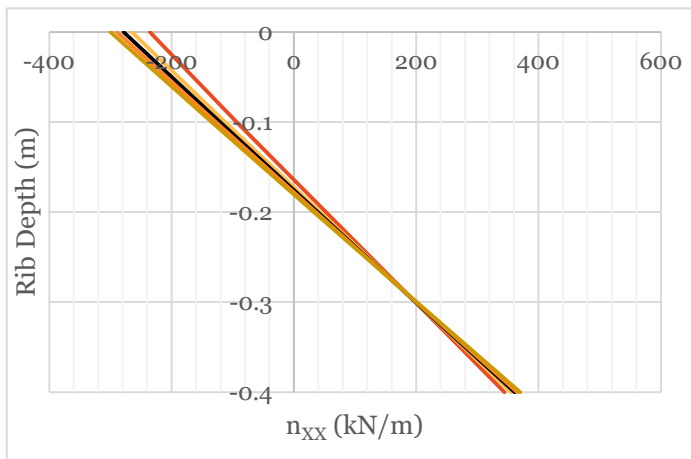
Figure 8-22: The Distributed Axial Forces n$_{XX}$ at (7.5m;5m) in the Rib Along x=7.5m for Varying Rib Thicknesses
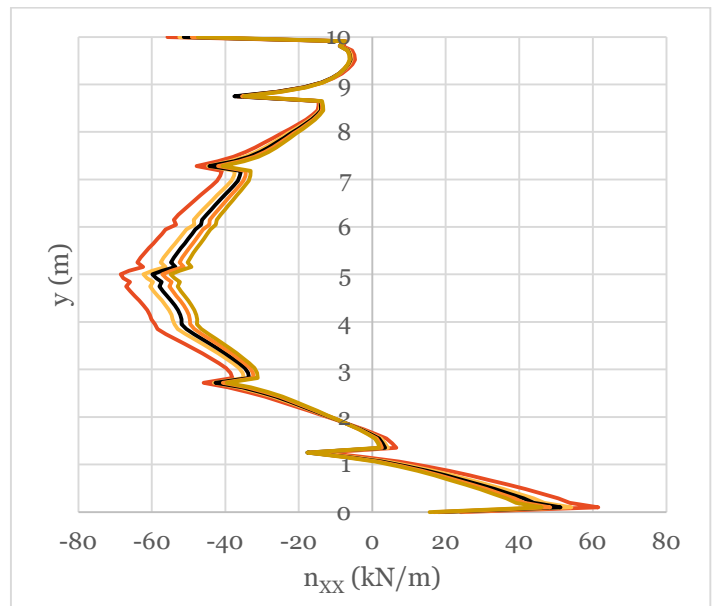
Figure 8-23: The Distributed Axial Forces n$_{XX}$ in the Deck Along x=5.0m for Varying Rib Thicknesses

8.5.3   Study 3: Secondary Load Transfer Mechanisms

In this study, the parameters' effects on the secondary transfer mechanisms are investigated. The secondary transfer mechanisms are the undesired load paths, which are any out-of-plane effects in the ribs, as ideally, the ribs would only take in-plane shear and normal forces. The maximum, minimum, mean, and median values for the distributed forces/moments in the ribs are given for three values of each of the design parameters. This data is produced in the same as was explained in Chapter 8.5.1.

Firstly, the effect of the deck thickness is shown in Table 8-7. The median values are the best measure for the average, as the mesh is evenly sized throughout the ribs, and the peak values will skew the mean. Increasing the deck thickness results in a significant reduction in the *average* values of v$_x$ and v$_y$. However, there is no correlation between the thickness of the deck and the *peak* shear forces. The same is true for distributed moments where the mean and

median values are reduced by increasing the deck thickness, but the maximum and minimum values do not correlate. Although, for the m_{yy} moments having a thin deck of 12mm causes very high peak values.

Table 8-7: The Distributed Forces and Moments in the Ribs for Varying Deck Thicknesses

Deck Thickness (mm)	n_{xx} (kN/m)			n_{yy} (kN/m)			n_{xy} (kN/m)			v_x (N/m)		
	12	24	50	12	24	50	12	24	50	12	24	50
Max.	16.7	16.5	18.9	1431.4	1308.4	1186.1	77.0	77.3	79.5	5546.0	4886.2	7390.5
Min.	-7.9	-8.5	-9.5	-815.3	-667.4	-669.2	-72.9	-68.6	-68.4	-5616.3	-5144.0	-8183.2
Mean	-1.0	-1.0	-0.9	78.2	99.5	114.9	18.0	17.5	16.9	172.7	117.4	125.7
Median	-0.7	-0.7	-0.6	52.4	61.5	69.8	13.9	13.8	13.1	32.8	13.2	6.0

Deck Thickness (mm)	v_y (N/m)			m_{xx} (Nm/m)			m_{yy} (Nm/m)			m_{xy} (Nm/m)		
	12	24	50	12	24	50	12	24	50	12	24	50
Max.	350.5	155.5	181.3	279.9	115.2	166.6	1246.6	340.3	213.6	220.2	98.4	111.3
Min.	-350.5	-155.3	-181.3	-279.6	-115.5	-104.5	-1222.2	-325.4	-404.9	-220.1	-95.0	-111.3
Mean	41.8	15.8	9.3	19.0	7.9	5.8	68.5	23.3	12.2	33.8	11.7	6.2
Median	24.8	9.4	5.0	9.1	4.0	2.4	23.5	11.1	7.1	22.0	7.2	2.9

Next, the effect of the rib thickness is shown in Table 8-8. There is a clear correlation between increasing the rib thickness and the absolute values of the peak out-of-plane distributed forces/moments. However, there is only a minor difference for the shear forces. The median and mean values also increase for increased rib thickness, but again this effect is less significant for the out-of-plane shear forces.

Table 8-8: The Distributed Forces and Moments in the Ribs for Varying Rib Thicknesses

Rib Thickness (mm)	n_{xx} (kN/m)			n_{yy} (kN/m)			n_{xy} (kN/m)			v_x (N/m)		
	51	69	81	51	69	81	51	69	81	51	69	81
Max.	17.8	16.5	15.9	1258.6	1308.4	1335.6	85.1	77.3	75.1	4475.8	4886.2	4894.1
Min.	-8.9	-8.5	-8.2	-625.3	-667.4	-666.0	-66.9	-68.6	-69.6	-4962.5	-5144.0	-5202.4
Mean	-0.9	-1.0	-1.0	180.3	99.5	95.1	17.3	17.5	17.6	84.2	117.4	138.6
Median	-0.6	-0.7	-0.7	110.5	61.5	61.6	13.7	13.8	13.9	10.7	13.2	14.3

Rib Thickness (mm)	v_y (N/m)			m_{xx} (Nm/m)			m_{yy} (Nm/m)			m_{xy} (Nm/m)		
	51	69	81	51	69	81	51	69	81	51	69	81
Max.	140.9	155.5	155.8	73.9	115.2	141.3	159.8	340.3	520.8	62.0	98.4	121.9
Min.	-140.9	-155.3	-155.8	-74.0	-115.5	-141.3	-169.4	-325.4	-473.6	-62.1	-95.0	-122.0
Mean	13.6	15.8	16.6	4.8	7.9	10.1	11.5	23.3	32.8	5.9	11.7	16.1
Median	8.0	9.4	10.0	2.3	4.0	5.2	5.9	11.1	15.0	3.4	7.2	10.2

Finally, the effect of the rib depth is shown in Table 8-9. Like the rib thickness, there is a correlation between the rib depth and peak out-of-plane distributed forces and moments, although in this case, it is a negative correlation. However, unlike the rib's thickness, changing the rib's depth does significantly affect the peak shear forces. There is also a negative correlation between the rib depth and the mean and median forces and moments.

Table 8-9: The Distributed Forces and Moments in the Ribs for Varying Rib Depths

	n_{xx} (kN/m)			n_{yy} (kN/m)			n_{xy} (kN/m)			v_x (N/m)		
Rib Depth (mm)	300	400	500	300	400	500	300	400	500	300	400	500
Max.	23.5	16.5	11.7	2196.4	1308.4	872.8	102.4	77.3	54.0	6958.4	4886.2	3508.9
Min.	-12.7	-8.5	-5.8	-1087.9	-667.4	-427.2	-122.3	-68.6	-49.8	-7615.0	-5144.0	-3736.5
Mean	-1.0	-1.0	-1.0	185.9	99.5	60.6	23.7	17.5	10.8	182.7	117.4	53.8
Median	-0.6	-0.7	-0.6	118.0	61.5	38.2	18.2	13.8	8.1	14.0	13.2	8.5

	v_y (N/m)			m_{xx} (Nm/m)			m_{yy} (Nm/m)			m_{xy} (Nm/m)		
Rib Depth (mm)	300	400	500	300	400	500	300	400	500	300	400	500
Max.	206.7	155.5	118.5	131.5	115.2	104.3	438.5	340.3	282.9	147.6	98.4	77.3
Min.	-206.6	-155.3	-119.2	-130.9	-115.5	-105.7	-476.0	-325.4	-285.2	-147.7	-95.0	-82.0
Mean	19.1	15.8	10.6	8.8	7.9	5.2	38.4	23.3	11.4	14.9	11.7	7.0
Median	12.1	9.4	5.8	4.0	4.0	2.1	18.6	11.1	5.1	9.2	7.2	3.9

8.6 Discussion and Conclusion

In conclusion, the models produced in this chapter can represent the structural system's behaviour and produce the required results. The model has been validated using a stepped development procedure, where a basic beam model was initially used, then a model with only the rib parts modelled as shell elements. Finally, the deck was added with additional shell elements.

In Chapter 7, it was found that significant changes were made in the principal stress trajectories when changing loading conditions from a constant UDL to a case where one half of the slab had a higher UDL. It was found in Section 8.5.1 that this does not result in higher forces in the rib or deck and the primary load case is dominant. However, the secondary load cases cannot be discounted entirely based on this result, as each force/moment was considered individually and the local combination of effects (e.g. the combination of compression and bending stresses) could produce a different result. A possible reason why the primary load case is dominant is that this case had the highest total load. Therefore, it may be that a secondary load case would alter the design if the difference in total load between the primary and secondary cases were smaller.

The primary load transfer mechanism of composite bending between the ribs and deck was investigated in section 8.5.2. It was found that increasing the deck thickness results in higher compression forces in the deck. Due to the increased isotropicity in the plywood with increased thickness, a more considerable change was observed in the weaker grain direction. Increasing the rib depth resulted in lower stresses in the ribs and the deck, which was equal in both directions. Changing the rib's thickness had only a minor effect compared to the other parameters, but it did result in an increased force in the ribs and a decreased force in the deck. These relations can be effectively used to create a slab design that balances the forces in each element. However, this is not the entire picture, as in the models, there was no consideration of connection stiffness, which will result in a redistribution of forces once included. However, this does serve a reasonable initial estimate of the effects.

In the third study, the secondary load transfer mechanisms in the rib were investigated. It was found that the most effective way of reducing the out-of-plane bending and shear effects in the ribs is to increase the rib height and decrease the rib thickness. Again, these effects should be considered in conjunction with the effects caused by the connections. Also, it should be noted that linear-elastic analysis has been performed and not buckling analysis. Therefore, as the ribs' slenderness is increased, buckling effects may become critical, although it is unlikely given that the compression flange is restrained for most the ribs, and the unrestrained lengths are small.

These findings will be used in the subsequent chapters, where the critical connections are analysed and designed.

9 DESIGN

9.1 Introduction

In Chapter 8, the isostatic slab's reaction to different load cases was investigated by creating a model of the entire system. Three design parameters (deck thickness, rib depth, and rib thickness) were also investigated. However, the system has yet to be designed. In this chapter two critical parts of the design will be determined; firstly, the rib elements must be connected to each other and to the deck, so the designs of these connections need to be made. Secondly, the deck and rib elements will be sized so that the peak stresses do not exceed the material's capacities.

As a starting point, the FE models created in Chapter 8 can be used as a basis for the maximum stresses. From this, the deck and ribs can be designed based on the ULS, and the required connection capacities can be calculated. Once the connections are designed, it is possible to calculate the stiffnesses.

Before beginning to design the connections, an assumption needs to be made about the connection design type. Looking at the geometry shown in Figure 8-2, four individual members need to be connected at each connection. A connection could be designed to achieve this (an example of this type of connection is shown in Figure 9-1) or the geometry could be altered so that at these connections there is always one continuous beam and two other beams which connect onto it. For this thesis, it was decided to follow the latter as this would result in a more straightforward and standard connection design, but it is equally valid to design a connection of the former case. On a real project, this choice will be determined by the needs of the stakeholders.

There are many moving parts to be solved to create a functional design. In this chapter, all of the essential information is first gathered, and then the decisions are made about the design parameters.
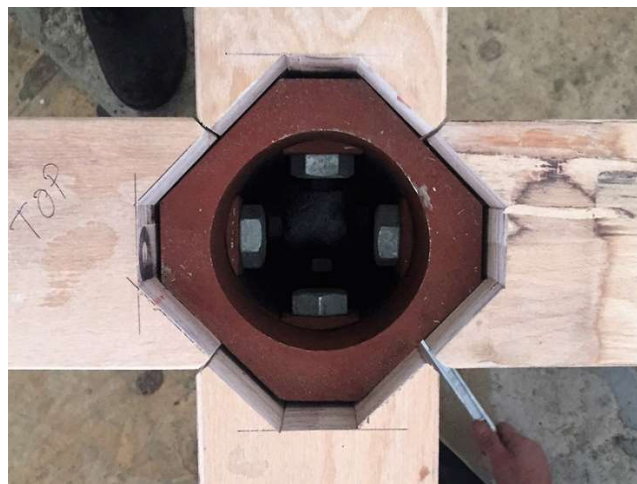
Figure 9-1: Peter Hall Performing Arts Centre - Connection of Four Individual Beams ©Price-Myers (TRADA, n.d.)

9.2 Methodology

The ribs' geometry must be altered to create a connection with one continuous beam and two discontinuous beams. Two of the four beams at each connection point are joined and straightened-out to form the continuous beam. This is a difficult problem to solve as moving the position of one connection affects the geometry of all the other connections around it. The Kangaroo 2 plugin for Grasshopper3D is used to solve this problem (Piker, 2017).

In the geometry shown in Figure 8-2, there are sets of ribs at the centre crossing in the x-direction separated by less than 200mm between their centrelines. This congestion in the centre is not feasible to manufacture. Therefore, the geometry will be modified to connect the outer ribs to the middle one.

The stress criteria in the ULS is investigated by first determining the minimum deck thickness required to resist the combined bending and axial effects. Then the required rib thickness of each rib depth option is calculated. For this, the FE models from Chapter 8 are used.

The manufacturing constraints are examined by determining what is possible to produce according to the LVL and Plywood manufacturers' standard product sizes.

As shown in Figure 9-2, there are four types of connections for the ribs. Only one of these will be designed to limit the scope, which is the dominant internal connection where one rib is continuous, and two ribs connect onto it. In addition to this, the connection between the rib and the deck will be designed.

The connection design is assessed by analysing the design of three crucial connections: the Rib-to-Deck Shear Connection, the Rib-to-Rib Moment Connection, and the Rib-to-Rib Shear Connection. The Rib-to-Deck Shear Connection covers the design of the fasteners that attach the deck to the ribs and create composite action. The Rib-to-Rib Connection is split into two parts: the plates and fasteners that carry moment forces predominately, and the plates and fasteners that carry predominately shear forces. This is done in two parts as the connections with the largest moment forces have minimal shear forces, and vice versa.
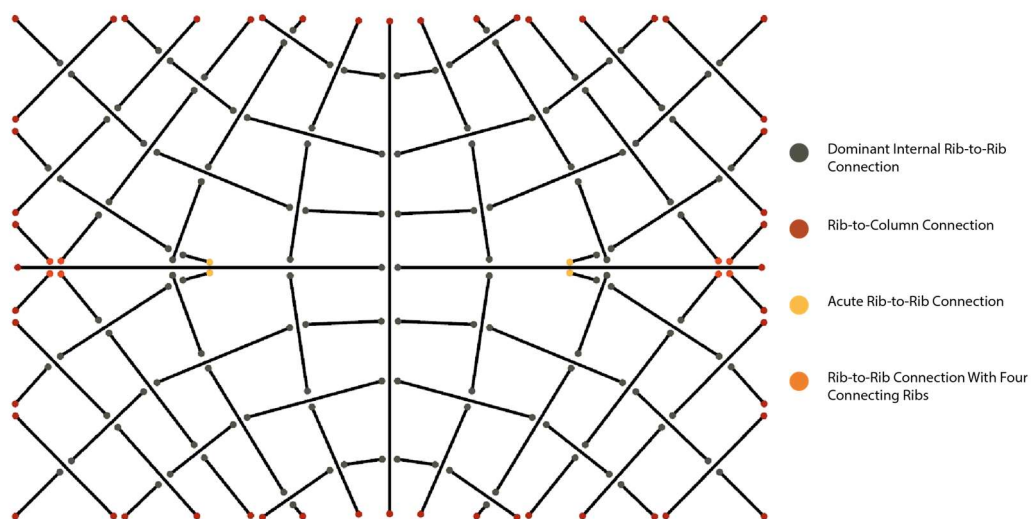
Figure 9-2: Rib Connection Types Shown as a Beam Layout Diagram with Different Coloured Ends for Each Connection Type

The connections are designed by assuming that the ribs are orthogonal to each other to simplify the design process. This step is taken purely for the basis of the calculations. The connection designs created can also be applied to all of the 'dominant internal rib-to-rib connections'.

All this information is combined to finalise the deck's thickness and the rib's thickness and depth. A final model of the entire slab is created with the finalised design parameters and centreline geometry. A final connection design for the three connections is then completed. Also using this model, the SLS is analysed and verified.

9.3 Centreline Geometry

The centreline geometry shown in Figure 8-2 needs to be modified before it is usable in the design. The start with the ribs needs to be "straightened out" so that there is at least one continuous beam at each connection. The Kangaroo 2 plugin for grasshopper is used to create this geometry (Piker, 2017). Kangaroo 2 works by the user specifying a list of goals (for example, moving point A to position B or increasing shape A's area) the software then tries to achieve all the different goals that the user has set. However, it is often the case that not all of the goals can be achieved.

An excellent example of this is setting two goals for a shape: minimise the perimeter and maintain the area; the edges of the shape can be distorted and deformed in any manner of ways. In this example, the perimeter can never be entirely reduced to zero as it would violate the area goal. (The solution for this is a circle; however, the solution becomes harder to grasp as more goals are added.) Kangaroo 2 allows the user to assign a strength to each goal, which sets the priority. As Kangroo2 is a physics-based solver, each of the goals results in applying a force onto the particles (vertices) that make up the model. The solver calculates all the resultant force on each particle and then gives each particle a velocity in that direction and moves them by a single time step and repeats the process. The solver finishes once the change in each time step is below the set tolerance. The goals' strengths act as multipliers to the forces thereby allowing different priorities.
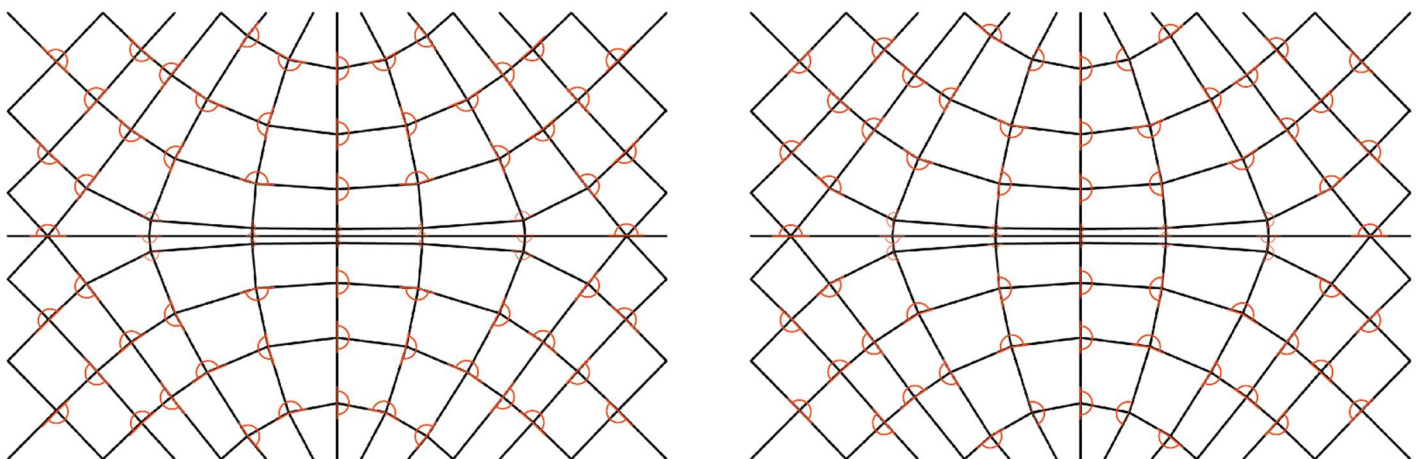
Figure 9-3: Angle Goal Locations and Orientations. Left: Option A, Right: Option B. The arcs indicate which ribs are continuous.

Two key goals are needed to create a centreline geometry where each connection has at least one continuous member: the "angle" goal and the "anchor" goal. The angle goal aims to make the angle between two lines equal to 180° by applying forces the endpoints of the lines; this is

used to straighten out some of the ribs. The anchor goal aims to keep a point in the same position by applying a force to return the point to the anchor, this is used to maintain the connections' locations.

Figure 9-3 shows the locations of the angle goals for two different layout options. In both cases, the ribs which pass vertically through the slab's centre are made into one member. The ribs which pass horizontally through the centre are made into two members, broken by the vertical rib. This is done as these two ribs are already straight. The rest of the rib segments are joined in alternating pairs. Two sets of anchor goals are used; the first is applied to all the perimeter vertices and given a strength of 10000 so that the edge connections cannot move, the second set of anchors is applied to the internal connections and is given a variable strength.

The design aim is to make the connected rib segments straight while minimising the connections' movement. To start with the angle goal strength is set to 50, and the anchor goal strength is set to 1. The angle of the lines that should be straight is measured and outputted. Then the strength of the anchor goal is increased by increments of one (as the anchor goal's strength is increased the connections are pulled back toward their original position) until any subsequent increase would result in an angle in a straight rib of >177°. This is done as in reality, the connections cannot be positioned precisely, and members are not entirely straight, so the 3° deviation is taken as acceptable within the tolerance limits. Also, a limit needs to be set on the straightness due to the competing goals used in this method, as the only way to create completely straight ribs is to remove the anchor goals but this results in the connection locations moving wildly. The initial 50:1 strength ratio is chosen based on preliminary testing as it had an appropriate balance between the two goals.

Figure 9-4: Kangaroo 2 Script in Grasshopper

Figure 9-5: The Rib Geometries Where Every Connection Has One Continuous Rib; Left – Option A, Right – Option B

Figure 9-6: The Rib Geometry with Reduced Congestion

Figure 9-5 shows the two solved geometries, both are valid designs, and there are only subtle differences between them. Option B is chosen as the preferred geometry based solely on aesthetic appeal as the differences between them are so minor.

Finally, to create a manufacturable geometry, the congestion of ribs at the slab's centre needs to be removed. Two more connections are created to connect the two external lines of ribs which cross the centre of the slab horizontally to the middle ribs. Figure 9-6 shows the ribs with the two additional connections. The connections have been placed at the midpoints of the continuous ribs. Figure 9-7 gives the connection coordinates of the final centreline geometry.
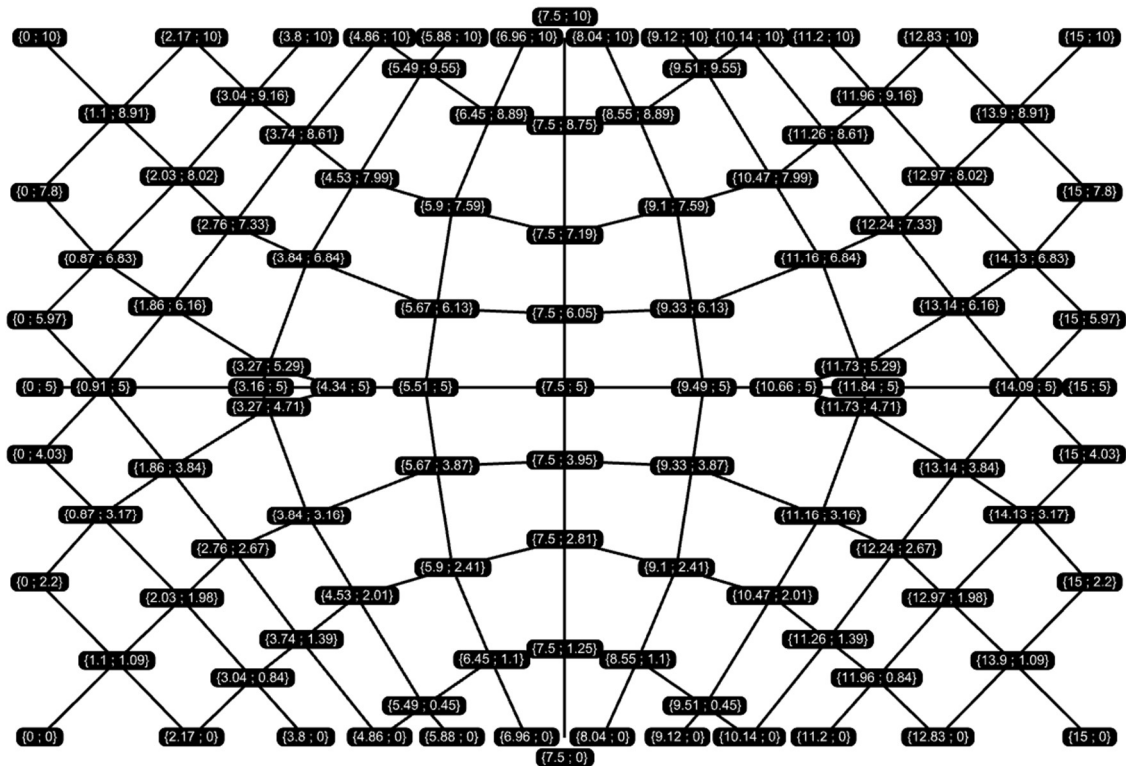
Figure 9-7: The Connection Coordinates of the Rib Centreline Geometry

9.4 Ultimate Limit State Design

In timber design, the overall design is often dependent on the connections due to the fasteners' requirements. However, it is still worth knowing what cross-sectional properties

are required based solely on stress considerations. Therefore, in this section, the minimum section properties required will be calculated from the FE models created in Chapter 8.

9.4.1 The Plywood Deck in Combined Bending and Axial Tension/Compression

The required deck thickness can be determined by looking at the combined axial and bending effects in each direction. For this equation 6.17 and 6.19 from EN 1995-1-1 are used:

$$\frac{\sigma_{t,0,d}}{f_{t,0,d}} + \frac{\sigma_{m,y,d}}{f_{m,y,d}} + k_m \frac{\sigma_{m,z,d}}{f_{m,z,d}} \leq 1 \quad Eq.\,9.1$$

$$\left(\frac{\sigma_{c,0,d}}{f_{c,0,d}}\right)^2 + \frac{\sigma_{m,y,d}}{f_{m,y,d}} + k_m \frac{\sigma_{m,z,d}}{f_{m,z,d}} \leq 1 \quad Eq.\,9.2$$

Eq. 9.1 is used for combined bending and axial tension and Eq. 9.2 is used for combined bending and axial compression. The plywood's strength properties are given in Table 9-1, where '‖' denotes the properties in the direction of the primary axis and '⊥' denotes the perpendicular axis. As the two directions are orthogonal, it is assumed that each direction has an independent stress state. Eq. 9.1 and Eq. 9.2 can be modified into Eq.9.3 to Eq. 9.6 for the two directions.

$$\frac{\sigma_{t,‖,d}}{f_{t,‖,d}} + \frac{\sigma_{m,‖,d}}{f_{m,‖,d}} \leq 1 \quad Eq.\,9.3$$

$$\left(\frac{\sigma_{c,‖,d}}{f_{c,‖,d}}\right)^2 + \frac{\sigma_{m,‖,d}}{f_{m,‖,d}} \leq 1 \quad Eq.\,9.4$$

$$\frac{\sigma_{t,⊥,d}}{f_{t,⊥,d}} + \frac{\sigma_{m,⊥,d}}{f_{m,⊥,d}} \leq 1 \quad Eq.\,9.5$$

$$\left(\frac{\sigma_{c,⊥,d}}{f_{c,⊥,d}}\right)^2 + \frac{\sigma_{m,⊥,d}}{f_{m,⊥,d}} \leq 1 \quad Eq.\,9.6$$

The design strengths are calculated from the characteristic strengths by equation 2.14 from EN 1995-1-1:

$$X_d = k_{mod} \frac{X_k}{\gamma_m} \quad Eq.\,9.7$$

For plywood γ_m is given as 1.2, and k_{mod} is 0.9 for short term loading and service class 1 or 2 (it is assumed that the critical load case is when short term loading occurs).

For every point in the slab, the utilisation values in both directions for combined bending and axial forces can be calculated. Apply this to the results from the FE model with a 12mm deck and 69x400mm ribs gives utilisations of: $U.C_{‖} = 65.8\%$ and $U.C_{⊥} = 57.4\%$. When a 24mm deck is used the utilisations are: $U.C_{‖} = 18.2\%$ and $U.C_{⊥} = 15.3\%$. Therefore, the deck has an extremely low utilisation for combined bending and axial forces, even when a thin thickness of 12mm is used. It is unlikely however that a 12mm deck would not resist buckling effects.

Plywood Thickness (mm)

	12	18	21	24	30	35	40	45	50
$f_{m,\parallel,k}(N/mm^2)$	42.9	40.2	39.4	38.9	38.4	37.6	37.2	37.0	36.8
$f_{c,\parallel,k}(N/mm^2)$	27.7	27.2	27.0	26.9	26.7	26.6	26.5	25.6	26.4
$f_{t,\parallel,k}(N/mm^2)$	40.0	39.2	39.0	38.8	38.5	28.4	38.3	37.0	38.1
$f_{m,\perp,k}(N/mm^2)$	33.2	34.1	34.3	34.4	34.6	34.7	34.7	34.8	34.8
$f_{c,\perp,k}(N/mm^2)$	24.3	24.8	25.0	25.1	25.3	25.4	25.5	26.4	25.6
$f_{t,\perp,k}(N/mm^2)$	35.0	35.8	36.0	36.2	36.5	36.6	36.8	38.0	36.9

9.4.2 The LVL Ribs in Bending

The ribs' capacity depends on the peak tensile force in the bottom fibre of the ribs from bending. The stress at this location is found from the FE models of Chapter 8. The utilisation for bending is given by equation 6.11 from EN 1995-1-1:

$$\frac{\sigma_{m,y,d}}{f_{m,y,d}} + k_m \frac{\sigma_{m,z,d}}{f_{m,z,d}} \leq 1 \quad Eq.\,9.8$$

Where in Eq. 9.8 $\sigma_{m,y,d}$ is the tension stress caused by bending and $\sigma_{m,z,d}$ is assumed to be zero as stress from minor axis bending is ~ 4% of the stress from major axis bending. $f_{m,y,k}$ for Kerto-S LVL produced by MestäWood is 44.0 N/mm² (Eurofins, 2020). Eq. 9.7 is also applicable here, where γ_m and k_{mod} are the same for LVL.

For the following calculations, it is assumed that the rib thickness does not impact the force distribution; this allows for a simplified calculation of the rib thickness required for each of the rib depths tested in Chapter 8. Therefore, $Rib\ Thickness \geq Tensile\ Force/f_{m,y,d}$. Table 9-2 gives the required rib thickness for each rib depth.

Table 9-2: Required Rib Thicknesses for the ULS per the Rib's Depth

Rip Depth	Peak Distributed Tensile Force	Required Rib Thickness
300 mm	2196kN/m	≥67mm
400 mm	1308kN/m	≥40mm
500 mm	873kN/m	≥27mm

9.5 Manufacturing Constraints

LVL and plywood are manufactured on production lines, so they have standard sizes and measurements. Therefore, these constrain the range of design options that would otherwise be possible. Metsä Wood has been selected as the manufacturer for the LVL and plywood.

Mestä Wood produces two plywood products: spruce plywood and Birch Plywood. The birch plywood has been selected as it is stronger and has more homogenous properties (for bending of a 24mm thick sheet the stiffness in the perpendicular direction of spruce plywood is ~46% of the parallel stiffness, which is compared to ~78% in the birch plywood). For the plywood, Mestä Wood produces sheets of 1200-2020mm widths and lengths of 2020-4110mm (Metsä Wood, 2020). The most critical dimension is the thickness of the sheets, as this has an enormous impact on the force distribution. Figure 9-8 is an extract from the datasheet of the birch plywood showing the available thicknesses.

For the LVL, the Kerto LVL S-beam product is used. For this product, all the veneers are orientated with the grain in the same direction. Metsa Wood produces the LVL with specific thicknesses and heights, where the height is the dimension perpendicular to the grain and parallel to the veneers. Table 9-3 shows which combinations of thickness and height are produced in the standard sizes.

THICKNESSES, STRUCTURES AND THICKNESS TOLERANCES
OF THE PANELS*

NOMINAL THICKNESS	NUMBER OF PLIES	THICKNESS TOLERANCE		WEIGHT
(mm)	(pcs)	min. (mm)	max. (mm)	kg/m²
6.5	5	6.1	6.9	4.4
9	7	8,8	9.5	6.1
12	9	11.5	12.5	8.2
15	11	14.3	15.3	10.2
18	13	17.1	18.1	12.2
21	15	20.0	20.9	14.3
24	17	22.9	23.7	16.3
27	19	25.2	26.8	18.4
30	21	28.1	29.9	20.4
35	25	33.5	35.5	23.8
40	29	38.8	41.2	27.2
45	32	43.6	46.4	30.6
50	35	48.5	51.5	34.0

* Moisture content of the product affects its dimensions
* Average density of Metsä Wood birch plywood is 680 kg/m³ (at relative humidity of RH 65%)
* Special structures and thicknesses are available on request
* Customised tolerances are possible but must be agreed separately

Figure 9-8: An Extract from the Data Sheet of the Birch Plywood Produced by Metsa Wood Showing the Thickness Specifications (Metsä Wood, 2020)

Table 9-3:Standard Sizes of Kerto Products- 'X' Marks Available Dimensions (Eurofins, 2020)

Product[1]	Thickness mm	Width / height (mm)								
		200	225	260	300	360	400	450	500	600
S/Q	27	X	X							
S/Q	33	X	X	X						
S/Q	39	X	X	X	X					
S/Q	45	X	X	X	X	X				
S/Q	51	X	X	X	X	X	X			
S/Q	57	X	X	X	X	X	X	X		
S/Q	63	X	X	X	X	X	X	X	X	
S/Q	69	X	X	X	X	X	X	X	X	X
S/Q	75	X	X	X	X	X	X	X	X	X
S	81	X	X	X	X	X	X	X	X	X
S	90	X	X	X	X	X	X	X	X	X

9.6 Connection Design: Rib-to-Deck Shear Connection

For the deck and the rib to act compositely, they need to be connected to transfer the shear forces. The shear force acts continuously along the LVL's top edge, so the connection force is distributed and in the form of kN/m. The peak shear force can be easily outputted from the Chapter 8 FE models. In this section, a rough initial design of the connection will be made by designing the connection for the peak shear force from the 'basic situation' model from Chapter 8.

Figure 9-9 shows a sketch of the connection design. The peak distributed shear force is 63.0 kN/m (see Figure 9-10) which is transferred through the mechanism shown in Figure 9-11. The strength of the connection can be altered by changing the distance between the screws, the diameter of screws, the length of the screws into the LVL, or the plywood's thickness. The connection can be design as a timber-to-timber single shear connection according to the rules given in EN 1995-1-1. The screws are chosen as Rotho Blass self-tapping screws as there is a European Technical Assessment (ETA) for these screws (ETA-Danmark, 2019) which gives in-depth supplementary rules
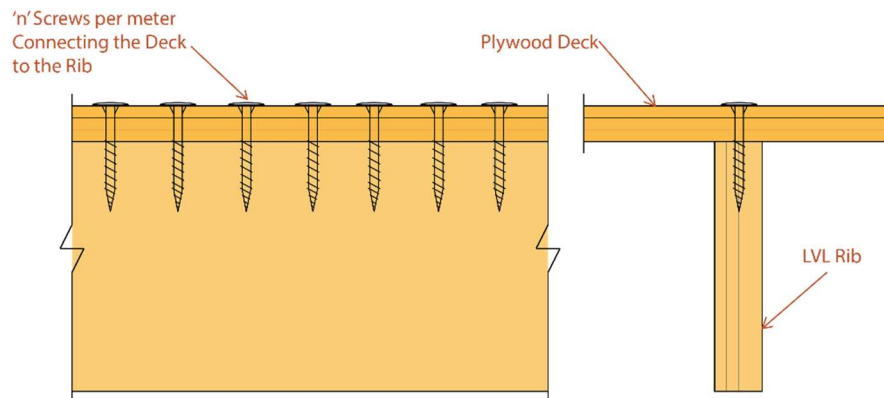
Figure 9-9: Cross-Sectional Sketches of the Rib-to-Deck Shear Connection

Figure 9-11: Shear Force Transfer Through the Rib-to-Deck Connection

Figure 9-10: Rib-to-Deck Shear Connection Peak Force Location. Load Case = Full ULS

The joint's resistance capacity can be made up of two parts, depending on the failure mode. The main component is the contribution from the Johansen yield theory, which results from bearing onto the timber and the bending resistance of the screws. The secondary component is the so-called "rope effect" that arises from the axial resistance of the screws. For screwed

connections, the rope effect can have a significant effect. There are two types of screws that can be used in this joint: partially threaded screws or fully threaded screws. The differences between these types do not affect the Johansen component but do affect the rope effect. For the fully threaded screws, the axial force is partly resisted in the plywood by the withdrawal capacity from the thread biting into the panel. In the partially threaded screws, there is no thread connecting the plywood to the screw, so the axial force must be resisted by the screw head bearing onto the plywood's top surface. The partially threaded screws are chosen for this connection because there is no information available about the axial withdrawal capacity for plywood, so it is impossible to design the fully threaded screws.

The characteristic shear capacity for the connection is given by equation 8.6 in EN 1995-1-1:

$$
F_{v,Rk} = \min \begin{cases}
f_{h,1,k} t_1 d & \text{(a)} \\
f_{h,2,k} t_2 d & \text{(b)} \\
\dfrac{f_{h,1,k} t_1 d}{1+\beta}\left[\sqrt{\beta+2\beta^2\left[1+\dfrac{t_2}{t_1}+\left(\dfrac{t_2}{t_1}\right)^2\right]+\beta^3\left(\dfrac{t_2}{t_1}\right)^2}-\beta\left(1+\dfrac{t_2}{t_1}\right)\right]+\dfrac{F_{ax,Rk}}{4} & \text{(c)} \\
1,05\dfrac{f_{h,1,k} t_1 d}{2+\beta}\left[\sqrt{2\beta(1+\beta)+\dfrac{4\beta(2+\beta)M_{y,Rk}}{f_{h,1,k} d\ t_1^2}}-\beta\right]+\dfrac{F_{ax,Rk}}{4} & \text{(d)} \\
1,05\dfrac{f_{h,1,k} t_2 d}{1+2\beta}\left[\sqrt{2\beta^2(1+\beta)+\dfrac{4\beta(1+2\beta)M_{y,Rk}}{f_{h,1,k} d\ t_2^2}}-\beta\right]+\dfrac{F_{ax,Rk}}{4} & \text{(e)} \\
1,15\sqrt{\dfrac{2\beta}{1+\beta}}\sqrt{2M_{y,Rk} f_{h,1,k} d}+\dfrac{F_{ax,Rk}}{4} & \text{(f)}
\end{cases}
\qquad Eq.\,9.9
$$
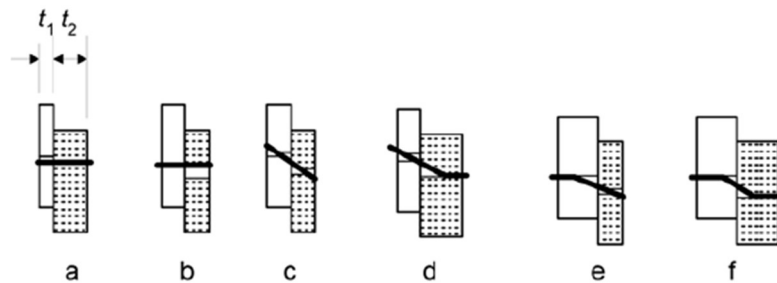
Figure 9-12: The Failure Modes of Timber-to-Timber Single Shear Connections (EN 1995-1-1)

Where (a) to (f) represent the different failure modes shown in Figure 9-12. $f_{h,i,k}$ is the embedment strength in member i, $M_{y,Rk}$ is the fastener yield moment, $F_{ax,Rk}$ is the axial withdrawal capacity, d is the fastener diameter, and β is $\frac{f_{h,2,k}}{f_{h,1,k}}$. Also, for this connection, t_2 is the penetration length of the screw in the LVL panel.

Table 9-4 shows the available diameters for partially threaded screws from Rotho Blaas. It also gives the minimum thickness of LVL required to prevent splitting, assuming that the holes are pre-drilled.

The plywood's embedment strength can be found using EN 1995-1-1 which gives Eq 9.10 when assuming d>6mm. α is the angle between the grain direction and the force, and is taken as 90° to give the worst-case scenario. ρ_k for the plywood is 630kg/m³.

Table 9-4: Partially Threaded Screw Properties (ETA-Danmark, 2019)

Outer Thread Diameter - d (mm)	Characteristic Tensile Strength - $f_{tens,k}$	Characteristic Yield Bending Moment - $M_{y,Rk}$	Head Diameter/s - d_h (mm)	Minimum LVL Thickness
3.0	2.8 kN	1.4 Nm	6.0	18 mm
3.5	3.8 kN	2.1 Nm	7.0	21 mm
4.0	5.0 kN	3.0 Nm	7.7, 8.0	24 mm
4.5	6.4 kN	4.1 Nm	8.7, 9.0	27 mm
5.0	7.9 kN	5.4 Nm	9.65, 10.0	30 mm
6.0	11.3 kN	9.5 Nm	12.0, 15.5	36 mm
8.0	20.1 kN	20.1 Nm	14.5, 19.0, 22.0, 24.5	48 mm
10.0	31.4 kN	35.8 Nm	18.25, 25	60 mm
12.0	33.9 kN	48.0 Nm	20.75	72 mm

$$f_{h,\alpha,k} = \frac{0.082(1 - 0.01d)\rho_k}{(1.35 + 0.015d)sin^2\alpha + cos^2\alpha} \ [N/mm^2] \quad Eq.\,9.10$$

The LVL embedment strength is found from the Rotho Blaas ETA (ETA-Danmark, 2019). Eq 9.11 applies to softwood LVL with pre-drilled holes. β is the angle between the screw axis and the LVL's wide face, which for this connection is 0°.

$$f_{h,\alpha,k} = \frac{0.082(1 - 0.01d)\rho_k}{(2.5 * cos^2\alpha + sin^2\alpha)(1.5 * cos^2\beta + sin^2\beta)}[N/mm^2] \quad Eq.\,9.11$$

The axial capacity is taken as the minimum value of the following failure modes:

- The withdrawal of the threaded part of the screw from the LVL.
- Pull-through failure of the screw head.
- Tensile failure of the screw.

The withdrawal capacity in the LVL is given by the Rotho Blaas ETA which provides Eq. 9.12 where n_{ef} is taken as 1 when analysing the rope effects, k_{ax} is 1, $f_{ax,k}$ is 29.0 kN/mm² and ρ_a is 730kg/m³ when pre-drilled holes are used, l_{ef} is the penetration length of the threaded part of the screw, and k_β is given by Eq. 9.13. ρ_k is 480kg/m³ for the LVL.

$$F_{ax,\alpha,Rk} = \frac{n_{ef} \cdot k_{ax} \cdot f_{ax,k} \cdot d \cdot l_{ef}}{k_\beta}\left(\frac{\rho_k}{\rho_a}\right)^{0.8} [N] \quad Eq.\,9.12$$

$$k_\beta = 1.5 * cos^2\beta + sin^2\beta \quad Eq.\,9.13$$

The head pull-through capacity for wood-based panels is also given in the Rotho Blass ETA, shown in Eq. 9.13. n_{ef} is 1, $f_{ax,k}$ is 10.5 N/mm² for most screws expect when d=8mm and d_h =24.5mm in which case $f_{ax,k}$ is 15 N/mm². d_h is the outer diameter of the screw head, and ρ_a is 350kg/m³. Eq. 9.13 only applies to timber panels with a minimum thickness of 20mm.

$$F_{ax,\alpha,Rk} = n_{ef} \cdot f_{head,k} \cdot d_h^2 \left(\frac{\rho_k}{\rho_a}\right)^{0.8} \ [N] \quad Eq. \ 9.13$$

The tensile capacities of the screws are given in Table 9-4. Therefore, $F_{ax,Rk}$ can be calculated as the minimum of these three values.

The characteristic capacity per screw needs to be modified by Eq. 9.7 to find the design capacity per meter length, where γ_m is 1.3 for connections. The number of screws per meter needs to be chosen (n), and then n$_{ef}$ is calculated from this using Eq. 9.14 where a_1 is the distance between screws. Finally, the design capacity of the connections is found by multiplying the design capacity per screw by n_{ef}.

$$n_{ef} = min \begin{cases} n \\ n^{0.9} \cdot \sqrt[4]{\dfrac{a_1}{13d}} \end{cases} \ [m^{-1}] \quad Eq. \ 9.13$$

The slip modulus per fastener is given in Table 7.1 of EN 1995-1-1. Eq 9.14 can be used to calculate the connection stiffness per meter length.

$$K_{connection} = n \cdot \frac{\rho_m^{1.5} \cdot d}{23} \ [N/mm/m] \quad Eq. \ 9.14$$

Finally, all of this can be combined to design the connection. Table 9-5 shows the number of screws required to fulfil the ULS design of the connection for different deck thicknesses and screw outer thread diameters. The penetration depth into the LVL is set to 200mm, so that failure modes (d) and (f) occur in place of (c) and (e). Also, the largest available head diameter is used for each screw, as the head pull-through capacity is always critical for the rope effect. Only outer thread diameters larger than 6mm have been used to simplify the problem, as at 6mm and below some of the equations will change. Note that a design for every combination of parameters cannot be produced (see the '*' next to the screw diameters), as the screws would need to be placed too close together. Thus, it is impossible to create the joint with a deck thickness of 21mm, and only 8mm screws satisfy the 24mm deck. Generally, using 10mm and 12mm screws results in more screws being required due to the effective number of fasteners and because when using 8mm screws a larger $f_{ax,k}$ can be used. For this reason, 8mm screws will be used in this connection design.

Deck thicknesses of 40mm and 50mm provide no additional benefit over the 35mm deck for 8mm screws; moving from a 30mm to 35mm deck only reduces the screws per meter slightly, so the 35mm deck also does not provide an immense benefit. Therefore, the choice of deck thickness is between 24mm and 30mm.

This gives the following choices: a 24mm deck with 27x8⌀ screws has a connection stiffness of 134kN/mm/m and a 30mm deck with 23x8⌀ screws has a connection stiffness of 114kN/mm/m.

Table 9-5: Rib-to-Deck Shear Joint – Design Options

Deck Thickness	Screw Diameter	Screws per m	Utilisation	Failure Mode	$K_{connection}$ (kN/mm/m)
21	**8***	33	98.1%	(a)	164
	10*	29	98.6%	(d)	180
	12*	31	99.3%	(d)	231
24	**8**	27	97.8%	(a)	134
	10*	28	98.2%	(d)	174
	12*	30	98.5%	(d)	223
30	**8**	23	99.2%	(d)	114
	10	25	99.3%	(d)	155
	12*	27	98.7%	(d)	201
35	**8**	22	98.6%	(f)	109
	10	23	99.3%	(d)	143
	12*	25	97.7%	(d)	186
40	**8**	22	98.6%	(f)	109
	10	21	99.6%	(d)	130
	12*	22	99.8%	(d)	164
50	**8**	22	98.6%	(f)	109
	10	21	98.6%	(f)	130
	12*	21	97.6%	(f)	157

* This arrangement does not fulfil the minimum spacing requirement between screws in the LVL of $a_1 = (4 + 3|cos\alpha|)d \ [mm]$ (Eurofins, 2020)

9.7 Connection Design: Rib-to-Rib Moment Joint

The rib-to-rib connections need to carry both moment and shear; however, they will be separated into two separate components. In a typical timber moment carrying connection, a bolt group carries the forces from the applied moment and the applied shear. In the isostatic slab, the deck already transfers a large proportion of the bending moment between the ribs and can also connect the ribs together. This means that to achieve a moment connection an additional load transfer mechanism only needs to be added to the ribs' bottom to carry the tension force (this will be a compression force in a connection transferring a hogging moment).

For this initial design, the location of the peak bending moment is used to design the connection. Also, the connection is assumed to be orthogonal to simplify the load transfer. Although the connection is designed so that it can be applied to the required geometries.

Figure 9-13 shows a sketch of the connection design. For a sagging moment, the deck transfers a compression force across the ribs, and the steel plate transfers a tension force. The compression force is in the deck due to the rib-to-deck shear joints. However, at the connection, the compression force reduces in the deck as the lever arm increases. Shear forces need to be transferred between the deck and rib so that the compression force be reduced. Laterally loaded single plane shear screws are used to the same specifications as the rib-to-deck shear connection.

The tension force is transferred into the steel plate by the inclined axially loaded screws. For the hogging connections these screws will need to be vertical so that the screws are not compressed, but this should not be an issue as the force's magnitude in hogging connections is ~20% of the peak sagging force.
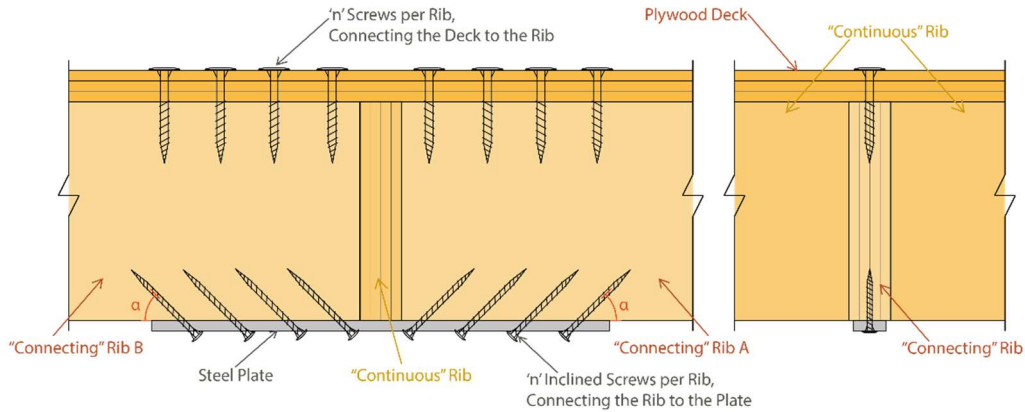
Figure 9-13: Cross-Sectional Sketches of the Rib-to-Deck Shear Connection
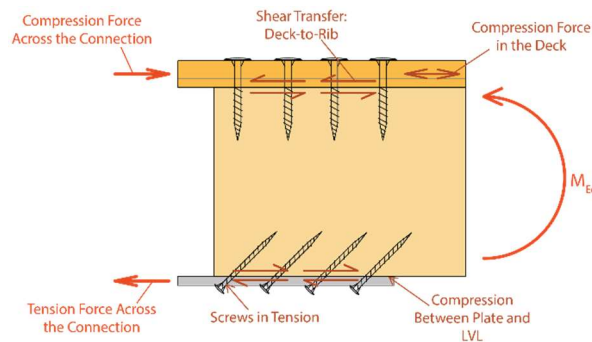
Figure 9-14: Force Transfer Through the Rib-to-Rib Moment Connection
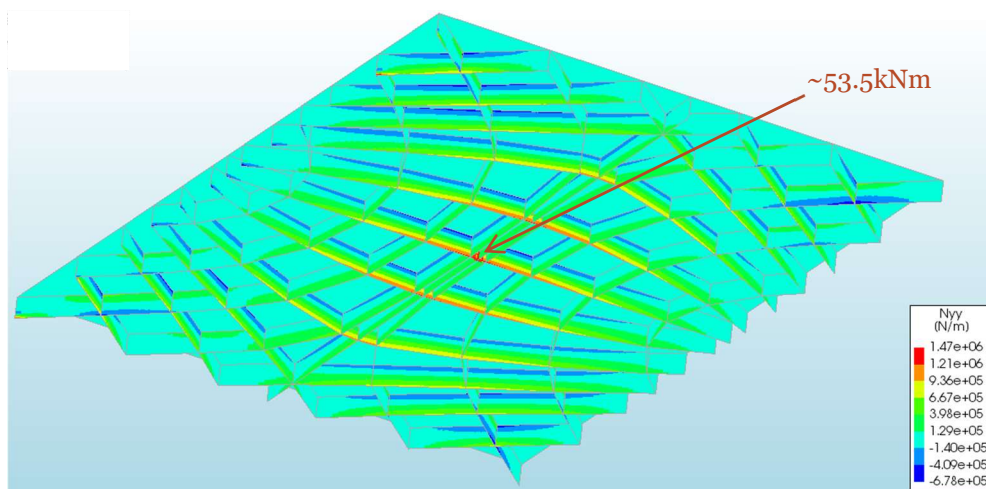
Figure 9-15: Location of Peak Internal Bending Moment. The Gradient Plot Shows the Distributed Axial Force in the Ribs

The peak moment is calculated by taking the sum of the moments acting about the deck; this eliminates the deck's axial force and simplifies the calculations. The force through the steel plate and deck can be calculated by dividing the moment by the lever arm (i.e. the distance between the steel plate's and the deck's centrelines). In this calculation, the stress is assumed to be constant through the deck's and the plate's depths. The force through the steel plate is also the shear force the screws must transfer. The shear force transferred between the deck and the ribs is the difference between the compression force found in the deck with no connection and the compression force carried across the connection. The compression force in the deck with no connection can be found by taking the sum of the ribs' horizontal forces. Figure 9-14 shows the forces through the joints.

Table 9-6 gives the connection forces for three different rib depths (see Figure 9-15 for the location of the peak bending moment). In the FE models, the rib thickness is 69mm, and the deck thickness is 24mm. The lever arm is calculated by assuming that the steel plate is 10mm thick.

Table 9-6: Rib-to-Rib Moment Connection Forces

Rib Depth (mm)	Peak Moment (kNm)	Lever Arm (mm)	Compression Force in the Deck	Tension / Compression Force Across the Connection	Shear Transfer: Deck-to-Rib
300	53.06	317	205.0 kN	167.4 kN	37.6 kN
400	53.48	417	144.5 kN	128.2 kN	16.3 kN
500	53.76	517	109.0 kN	104.0 kN	5.0 kN

9.7.1 Steel Plate: Shear Transfer

The shear force is transferred from the rib to the steel plate through tension in the inclined screws and bearing of the rib onto the plate (it is assumed that the screws are subjected to exclusively axial force). The force component along the screw axis is found by Eq. 9.15, where V_{Ed} is the shear force and α is the angle been the screw axis and the grain.

$$F_{ax,Ed} = \frac{V_{Ed}}{cos\alpha} \quad [kN] \quad Eq.\,9.15$$

There are three failure modes for the screws:

- The withdrawal of the threaded part of the screw from the LVL.
- Tear-off failure of the screw head.
- Tensile failure of the screw.

Firstly, it is assumed that the tensile failure of the screw of countersunk Rotho Blaas screws is smaller than the tear-off failure of the screw head. The axial withdrawal capacity of the screws is given by Eq. 9.12, where for this connection k_{ax} is 1 for 45°≤α≤90° or as Eq. 9.16 for 0°≤α<45°. The effective number of screws (n_{ef}) is given by Eq. 9.17 (ETA-Danmark, 2019). Eq. 9.17 is limited to applications of 30°≤α≤60°. The penetration length of the threaded part of the screws (l_{ef}) is the distance between the screw tip and the edge of the rib.

$$k_{ax} = 0.5 + 0.5 \cdot \frac{\alpha}{45°} \quad Eq.\,9.16$$

Outer Thread Diameter - d	Characteristic Tensile Strength - $f_{tens,k}$	Minimum Thread Length	Maximum Thread Length	Required Penetration Depth	Required LVL Thickness
7.0 mm	15.4 kN	50 mm	390 mm	>42 mm	>45 mm
9.0 mm	25.4 kN	90 mm	510 mm	>54 mm	>57 mm
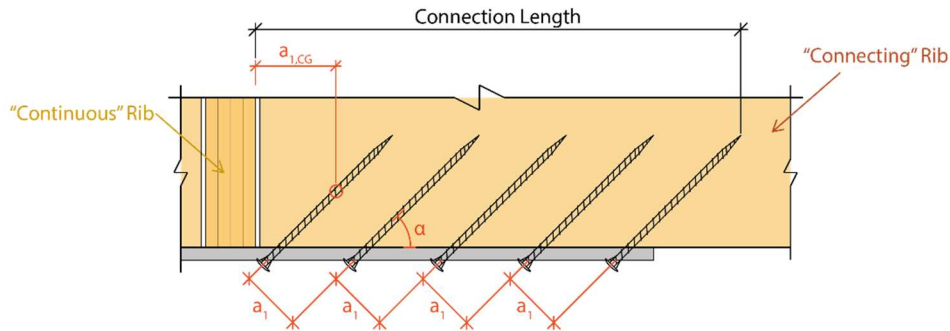
Figure 9-16: Spacing of the Inclined Screws for the Rib-to-Rib Moment Connection

Table 9-8: Rib-to-Rib Steel Plate Joint – Design Options

Rib Depth (mm)	Screw Diameter	α	No. Screws	Screw Length	U.C	Connection Length	$K_{connection}$ (kN/mm)
300	**7mm**	**30°**	21	160 mm	95.9%	629 mm	588
		45°	25	130 mm	98.7%	948 mm	796
	9mm	**30°**	13	200 mm	94.0%	555 mm	585
		45°	15	170 mm	99.7%	774 mm	574
400	**7mm**	**30°**	16	160 mm	96.4%	506 mm	488
		45°	19	130 mm	99.4%	740 mm	432
	9mm	**30°**	10	200 mm	93.5%	460 mm	450
		45°	12	170 mm	95.5%	640mm	459
500	**7mm**	**30°**	13	160 mm	96.3%	433 mm	364
		45°	16	130 mm	95.8%	636 mm	364
	9mm	**30°**	8	200 mm	94.9%	397 mm	360
		45°	10	170 mm	92.9%	551 mm	383

$$n_{ef} = max \begin{cases} n^{0.9} \\ 0.9n \end{cases} \quad Eq. \, 9.17$$

Table 9-7 gives the tensile strength of the Rotho Blaas screws along with the maximum and minimum thread lengths available, the required penetration depths of the screw tip (as specified by EN 1995-1-1), and the required LVL thicknesses. The total tensile strength capacity is found by multiplying the individual screw strengths by n_{ef}. For axially loaded screws, Rotho Blaas only specifies the minimum LVL thicknesses for 7mm and 9mm screws, so all other outer thread diameters are not recommended.

Minimum spacings between screws given in EN 1995-1-1. The spacing between screws (measured perpendicular to the screw axes) is $a_1 = 7d$ and the minimum end distance in the grain direction (measured from the edge to the centre of gravity of the threaded part of the screw) is $a_{1,CG} = 10d$. With this, the connection length from the connecting rib's edge to the last screw's tip is found. Figure 9-16 shows these geometries graphically.

The Rotho Blaas screws' ETA provides equations for the axial slip modulus of a screw used in either softwood or hardwood (ETA-Danmark, 2019). Unfortunately, there is no data available from the Eurocode or the LVL manufacturer about the axial slip modulus of screws in LVL, so the equation provided for Rotho Blaas screws in softwood will be used as a substitute. The horizontal stiffness of the connection is found by assuming that any axial movement results in an equal horizontal moment; Eq. 9.18 gives the stiffness for the entire joint.

$$K_{connection} = 25 \cdot d \cdot l_{ef} \cdot n_{ef} \quad Eq.\,9.18$$

Finally, the inclined screws can be designed. Table 9-8 shows different joint designs for a range of rib depths, screw diameters, and inclination angles. The length of the screws is set so that the withdrawal capacity is always slightly larger than the tensile capacity. Increasing the inclination angle reduces the required screw length for the ULS design but results in more screws being needed and extends the connection's length, so unless the screw length is critical, the minimum inclination angle should be used. Decreasing the screw diameter naturally results in more screws, which causes the connection length to extend. However, this also results in a shorter screw length. As the length and number of screws are reduced, the connection stiffness is also reduced, although, if a higher stiffness is required, then the screw length can be increased.

9.7.2 Deck: Shear Transfer

Vertical shear screws transfer the shear force between the deck and the rib for the moment connection—the same screw specification as the deck-to-rib shear joint are used. Therefore, most of the process for this connection is the same as is used in Section 9.6. The main difference here is that the force is no longer a distributed shear force of kN/m but is instead a shear force of kN. This means that the screws are not calculated as screws per meter. Due to this, there is more freedom in the spacing between screws. Although there must be at least a distance of $a_{3,t} = \max\,(7d;\,105mm)$ between rib's end and the first screw, and the spacing between the screws must be larger than $a_1 = (4 + 3|cos\alpha|)d$ $[mm]$ (Eurofins, 2020).

Table 9-9 shows design solutions where a range of rib depths, deck thickness, and screw spacings (a_1). Due to the design results from Section 9.6, 8mm screws are used, and the deck has a thickness of 24mm or 30mm. For each set of design parameters, the number of screws required to reach a utilisation check (U.C) below 100% was found, and the failure mode, connection length, and connection stiffness are calculated. The connection length is the distance from the end of the connecting rib to the axis of the furthest screw.

Reducing the rib's depth reduces the design shear force, so the number of screws required is also reduced. By increasing the spacing, the effective number of screws (n_{ef}) is increased so less screws are required, but this does increase the connection length. The connection stiffness also reduces as fewer screws are used. The joint options are designed based on the ULS so the connection stiffnesses are not the focus, If a higher stiffness is needed, then more screws can be added, but this would result in a longer connection.

Table 9-9: Rib-to-Rib Deck Joint – Design Options

Rib Depth	Deck Thickness	a_1 (mm)	No. of Screws	U.C	Failure Mode	Connection Length	$K_{connection}$ (kN/mm)
300 mm	24	32	16	96.9%	(a)	585 mm	79.5
		40	15	97.1%	(a)	665 mm	74.6
		50	14	97.7%	(a)	755 mm	69.6
	30	32	14	99.9%	(d)	521 mm	69.6
		40	14	94.5%	(d)	625 mm	69.6
		50	13	95.5%	(d)	705 mm	64.6
400 mm	24	32	7	88.4%	(a)	297mm	34.8
		40	6	96.0%	(a)	305 mm	29.8
		50	6	90.8%	(a)	355 mm	29.8
	30	32	6	92.8%	(d)	265 mm	29.8
		40	6	87.8%	(d)	305 mm	29.8
		50	5	97.8%	(d)	305 mm	24.9
500 mm	24	32	2	83.7%	(a)	137 mm	9.9
		40	2	79.2%	(a)	145 mm	9.9
		50	2	74.9%	(a)	155 mm	9.9
	30	32	2	76.5%	(d)	137 mm	9.9
		40	2	72.4%	(d)	145 mm	9.9
		50	2	68.5%	(d)	155 mm	9.9

9.8 Connection Design: Rib-to-Rib Shear Connection

The connection between the ribs to carry the shear forces is now investigated. In this connection, the shear forces must be transferred from the connecting rib to the continuous rib and the other connecting rib. Figure 9-17 shows a sketch of the connection design. The shear force is transferred by the bolts and the cold-formed steel plates.

This connection does not distribute the applied shear equally to all members. For example, when a shear force is applied from one of the connecting ribs, all the shear force is first transferred to the continuous rib, then part of shear force is transferred to the other connecting rib (see Figure 9-18). This transfer mechanism results in a less stiff connection between the two connecting ribs as there are more locations where connection slip will occur. If the ribs were connected orthogonally, this could be solved by connecting all the ribs with a cross screw connection. However, as the connecting ribs are not aligned, this is not possible. Therefore, the shear force must first be transferred to the continuous rib and then to the other connecting rib.
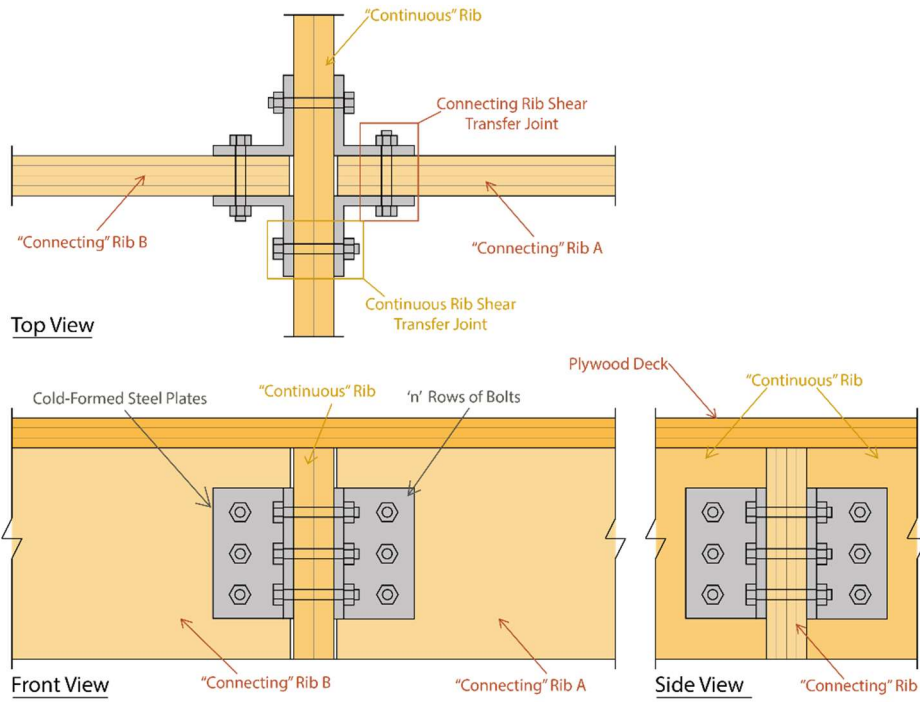
Figure 9-17: Third Angle Projection Sketch of the Rib-to-Rib Shear Connection
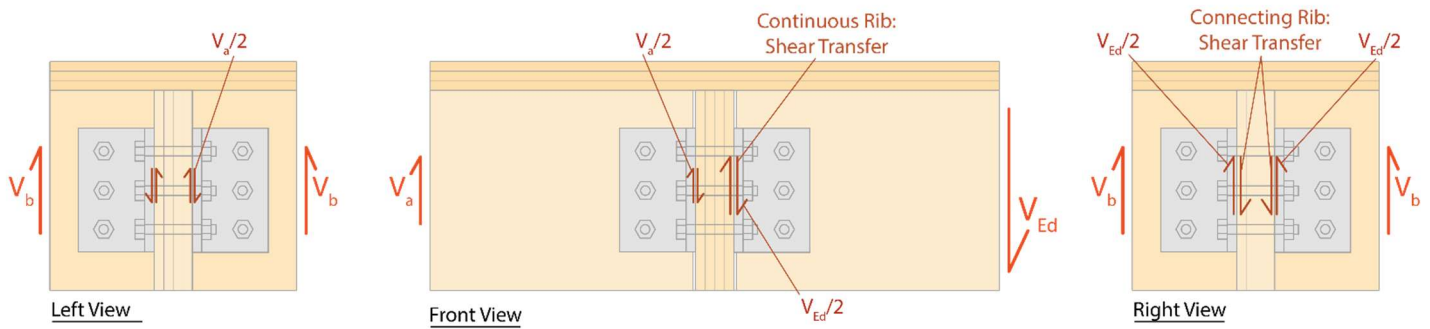
Figure 9-18: Force Transfer Through the Rib-to-Rib Shear Connection. A shear force of V_{Ed} is applied to the end of Connecting Rib A and is resisted by the resultant shear forces in the ends of the other ribs (V_a and two lots of V_b)
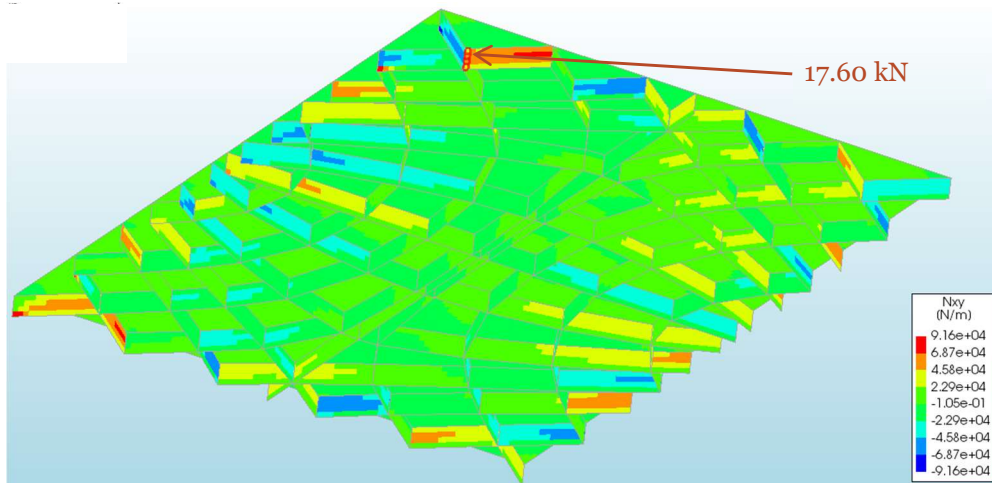
Figure 9-19: Location of Peak Internal Shear Force Throughout the Ribs. The Gradient Plot Shows the Distributed Shear Forces

The connection will be based on the highest shear force experienced at an internal connection from the 'basic case' model. The largest shear force found is 17.60kN distributed across the depth of the rib, see Figure 9-19.

This connection will be designed in two parts: the joint between the connecting rib to the steel plates, and the joint from steel plates to the continuous rib. The joint of the connecting rib to the steel plate is designed as a steel-to-timber double shear connection. Whereas the continuous rib joint is designed as double shear for transferring the force *to* the connecting ribs, but when the force is transferred *from* a connecting rib, the joint is single shear. The connection is also designed with thick steel plates (plate thickness ≥ bolt diameter) to limit the possible failure modes.

9.8.1   Connecting Rib: Shear Transfer

For double shear steel-to-timber connections, there are four possible failure mechanisms, as shown in Figure 9-20. Mechanism (j) and (k) apply to thin planes, and (l) and (m) apply to thick plates. Only (l) and (m) need to be checked as the connection has thick plates. Eq. 9.19 gives the characteristic load-carrying capacity per shear plane per fastener as provided in EN 1995-1-1.
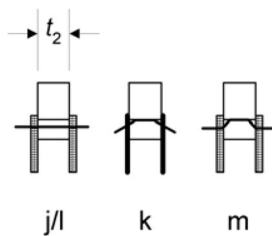
$$F_{v,Rk} = \min \begin{cases} 0,5\, f_{h,2,k}\, t_2\, d & (l) \\ 2,3\sqrt{M_{y,Rk}\, f_{h,2,k}\, d} + \dfrac{F_{ax,Rk}}{4} & (m) \end{cases} \qquad Eq.\,9.19$$

Figure 9-20: Steel-to-Timber Double Shear Connection Failure Mechanisms (EN 1995-1-1, 2014)

The yielding moment of the bolts ($M_{y,Rk}$) is calculated by Eq. 9.20, and the characteristic embedment strength for bolts in LVL is calculated by Eq. 9.21. α is the angle between the grain and the force, which is 90° (EN 1995-1-1, 2014). For this connection, no rope effects are considered so $F_{ax,Rk}$ is 0.

$$M_{y,Rk} = 0.3 \cdot f_{u,k} \cdot d^{2.6} \; [Nmm] \qquad Eq.\,9.20$$

$$f_{h,\alpha,k} = \frac{0.082(1 - 0.01d)\rho_k}{(1.30 + 0.015 \cdot d) \cdot \sin^2 \alpha + \cos^2 \alpha} \; [N/mm^2] \qquad Eq.\,9.21$$

The total connection design strength is found by multiply $F_{v,Rk}$ by 2 (for the shear planes) and by the number of bolts (the 'effective' number of fasteners is not required as the applied force is perpendicular to the grain). The characteristic capacity is again transformed into the design capacity using Eq. 9.7, where γ_m is 1.3, and k_{mod} is 0.9 (EN 1995-1-1, 2014).

The bolts need to be spaced from the end of the rib by a distance of max($7d; 80mm$), and from the top and bottom of the rib by $4 \cdot d$. The bolts need to be spaced apart vertically by $4 \cdot d$.

The fasteners' joint slip is given per shear plane per fastener in Table 7.1 of EN 1995-1-1. From this, the connection stiffness between the steel plate and the connecting beam can be calculated (see Eq. 9.22, where ρ_{mean} is 510 kg/m³ (Eurofins, 2020)).

$$K_{joint} = 2n \cdot \frac{\rho_{mean}^{1.5} \cdot d}{23} \ [N/mm] \qquad Eq. 9.22$$

Table 9-10 shows the different design options for this connection using a range of rib thicknesses and bolt diameters. For these designs all the bolts have a grade of 4.6, so $f_{u,k}$ is 400 N/mm². For each of the design options, the number of bolts required to fulfil the ULS is found, and the corresponding failure mode, bolt group height, and connection stiffness are given. The bolt group height is measured as the distance between the highest and lowest bolts' centres.

Increasing either the rib's thickness or the bolt diameter reduces the required amount of bolts. Generally, increasing the diameter reduces the bolt group height, although this is not a critical factor for this joint as there is plenty of space to fit the bolts. The minimum rib depth required is equal to the bolt group height plus 48mm for 6mm bolts, 64mm for 8mm bolts, and 80mm for 10mm bolts. Once a failure mode (m) occurs, there is no benefit to increasing the rib width any further as this does not result in increased resistance. The joint stiffness has not been considered when finding the appropriate amount of bolts; however, to achieve a higher stiffness the diameter or the number of bolts could be increased.

Table 9-10: Rib-to-Rib Shear Joint, Connecting Rib – Design Options

Rib Thickness	Bolt Diameter	No. of Bolts	U.C	Failure Mode	Bolt Group Height	K_{joint} (kN/mm)
51 mm	**6mm**	4	97.2%	(m)	72 mm	24.0
	8 mm	3	81.4%	(l)	64 mm	24.0
	10 mm	3	68.0%	(l)	80 mm	30.0
57 mm	**6mm**	4	97.2%	(m)	72 mm	24.0
	8 mm	3	78.9%	(m)	64 mm	24.0
	10 mm	2	91.3%	(l)	40 mm	20.0
63 mm	**6mm**	4	97.2%	(m)	72 mm	24.0
	8 mm	3	78.9%	(m)	64 mm	24.0
	10 mm	2	82.6%	(l)	40 mm	20.0
69 mm	**6mm**	4	97.2%	(m)	72 mm	24.0
	8 mm	3	78.9%	(m)	64 mm	24.0
	10 mm	2	80.9%	(m)	40 mm	20.0

9.8.2   Continuous Rib: Shear Transfer

The joint between the continuous rib and the steel plate must be designed separately to the other part of the connection due to the single shear transfer mechanism. The peak shear connection force of 17.6kN is divided by two as the force is distributed between the two steel plates. The possible failure mechanisms for this connection are (c), (d) and (e), as shown in Figure 9-21. The characteristic load-carrying capacity per fastener for this connection is given

by Eq. 9.23, where $M_{y,Rk}$ is calculated by Eq. 9.20 and $f_{h,k}$ is calculated by Eq. 9.21 with the same inputs as given in Section 9.8.1.
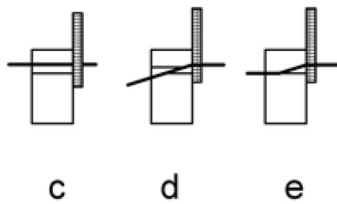
$$F_{v,Rk} = min \begin{cases} f_{h,k} \cdot t \cdot d & (c) \\ f_{h,k} \cdot t \cdot d \left[\sqrt{2 + \dfrac{4M_{y,Rk}}{f_{h,k} \cdot d \cdot t^2}} - 1 \right] & (d) \\ 2.3 \sqrt{M_{y,Rk} \cdot f_{h,k} \cdot d} & (e) \end{cases} \qquad Eq.\,9.23$$

Figure 9-21: Single Shear Steel-to-Timber Failure Modes with a Thick Plate

The total connection capacity is equal to $F_{v,Rk}$ multiplied by the number of bolts. The design capacity is found in the same way as in Section 9.8.1.

The bolts must be spaced by $4 \cdot d$ from the top and bottom of the rib, and they should be spaced apart vertically by $4 \cdot d$.

The connection stiffness between each steel plate and the continuous rib can be calculated using Eq. 9.22 and dividing the result by 2, as only one shear plane exists.

Table 9-11 shows the design options for this connection. Comparing these joint designs to those shown in Table 9-10 shows that either the same number of bolts is required or less. This means that the required connection heights are also similar, and the joint stiffnesses are exactly half of those for the continuous rib. For this joint, once failure mode (e) occurs, increasing the rib thickness any further does not improve the connection resistance. For simplicity, this joint will have the same bolt group specifications as the joint with the connecting rib because the results are so similar.

Table 9-11: Rib-to-Rib Shear Joint, Continuous Rib – Design Options

Rib Thickness	Bolt Diameter	No. of Bolts	U.C	Failure Mode	Bolt Group Height	K_{joint} (kN/mm)
51 mm	6mm	4	97.2%	(e)	72 mm	12.0
	8 mm	3	84.2%	(d)	64 mm	12.0
	10 mm	2	98.7%	(d)	40 mm	10.0
57 mm	6mm	4	97.2%	(e)	72 mm	12.0
	8 mm	3	78.9%	(e)	64 mm	12.0
	10 mm	2	91.8%	(d)	40 mm	10.0
63 mm	6mm	4	97.2%	(e)	72 mm	12.0
	8 mm	3	78.9%	(e)	64 mm	12.0
	10 mm	2	85.6%	(d)	40 mm	10.0
69 mm	6mm	4	97.2%	(e)	72 mm	12.0
	8 mm	3	78.9%	(e)	64 mm	12.0
	10 mm	2	80.9%	(e)	40 mm	10.0

9.9 Design Finalisation

In the previous sections, the minimum requirements for deck thickness, rib thickness, and rib depth were found for the yield stresses and connection designs in the ULS. In this section, all the information on these will be brought together to conclude a final design. Once the design parameters have been decided upon, a final FE model of the entire slab can be produced with the finalised geometry and properties.

Chapter 8 found that as the ribs became more slender, there are less secondary load transfer mechanisms like torsion. These are a problem because they will load the wood in its weak axes, reducing the system's capacity. So, one of the goals for selecting the design parameters will be to create slender ribs.

Often the connection can be made much simpler by increasing the sections of the members (i.e., increasing the rib's depth), but this results in less utilisation of the material for the stresses. Therefore, a balance needs to be struck between creating an efficient connection design and efficiently utilising the material. The second goal for selecting the design parameters will be: To only increase the section dimensions for the connections where it is necessary.

9.9.1   Rib Depth and Rib Thickness

A good starting point is to look at the absolute minimum requirements for the design parameters. Firstly, for the axially loaded screws used in the rib-to-rib steel plate joint, the screw manufacturer specified that only 7mm and 9mm screws could be used, and that the LVL should have a minimum tohickness of 45mm and 57mm respectively for each screw diameter. This means that the minimum available LVL thickness is 45mm. However, the standard Panel sizes from the LVL manufacturer require a minimum thickness of 51mm for a depth of 400mm, and 63mm for a depth of 500mm.

In Section 9.4.2, the required rib thickness for each rib depth was found for the ULS stresses. This specified the following requirements:

- Rib Depth =300mm: Rib Thickness >69mm,
- Rip Depth =400mm: Rib Thickness >45mm,
- Rip Depth =500mm: Rib Thickness >27mm.

Combining all these limits results in the requirements given in Table 9-12. The 300mm deep rib is the only case where the ULS stresses limit the design; however, for this design, the rib is not as slender compared to the other options. Although the 400mm deep rib is limited by the available standard sizes of the LVL, this only increases the rib thickness by 6mm compared to the requirement due to the stresses. The available sizes of LVL also limit the 500mm deep rib; however, this causes an increase of 36mm to the stress state requirements. The 400mm rib is chosen as the best depth to use as it results in the minimum use of material, and it is possible to design the connections for this depth.

The rib's thickness could be increased to 57mm so that 9mm axially loaded screws can be used. This impacts the rib-to-rib steel plate joint's design, where if the screws are inclined at an angle of 30° 10 screws can make the connection, as opposed to 16 7mm diameter screws (see Table 9-8). Changing the screw diameter also changes the length of the connection from

506mm for 7mm screws, to 460mm for 9mm screws. It is decided here that having a thinner rib is better due to its structural performance, so a 51mm rib will be used with 7mm screws.

Table 9-12: Rib Thickness Requirements Based on the Rib Depth

Rib Depth	Rib Thickness Requirement	Limiting Factor
300 mm	>69mm	ULS Stresses
400 mm	>51mm	Available Standard Sizes
500 mm	>63mm	Available Standard Sizes

9.9.2 Deck Thickness

The Rib-to-Deck Shear Joint gives the minimum requirement for the deck's thickness for composite action. From the design options given in Table 9-5, the deck had to have a minimum thickness of 24mm so that a connection could be created with enough strength. From these results, it was also found that it is best to use 8mm screws for this connection. The deck could also be increased to 30mm to create a slight reduction in the number of screws required. The same can also be stated for the Rib-to-Rib Deck Joint (see Table 9-9).

The stress consideration in the ULS does not provide any additional limitations on the deck's thickness as a 12mm thick deck was already safe. Although, if second-order effects were to be taken account of in the analysis, a different result would be produced.

The use of a 24mm thick deck is chosen here as it has the smallest volume, and increasing the deck's thickness does not improve the performance of the connection significantly.

9.9.3 Modelling of the Final Geometry

In Section 9.3, the final centreline geometry was created. This can be combined with the final design parameters (deck thickness =24mm, rib thickness = 51mm, and rib depth = 400mm) to create a FE model to analyse the final slab. The model is constructed using Diana FEA, and the same process and properties used for 'The Shell Rib and Deck Model' from Chapter 8. The only other difference for this model is that the self-weight is a global load instead of the area and line loads used in Chapter 8.

Figure 9-22 shows the deflections of the final model for the SLS load combination as seen from above. Figure 9-23 gives the distributed forces along the ribs' axial direction, which is needed to determine the Rib-to-Rib Moment Connection's final design. Figure 9-24 displays the ribs' distributed shear forces, needed for designing the Rib-to-Deck Shear Connection and the Rib-to-Rib Shear Connection.

9.9.4 Rib-to-Deck Shear Connection - Final Design

The connection force that needs to be carried between the rib and the deck for composite action can be found from the final model. The connection force from this model is 65.0 kN/m
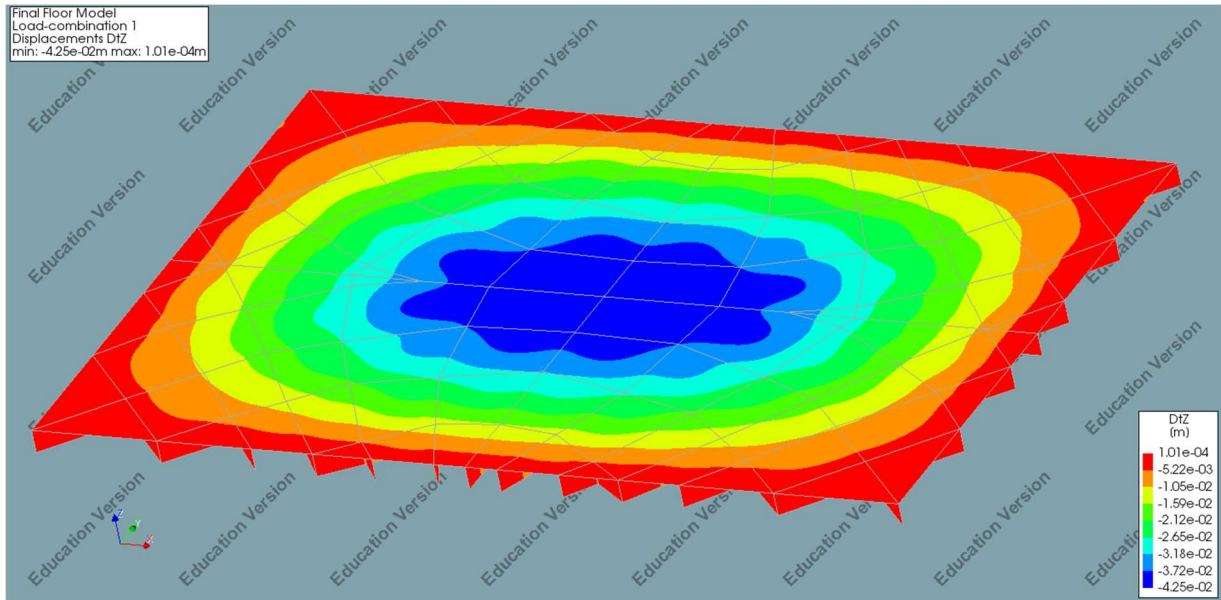
Figure 9-22: Deflection Plot of Final Slab Model for the SLS Load Combination
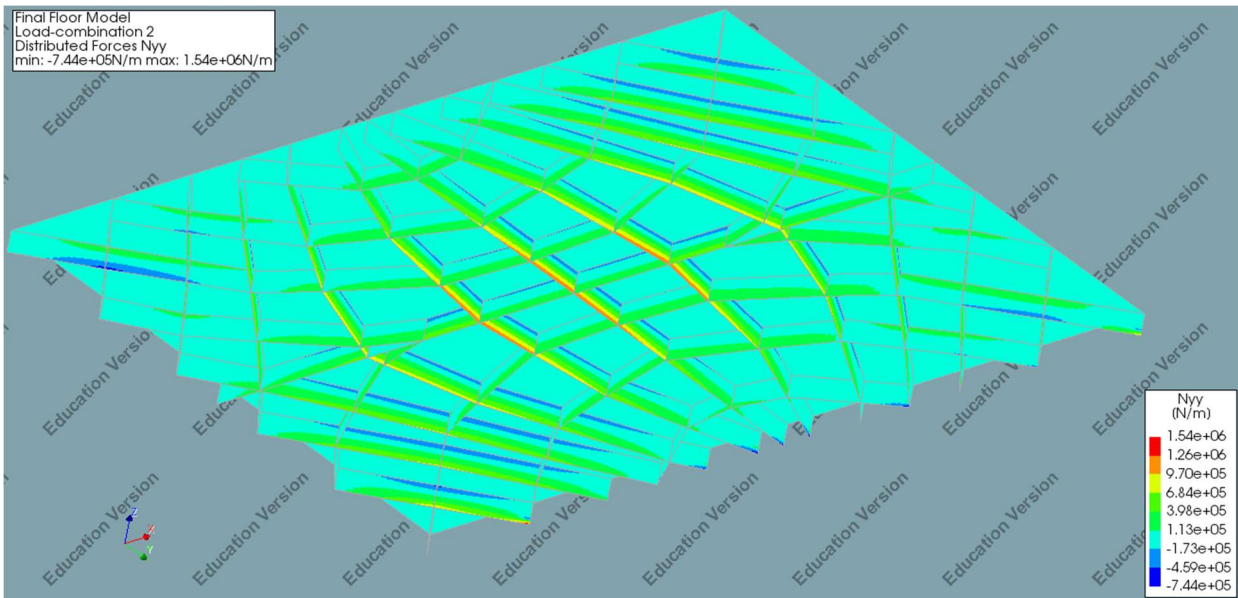
Figure 9-23: Distributed Force in the Axes of the Ribs for the Full ULS Load Case as Seen from the Bottom of the Slab
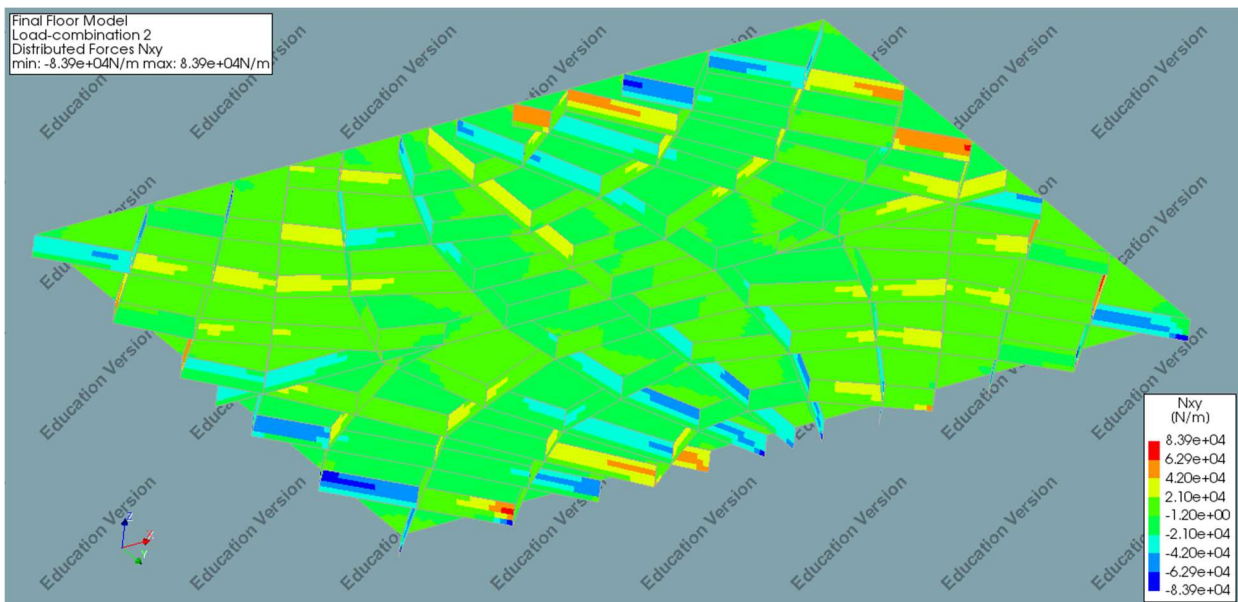
Figure 9-24: Distributed Shear Forces in the Ribs for the Full ULS Load Case as Seen from the Bottom of the Slab

This connection can now be designed using the equations from Section 9.6 and the new connection force. This gives a final connection design of:

- 8mm∅ x 28 screws/m
- Screw Length: >120mm.
- Screw Type: Rotho Blaas, Partially Thearded, Washer Head Screws
- Connection Utilisation: 98.4%
- Failure Mode: (a)
- Connection Stiffness: 139 (kN/mm)/m

9.9.5   Rib-to-Rib Moment Connection – Final Design

In Section 9.7, the connection was designed for the peak moment experienced in the slab. For the connection's final design, the peak moment at the end of a connecting rib is found from the Final FE model. This gives a design moment of 54.4 kNm. Dividing this by the lever arm of 0.417m provides the force transferred across the connection by the deck and the steel plate: 130.5kN. The joint between the steel plate and the LVL ribs must transfer 130.5kN. The force transferred at the joint with the deck is the difference between 130.5kN and the deck's compression before the connection (163.6 kN). Therefore, the joint between the rib and the deck must carry 33.1 kN.

9.9.5.1 Rib-to-Rib Steel Plate Joint – Final Design

Taking the new design force of 130.5kN and the equations from Section 9.7.1, the Rib-to-Rib Steel Plate Joint's final design can be created. For this 7mm Rotho Blaas fully threaded screws are used. The screw inclination angle is set to 30° as from the results from Table 9-8 this produced the shortest connection length, and an inclination angle below 30° cannot be used (ETA-Danmark, 2019). The final joint design per rib is:

- 7mm∅ x 16 screws
- Screw Length: >170mm.
- Screw Type: Rotho Blaas, Fully-Theard Screws
- Connection Utilisation: 98.2%
- Failure Mode: Tensile Failure of the Screw
- Total Steel Plate Length: 831 mm
- Connection Length: 507 mm
- Connection Stiffness: 448 kN/mm

9.9.5.2 Rib-to-Rib Deck Joint

Taking the new design force of 33.1 kN and the equations from Section 9.7.2, the Rib-to-Rib Deck Joint's final design can be created. For this, the same specification of screws is used as is used for the Rib-to-Deck Shear Connection. The screws are spaced as close together as possible so that the connection is as short as possible. The final joint design per rib is:

- 8mm∅ x 14 screws
- Screw Length: >120mm.
- Screw Type: Rotho Blaas, Partially Theard, Washer Head Screws
- Screw Spacing: 32mm
- Connection Utilisation: 96.2%
- Failure Mode: (a)
- Connection Stiffness: 69.6 kN/mm

9.9.6 Rib-to-Rib Shear Connection

In Section 9.8, the design was split into two stages: the joint between the connecting rib and the steel plates, and the joints between the steel plates and the continuous rib. However, these two joints had similar design requirements for the ULS, so to simplify the final design, the connection design is based solely on the joint between the connecting rib and steel plates. Therefore, the joint will be designed using the method from Section 9.8.1. For this, the design shear force is taken from the final FE model by finding the maximum shear force at the end of a connecting rib, which is 17.00kN. The final design for the Rib-to-Rib Shear Connection is:

- Bolt Diameter: 8mm
- No. of Rows: 3
- No. of Columns: 1
- Total no. of Bolts: 3
- Bolt Group Height: 64 mm
- Connection Utilisation: 79.7%
- Failure Mode: (l)
- Connection Stiffness: 24.0 kN/mm

9.9.7 Serviceability Limit State

The final deflection of the structure is a combination of the instantaneous deflection and the long-term creep effects. EN 1995-1-1 specifies that the long-term deformation, including creep effects, can be found by modifying the modulus of elasticity, and shear modulus. Eq. 9.24 and Eq. 9.25 provide the modified values, where k_{def} is 0.6 for LVL and 0.8 for plywood in service class 1.

$$E_{mean,fin} = \frac{E_{mean}}{(1 + k_{def})} \qquad Eq.\,9.24$$

$$G_{mean,fin} = \frac{G_{mean}}{(1 + k_{def})} \qquad Eq.\,9.25$$

The total deformation is found by inserting $E_{mean,fin}$ and $G_{mean,fin}$ into the FE model and determining the deformation under permanent loading, and then adding to this the deformations from the imposed loading using E_{mean} and G_{mean}. The deflections under the permanent and imposed actions are shown below with the final slab deformation.

$$w_G + w_{creep} = 27.4mm$$

$$w_Q = 25.9 \; mm$$

$$w_{final} = 53.3 \; mm$$

9.10 Discussion and Conclusions

In this chapter, the isostatic slab's design has been validated to show that it is possible to produce. Firstly, a centreline geometry has been created, which can be manufactured using straight elements. However, this centreline geometry production meant that the ribs were moved away from their stress lines. This, combined with the discretisation step from Chapter

7, means that the ribs are only roughly based on the original stress line geometry. Chapter 5 developed a more accurate method for developing stress lines, but as the slab has been developed and designed the requirement for this accuracy has been reduced.

To validate that it is possible to construct this slab, three critical connections have been designed: the Rib-to-Deck Shear Connection, the Rib-to-Rib Shear Connection, and the Rib-to-Rib Moment Connection. The requirements for these connections have been used to determine what design parameters are required. This was all combined into creating a final FE model of the slab. The connection stiffnesses have not been added into the model. This is an essential next step as this will result in force redistribution through the ribs and the deck.

It is difficult to determine how well the rib-to-rib shear connection will transfer the load from one connecting rib, through the steel plates and the continuous rib, to the other connecting rib. This would largely be dependant on the bending stiffness of each element and the amount of slip in the joint. The core issue is that the force must first be transferred to the continuous rib and then to the other steel plate or by bending through the bolts. Alternatively, the shear force could be transferred entirely through the deck; however, the ribs must be placed first in the construction process, followed by the deck. This means that although the deck could transfer the shear force in the final situation, the ribs would still need to be initially connected. The shear force will ultimately be partially transferred by the steel plates and bolts, and partially by the deck, but the exact distribution of this has not been calculated

The connection designs needed to have a lot of exposed steel as they need to apply to orthogonal and non-orthogonal connections. This could be a "deal breaker" for some stake holders as these types of connections can be viewed as unappealing in terms of aesthetics. However, this could be countered by arguing that the connection should be exposed and visible as the system is based on a structural form, so it would fit with the overall aesthetic. If exposed connections are a significant barrier to this system's use, then rib-to-rib connections with glued-in rods could be an alternative, see Figure 9-1.

The final FE model has also been used to determine the total deflection of the slab for the SLS. This value is likely beyond acceptable limits, but this would need to be determined in coordination with an architect and a roofing contractor. To reduce the deflection, the rib depth can be increased to 500 mm, which would increase the material volume, but would also be beneficial for the Rib-to-Rib Moment Connection.

10.1   Introduction

In the previous chapter, the design of an isostatic timber slab was made for a single case study. In this chapter, the design created in Chapter 9 will be compared to other systems to answer the research question: How does an Isostatic Timber Slab compare to other systems?

The purpose of this comparison is to indicate the advantages and disadvantages of this system so that engineers and designs can make an informed decision about whether it is a useful design alternative to apply to their project.

10.2   Methodology

The system is compared using three basic metrics: material volume, structural weight, and structural depth. For simplicity, the volume and weight of fasteners are excluded. The isostatic slab is compared to three off-the-shelf systems: A flat CLT slab, the Kerto-Ripa LVL slab, and a hollow-core slab. A comparison is also made to a one-way spanning equivalent of the timber isostatic slab, a simple 'T'-beam with an LVL web and a plywood flange.

The comparisons are made on the case study used in Chapter 9, as shown in Figure 8-1. The comparison systems are one-way-spanning, so they are designed for a span of 10m and the same applied load cases as given in Section 8.3 (G_{Dead}=0.65kN/m², Q_{Live}=1.0kN/m², and Q_{Snow}=1.0kN/m²).

The off-the-shelf systems are designed using the preliminary design tools available from the product manufacturers. The designs are then used to provide the cross-sectional geometries used to calculate the three comparison metrics. The required cross-section for the 'T'-beam is calculated by hand calculations using the rules provided by EN-1995-1-1, and subsequently, the same process is followed.

10.3   Structural System Evaluations

In this section, the designs for each of the comparison systems are made, and their comparison metrics are calculated.

10.3.1   The Isostatic Timber Slab

The timber isostatic slab design has a plywood deck of 24mm, and LVL ribs with a 400mm depth and 51mm thickness. The total length of ribs can be calculated using the geometry shown in Figure 9-7, which gives 227m (note that this includes some overlap at the connections). The surface area of the plywood sheets is simply 10x15m. Therefore, the material volumes are:

$$\text{Volume of LVL}: 4.641\ m^3$$

$$\text{Volume of Plywood}: 3.6\ m^3$$

The mean density of the LVL is 510 kg/m³ (Eurofins, 2020), and the density of the plywood is 680 kg/m³ (Metsä Wood, 2020). Therefore, the mass of the entire structure is:

$$\text{Structural Mass}: 4,815\ kg$$

Finally, the peak structural depth is the thickness of the plywood plus the depth of the LVL, giving:

$$\text{Structural Depth}: 424\ mm$$

10.3.2   The Flat CLT Slab

The CLT slab is designed using the Calculatis software created by the CLT manufacturer Stora Enso (Stora Enso, 2020). The following parameters are used in the software:

- Panel width: 2.750 m
- Material: C24 spruce
- Fire Resistance Class: R0
- SLS Limit w_{inst} = L/300
- SLS Limit $w_{net,fin}$ = L/250
- SLS Limit w_{fin} = L/187 - *This value is used as this is the deflection limit of the isostatic slab.*
- Vibration analysis is not performed.

It is found that the CLT 240 L7s slab fulfils the Eurocode checks. This panel is 240mm thick, which results in the following values:

$$\text{Structural Depth}: 240\ mm$$

$$\text{Volume of CLT}: 36\ m^3$$

The mean density of C24 timber is 420 kg/m³ (NEN-EN338:2016). Therefore, the total mass of the structure is:

$$\text{Structural mass}: 15120\ kg$$

10.3.3   The Kerto-Ripa LVL Slab

The slab is designed using the span tables available from the Kerto-Ripa brochure (Metsä Wood, 2017). It is found that for a box type element the web height most be 300mm, and flange thickness is 27mm. The element must also have four 45mm thick ribs in a standard 2400mm wide panel. To find this the medium load case is used which is the closest load case to the loads used for the case study (Permanent: 60 kg/m², and Snow: 72kg/m², it's assumed that maintenance loading is taken into account in Metsä Wood's calculations); this gives a max span of 12.3m.

The total volume flange panel is shown in Eq 10.1, and the volume of the ribs is given by Eq. 10.2.

$$Volume\ of\ the\ Flanges = 10m \times 15m \times Flange\ Thickness \times 2 = 8.1\ m^3 \qquad Eq.10.1$$

$$Volume\ of\ the\ Ribs = \frac{15m}{Panel\ Width} \times no.of\ Ribs \times Thickness \times Span = 11.25\ m^3 \qquad Eq.10.2$$

Figure 10-1: An Image of the Kerto-Ripa Roof and Floor System (Metsä Wood, 2017)

Therefore, the total structural volume for this system is:

$$\textbf{Volume of } LVL: \textbf{19}.\textbf{35 } \textbf{\textit{m}}^{\textbf{3}}$$

The mean density of the LVL is 510 kg/m³ (Eurofins, 2020). Therefore, the mass of the total structure is:

$$\textbf{Structural Mass}: \textbf{9869 } \textbf{\textit{kg}}$$

Finally, the peak structural depth is the depth of the ribs plus two times the thickness of the panels:

$$\textbf{Structural Depth}: \textbf{354 } \textbf{\textit{mm}}$$

10.3.4   The Hollow Core Slab

The hollow core slab is designed using the load-span tables available from the precast concrete manufacturer Milbank (Milbank, n.d.). From this, it is found that the PS-200 slab is adequate for the required 10m span, with no additional in-situ concrete. The loading condition is chosen as the self-weight, plus a dead load of 1.5kN/m², plus an imposed load of 0.75kN/m², which is the option with the closest loading to the case study in the ULS.
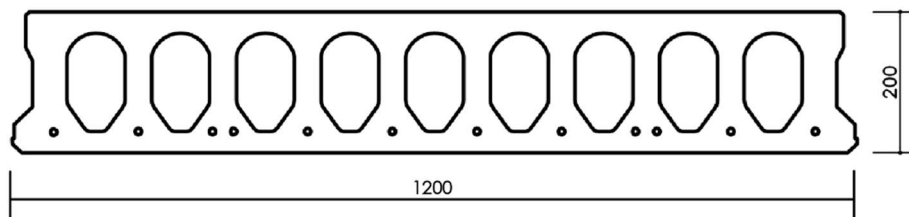
Figure 10-2: A Cross-Section of the PS-200 Hollow Core Slab Produced by Milbank (Milbank, 2016)

The PS-200 panel has a cross-sectional area of 0.146 m² for a standard width of 1.2 m, a depth of 200 mm, and a structural weight of 2.97 kN/m² (Milbank, 2016). The structural volume is calculated as shown in Eq. 10.3, and the structural mass is calculated by Eq. 10.4

$$Structural\ Volume = \frac{15m}{Panel\ Width} \times Panel\ Area \times Span = 18.25\ m^3 \qquad Eq.\ 10.3$$

$$\textbf{Volume of Precast Concrete}: \textbf{18}.\textbf{25 } \textbf{\textit{m}}^{\textbf{3}}$$

$$\textbf{Structural Mass} = \frac{2970}{9.81} \times 10m \times 15m = \textbf{45412 } \textbf{\textit{kg}} \qquad Eq.\ 10.4$$

$$\textbf{Structural Depth}: \textbf{200 } \textbf{\textit{mm}}$$

10.3.5   The Plywood-LVL 'T'-Beam

The T-beam is made with a plywood deck which creates the flange, and LVL ribs which create the web. The ribs are spaced at 1.4m apart which is approximately the rib-to-rib spacing in the isostatic slab. The deck is 24mm thick with the stiff axis aligned with the 10m span to match the isostatic slab. The ribs' depth is set to 400mm, but the thickness is varied to achieve the limit state criteria. The system is designed as a mechanically joint beam using Annex B from EN 1995-1-1, where it is assumed that the system can be simplified down to a T-beam with a 1400mm wide flange, as shown in Figure 10-3. The chosen joint design from the Rib-to-Deck Shear connection is used in this calculation, see Section 9.9.4. Using EN 1995-1-1, the effective bending stiffness for instantaneous loading and creep effects is calculated for a rib thickness of 57mm:

$$(EI)_{ef,insta} = 10.47 \times 10^{12} \; N/mm^2$$

$$(EI)_{ef,fin} = 6.17 \times 10^{12} \; N/mm^2$$
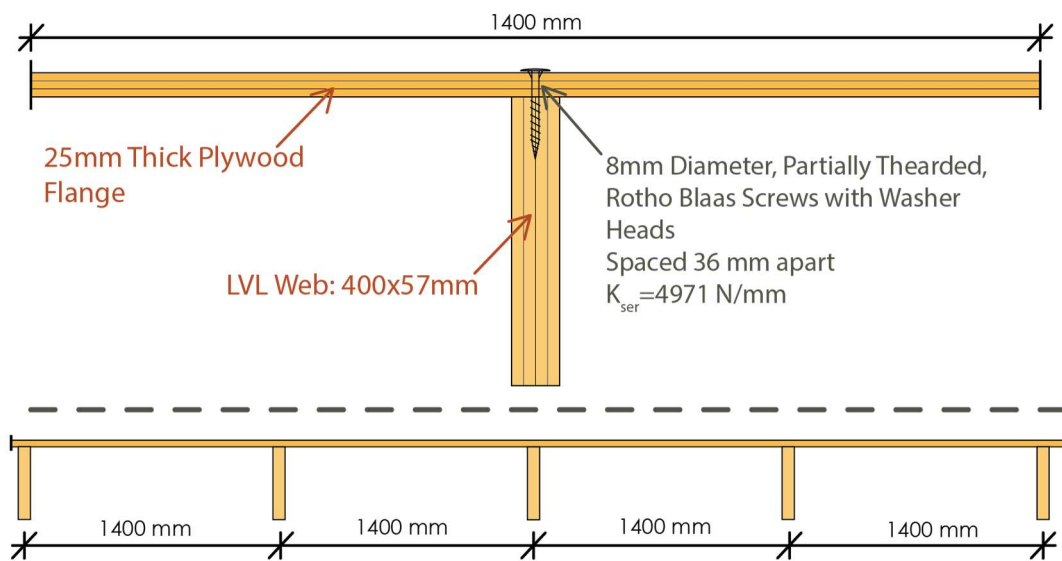
Figure 10-3: Cross-Sectional Views of the Plywood-LVL 'T'-Beam, Top: The Geometry Used in the Beam Analysis; Bottom: Macro Scale Cross-Section

The uniformly distributed load line loads are calculated using the 1.4m width:

$$q_{ULS} = 1.35 * G_{Dead} + 1.35 * G_{self-weigh} + 1.5 * Q_{Live} + 0.75 * Q_{snow} = 4.88 kN/m \quad Eq. 10.5$$

$$q_{SLS,G} = 1.0 * G_{Dead} + 1.0 * G_{self-weigh} = 1.28 kN/m \qquad Eq. 10.6$$

$$q_{SLS,Q} = 1.0 * Q_{Live} + 0.5 * Q_{snow} = 2.1 kN/m \qquad Eq. 10.7$$

For the ULS the peak moment and shear are calculated as follows:

$$M_{Ed} = \frac{q_{ULS} l^2}{8} = 60.34 \; kNm \qquad Eq. 10.8$$

$$V_{Ed} = \frac{q_{ULS} l}{2} = 24.14 \; kN \qquad Eq. 10.9$$

Using Eq. 10.8 and Eq. 10.9 and the method from Annex B of EN 1995-1-1 with $(EI)_{ef,instant}$, the peak normal stresses in the flange and web can be found, as well as the peak shear stress in the web:

$$\sigma_{Ed,Flange} = 5.71 \, N/mm^2 \qquad Eq. \, 10.10$$

$$\sigma_{Ed,Web} = 23.45 \, N/mm^2 \qquad Eq. \, 10.11$$

$$\tau_{Ed,Web} = 1.38 \, N/mm^2 \qquad Eq. \, 10.12$$

The design resistances are obtained using the data from the relevant product declarations for the plywood (Metsä Wood, 2019) and the LVL (Eurofins, 2020) and the values of $k_{mod} = 0.9$ (for short term loading, and service class 1) and $Y_m = 1.2$. By dividing the peak stresses by the design resistances, the ULS utilisation checks are:

$$U.C_{\sigma,Flange} = \frac{5.71}{\frac{39.5 * 0.9}{1.2}} = 19.3\% \qquad Eq. \, 10.13$$

$$U.C_{\sigma,Web} = \frac{23.45}{\frac{44.0 * 0.9}{1.2}} = 71.1\% \qquad Eq. \, 10.14$$

$$U.C_{\tau,Web} = \frac{1.38}{\frac{4.2 * 0.9}{1.2}} = 43.8\% \qquad Eq. \, 10.15$$

$$w = \frac{5ql^4}{384(EI)_{ef}} \qquad Eq. \, 10.16$$

The deflection at the mid-span can be found by using Eq. 10.16. The final deflection of the system is made up the permanent deflection including creep deformation, and the instantaneous deflection:

$$w_G + w_{creep} = 26.5mm \qquad \#(EI)_{ef,fin} \, is \, used$$

$$w_Q = 26.1 \, mm \qquad \#(EI)_{ef,instant} \, is \, used$$

$$w_{final} = 52.6 \, mm$$

To check the SLS, the deflection limit of $Span/187$ is used as this is the deflection limit that the isostatic slab achieves. This gives the result shown in Eq. 10.17.

$$U.C_{SLS} = \frac{52.6}{\frac{10,000}{187}} = 98.3\% \qquad Eq. \, 10.17$$

This shows that the T-beam slab system can achieve the same utilisation checks as the isostatic slab when: the ribs are spaced 1.4m apart, the ribs have a cross-section of 51mmx400mm, and the deck is 51mm thick.

The total volume of plywood is equal to the slab area of 10x15m multiplied by the thickness:

Volume of Plywood: $3.6 \, m^3$

Across the 15m span of the slab, there needs to be 11 ribs to fulfil the 1.4m spacing. Therefore the total LVL volume is:

Volume of LVL: $2.51 \, m^3$

The mean density of the LVL is 510 kg/m³ (Eurofins, 2020) and the density of the plywood is 680 kg/m³ (Metsä Wood, 2020). Therefore, the mass of the total structure is:

Structural Mass: $3727 \, kg$

Finally, the peak structural depth is the thickness of the plywood plus the depth of the LVL, giving:

$$\text{\textbf{\textit{Structural Depth}}}: \textbf{\textit{424 mm}}$$

10.4   System Comparison

The different systems can be compared and contrasted against the isostatic slab to provide a means of comparison. Table 10-1 summaries the metrics for each of the slab systems, and compares them to the timber isostatic slab. Excluding the T-beam slab, the isostatic slab has less volume and mass than the other systems, but it is a deeper structure. Comparing the isostatic slab to the T-beam system shows that the T-beam performs better as it has the same depth but less mass and volume.

Table 10-1: Comparison Between the Slab Systems

Slab System	Volume (m³)	Depth (mm)	Mass (kg)	Material/s by volume
Timber Isostatic Slab	8.241	424	4,815	56.3% LVL 43.7% Plywood
Flat CLT Slab	36.0 *336% Bigger*	240 *43% Thinner*	15,120 *214% Heavier*	CLT
Kerto-Ripa System	19.35 *134% Bigger*	354 *17% Thinner*	9,869 *99% Heavier*	LVL
Hollow Core	18.25 *121% Bigger*	200 *52% Thinner*	45,412 *843% Heavier*	Precast Concrete
T-Beam	6.11 *25.9% Smaller*	424 *identical*	3,727 *23% Lighter*	41.1% LVL 58.9% Plywood

There are more benefits to the isostatic slab then is shown by these metrics. It has a lot more architectural appeal due to its flowing form and novel geometry, and it is a structurally expressive system. Also, the element size is smaller, making it easier to transport. However, it needs more on-site construction, many exposed steel connections, and the complex geometry will make it harder to construct.

Comparing the peak moment and shear force of 60.34 kNm and 24.14 kN from the T-beam to the values of 54.4 kNm and 17.00 kN from the isostatic timber slab shows that the one-way system has higher design forces. However, the isostatic system's lower force does not provide much benefit because these forces need to be carried through its connections.

10.5   Discussion

This chapter shows that the timber isostatic slab design produced in Chapter 9 is advantageous - compared to the "off-the-shelf" systems - in situations when a lightweight structure is needed or when material usage is a core design objective. However, an

unexpected result is seen in comparing the plywood-LVL T-Beam, which outperformed the isostatic slab.

The plywood-LVL T-Beam is a one-way spanning alternative to the two-way spanning isostatic slab, so it would be expected that the isostatic slab would perform better, but this is not the case. The T-Beam slab's critical criterion is the SLS as this has the highest utilisation. Both systems deflect similar amounts with a 53.3mm deflection for the isostatic slab and a 52.6mm deflection for the T-Beam slab. This means that even though the isostatic slab has more material, it has a higher peak deflection. This is even more significant when considering that connection slip between the ribs and deck is used in the calculation process for the T-beam, whereas it has not been considered in the isostatic slab design. It should also be noted that the calculation method used for the T-beam does not consider the distribution of stresses in the lateral cross-sectional direction; this is accounted for in the FEA conducted for the isostatic slab. Excluding this increases the calculated stiffness. Although the peak deflections are roughly equal, the average deflection will be higher in the T-Beam because the mid-span deflection in every rib will be equal.

The high deflection in the isostatic slab could result from the rib geometry used, as the peak deflection was not incorporated into the selection process. Therefore, a better design may be produced if the deflection result is used to improve the geometry iteratively. Alternatively, it could be that two-way spanning isostatic slabs intrinsically have a similar deflection to their one-way spanning counterpart.

The methods used to generate the alternative systems' designs are simpler than the method used to design the isostatic slab, which means that this comparison is not entirely fair. However, it provides a reasonable indication of how the slabs compare as the timber isostatic slab's design is yet to be optimally designed.

The isostatic slab also has additional benefits in terms of its aesthetical appeal. However, this is a subjective aspect and is extremely difficult to measure quantitively. The easy of construction is another a useful metric to compare these systems, but this is also difficult to measure quantitively.

10.6   Conclusions

This chapter has answered the question: How does an Isostatic Timber Slab compare to other systems? In summary, the isostatic timber slab design created in Chapter 9 had less volume and mass than a flat CLT slab, Metsä Wood's Kerto-Ripa slab, and a hollow core slab. However, the isostatic slab had more structural depth.

A comparison was also made to a slab with a plywood deck with ribs spanning in one way; designed as a mechanically jointed T-beam. The comparison with the T-beam showed that the one-way spanning alternative to the isostatic slab had less material volume and mass, with the same structural depth. This showed that either the isostatic slab's design is not optimised well enough or there is an inherent flaw in these systems for the peak slope limit.

11 DISCUSSION AND CONCLUSIONS

11.1 Introduction

This chapter summarises all the findings and conclusions produced in this thesis and gives final remarks about the work. The chapter is split into the same two parts the thesis is made of: Part A – Investigation into Stress Line Geometries for Use in Isostatic Slabs, and Part B – Development of the Isostatic Timber Slab Design. These parts are followed by the answer to the main research question.

11.2 Part A: Investigation into Stress Line Geometries for Use in Isostatic Slabs

This thesis part investigated the methods used to produce the stress lines and the rib geometries produced from them.

Chapter 3 creates a literature review relating to the structural benefits of producing structures from stress line geometries. It was found that for in-plane loaded plates, the stress lines show the natural flow of compression and tension forces through a solid body. This knowledge has been used in the seminal paper covering the creation of strut-and-tie models for reinforced concrete (Schlaich, et al., 1987). For out-of-plane loaded plates, the stress lines show the natural flow of bending forces. It was found that the reason stress lines produce efficient geometries is because when a solid body is loaded, the forces are transferred through the mechanism with the lowest internal strain energy and work done. The stress lines show this load transfer mechanism for the body for the specified load case. Therefore if a network of interconnected elements shaped to the principal stress lines replaces the solid body, the same load transfer mechanism is produced when the loading conditions are the same. This is of significance because the minimisation of the work done means that if the loading remains constant, the displacements are minimised compared to any other arrangement of the same volume of material. There are also similarities drawn between principal stress lines and Michell's structures. This is important because Michell (1904) showed that their structures have the absolute minimum volume of material necessary to carry a specified load to the support locations.

Chapter 4 review the current methods for generating stress lines. The literature consistently agrees that the commercially available stress line generation tools are inadequate for generating stress lines for form-finding structures. The literature provided several methods which could be applied to a new stress line generation tool. In Chapter 5, the methods were tested against each other to determine which combination could produce the most accurate stress lines. The methods were grouped into three parts of the stress line generation process: interpolation, integration, and seeding. As there are no analytical solutions to test the methods against, three axioms of stress lines were created from Mohr's theory of principal stresses. The compliance of the methods to these axioms was measured. For the interpolation

method, the new 8-node shape function method, produced by the author from the theory of finite element analysis, could produce improvements over the previously developed method from the literature, as it has a higher level of accuracy at the model edges. All previous generation tools used an Euler integration method; however, it was found that more accurate results can be produced by the RK4 method if the sample step size is small. In general, it was found that accuracy increased as the step size was decreased, which agrees with the results from previous studies. In the literature, there had been no development of a holistic approach to selecting seeding points for starting stress lines from, and very primitive methods were used. A seeding method was not required for the overall progress of this thesis. However, it was necessary to compare the tested methods fairly, and the inclusion of a holistic seeding method has advanced stress line generation. Two seeding methods from the field of computer imaging of fluid flows have been applied to stress lines. It was found that both methods produced clean results with an excellent visual distribution of stress lines, but the farthest point seeding method had a more even density distribution. Additionally, an adaptive step size was implemented in the algorithm. The literature consistently agrees that this reduces computational time by increasing and decreasing the step size when the integration method's estimated error is too large or when the angles between successive steps are too large.

The improvements made in the stress line accuracy likely did not impact the final rib centreline geometry produced in Chapter 9. Firstly, the stress lines were discretised into straight elements between the intersections, and then this geometry was modified to create the connections. Although these accuracy improvements may not have been essential for this thesis's final result, they have developed the theory for future research on stress lines.

In Chapter 6, the only known method for selecting stress lines for realisation into real structures was applied to slabs and tested. The objective was to create the needed rib centrelines for an isostatic slab design. The method was originally developed to reduce the approximation error of trusses produced from stress lines in in-plane loaded plates. It was found that this method can not be applied to slabs as it creates large clusters of elements around the areas of highest curvature, which would be impossible to construct. Also, this method does not consider any mirror or rotational symmetry which led to uneven structures. The performance of the rib geometries was partly measured by the deck elements' span lengths as it was believed that this condition would be critical for the deck thickness. However, it was later found in Chapter 9 that the bending resistance is not critical for the deck and in-fact the deck thickness was determined by the connection requirements. As the algorithmic selection method did not produce useful results, the stress lines used in the isostatic timber slab design were selected manually. This manual selection process focused on reducing creating consistent span lengths in the deck. However, it was later found in Chapter 10, that the slab design did not perform better than a one-way spanning alternative and the most likely reason for this a poor choice of rib geometry.

The stress lines are created based on a single load case. In Chapter 7, the differences between the stress lines produced from each load case were measured. Two case studies were analysed to see a range of results. It was found that concentrated loads have a very minor to virtually zero effect on the stress lines. The most significant difference in stress lines was measured when half of the slab was loaded with a maximum load, and the other half had a minimum load. However, in Chapter 8, this difference in stress lines did not produce any higher stresses than was already experienced from the primary load case, which means that the primary load case is still dominant. The reason for this is that the primary load case always has the

maximum load. A different result could occur if there is a load case with snow drift actions which causes a higher total load in the ULS combination.

11.3 Part B: Development of the Isostatic Timber Slab Design

This part of the thesis focused on developing a design of the isostatic slab using the stress line geometry created in Part A.

Firstly, in Chapter 8, an initial finite element model of the timber isostatic slab was created to analyse each element's stresses. This was used to find that increasing the plywood deck's thickness causes the compression forces to increase in the deck, and peak tension forces in the ribs to decrease. This effect was more significant in the plywood's weaker grain direction. As the thickness is increased, the amount of plies is also increased, making the deck more isotropic, meaning that less load is carried through bending along the major grain direction, and more load is carried along the minor grain direction. The plywood's orthotropic properties mean that there is less composite action along the minor plywood grain direction. Increasing the rib depth produced lower peak stresses in the ribs and deck, and the effect was of an equal proportion in the two orthogonal directions, meaning that this occurs irrespective of the plywood's orthotropicity. Altering the rib thickness had only a small impact on the composite force distributions as there is only a small range of available LVL thicknesses from the chosen manufacturer. Naturally, increasing the rib thickness will result in a reduction of peak stress in the ribs.

The finite element model was also used to assess the impact the design parameters had on the unwanted second-order effects; i.e. stresses occurring from torsion. It was found that these effects could be effectively reduced by using slender ribs. These perform better as they are stiff in major axis bending and flexible in torsion.

In Chapter 10, a design for the isostatic slab was made using the results from the initial finite element model to determine the deck thickness, rib thickness, and rib depth required to meet the maximum stress utilisation, and produce working connection designs. Three critical connections were chosen as these would have the biggest impact on the overall design. A new finite element model was created that used the final rib centrelines – which were modified for the connections and constructability. Using this, the finalised connection designs were made, and the SLS was checked. It was found that the peak deflection was equal to span/187 for the short span direction. This means that the maximum slope is greater than with the standard deflection limit of span/200. This deflection could be an issue, but this would need to be decided with a roofing contractor.

The isostatic timber slab has been designed using a simplified method as the FE model omits the connections' partial stiffness, and only a linear elastic analysis has been conducted. Also, there are no in-plane loads on the slab, which would occur from lateral wind loading. Including the correct connection stiffnesses would change the force distribution, but more importantly, the slab would deflect more, making the SLS more erroneous. As the elements are thin, buckling might occur in an individual element or as a system-wide mechanism so a second-order analysis would inform on whether the structure is safe. Including in-plane loads

will affect the peak stress values due to the additional tension and compression forces. However, it is expected that the deck has sufficient capacity to carry the additional load.

The isostatic timber slab design was compared to one-way spanning systems in Chapter 10. It was found that the isostatic slab had a better performance compared to the off-the-shelf systems. However, a one-way spanning equivalent to the two-way spanning isostatic timber slab required less material volume and less weight while maintaining the same structural depth. This finding is an incredibly significant result because it shows that the additional material is wasted in the isostatic slab in terms of structural performance. This means that either the system is inherently flawed, or the created design has been poorly optimised.

Experimental results from the literature have shown for in-plane loaded plates that stress line structures do have increased stiffness compared to the same volume of material arranged in a regular grid. However, similar tests have not been conducted for slabs, so these results may not transfer to out-of-plane loaded plates. Therefore, further research should be conducted to assess if isostatic slabs are stiffer than when the ribs are arranged in a regular diagrid.

The design process carried out in part B of this thesis is only the first design cycle. Therefore, this design's outcomes can be used to optimise the isostatic timber slab. In the next design cycle, the ribs' centreline geometry should be altered to add more beams to the centre of the slab spanning in the short direction, as this will decrease the peak moment forces and peak deflection, which are the most critical factors in the design. Different rib cross-sections should be used across the slab so that volume is minimised, but this needs to be achieved while maintaining the deflection limits. Creating a parametric model for the slab could help find an adequate design solution that combines all the calculations into a single model.

11.4 How Should an Isostatic Timber Slab be Designed?

This thesis aims to answer the research question: How Should an Isostatic Timber Slab be Designed? In part A, a new, more accurate method for generating stress lines was created and used to find the ribs' centreline geometry. In Part B, this geometry was used to create a design for an isostatic timber slab. The created design is a functional first pass and highlights key problematic areas. The isostatic timber slab has been designed using Kerto-S LVL for the ribs and Birch plywood for the deck, as these are robust timber products.

To create a design, firstly, the principal bending stress lines need to be created. A new method for stress line generation has been created with a higher accuracy than the previous methods. This method can be easily used to produce the stress lines from any out-of-plane loaded plates analysed using FEA.

A key part of the design process is selecting the stress lines used to create the ribs' centrelines. To create these, the stress lines are first discretised into straight elements between the connections. Then they are partially straightened-out so that each connection between the ribs can be made with at least one continuous beam. This process makes elements which are simple to manufacture. An alternative design process is to use curved ribs that directly follow the stress lines; this will create simpler orthogonal connections at the cost of more complicated ribs. The choice of stress lines has a direct impact on the slab's structural

performance. The stress lines should be selected by taking into account the peak moment through the ribs, and the peak deflection, as these are the critical design constraints.

The LVL manufacturing constraints should also be incorporated into the design process as these limit the available cross-sections. The LVL thickness is also constrained by the minimum limit required for the axially loaded screws in the moment connection. The rib-to-deck connection's strength also limits the plywood's thickness due to the screw manufacture's requirements.

As this is a complex system, it should be designed using a parametric model, including all of the constraints and the critical connections. The start-up time required to create this model will be saved by the ease of performing iterative design cycles.

The geometry of the isostatic slab directly depends upon its boundary and loading conditions. Therefore, the engineering will, to an extent, dictate the architecture, as particular loading and boundary conditions will result in stress line patterns which are difficult to construct. The first stage of designing an isostatic slab should be to work with the architect and client using the stress line generation tool to investigate different boundary and loading conditions and determine how severe the stress line clustering is. Stress line clustering occurs when stress lines are initially far apart but then progressively move closer together. This can be an issue because it requires acute connections between ribs which are challenging to design.

12 RECOMMENDATIONS

In this last chapter, the recommendations for future research produced from the thesis's findings are given.

1. **Stress Line Generation Improvements**
   Although it was found that using the 8-node shape function interpolation method, with the RK4 integration method and the farthest point seeding method produced the most accurate results, this method still has errors and room for improvement. The stress lines currently consist of discretised polylines and an improvement on this would be to use a higher-order curve interpolation method between each point. This would create smoother stress lines with less unwanted intersections, and better angles in the desired intersections. It would also be of interest to investigate the influence of the mesh density on the stress lines, particularly to determine whether increasing the mesh density around critical locations such as the umbilic points has a positive effect.

2. **Stress Line Selection Methods**
   An appropriate method for creating the ribs' centrelines needs to be developed by taking a holistic approach. It is recommended that this method considers the slab's peak deflection and the distribution of peak moments in the ribs when creating the centreline geometry. These factors were found to be the critical design conditions. This method should also include the "straightening-out step" where the centrelines are modified for necessary connection geometry to streamline the process.

3. **FE Modelling of the Isostatic Slab**
   The design of the isostatic slab was based on a simplified FE model. Future analysis models of the system need to include: the partial fixities in the connections, a second-order buckling analysis, and in-plane and out-of-plane loads from wind forces.

4. **Fire Analysis**
   An investigation should be conducted into the system's performance under fire conditions to ascertain if the isostatic timber slab can provide the required fire resistance. Particular attention should be drawn to whether self-extinguishment occurs, as this will directly impact the available uses.

5. **Design Cycles**
   Only the first design cycle has been completed in this thesis. It is recommended that future design cycles are undertaken to optimise the design and improve upon the identified limitations; namely, the peak deflection, and peak moments. To perform this task efficiently, it is recommended that a parametric model of the system is created which incorporates the entire design process into a single model.

6. **Connection Designs**
   Only the three most critical connections have been designed in this thesis. Designs for all of the other connections should be made and incorporated into the relevant models.

7. **Case Studies**
   The design of an isostatic slab has been made for a single case study. It is recommended that designs for other case studies are made to understand better where it is appropriate to apply the system.

13 REFERENCES

Aldinger, L. et al., 2019. *Design and Structural Modelling of Surface-Active Timber Structures Made from Curved CLT - Urbach Tower, Remstal Gartenschau 2019*. Berlin, s.n.

Antony, F., Griesshammer, R., Speck, T. & Speck, O., 2014. Sustainability Assessment of a Lightweight Biomimetic Ceiling Structure. *Bioinspiration & Biomimetics,* 9(1), p. 016013.

Blaauwendraad, 2010. *Plates and FEM: Surprises and Pitfalls*. 1st ed. Dordrecht, Heidelberg, London,edition New York: Springer.

Blaauwendraad, J., 2006. *Plate analysis, theory and application: Volume 1, Theory,* s.l.: s.n.

Blaauwendraad, J., 2006. *Plate analysis, theory and application: Volume 2, Numerical Methods,* s.l.: s.n.

Brandner, R. et al., 2016. Cross laminated timber (CLT): overview and development. *European Journal of Wood and Wood Products,* 74(3), pp. 331-351.

BSi, 2010. *BS EN 1990:2002 +A1:2005; Eurocode — Basis of structural design,* s.l.: s.n.

BSi, 2010. *BS EN 1991-1-1:2002; Eurocode 1: Actions on structures — Part 1-1,* s.l.: s.n.

BSi, 2014. *BS EN 1995-1-1:2004 +A2:2014; Eurocode 5: Design of timber structures — Part 1-1,* s.l.: s.n.

Butcher, J. C., 2016. *Numerical Methods for Ordinary Differential Equations*. 3rd ed. Chichester: Wiley.

Cobb, F., 2015. *Structural Engineer's Pocket Book*. 3rd ed. Boca Raton: CRC Press.

Czaderski, C. e. a., 2007. Versuche und Berechnungen an allseitig gelagerten 3-schichtigen Brettsperrholzplatten. *Holz als Roh-und Werkstoff,* 65(5), pp. 383-402.

DIANA FEA bv., 2020. *DIANA FEA*. [Online]
Available at: https://dianafea.com/
[Accessed 01 December 2020].

ETA-Danmark, 2019. *European Technical Assessment ETA-11/0030 of 2019/10/08*. s.l.:s.n.

Eurofins, 2020. *Product Certificate - No. EUFI29-20000676-C/EN*. s.l.:s.n.

Fiser, M., 2013. *Real time visualization of 3D vector field with CUDA*. [Online]
Available at: http://www.marekfiser.com/Projects/Real-time-visualization-of-3D-vector-field-with-CUDA/4-Vector-field-integrators-for-stream-line-visualization
[Accessed 04 February 2021].

Fonseca, J., 1997. The Loadpath-A way to understand the quality of structures. *Journal of the Interational Association for Shell and Spatial Structures:IASS,* Volume 38, pp. 129-135.

Halpern, A. B., Billington, D. P. & Adriaenssens, S., 2013. *The Ribbed Floor Slab System of Pier Luigi Nervi*. Wroclaw, s.n.

Jobard, B. & Lefer, W., 1997. Creating Evenly-Spaced Streamlines of Arbitrary Density. *Proceedings of Eurographics Workshop on Visualization in Scientific Computing '97,* Volume 7, pp. 45-55.

Karamba3D, 2020. *Karamba 3D*. [Online]
Available at: https://www.karamba3d.com/
[Accessed 01 July 2020].

Liew, A., López López, D., van Mele, T. & Block, P., 2017. Design, fabrication and testing of a protoype, thin-vaulted, unreinforced concrete floor. *Engineering Structures,* Volume 137, pp. 323-335.

Liu, Z., Moorhead, R. J. & Groner, J., 2006. An Advanced Evenly-Spaced Streamline Placement Algorithm. *IEEE Transactions on Visualization and Computer Graphics,* 12(5), pp. 965-972.

Li, Y. & Chen, Y., 2010. *Beam Structure Optimization for Additive Manufacturing based on Principal Stress Lines*. Austin, s.n.

López López, D., Veenendaal, D., Masoud, A. & Block, P., 2014. *Prototype of an ultra-thin, concrete vaulted floor system*. Brazil, International Association for Shell and Spatial Structures (IASS).

Magan, C., 2016. *Topology Optimization of a Concrete Floor Slab Guided by Vacuumatic Formwork Constrains,* Delft: TU Delft.

McLoughlin, T. et al., 2010. Over Two Decades of Integration-Based Geometric Flow Visualization. *Computer Graphics Forum,* Volume 6, pp. 1807-1829.

McNeel, 2020. *RhinoCommon Plug-in SDK*. [Online]
Available at: https://wiki.mcneel.com/developer/rhinocommon
[Accessed 10 January 2021].

Mebarki, A., Alliez, P. & Olivier, D., 2005. Farthest Point Seeding for Efficient Placement of Streamlines. *Proceedings IEE Visualization 2005,* pp. 479-486.

Metsä Wood, 2017. *Kerto-Ripa® Roof & Floor Elements*. [Online]
Available at: https://issuu.com/metsagroup1/docs/ 2017-06 kerto-ripa design and refe
[Accessed 20 January 2021].

Metsä Wood, 2019. *Declaration of Purformance - No. MW/PW/411-001/CPR/DOP*. s.l.:s.n.

Metsä Wood, 2020. *Birch Ply*. [Online]
Available at: https://www.metsawood.com/global/Products/plywood/birch-plywood/Pages/Birch-plywood.aspx
[Accessed 27 December 2020].

Michalatos, P., 2014. *Millipede*. [Online]
Available at: https://www.grasshopper3d.com/group/millipede
[Accessed 01 July 2020].

Milbank, 2016. *Hollowcore Concrete Flooring Systems*. [Online]
Available at: https://www.milbank.co.uk/hollowcore-concrete-flooring/
[Accessed 20 January 2021].

Milbank, n.d. *Hollowcore and Beam & Block Load Span Tables.* [Online]
Available at: https://www.milbank.co.uk/load-span-tables/
[Accessed 20 January 2021].

Mitchell, A., 1904. The limits of economy of material in frame-structures. *The London, Edinburgh, and Dublin Philosophical Magazine and Journal of Science,* 8(47), pp. 589-597.

Momentum structural engineers, n.d. *Cedars Hall.* [Online]
Available at: http://www.momentumengineering.com/projects/performing-arts/cedars-hall/
[Accessed 30 January 2021].

NCCR Digital Fabrication, n.d. *SMART SLAB.* [Online]
Available at: https://dfabhouse.ch/smart-slab/
[Accessed 30 January 2021].

NEN, 2016. *NEN-EN 338:2016; Structural timber - Strength classes,* s.l.: s.n.

Nervi, P., 1965. *Aesthetics and Technology in Building.* Boston: Harvard University Press.

Oasys, 2020. *GSA — Structural Design & Analysis Software.* [Online]
Available at: https://www.oasys-software.com/products/structural/gsa/
[Accessed 01 December 2020].

Piker, D., 2017. *KANGAROO PHYSICS (by Daniel Piker).* [Online]
Available at: https://www.food4rhino.com/app/kangaroo-physics
[Accessed 5 December 2020].

Rippmann, M. & Block, P., 2013. Rethinking structural masonry: unreinforced, stone-cut shells. *Construction Materials,* 166(CM6), pp. 378-389.

Rippmann, M., Liew, A., van Mele, T. & Block, P., 2018. Design, fabrication and testing of discrete 3D sand-printed floor prototypes. *Materials Today Communications,* Volume 15, pp. 254-259.

Robeller, C., Gamerro, J. & Weinand, Y., 2017. THÉÂTRE VIDY LAUSANNE – A DOUBLE-LAYERED TIMBER FOLDED PLATE STRUCTURE. *Journal of the International Association for Shell and Spatial Structures,* 58(4), pp. 295-314.

Robert McNeel & Associates, 2021. *Rhinoceros®.* [Online]
Available at: https://www.rhino3d.com/
[Accessed 10 January 2021].

ROCKWOOL, 2020. *Flat Roof Insulation Products.* [Online]
Available at: https://www.rockwool.com/products/flat-roof/
[Accessed 30 November 2020].

Schlaich, J., Schäfer, K. & Jennewein, M., 1987. Towards a Consistent Design of Structural Concrete. *Journal of the Prestressed Concrete Institute,* 32(3), pp. 74-150.

Sebera, V. et al., 2015. FE analysis of CLT panel subjected to torsion and verified by DIC. *Materials and Structures,* Volume 48, pp. 451-459.

Stora Enso, 2020. *Calculatis.* [Online]
Available at: https://www.storaenso.com/en/products/wood-products/calculatis
[Accessed 20 January 2021].

Stürzenbecher, R., Hofstetter, K. & Eberhardsteiner, J., 2010. Structural design of Cross Laminated Timber (CLT) by advanced plate theories. *Composites Science and Technology,* Volume 70, pp. 1368-1379.

Tam, K.-M. M., 2015. *Principal Stress Line Computation for Discrete Topology Design,* Boston: Massachusetts Institute of Technololgy.

Tam, K.-M. M. & Mueller, C. T., 2017. Additive Manufacturing Along Principal Stress Lines. *3D Printing and Additive Manufacturing,* 4(2), pp. 63-81.

Tayar, M. A., 1986. *DESIGN APPROACHES TO STRUCTURAL OPTIMIZATION,* Boston: MASSACHUSETTS INSTITUTE OF TECHNOLOGY.

Thiel, A. & Brandner, R., 2016. ULS Design of CLT Elements–Basics and some Special Topics. *Proceedings of the Joint Conference of COST Actions FP1402 & FP1404 KTH Building Materials,* pp. 65-87.

Tigg+Coll Architects, n.d. *House for Theo + Oskar.* [Online]
Available at: https://www.tiggcollarchitects.com/projects/house-for-theo-oskar/
[Accessed 15 June 2020].

TRADA, n.d. *Peter Hall Performing Arts Centre, Cambridge.* [Online]
Available at: https://www.trada.co.uk/case-studies/peter-hall-performing-arts-centre-cambridge/
[Accessed 16 December 2020].

Turk, G. & Banks, D., 1996. Image-guided streamline placement. *Proceedings of the 23rd annual conference on Computer graphics and interactive techniques,* pp. 453-460.

Wells, G. N., 2020. *The Finite Element Method: An Introduction.* 0.3 ed. s.l.:s.n.

Whitney, J., 1973. Shear correction factors for orthotropic laminates under static load. *Journal of Applied Mechanics,* 40(1), pp. 302-304.

ANNEX A: CODE

A.1 Introduction

This annex provides additional detail about how the code used in this thesis has been programmed. The code has been implemented using C# to produce a plugin for Grasshopper. Heavy use has been made of the 'RhinoCommon' SDK (McNeel, 2020) for Rhino 3D (Robert McNeel & Associates, 2021). This is a library that provides geometry classes with predefined properties and methods. The documentation for RhinoCommon can be found here: https://developer.rhino3d.com/api/RhinoCommon/html/R_Project_RhinoCommon.htm

A.2 Interpolation Methods

A.2.1 N+1 Order Method

The code developed for the N+1 order interpolation method has been based on Tam's (2015) writing and illustrations.

```
EVALUATE N+1 ORDER

Input:      Principal Vectors – Type: List of Vectors
            Centre Points – Type: List of Points
            Radius – Type: Double
            Evaluation Point – Type Point

Output:     Principal Stress Trajectory – Type: Vector

Method:
Begin
            find all Centre Points that are closer than the Radius to the Evaluation Point; "Contained Points" – Type: List of Points
            set new vector "Cumulative Vector" and new double "Cumulative Weight" = 0
            Loop for the length of Contained Points; Do:
                    calculate the distance between the Contained Point and Evaluation Point; "Distance" – Type: Double
                    Cumulative Vector = Cumulative Vector + the Principal Vector at location of the Contained Point
                    Cumulative Weight = Cumulative Weight + (Radius – Distance)
            EndLoop
            If Cumulative Weight is = 0; Then:
                    there are no points within the Radius around the Evaluation Point and method is Ended
            Else:
                    Principal Stress Trajectory = Cumulative Vector / Cumulative Weight
                    unitise Principal Stress Trajectory
            EndIf
End
```

A.2.2 Shape Function Method

EVALUATE 4-NODE SHAPE FUNCTION

Input: Node Location of each node (Node 1 … Node 4) – Type: Point
            Displacement Vector at each node (Vector 1… Vector 4) – Type: Vector
            Poisson's Ratio "v" – Type: Double
            Evaluation Point – Type Point

Output: Principal Stress Trajectory 1– Type: Vector
            Principal Stress Trajectory 2– Type: Vector

Method:
Begin

      CALCULATE NATURAL COORDINATES for the *Evaluation Point*; "Natural Evaluation Point" – Type: Point
      CALCULATE DIFFERENTIATED CARTESIAN SHAPE FUNCTIONS
      CALCULATE STRAINS
      CALCULATE STRESSES

      $\theta = \arctan(2 * \tau_{xy}/(\sigma_x - \sigma_y))/2$
      If $\sigma_y > (\sigma_x + \sigma_y)/2$; **Then:**
            If $\tau_{xy} > 0$, **Then:**
                  $\theta = \theta - \pi/2$
            Else:
                  $\theta = \theta + \pi/2$
            EndIf
      EndIf
      Principal Stress Trajectory 1 = $(\cos(\theta), \sin(\theta))$
      Principal Stress Trajectory 2 = $(-\sin(\theta), \cos(\theta))$

End

CALCULATE NATURAL COORDINATES

Input: Cartesian Coordinate Location – Type: Point

Output: Natural Coordinate Location – Type: Point

Method:
Begin

      create a new rectangle "Natural Rectangle" starting at (-1.0,-1.0) and ending at (1.0,1.0)
      Loop for i=0…15; **Do:**
            If *i* is even, **Then:**
                  split *Natural Rectangle* in half vertically and replace *Natural Rectangle* with the right half
                  calculate *Natural Rectangle* in cartesian coordinates using CALCULATE CARTESIAN COORDINATES;
                        "Cartesian Rectangle" – Type Rectangle
                  If *Cartesian Coordinate Location* is located inside *Cartesian Rectangle*; **Then:**
                      Natural Rectangle stays the same
                Else:
                    replace *Natural Rectangle* with the left half
                EndIf
            Else:
                  split *Natural Rectangle* in half horizontally and replace *Natural Rectangle* with the top half
                  calculate *Natural Rectangle* in cartesian coordinates using CALCULATE CARTESIAN COORDINATES;
                        "Cartesian Rectangle" – Type Rectangle
                  If *Cartesian Coordinate Location* is located inside *Cartesian Rectangle*; **Then:**
                      Natural Rectangle stays the same
                Else:
                    replace *Natural Rectangle* with the bottom half
                EndIf
            EndIf
      EndLoop
      Natural Coordinate Location is equal to the centre of *Natural Rectangle*

End

CALCULATE CARTESIAN COORDINATES

Input: Natural Coordinates (ξ,η) – Type: Point

Output: Cartesian Coordinates – Type: Point
Method:
Begin

        CALCULATE SHAPE FUNCTIONS
        Calculate "x"; x= N1*ξ + N2*ξ + N3*ξ + N4*ξ
        Calculate "y"; y= N1*η + N2*η + N3*η + N4*η
        Cartesian Coordinates = (x,y)
End

CALCULATE SHAPE FUNCTIONS

Input: Natural Coordinates (ξ,η) – Type: Point

Output: Shape Functions (N1…N4) – Type: Double
Method:
Begin

        N1 = (1.0 / 4) * (1 - ξ) * (1 + η)
        N2 = (1.0 / 4) * (1 + ξ) * (1 + η)
        N3 = (1.0 / 4) * (1 - ξ) * (1 - η)
        N4 = (1.0 / 4) * (1 + ξ) * (1 - η)
End

CALCULATE DIFFERENTIATED NATURAL SHAPE FUNCTIONS

Input: Natural Coordinates (ξ,η) – Type: Point

Output: Differentiated Natural Shape Functions (N1ξ … N4ξ, and N1η… N4η) – Type: Double
Method:
Begin

        N1ξ = -0.25 * η - 0.25
        N1η = -0.25 * ξ + 0.25
        N2ξ = +0.25 * η + 0.25
        N2η = +0.25 * ξ + 0.25
        N3ξ = +0.25 * η - 0.25
        N3η = +0.25 * ξ - 0.25
        N4ξ = -0.25 * η + 0.25
        N4η = -0.25 * ξ - 0.25
End

CALCULATE DIFFERENTIATED CARTESIAN SHAPE FUNCTIONS

Input: Natural Coordinates (ξ,η) – Type: Point

Output: Differentiated Cartesian Shape Functions (N1x … N4x, and N1y… N4y) – Type: Double
Method:
Begin

        CALCULATE DIFFERENTIATED NATURAL SHAPE FUNCTIONS
        CALCULATE JACOBIAN MATRIX TERMS
        Calculate the determinant of the Jacobian Matrix "DetJ": DetJ = (Dydη * Dxdξ) - (Dydξ * Dxdη)
        N1x = (1 / DetJ) * (Dydη * N1ξ - Dydξ * N1η)
        N1y = (1 / DetJ) * (- Dxdη * N1ξ + Dxdξ * N1η)

        N2x = (1 / DetJ) * (Dydη * N2ξ - Dydξ * N2η)
        N2y = (1 / DetJ) * (-Dxdη * N2ξ + Dxdξ * N2η)

        N3x = (1 / DetJ) * (Dydη * N3ξ - Dydξ * N3η)
        N3y = (1 / DetJ) * (-Dxdη * N3ξ + Dxdξ * N3η)

        N4x = (1 / DetJ) * (Dydη * N4ξ - Dydξ * N4η)
        N4y = (1 / DetJ) * (-Dxdη * N4ξ + Dxdξ * N4η)
End

CALCULATE JACOBIAN MATRIX TERMS

Input: Node Location of each node (Node1 … Node4)
                Differentiated Natural Shape Functions (N1ξ … N4ξ, and N1η… N4η) – Type: Double

Output: Jacobian Matrix Terms (Dxdξ, Dxdη, Dydξ, and Dydη) – Type: Double
Method:
Begin

        extract x and y coordinates from the *Node Locations;* Node1x … Node4x and Node1y … Node4y – Type: Double
        Dxdξ = N1ξ * Node1x + N2ξ * Node2x + N3ξ * Node3x + N4ξ * Node4x
        Dxdη = N1η * Node1x + N2η * Node2x + N3η * Node3x + N4η * Node4x
        Dydξ = N1ξ * Node1y + N2ξ * Node2y + N3ξ * Node3y + N4ξ * Node4y
        Dydη = N1η * Node1y + N2η * Node2y + N3η * Node3y + N4η * Node4y
End

CALCULATE STRAINS

Input: Displacement Vector at each node (Vector1… Vector4) – Type: Vector
                Differentiated Cartesian Shape Functions (N1x … N4x, and N1y… N4y) – Type: Double

Output: Strains (εx, εy, Yxy) – Type: Double
Method:
Begin

        extract x and y coordinates from the *Displacement Vectors;* U1x … U4x and U1y … U4y – Type: Double
        εx = N1x * U1x + N2x * U2x + N3x * U3x + N4x * U4x
        εy = N1y * U1y + N2y * U2y + N3y * U3y + N4y * U4y
        Yxy = N1y * U1x + N2y * U2x + N3y * U3x + N4y * U4x + N1x * U1y + N2x * U2y + N3x * U3y + N4x * U4y
End

CALCULATE STRESSES

Input: Strains (εx, εy, Yxy) – Type: Double
                Poisson's Ratio (v) – Type: Double

Output: Stresses (σx, σy, τxy) – Type: Double
Method:
Begin

        extract x and y coordinates from the *Displacement Vectors;* U1x … U4x and U1y … U4y – Type: Double
        σx = (εx + v * εy);
        σy = (εy + v * εx);
        τxy = (((1 - v) / 2) * Yxy);
End

A.3 Integration Methods

Most of the process for each integration method is the same. "SOLVE STEP" denotes where the integration step is solved by the chosen integration method. "EVALUATE" denotes where the principal stress trajectory is evaluated at a point using the chosen interpolation method

---

CREATE STRESS LINE

Input: Seed – Type: Point

Output: Stress Line – Type: Polyline Curve

Method:
Begin

    CREATE STRESS LINE PART by starting at the *Seed* and integrating forwards (*Direction* = 1)
    If the first stress line part is closed; **Then:**
        Stress Line = Stress Line Part
    Else:
        CREATE STRESS LINE PART by starting at the *Seed* and integrating backwards (*Direction* = -1)
        join the two *Stress Line Parts* into a single curve and set this to *Stress Line*
    EndIf

End

CREATE STRESS LINE PART

Input: Seed – Type: Point
            Initial Step Size – Type: Double
            Max. Error – Type: Double
            Direction (1=forwards, -1=backwards) – Type: Int
            Model's Edge – Type: Polyline Curve

Output: Stress Line Part – Type: Polyline Curve

Method:
Begin

    set new int "Level" = 0 to trace the level of step size reduction
    set new vector "v0" = (0,0)
    set new vector "v1" = (0,0)
    set new point "Start Point" = *Seed*
    set new point "End Point" = (0,0)
    set new int "i" =0
    create new list of points "Stress Line Points"

    SOLVE STEP
    v0 = End Point – Start Point
    set new vector "First Vector" = v0

    Loop while *Test* = true; **Do:**
        i = i + 1
        If the *End Point* is beyond the *Model's Edge*; **Then:** *Test* = False
        EndIf
        If *Test* = True; **Then:**
            SOLVE STEP using *End Point* as the input and outputting a new point "Next Point"
            v1 = Next Point – End Point
            measure the angle between *v0* and *v1*; "Angle" – Type: Double
            If *Error > Max. Error* **Or** *Angle > 0.1*π*; **Then:**
                Step Size = Step Size/2
                Level = Level + 1
                SOLVE STEP again using the *Start Point* as the input
            Else If *Error < Max. Error/2* **And** *Angle < 0.05*π* **And** *Level > 0*; **Then:**
                Step Size = Step Size *2
                Level = Level - 1
                SOLVE STEP again using the *Start Point* as the input
            Else:
                add *End Point* to the end of *Stress Line Points*
            EndIf
            If the length of *Stress Line Points* > 3 **And** the distance between the *Seed* and *End Point* < *Initial Step Size*
                And the angle between *First Vector* and *v1* < 0.1*π; **Then:**
                add *Seed* to the end of *Stress Line Points* as the stress line is looping
                Test = False
            EndIf
        EndIf
    EndLoop
    convert *Stress Line Points* to a polyline curve to create *Stress Line Part*

End

A.3.1 Euler Integration Method

```
SOLVE EULER STEP

Input:      Start Point – Type: Point
            Direction (1=forwards, -1=backwards) – Type: Int
            Step Size – Type: Double

Output:     End Point – Type: Point
            Error – Type: Double

Method:
Begin
            EVALUATE the principal stress trajectory at the Start Point; "V1" – Type: Vector
            calculate the vector from the Start Point to the End Point; "Vector1" – Type Vector:
                    Vector1 = V1*Step Size*Direction
            End Point = Start Point + Vector1

            EVALUATE the principal stress trajectory at the End Point; "V2" – Type: Vector
            calculate the vector step from the End Point; "Vector2" – Type: Vector:
                    Vector2 = V2*Step Size*Direction
            calculate Error:        Error = |(Vector1 – Vector2)/2|
End
```

A.3.2 RK4 Integration Method

```
SOLVE RK4 STEP

Input:      Start Point – Type: Point
            Direction (1=forwards, -1=backwards) – Type: Int
            Step Size – Type: Double

Output:     End Point – Type: Point
            Error – Type: Double

Method:
Begin
            EVALUATE the principal stress trajectory at the Start Point; "V1" – Type: Vector
            calculate the vector from the Start Point; "Vector1" – Type Vector:
                    Vector1 = V1*Step Size*Direction
            calculate the next sample point; "Point1" – Type: Point:
                    Point1= Start Point + Vector1/2

            EVALUATE the principal stress trajectory at Point1; "V2" – Type: Vector
            calculate the new vector from the Start Point; "Vector2" – Type Vector:
                    Vector2 = V2*Step Size*Direction
            calculate the next sample point; "Point2" – Type: Point:
                    Point2= Start Point + Vector2/2

            EVALUATE the principal stress trajectory at Point2; "V3" – Type: Vector
            calculate the new vector from the Start Point; "Vector3" – Type Vector:
                    Vector3 = V3*Step Size*Direction
            calculate the next sample point; "Point3" – Type: Point:
                    Point3= Start Point + Vector3/2

            EVALUATE the principal stress trajectory at Point3; "V4" – Type: Vector
            calculate the new vector from the Start Point; "Vector4" – Type Vector:
                    Vector4 = V4*Step Size*Direction

            End Point = Start Point + (Vector1+2*Vector2+2*Vector3+Vector4)/6

            EVALUATE the principal stress trajectory at the End Point; "V5" – Type: Vector
            calculate the vector step from the End Point; "Vector5" – Type: Vector:
                    Vector5 = V5*Step Size*Direction
            calculate Error:        Error = |(Vector4 – Vector5)/6|
End
```

A.4 Seeding Methods

The code for the seeding method has been developed using the pseudo-code provided in the literature.

A.4.1 Neighbour Seeding Method

The neighbour seeding method pseudo-code is provided by Jobard & Lefer (1997), as shown in the text below, extracted from their original paper. Where their pseudo-code references "streamline", this should be replaced with "stress line".

```
Compute an initial streamline and put it into the queue
Let this initial streamline be the current streamline
Finished := False
Repeat
    Repeat
        Select a candidate seedpoint at d = d_sep apart from the current streamline
    Until the candidate is valid or there is no more available candidate
    If a valid candidate has been selected Then
        Compute a new streamline and put it into the queue
    Else
        If there is no more available streamline in the queue Then
            Finished := True
        Else
            Let the next streamline in the queue be the current streamline
        EndIf
    EndIf
Until Finished=True
```

A.4.1 Farthest Point Seeding Method

The farthest point seeding method was developed by Mebarki, et al. (2005). The code developed for this thesis was done so using the pseudo-code provided in their paper. However, for clarity, the pseudo-code is rewritten below:

```
FARTHEST POINT SEEDING

Input:      First Seed – Type: Point
            dsep – Type: Double
            Model's Edge – Type: Polyline Curve

Output:     Stress Lines – Type: List of Polyline Curves

Method:
Begin
            calculate the number of division points required for dividing up the Model's Edge: "n" – Type: int:
                    n = the Model's Edge's length / dsep
            create n evening distributed points all the Model's Edge; "Edge Points" – Type: List of Points
            create a delaunay mesh from the Edge Points; "Triangulation"- Type: Mesh

            set new point "Seed" = First Seed
            Loop while Test = true; Do:
                    CREATE STRESS LINE using the Seed; "Stress Line" – Type: Polyline Curve
                    add Stress Line to Stress Lines
                    extract the points from Stress Line; "Stress Line Points" – Type: List of Points
                    insert Stress Line Points into Triangulation and recompute the mesh
                    calculate the circles that circumscribe each triangle in Triangulation; "Circumcircles" – Type: List of Circles
                    sort Circumcircles from the circles with the largest diameter to the smallest diameter
                    If the first circle's diameter in Circumcircles is < dsep*2; Then:
                            Test = false
                    EndIf
                    Seed = the centre of the first circle in Circumcircles
            EndLoop
End
```

A.5   Li and Chen Growth Method

This pseudo-code outlines the implementation of the method produced by Li and Chen (2010). This method has two subroutines: 'Discretise' and 'Find Largest Deviation'.

LI AND CHEN GROWTH METHOD

<u>Input:</u>   Initial Stress Lines (for each family: Initial Stress Lines 1 and Initial Stress Lines 2) – Type: List of Polyline Curves
No. of Iterations – Type: Int

<u>Output:</u>   Stress Line Structure – Type: List of Polyline Curves

<u>Method:</u>
Begin

    set new list of polyline curves "Stress Lines 1"= *Initial Stress Lines 1*
    set new list of polyline curves "Stress Lines 2"= *Initial Stress Lines 2*
    DISCRETISE *Stress Lines 1* into a new list of polyline curves "Discretised 1" – Type: List of Polyline Curves
    DISCRETISE *Stress Lines 2* into a new list of polyline curves "Discretised 2" – Type: List of Polyline Curves

    Loop for i=0…*No. of Iterations*; **Do:**
        FIND LARGEST DEVIATION for *Stress Lines 1* and *Discretised 1*
        FIND LARGEST DEVIATION for *Stress Lines 2* and *Discretised 2*
        Set new point "Seed" = the point with the largest deviation from either family of stress lines
        CREATE STRESS LINE using the *Seed*; "Stress Line" – Type: Polyline Curve
        Add S*tress Line* to the relevant list of stress lines: *Stress Lines 1/ Stress Lines 2*
        DISCRETISE *Stress Lines 1* and replace *Discretised 1*
        DISCRETISE *Stress Lines 2* and replace *Discretised 2*
    EndLoop

    Combine *Discretised 1* and *Discretised 2* into a single list of polyline curves; "Stress Line Structure"
End

DISCRETISE

<u>Input:</u>   Stress Lines (for each family: Stress Lines 1 and Stress Lines 2) – Type: List of Polyline Curves

<u>Output:</u>   Discretised Stress Lines "Discretised 1" and "Discretised 2" – Type: List of Polyline Curves

<u>Method:</u>
Begin

    set new list of polyline curves "Discretised 1" - Type: List of Polyline Curves
    Loop for each item in *Stress Lines 1*; **Do:**
        set new list of points "Intersection Points" – Type: List of Points.
        Loop for each item in *Stress Lines 2*; **Do:**
            Add each intersection point between the stress line from *Stress Lines 1* and the stress lines from *Stress Lines 1* to *Intersection Points*
        EndLoop
        Sort *Intersection Points* in order along the stress line from *Stress Lines 1*

        set new polyline curve using *Intersection Points* "Discretised Stress Line" – Type: Polyline Curve
        add *Discretised Stress Line* to *Discretised 1*
    EndLoop

    set new list of polyline curves "Discretised 2" - Type: List of Polyline Curves
    Loop for each item in *Stress Lines 2*; **Do:**
        set new list of points "Intersection Points" – Type: List of Points.
        Loop for each item in *Stress Lines 1*; **Do:**
            Add each intersection point between the stress line from *Stress Lines 1* and the stress lines from *Stress Lines 1* to *Intersection Points*
        EndLoop
        Sort *Intersection Points* in order along the stress line from *Stress Lines 2*

        set new polyline curve using *Intersection Points* "Discretised Stress Line" – Type: Polyline Curve
        add *Discretised Stress Line* to *Discretised 2*
    EndLoop
End

FIND LARGEST DEVIATION

Input: Stress Lines – Type: List of Polyline Curves
                Discretised Stress Lines "Discretised" – Type: List of Polyline Curves

Output: Location of Largest Deviation "Seed" – Type: Point
                Distance of Largest Deviation "Distance" – Type: Double

Method:
Begin
        set new double "Distance" = 0.0
        set new point "Seed" = (0 ,0, 0)
        Loop for i=0…length of list, *Discretised*; **Do:**
                set new polyline curve "Discretised Stress Line" = item *i* in *Discretised*
                Loop for each "Line" in *Discretised Stress Line*; **Do:**
                        set new point "Start Point" = start point of *Line*
                        set new point "End Point" = end point of *Line*
                        Loop while *Largest Deviation Distance - Largest Deviation Distance* from the last loop < 0.001; **Do:**
                                create 10 points between Start Point and End Point inclusively; "Sample Points" – Type: List of
                                        Points
                                for each point in *Sample Points* find the closest point on stress line *i* from *Stress Lines*; "Closest
                                        Points" - Type: List of Points
                                calculate the "Deviation Distance" between each point in *Sample Points* and *Closest Points*
                                set "Start Point" = the point from *Sample Points* with the largest *Deviation Distance*
                                set "End Point" = the point from *Sample Points* with the second largest *Deviation Distance*
                                set new double "Largest Deviation Distance"
                      EndLoop
                EndLoop
        EndLoop

        set new point "Seed" = the *Start Point* with the most erroneous *Largest Deviation Distance*
        set new double "Distance" = the most erroneous *Largest Deviation Distance*
End